

SOFT X-RAY SPECTROMICROSCOPY OF PROTEINS

SOFT X-RAY SPECTROMICROSCOPY
OF PROTEINS ON PATTERNED POLYMER FILMS

By

Cynthia Morin, M.Sc.

A Thesis

Submitted to the School of Graduate Studies

in Partial Fulfillment of the Requirements

for the Degree of

Doctor of Philosophy

McMaster University

© Cynthia Morin, December 2004

DOCTOR OF PHILOSOPHY (2004)
(Chemistry)

McMaster University
Hamilton, Ontario

TITLE: Soft X-ray Spectromicroscopy of Proteins on
 Patterned Polymer Films

AUTHOR: Cynthia Morin, M.Sc. (Université Laval)

SUPERVISOR: Professor A. P. Hitchcock

NUMBER OF PAGES: 221, xxviii

ABSTRACT

Synthetic biomaterials are widely used in medical applications. Their biocompatibility is believed to be related to first interactions with proteins. Thus, quantitative techniques which provide information on the spatial distribution of adsorbed proteins are of interest.

In this work, two soft X-ray spectromicroscopy techniques, scanning transmission x-ray microscopy (STXM) and photoemission electron microscopy (X-PEEM), were used for the determination of the preferred sites of interaction of blood proteins on phase segregated polymer films. These techniques are advantageous due to their high chemical speciation, which is provided by near edge X-ray absorption fine structure (NEXAFS) spectroscopy, and their high spatial resolution of ~50 nm for STXM and ~100 nm for X-PEEM. STXM, X-PEEM and atomic force microscopy (AFM) were used to characterize thin film polymer blends of polystyrene (PS) and poly(methylmethacrylate) (PMMA). PEEM was used to map the adsorption of fibrinogen (Fg) on this surface from both isotonic, buffered, and low ionic strength, unbuffered aqueous solutions at varying fibrinogen concentrations. STXM was used to locate human serum albumin (HSA) and Fg on microtomed sections of polyurethanes containing copolymer filler particles. The results shown in this thesis demonstrate for the first time that STXM and X-PEEM have the capability to simultaneously locate and detect both adsorbed proteins at the submonolayer level, and the underlying polymer phases, and to map the protein distribution relative to the polymer phases. The STXM measurements are quantitative and can be carried out in the presence of an overlayer of the protein solution.

ACKNOWLEDGEMENTS

First and foremost, I wish to thank God for leading me through these challenging and growing years of graduate school. Deuteronomy, 8:1-18, summarizes this very well.

Acknowledgements to my supervisor, Prof. Adam Hitchcock, are most rightly due. I am sincerely grateful that he has allowed me to pursue this project. I am also thankful for his scientific guidance, numerous suggestions and generous encouragements throughout the years.

I would also like to thank my supervisory committee members, Dr. John Brash and Dr. Harald Stöver, for their suggestions throughout our yearly committee meetings since March 2000, and for reading and commenting on a draft of this thesis.

From the Hitchcock group, many thanks to all the former and current lab members: Dr. Gabi Eustatiu, Dr. Ivaylo Koprinarov, Dr. Tolek Tyliczszak, visiting scientist Dr. Hiromi Ikeura-Sekiguchi, Robert Lessard, Peter Brodersen, Dr. Tohru Araki, Dr. Glyn Cooper, Dr. Cassia Turci, Antonio Guerrero, Jian Wang, Li Li and Hua Jiang. Thank you for your wonderful camaraderie and support.

At the ALS, I would like to thank the doctoral fellowship committee for granting me the opportunity to spend a full year (2002) in Berkeley when a lot of the results from this thesis were obtained. Also, the support from beamline scientists Dr. Andreas Scholl and Andrew Doran (PEEM2), and Dr. David Kilcoyne and Dr. Tolek Tyliczszak (STXM532), were always very appreciated.

Special warm thanks to all my dear friends, for making my life all that much better, complete, and enjoyable throughout the PhD experience. The list of their names would be too exhaustive...

Finally, for my family, to whom this thesis is dedicated: Maman (Rollande), Papa (Raymond), Yves, Josée, Alex, Carl, Nicolas, Chaintha, Sotheavy, David, and all the others to come...

Je Reviens Chez Nous

(words from Jean-Pierre Ferland : Master Serie –PolyGram 839 671-2)

Il a neigé à Port-au-Prince
Il pleut encore à Chamonix
On traverse à gué la Garonne
Le ciel est plein bleu à Paris
Ma mie l'hiver est à l'envers
Ne t'en retourne pas dehors
Le monde est en chamaille
On gèle au sud, on sue au nord

Fais du feu dans la cheminée
Je reviens chez nous
S'il fait du soleil à Paris
Il en fait partout

La Seine a repris ses vingt berges
Malgré les lourdes giboulées
Si j'ai du frimas sur les lèvres
C'est que je veille à ses côtés
Ma mie j'ai le cœur à l'envers
Le temps ravive le cerfeuil
Je ne veux pas être tout seul
Quand l'hiver tournera de l'œil

Fais du feu dans la cheminée
Je reviens chez nous
S'il fait du soleil à Paris
Il en fait partout

Je rapporte avec mes bagages
Un goût qui m'était étranger
Moitié dompté, moitié sauvage
C'est l'amour de mon potager

Fais du feu dans la cheminée
Je reviens chez nous
S'il fait du soleil à Paris
Il en fait partout

Fais du feu dans la cheminée
Je rentre chez moi
Et si l'hiver est trop buté
On hivernera

TABLE OF CONTENTS

Preliminaries	Page
Descriptive Note	ii
Abstract	iii
Acknowledgements	iv
Table of contents	vi
List of Figures	ix
List of Tables	xxi
List of Abbreviations and Symbols	xxiii
Chapter 1. INTRODUCTION	1
1.1 Introduction to Biomaterials	1
1.2 Capabilities of Techniques Commonly Used in Biomaterials Development	7
1.3 Role of X-Ray Spectromicroscopy in This Field?	10
1.4 Outline of Thesis Chapters	19
Chapter 2. METHODS	24
2.1 Synchrotron Radiation	24
2.2 NEXAFS Spectroscopy	30
2.3 STXM principles	40
2.4 X-PEEM principles	52
2.5 Atomic Force Microscopy	60
Chapter 3. EXPERIMENTAL	67
3.1 Data Acquisition in STXM	67

3.2	Data Acquisition in X-PEEM	73
3.3	Spectromicroscopy Data Analysis	98
3.4	Sample Preparation	113

Chapter 4.	X-RAY SPECTROMICROSCOPY OF IMMISCIBLE POLYMER BLENDS: POLYSTYRENE/POLY(METHYL METHACRYLATE)	129
-------------------	--	------------

	Permission from the publisher to reprint	130
--	--	-----

4.1	Introduction	131
4.2	Experimental	135
4.3	Results	138
4.4	Discussion	149

Chapter 5.	SELECTIVE ADSORPTION OF PROTEIN ON POLYMER SURFACES STUDIED BY SOFT X-RAY PHOTOEMISSION ELECTRON MICROSCOPY.	153
-------------------	---	------------

	Permission from the publisher to reprint	154
--	--	-----

5.1	Introduction	155
5.2	Experimental	156
5.3	Results	158
5.4	Discussion and summary	162

Chapter 6.	TOWARDS PRACTICAL SOFT X-RAY SPECTROMICROSCOPY OF BIOMATERIALS	165
-------------------	---	------------

Permission from the publisher to reprint	166
6.1 Introduction	167
6.2 Experimental	168
6.3 Results	173
6.4 Discussion and summary	181
Chapter 7. SUMMARY AND FUTURE WORK	186
Appendices	191
A.1. Published work	191
A.2. Oral presentations by the author	194
A.3. Posters presented by the author	196
B.1 Software Packages	199
References	202

LIST OF FIGURES

Chapter 1	
Fig. 1.1	Qualitative comparison of the relative performance of various microanalytical techniques applicable to soft matter. Chemical information refers to speciation, not simply elemental analysis. Spatial resolution is that typically achieved rather than the absolute state-of-the-art. 18
Chapter 2	
Fig. 2.1	Emission patterns of radiation from electrons in circular motion; case (a): at a low velocity compared to the velocity of light; and case (b): approaching the velocity of light. 25
Fig. 2.2	Schematic of the three approaches used for synchrotron light generation. Bending magnet light is available at all sources. Wigglers or undulators, which are periodic magnet structures installed in straight sections, provide much enhanced flux and brightness. (Figure courtesy of ALS, LBNL). 27
Fig. 2.3	Comparison of the brightness of the bending magnet and undulator sources at the Advanced Light Source (ALS) to that of other common light sources. 29
Fig. 2.4	X-ray absorption response [HGD93] of fibrinogen, a blood protein, in the region of carbon, nitrogen and oxygen K-edges (thick line) normalized to optical density for 1 nm of protein at its standard density. NEXAFS spectra of fibrinogen recorded by X-PEEM scaled to the predicted elemental response (thin line). A rapid increase of the absorption occurs at the threshold of energy required to excite electrons from these inner shells. 32
Fig. 2.5	Two methods of recording X-ray absorption spectra: a) transmission and b) electron yield. c) A cartoon of electron generation and propagation in the near surface region. A represents an Auger electron and p is a primary electron. See text for further explanation of the figure. 33
Fig. 2.6	PEEM2 and PEEM3 spatial resolution as a function of lens

	transmission [P].	36
Fig. 2.7	C1s, N1s, and O1s NEXAFS spectra of PS, PMMA and Fg recorded as pure materials with X-PEEM. The straight lines indicate the elemental response. The intensities within each panel are on the same scale, although offsets are used for clarity. Different scaling is used for each panel.	37
Fig. 2.8	Comparison of PS and PMMA C1s energy diagrams and spectra.	37
Fig. 2.9	Chemical structures representative of PMMA, Fg and PS.	38
Fig. 2.10	Focusing scheme of a STXM: a) in diagram form, b) a picture c) scanning electron microscope image of the inner part of a Fresnel Zone Plate Lens. This lens has 318 nickel zones, a diameter of 45 μm , and the smallest (outermost) zone is 35 nm wide. Courtesy of Center for X-Ray Optics, LBNL.	41
Fig. 2.11	5.3.2 STXM components a) schematically, b) top view picture	45
Fig. 2.12	Geometry of the 5.3.2 detector for transmitted photons	46
Fig. 2.13	Beamline 5.3.2 layout (Plan view)	50
Fig. 2.14	Beamline 7.0.1 layout	50
Fig. 2.15	The X-PEEM spatial resolution is limited to ~ 100 nm for polymer samples. (a) PS component map from a stack fit analysis of a 30:70 PS:PMMA sample, annealed 8 hours at 160 $^{\circ}\text{C}$. (b) blow up of the black/white box in (a). (c) Line profile from the region between the two black/white lines shown in (b). (d) The blow up from the dotted box in (c) shows that the resolution is approximately 100 nm. This is the distance between 20% and 80% of the maximal intensity where 100% corresponds to the center of the PS microdomain	55
Fig. 2.16	PEEM2 beamline layout.	57
Fig. 2.17	Schematics of PEEM2	58
Fig. 2.18	Schematic representation of an AFM	60
Fig. 2.19	(A) Typical force-vs-sample z displacement curve. (B) The cycle	

in (A) is shown in terms of a schematic potential between the tip-sample functional groups (for a functionalized tip). 62

Chapter 3

- Fig. 3.1 Images of PS:PMMA floated on Si_3N_4 a) $10\mu\text{m} \times 10\mu\text{m}$ at 285.1 eV, in transmission; b) Figure a) converted to optical density (OD); c) $4\mu\text{m} \times 4\mu\text{m}$ at 285.1 eV, in transmission, showing the presence of micro domains in both phases; d) OD of c). 69
- Fig. 3.2 (left) location of points where the spectra were acquired, (right) spectra derived from point signals and hole signal (out of image range) recorded at same time. 70
- Fig. 3.3 Example of a linescan and subsequent analysis (see text for detail). 71
- Fig. 3.4 Representation of a “stack”, or image sequence. Same sample as figure 3.1. 72
- Fig. 3.5 PEEM2 FOV as a function of voltages. 75
- Fig. 3.6 a) Histograms of dark noise for the flashlight (FL) OFF and ON, showing the shift in pixel intensity with FL ON, and an example of a dark image from the old PEEM2 camera; b) Intensity of pixels for dark and gain as a function of time; c) histogram of a gain image, the circle shows a saturated pixel with intensity $4096, 2^{12}$. 79
- Fig. 3.7 The measured X-PEEM signal consists of several variables which are described in equations 2.6-2.8. Consequently, it is a function of the sum of the electrons that are emitted from the outer layer of the surface of the material, the polymer or organic film and the substrate on which the film is adsorbed. The desired signal is that from only the electrons emitted from the sample. 81
- Fig. 3.8 Comparison of strong signal (40 nm PS:PMMA) versus weak signal (patterned SAM). a) 285 eV image of a 66:33 PS:PMMA film (40 nm); b) spectra of internal Si- I_0 and PS:PMMA region, from stack not normalized, and from stack normalized with internal I_0 ; c) 280 eV image of a patterned film (< 4 nm) made of streptavidin (SA) stamped into $2\mu\text{m} \times 2\mu\text{m}$ lines, backfilled with thiolated polyethylene glycol (PEG-SH), exposed to a biotinylated-ferritin (BFe) solution; d) Rescaled spectra of light and dark stripes: lower

	curves, before normalization with an external I_0 , upper curves, after normalization.	82
Fig. 3.9	HF-etched Si C1s NEXAFS spectra acquired in sequence under similar beamline and microscope conditions, except for the dwell time. A: 2.4 seconds, B: 0.3 seconds. The rescaled spectra in the inset show that their shapes are similar.	84
Fig. 3.10	Schematic representations of sample alignment and its effect on illumination on the CCD. a) ideal case: the sample is perfectly aligned, large number of photoemitted electrons are detected on the CCD; b) the sample is misaligned, very few photoelectrons reach the camera; c) the sample is misaligned, but the larger X-ray spot size, from the opened exit slit, allows to see more electrons at the detector and the sample position may be better optimized by adjusting the sample tilt and height.	86
Fig. 3.11	Example of C1s NEXAFS spectra of an internal I_0 signal through a scratched polymer film and an external (HF-etched Si) I_0 spectrum. These were acquired at different times under different beamline and microscope settings, so their shapes are expected to be different. The sharp feature between 288-289.5 eV, and the shoulder between 284.9-285.8 eV in the internal spectrum are from a carbonaceous contaminant which is likely from remaining polymer film. These spectra were arbitrarily energy calibrated so that their dips would coincide, and their intensities were rescaled.	87
Fig. 3.12	Photon flux (in photons/second normalized at 400 mA ALS ring current) from 7.3.1.1 monochromator measured by an X-ray photodiode. The insert shows the effect of a Ti filter on the relative shape and flux at the C1s edge.	89
Fig. 3.13	I_0 spectra measured off an HF-etched piece of Si, with and without Ti.	90
Fig. 3.14	Curve of the relative intensity of light hitting a sample in PEEM2 as a function of the chopper value for a fixed mask value of 2.5 with Ti-in.	91
Fig. 3.15	Appended C1s PMMA spectra show the effect of radiation damage on the PMMA C1s NEXAFS spectrum. The exposure time for each spectrum was 150 seconds (see text for more details).	95

Fig. 3.16	C1s spectral changes in PMMA (X-PEEM), Fg (STXM) and PS (STXM) with radiation damage. The spectral changes with damage are the same in the two microscopes..	96
Fig. 3.17	N1s and O1s spectral changes in PMMA (X-PEEM) and Fg (X-PEEM)	97
Fig. 3.18	Scheme of the general methods used to analyze an image sequence in STXM and X-PEEM.	99
Fig. 3.19	Zstack_align widget (see text for details).	101
Fig. 3.20	C1s NEXAFS spectra of PS, PMMA recorded as pure materials with STXM (thick lines) and with X-PEEM (lines of medium thickness). The straight lines indicate the elemental response. The intensities are on the same scale, although an offset is used for clarity.	104
Fig. 3.21	Evaluation of three stack fitting routines for a STXM C1s stack of PS:PMMA: a) to d) were generated using “SVD”; a) PS component map; b) PMMA component map; c) chi square map; d) rescaled color-coded composite map: R = PS, G = PMMA; e) to i) were generated using “stack-fit”; e) PS component map; f) PMMA component map; g) chi square map; h) rescaled color-coded composite map; l) constant map; j) to m) were generated using “CGO”; j) PS component map; k) PMMA component map; l) chi square map; m) rescaled color-coded composite map; n) Non-contact mode height AFM images of the same sample.	107
Fig. 3.22	SVD analysis of PS:PMMA/Si (last entry of table 3.4), C1s aligned stack and ROI images shown at 285.1 eV; a) PS component map; b) PMMA component map; c) chi-square map; d) rescaled color-coded composite map; e) PS 1.01; f) PS 1.5; g) PS 1.01-1.5; h) PS 1.8; i) PMMA 0.7; j) PMMA 0.95; k) PMMA 0.7-0.95; l) PMMA 1.4.	111
Fig. 3.23	SVD analysis of PS:PMMA/Si (last entry of table 3.4), C1s simulated misaligned stack and ROI images shown at 285.1 eV; a) PS component map; b) PMMA component map; c) chi-square map; d) rescaled color-coded composite map; e) PS 1.05; f) PS 1.45; g) PS 1.05-1.45; h) PS 1.6; i) PMMA 0.45; j) PMMA 1.1; k) PMMA 0.45-1.1; l) PMMA 1.2.	112
Fig. 3.24	25 μm^2 non-contact mode AFM image of a clean Si wafer chip	

	(see text above).	118
Fig. 3.25	(a) AFM height image (10 μm x 10 μm) of 30:70 PS:PMMA (1M:310K), 1% w/w in toluene spun cast on SiO _x at 4000 rpm, annealed 8 hours at 160 °C, (b) phase mode, simultaneous acquisition. Last entry of table 3.4.	122
Fig. 3.26	AFM images (non-contact mode, height, 10 μm x 10 μm) of 30:70 PS:PMMA films in toluene, 1%, spun cast at 4000 rpm: a) 1.1M:317K on Au/Si ₃ N ₄ , annealed 2 hours at 140°C (October 2000); b) 1.1M:317K on mica floated on Si ₃ N ₄ , annealed 8 hours at 160°C (April 2003); c) 100K:100K on thin region of 250 μm wide Si ₃ N ₄ window, annealed 2 hours at 140°C (January 2002); d) 100K:100K on thick region of 250 μm wide Si ₃ N ₄ window, annealed 2 hours at 140°C (January 2002); e) 100K:100K on thin region of 2 mm wide Si ₃ N ₄ window, annealed 2 hours at 140°C (January 2002); f) 100K:100K on wafer off of 2 mm wide Si ₃ N ₄ window, annealed 2 hours at 140°C (January 2002).	126
Fig. 3.27	Schematic representations of the protein adsorption procedures for X-PEEM and STXM samples.	128
Chapter 4		
Fig. 1	(a) STXM optics. (b) C 1s NEXAFS spectra of PMMA and PS derived from STXM image sequences. The as-recorded spectra are indicated by the thin lines, while the estimated pure material response are the thick lines (see text). The measured OD intensities have been converted to linear absorption coefficient by normalization below 284 and above 300 eV to the linear absorption for pure PS and PMMA computed from elemental absorption parameters [32] and the known densities. (c) ALS X-PEEM optics. (d) C 1s NEXAFS spectra of PS and PMMA derived from X-PEEM image sequences. A portion of the PS signal has been subtracted from the PMMA signal to reduce the intensity of the 285-nm signal to baseline. In (b) and (d) the PMMA spectrum has been offset by 1 and 10 units, respectively.	137
Fig. 2	STXM (upper) and X-PEEM (lower) images of annealed 30/70 (w/w) PS/PMMA recorded at 285.1, 288.4 and 300 eV. The images are presented on the same spatial scale. The sample for STXM was spun cast on Au-coated silicon nitride, while that for X-PEEM was spun cast on an oxidized silicon wafer. The STXM images are	

displayed in optical density using a common gray scale (B50,W51.4 OD units). The X-PEEM images have been normalized to incident flux (recorded independently from an HF-etched Si wafer) and are plotted on a common gray scale (B50,W5110 arbitrary intensity units). In each case lighter pixels indicate stronger X-ray absorption (and/ or, in case of X-PEEM, higher probability of electron emission). (ALS X-PEEM, ALS STXM). 138

Fig. 3 Comparison of AFM, X-PEEM and STXM results for annealed 30/70 (w/w) PS/PMMA. The STXM was measured from a film spun cast on a Au-coated silicon nitride window, whereas the AFM and X-PEEM were recorded from the blend spun cast on a Si wafer covered with native oxide. The AFM height-mode images located above each X-ray micrograph are for samples prepared on the same substrate as the corresponding X-ray micrograph. Ex-situ vacuum annealing was carried out as indicated in Table 1. The X-PEEM and STXM are color coded composite images derived from the individual PS and PMMA component maps obtained by linear regression analysis of the C 1s spectrum at each pixel (Figs. 5 and 6). The color intensities in STXM are independently scaled to better represent spatial relationship, although at the cost of relative intensities. A third, impurity component was not included in this composite (see spectral fits in Figs. 7 and 8). The thickness of the sample was 60 nm as determined by AFM from the step height at a scratch. (McMaster AFM, ALS X-PEEM, ALS STXM). 140

Fig. 4 Comparison of AFM, X-PEEM and STXM results for as-prepared 30/70 (w/w) PS/PMMA. Details as indicated in the caption of Fig. 3. (McMaster AFM, ALS X-PEEM, ALS STXM). 141

Fig. 5 PS and PMMA component maps derived from X-PEEM for annealed 30/70 (wt.%/wt.%) PS/PMMA. The vertical scales are in units of normalized response derived by setting the 300–282-nm intensity jump in the PS and PMMA reference spectra to 10. The lower plot is the intensity profile along the line indicated in the component maps. Note that the PMMA signal goes close to zero in the PS-rich regions but the PS-signal always is offset from the zero. (ALS X-PEEM). 142

Fig. 6 PS and PMMA component maps derived from STXM for annealed 30/70 (w/w) PS/PMMA. The vertical scales are thickness in nm, derived by using the PS and PMMA reference spectra calibrated in linear absorption coefficient. The lower plot is the intensity profile along the line indicated in the component maps. (ALS X-STXM). 142

- Fig. 7 Spectral decomposition of the C 1s spectra extracted from the PS-rich (2.5*PS, 1.5*impurity, 0.2*PMMA, where the reference spectra are jump-normalized) and PMMA-rich (0.25*PS, 1.0*impurity, 1.8*PMMA) domains of the near surface region of the annealed 30/70 PS/PMMA measured by X-PEEM. The pixels contributing to the spectra are indicated in the insert images. In addition to a significant PS component in the PMMA domains and a small but detectible PMMA signal in the PS domains, the fit to the NEXAFS spectra indicates there is a third component ('impurity') at the surface with an aliphatic character. This could be a surface contaminant such as a siloxane or silicone from the preparation. (ALS X-PEEM). 144
- Fig. 8 Spectral decomposition of the C 1s spectra extracted from the PMMA-rich (45 nm PS, 22 nm PMMA) and PS-rich (5 nm PS, 72 nm PMMA) domains of the annealed 30/70 PS/PMMA measured by STXM. The component thicknesses were derived by extracting the sum of the spectra at the indicated pixels (black on upper image, and white on lower image) and fitting to the linear absorption coefficient reference spectra for pure PS and PMMA. The spectra could be fit satisfactorily using only the PS and PMMA components. (ALS STXM). 144
- Fig. 9 (a) Surface friction image (SFM); and (b) PS, (c) PMMA and (d) total thickness maps derived by SVD analysis of NEXAFS images recorded with STXM from a 50/50 w/w PS/PMMA (27K/27K) blend annealed for 10 min at 1808C. (NSLS STXM. Adapted from Ref.[16]). 146
- Fig. 10 Morphology of 50/50 w/w PS/PMMA (27K/27K) blend annealed for 1 week at 1808C. (a) AFM topography after preferential dissolution of PS via cyclohexane washing; (b) PS map, (c) PMMA map, (d) total thickness map derived from STXM. (NSLS STXM. Adapted from Ref. [16]). 147
- Fig. 11 (a) PS and (b) PMMA component maps derived from X-PEEM of an aggressively annealed low MW 50/50 PS/PMMA blend spun cast on a SiO surface. Spectral decomposition of the C 1s spectra extracted from (c) the PMMA-rich (2.5*PS, 1.5*impurity, 0.2*PMMA) and (d) PS-rich (0.25*PS, 1.0*impurity, 1.8*PMMA) regions, at the locations indicated in the insert images (the reference spectra are edge jump-normalized). For this measurement the flux used was too high and the PMMA was damaged. However only part of the 285-eV signal in the PMMA-rich spectrum arises from beam damage, as can be seen by comparison to the C 1s spectrum of pure PMMA which has been radiation damaged to produce a similar level of reduction of the $\pi^*_{C=O}$

	peak relative to the continuum. (ALS X-PEEM).	148
Fig. 12	(a) AFM image of the annealed low MW 50/50 PS/PMMA blend after washing with cyclohexane to remove surface PS. (b) Expanded region of the AFM shown in (a) which shows the pits where small droplets of PS have been removed (NCSU). (c) AFM (height mode) image of a 21K/21K 50/50 w/w PS/PMMA blend spun cast from toluene solution and vacuum annealed for 1 h at 180°C. (d) Expanded perspective view of the PMMA domain showing small PS droplets sitting on the surface (McMaster).	149
Fig. 13	(a) High resolution C 1s STXM image at 285.2 eV of 40/60 w/w PS/PMMA (21K/22K) blend annealed for 1 day at 165°C. (b) Expanded region of the STXM image shown in (a). Numerous small PS domains are readily visible. The area indicated in the lower part of (b) was used for the quantitative analysis discussed in the text. (NSLS STXM).	150
Chapter 5		
Fig. 1	(a) X-PEEM images at 283, 285.1, 288.4 and 290 eV, 4 of the 40 images in the C 1s region of an annealed 28:72 (w/w) PS:PMMA blend thin film spun cast on native oxide Si (note the actual average surface composition is 57:43; see text). (a) Spectra from the indicated spots. (c and d) Component maps of PS and PMMA derived by singular value decomposition of the C 1s image sequence. (e) Color coded composite map (red: PS; green: PMMA).	157
Fig. 2	Isotherms for adsorption of ¹²⁵ I-labeled Fg from phosphate buffer (pH 7.2) to pure PS, pure PMMA and the PS:PMMA blend surface. The inset compares the isotherms at low concentration from phosphate buffer and water.	158
Fig. 3	C 1s, N 1s and O 1s NEXAFS spectra of PS, PMMA and Fg recorded as pure materials with X-PEEM. The dashed lines indicate the elemental response [10]. The intensities within each panel are on the same scale, although offsets are used for clarity. Different scaling is used for each panel.	159
Fig. 4	(a) Composite map (red: PS; green: PMMA; blue: Fg) derived from component maps extracted by stack fit analysis of a C 1s image sequence for fibrinogen (0.05 mg/ml in buffer) adsorbed on the	

PS:PMMA blend surface. (b–d) Component maps indicating the regions from which spectra of high-PS, high-PMMA and high-Fg signals were extracted and displayed in (e–g) which also plot the curve fits of the extracted spectra (dots: data; black line: sum of component signals; colored lines: component signals). Most of the 285 eV signal in the spectrum of the PMMA-rich pixels comes from radiation damage. 160

Fig. 5 (a) Spectra from high-PS pixels of the PS component maps generated from stack fit analysis of C 1s image sequences recorded for fibrinogen (0.005, 0.01, 0.05 and 1.0 mg/ml in buffer) adsorbed on the PS:PMMA blend surface. (b) Same for spectra of high-Fg pixels of the Fg component map. 161

Fig. 6 (a) Color composite map (top) (red: PS; green: PMMA; blue: Fg) and high-PS, high-PMMA and high-Fg spectra derived from a C 1s image sequence recorded for 0.05 mg/ml Fg(water) (bottom). The inset map in the spectral plot indicates the region from which the spectrum was extracted, identified by threshold masking the component maps. (b) Same for N 1s image sequence. In this case, only a two-component fit was carried out (green: PS and PMMA; blue: Fg). (c) Same for O 1s image sequence. The image sequences were collected over three different regions of the sample which is why the domain patterns differ for each core edge study. 162

Chapter 6

Fig. 1 (a) Schematic of undulator beamline 7.0 and the STXM endstation at the Advanced Light Source (ALS) BL 7.0. The inset shows details of the STXM optics. (b) Images of sample #355, a compressed polyurethane foam with styrene acrylonitrile (SAN) and poly-isocyanate poly-addition product (PIPA) filler particles. This image was recorded at 287.2 eV, the energy of the C 1s \rightarrow π^* CN transition at which the SAN particles selectively absorb. (c) Spectra from spatially selected regions compared to a defocused sample average spectrum. These spectra were actually obtained from an image sequence, but equivalent point spectra can be acquired with the STXM. (d) Illustration of the image sequence (stack) concept. Four of 120 images are displayed, along with a color coded chemical constituent map derived by pixel-by-pixel curve fitting (R = PIPA, G = SAN, B = matrix). 171

- Fig. 2 (top) Comparison of the C 1s NEXAFS spectra of albumin and fibrinogen recorded in the STXM. (lower) Illustration of monolayer sensitivity of STXM spectroscopy to pure albumin. The central panel displays an image (288.2 eV) of a deposit of pure albumin on a silicon nitride window (dry), and the signal from a linescan spectrum across the dotted line. The spectra shown in the lower panel were extracted from the linescan by adding signal over less than 1 micron in the areas indicated by dashed lines, labeled A and B. Spectrum B is offset vertically by 0.02 units. The OD of only 0.01 in the C 1s continuum is equivalent to 3 nm protein. An albumin molecule in its standard conformation is 3 x 8 nm, indicating monolayer sensitivity. 174
- Fig. 3 Reference spectroscopy (left), transmission images at 285.1 eV (highlight PIPA) and 288.2 eV (highlight protein) (center); and (right) component maps of albumin and PIPA derived from a C1s image sequence recorded from a thin section sample of #529 (PIPA-in-TDI polyurethane) with deposited albumin, measured in the dry state. In the weakest regions of the albumin 'smear' (e.g. the circled region), the signal is at the monolayer level. 176
- Fig. 4 Analysis of STXM of fibrinogen adsorbed on #355 (TDI polyurethane with PIPA and SAN filler particles) measured in the dry state. The sample was prepared by a true adsorption process from buffer at low concentration (0.1 mg/ml) followed by carefully washing off the expense protein then drying. (left) reference spectra, placed on absolute linear absorption scale. Four of the six 'image' panels are the quantitative component maps of the SAN, PIPA, fibrinogen and matrix components; the vertical gray scale of each is the approximate thickness of that component in nm. The other two are the map of the residuals averaged over the full energy range measured and a color coded component map (red = SAN, green = PIPA, blue = Fg). 178
- Fig. 5 (left) Color-coded composite image derived from a C1s STXM image sequence of fibrinogen adsorbed from a 0.1 mg/ml buffer solution onto #355 substrate. The measurements were made with the sample rehydrated by a ~ 1 μm thick layer of deionized water in silicon nitride wet cell, in order to explore the masking effect of overlayer water. The combined byte-scaled SAN (red), PIPA (green) and protein (blue) component maps displays the spatial relationship of the protein relative to the two types of filler particles and the matrix. (right) Spectrum of the blue highlighted regions in the insert image (pixels where the Fg indicates more than 60 nm) along with

LIST OF TABLES

Chapter 1		
Table 1.1	Medical implants used in the United States (as of 2002) [CR02]	3
Table 1.2	Strategies to achieve protein-resistant (non-fouling) surfaces [CR02]	7
Table 1.3	Methods to Characterize Surfaces, <i>bold italic</i> methods were used in this thesis.	9
Table 1.4	Summary of selected literature in soft X-ray microscopy	12
Chapter 2		
Table 2.1	Advantages and disadvantages of beamline and microscope 5.3.2	51
Table 2.2	Advantages and disadvantages of beamline and “old” 7.0.1 microscope	51
Chapter 3		
Table 3.1	Maximum image size available for coarse and fine stages at STXMs 7.0.1 and 5.3.2	68
Table 3.2	Maximal exposure times for PS, PMMA, Fg with mask 2.5 and chopper 17.	94
Table 3.3	Curve fit results of PS and PMMA masked regions from figure 3.19 (aligned C1s PS:PMMA/Si X-PEEM stack)	111
Table 3.4	Curve fit results of PS and PMMA masked regions from figure 3.19 (simulated misaligned C1s PS:PMMA/Si X-PEEM stack)	112
Table 3.5	AFM investigation of all PS:PMMA samples explored in X-PEEM	119
Table 3.6	PS:PMMA samples explored in X-PEEM	124

Chapter 4

Table 1	Details of fabrication and AFM characterization of the PS/PMMA blend samples	136
Table 2	Composition of as-prepared and annealed bulk and surface of 30/70 PS/PMMA films as determined by STXM, X-PEEM and AFM.	143

Chapter 5

Table 1	Advancing water contact angles for PS, PMMA and PS:PMMA.	158
Table 2	Composition of selected PS-rich, PMMA-rich and Fg-rich regions from analysis of C 1s image sequences of a PS/PMMA sample exposed for 10m to phosphate-buffered Fg solution	161
Table 3	Composition of selected PS-rich, PMMA-rich and Fg-rich regions from analysis of C 1s, N 1s, and O 1s image sequences of Fg(water)/PS:PMMA samples.	163

Appendix

Table B.1	List of PEEM2 software.	201
-----------	---------------------------------	-----

LIST OF ABBREVIATIONS AND SYMBOLS

Å	Angstrom
$a^{1/2}$	Characteristic Critical Dose
a	Dose in MGy (mega grays)
A	Scale Factor
A/D	Analog-to-Digital
AFM	Atomic Force Microscopy
ALS	Advanced Light Source
Alb	Albumin
AOI	Area of Interest, region of a sample in PEEM2
BFe	Biotinylated-Ferritin Solution
BESSY	Berliner Elektronenspeicherring-Gesellschaft für Synchrotronstrahlung
B_{ij}	Background (Signal With No X-Rays) Intensity for Pixel ij
BIMR	Brockhouse Institute for Materials Research
BNL	Brookhaven National Laboratory
BO	Butane Oxide
BPDA-PDA	poly(biphenyltetracarboxylic dianhydride-p-phenylenediamine) polyimide
BW	Band Width
c	Speed of Light in Vacuum
°C	Degree Celsius
CaPeRS	Canadian Photoelectron emission Research Spectromicroscope
CCD	Charge Coupled Device
CGO	Conjugate Gradient Optimization
CLS	Canadian Light Source
CM-AFM	Contact Mode- Atomic Force Microscopy
CPP	Copolymer Polyol
CXRO	Center for X-Ray Optics
δ	Polydispersity, M_w/M_n

δ_{rN}	Width of the Most Outer Zone (Nth) of a Zone Plate
$\Delta\phi$	Angular Spread of Synchrotron Radiation
Δr	Diffraction Limited Spatial Resolution
D	Zone Plate Diameter
Da	Dalton: one-twelfth the weight of an atom of ^{12}C
DDI	Distilled Deionized Water
DI	Digital Instruments
DMF	Dimethylformamide
D_{∞}	Signal at Saturation Damage
DTB	Device and Technology Branch
ePTFE	expanded Polytetrafluoroethylene
E	Energy
EDS	Energy Dispersive Spectroscopy
EELS	Electron Energy Loss Spectroscopy
ESCA	Electron Spectroscopy for Chemical Analysis
F	Absorbed Flux
f	Focal Length
(F-D)	Force-Versus-Sample Displacement Curves
Fg	Fibrinogen
F_{ij}	Flat-Field Correction at Pixel ij
FM	Fluorescence Microscopy (confocal)
FOV	Field of View
FTIR-ATR	Fourier Transform Infrared Spectroscopy in the Attenuated Total Reflection Mode
FWHM	Full Width at Half Maximum
F_x	Friction Forces
F_z	Surface Normal Forces
γ_A	Surface Tension of Material A
γ_{AB}	Interfacial Tension Between Materials A and B

Gb	Gigabyte
HOMO	Highest Occupied Molecular Orbital
HPLC	High Performance Liquid Chromatography
HSA	Human Serum Albumin
I_{ij}	Pixel Intensity of As-Recorded image in PEEM
IR	Infrared Microspectroscopy (in figure 1.1)
ISEELS	Inner Shell Electron Energy Loss Spectroscopy
I_t	Transmitted Photon Intensity
I_0	Incident Photon Intensity
K	1000
k_{lat}	Lateral Spring Constant
k_n	Normal Spring Constant
λ	Wavelength of light
LBNL	Lawrence Berkeley National Laboratory
LCP	Liquid Crystalline Polymer
LEED	Low Energy Electron Diffraction
LEEM	Low Energy Electron Microscopy
LFM	Lateral Force Microscopy
LUMO	Lowest Unoccupied Molecular Orbital
$\mu(E)$	Energy Dependent Mass Absorption Coefficient
mA	milliampere, Unit of Current
MAXIMUM	Multiple Application X-Ray Imaging Undulator Microscope
Mb	Megabyte
MDI	Methylene Diphenyl Diisocyanate
MGy	Mega Grays
M_n	Number Average Molecular Weight
M_w	Weight Average Molecular Weight
MW	Molecular Weight
N	Newton

NC-AFM	Non Contact Mode- Atomic Force Microscopy
NEXAFS	Near Edge X-Ray Absorption Fine Structure
NHLBI	National Heart, Lung, and Blood Institute
NSLS	National Synchrotron Light Source
NSOM	Near Field Optical Microscopy
OD	Optical Density
OM	Optical Microscopy
OSA	Order Sorting Aperture
PE	Polyethylene
PEG-SH	Thiolated Polyethylene Glycol
PEO	Polyethylene Oxide
PET	Poly (ethylene terephthalate)
PHEMA	Poly(2-hydroxyethyl methacrylate)
PIPA	polyisocyanate poly-addition product
PMMA	Polymethyl(methacrylate)
PP	Polypropylene
PS	Polystyrene
PTFE	Polytetrafluoroethylene
PTMO-ED-	
MDI	Polytetramethylene Oxide - Ethylene Diamine - Methylene Diphenyl Diisocyanate
r	Distance Between Two Bodies
RM	Raman Microspectroscopy
rms	Root Mean Square
ROI	Region of Interest on PEEM Cameras, or Masked Region on Component Map
rpm	Revolution per Minute

ρ	Sample Density
σ	Linear Absorption Coefficient
s	Second
S	Spreading Parameter
SA	Streptavidin
SAM	Self-Assembled Monolayer
SAN	Styrene Acrylonitrile
SDS-PAGE	Sodium Dodecyl Sulphate – Polyacrylamide Gel Electrophoresis
SEM	Scanning Electron Microscopy
SFM	Surface Friction Microscopy
SFXM	Scanning Fluorescence X-ray Microscope
SGM	Spherical Grating Monochromator
SIMS	Secondary Ion Mass Spectrometry
SLS	Swiss Light Source
S_{lat}	Lateral Sensitivity
S_n	Normal Sensitivity
SPEM	Scanning Photoemission Electron Microscopy
SPLEEM	Spin-Polarized Low Energy Electron Microscopy
SRC	Synchrotron Radiation Centre
STM	Scanning Tunneling Microscopy
STXM	Scanning Transmission X-Ray Microscopy
SVD	Singular Value Decomposition
t	Sample Thickness
TDI	Toluene Diisocyanate
TEM	Transmission Electron Microscopy
TEY	Total Electron Yield
T_g	Glass Transition Temperature
TOF	Time of Flight
TXM	Transmission X-Ray Microscopy

UHV	Ultra High Vacuum
v	Particle's Velocity
V_x	Lateral Deflection Signal
V_z	Vertical Deflection Signal
wt%	Weight Percent
XMCD	X-Ray Magnetic Circular Dichroism
XMLD	X-Ray Magnetic Linear Dichroism
XMT	X-ray Microtomography
X-PEEM	X-Ray Photoemission Electron Microscopy
XPS	X-Ray Photoelectron Spectroscopy
ZP	Fresnel Zone Plate

Chapter 1

INTRODUCTION

This chapter presents a general introduction to biomaterials and the motivation for developing X-ray microscopy as a new tool to study them. Existing analytical techniques for biomaterials are briefly described and their ability to help design new biomaterials is discussed. A review of X-ray microscopy techniques used to study polymers and biological materials leads to a short discussion of the possible contributions of soft X-ray spectromicroscopies to study protein-polymer interactions in the context of biomaterial interface optimization. The chapter closes with an outline of the whole thesis.

§ 1.1 Introduction to Biomaterials

Nearly twenty-five years ago, the editorial written for the very first issue of the journal *Biomaterials* categorized biomaterials to “(...) include synthetics as well as those of natural origin, and comprise materials that may be implanted in the body to provide specific prosthetic functions, used in diagnostic, surgical, therapeutic, and storage applications without causing adverse effects on blood or other tissues” [BH80].

At a National Institutes of Health consensus development conference in 1987, biomaterials were defined as “any substance other than a drug, or combination of substances, synthetic or natural in origin, which can be used for any period of time, as a

whole or as a part of a system which treats, augments, or replaces any tissue, organ, or function of the body" [W87]. This definition remains the most commonly accepted today.

Clearly, under the umbrella of biomaterials there exist many classes (biological materials, polymers, ceramics, metals, composites), and applications (prosthetics, diagnostic, surgical, therapeutic, storage and sensing). In order for a material to be suitable for medical applications it must be biocompatible. Biocompatibility is an ill-defined term with poor methods of characterizing a material as being "biocompatible", or not. Over 10 years ago, Professor Buddy Ratner wrote a paper titled "The blood compatibility catastrophe" [R93a]. The motivation for this publication stemmed from the fact that at a "National Heart, Lung, and Blood Institute" (NHLBI) Device and Technology Branch (DTB)-sponsored meeting on cardiovascular devices and materials, a distinguished panel of experts on blood compatibility was challenged to name a blood-compatible material. The group declined to do so (although pharmacologic approaches were suggested). Ratner [R93a] believes this seriously problematic response is symptomatic of a crisis in understanding that is observed throughout the field of cardiovascular materials. For example, the literature is abundant with controversies about what is "blood compatible", with widely differing classes of materials labelled "blood compatible".

Millions of medical devices are implanted into humans each year with reasonable levels of success (table 1.1) [CR02]. Regulatory agencies categorize these medical devices as biocompatible. Castner and Ratner [CR02] suggest two ideas as to why this word is so poorly defined. First, smooth materials that do not leach biologically reactive

Table 1.1 Medical implants used in the United States (as of 2002) [CR02].

Device	Number/year	Biomaterial
Intraocular lens	2,700,000	PMMA
Contact lens	30, 000, 000	Silicone acrylate
Vascular graft	250, 000	PTFE, PET
Hip and knee prostheses	500, 000	Titanium, PE
Catheter	200, 000, 000	Silicone, Teflon
Heart valve	80, 000	Treated pig valve
Stent (cardiovascular)	> 1, 000, 000	Stainless steel
Breast implant	192, 000	Silicone
Dental implant	300, 000	Titanium
Pacemaker	130, 000	Polyurethane
Renal dialyzer	16, 000, 000	Cellulose
Left ventricular assist devices	> 100, 000 (since inception)	Polyurethane

substances will heal in the body in a manner now considered biocompatible. Is the biocompatibility of these non-leaching materials independent of their surface properties?

The second idea put forth by Castner and Ratner [CR02] is that of the foreign body reaction. The body reacts similarly to nearly all materials that are called biocompatible by segregating a thin avascular, tough, collagenous bag, roughly 50-200 μm thick. This reaction can be described in 6 steps:

- 1) A biomaterial is implanted.
- 2) Within one minute, the implant adsorbs a layer of proteins. This is a normal process for a solid surface in biological fluids [A85].
- 3) Cells (neutrophils and then macrophages) interrogate and attack the invader, or biomaterial. The main mammalian phagocytes are neutrophils (granular, with a nucleus containing three to five lobes) and macrophages (round, granular, mononuclear). Phagocytosis is the uptake of material into a cell by the formation of a membrane bound vesicle.

- 4) When the macrophages find they cannot digest the implant, they fuse into giant cells to engulf the object. However, most macroscopic implants are too large to completely ingest. The giant cells then send out chemical messengers (cytokines) to call in other cells.
- 5) Fibroblast cells arrive and begin synthesizing collagen.
- 6) At the end stage of the reaction the implant is completely encased in an acellular, avascular collagen bag. There are macrophages between the collagen sac and the implant.

The presence of this capsule may inhibit the biomaterials from functioning as intended due to the lack of intimate contact between device and tissue. The long term, low level inflammation and macrophage activation due to the foreign body reaction may lead to the following problems: healing of vascular grafts does not occur ([JWR&91], [WJK94], [WRJ94], [W95], [WJ96]), capsular opacification found with intraocular lenses [AAS&02], [BFM&02], [DSD&02]), extrusion of percutaneous devices ([WSQ&98], [TPY00], [W01]), device calcification ([SSC&01], [SMG&02], [SML&02]), contact lens discomfort, other complications and undesirable outcomes associated with today's medical devices.

Castner and Ratner [CR02] note that, in contrast, our body has an excellent capacity to heal wounds and injuries with healthy, vascularized tissue, and thus ask: Could this normal healing be wrong? Why do "biocompatible" implants shut off normal wound healing?

Given a list of 10 common materials used in medicine (for example, gold, polyurethane, silicone, rubber, polytetrafluoroethylene (PTFE), polyethylene (PE), poly(methyl methacrylate) (PMMA), poly(2-hydroxyethyl methacrylate) (PHEMA), poly(ethylene terephthalate) (PET), titanium, alumina), one finds materials that are hydrophobic, hydrophilic, hard, soft, polymeric, ceramic, and metallic. Yet, after one month implantation in mammals, they are all found to heal essentially identically. On the other hand, each material will be found, *in vitro*, to adsorb different proteins, and to show substantially different cell attachment and cell growth behaviour.

The commonality among the ten materials listed in the previous paragraph is that they adsorb a complex, non-specific layer of proteins. Each will have a different protein mixture at its surface, but all the materials will quickly acquire a layer that contains many proteins (possibly comprised of 200 or more proteins) in many states of orientation and denaturation [H93]. However, nature never uses such non-specific layers. Nature's use of proteins as signalling agents comes from one (or a few) specific proteins in fixed conformations and orientations so they optimally deliver signals. A hypothesis has been developed suggesting that the body views this non-physiologic proteinaceous layer as something with which it has no experience and reacts to it as an unrecognized foreign invader that must be walled off [R97], [R98]. In a normal wound, the macrophage cell responsible for orchestrating wound healing is activated. In the presence of an uncomplicated wound, the macrophage turns on the pathways leading to normal healing by first cleaning up the wound site and then secreting the appropriate cytokine messenger molecules. These soluble messengers activate processes in the cell types needed for

healing. The biological reaction to the surfaces of today's biomaterials turns this normal healing process off. Is it possible to design a biomaterial with a surface that is truly biocompatible, i.e. one which stimulates normal healing rather than the foreign body rejection response?

Castner and Ratner [CR02] suggest a number of steps that must be taken to realize "biomaterials that heal". First, a serious investment must be made in the study of the basic biology of normal wound healing, in contrast to wound healing with a biomaterial present. Second, the non-specific adsorption of proteins and other biomolecules must be inhibited. Finally, the surfaces of biomaterials must be synthesized to present to the body the same signalling groups as the surface of a clean, fresh wound. In order to go beyond the current situation in which biomaterials elicit only the foreign body response, surfaces must be developed that control the conformation and orientation of proteins with precision so that the body will specifically recognize them.

Many ways to inhibit non-specific protein adsorption, the second step in the paragraph above, have been developed (see table 1.2). Several questions driving research in this area have been formulated and are summarized in the *Journal of Biomaterials Science: Polymer Edition* (Volume 11, 2000). These questions are: How resistant to protein pickup can such surfaces be made? Why are they resistant to protein adsorption? How long can they remain resistant to protein fouling? Can they be functionalized with organic groups permitting the immobilization of active biomolecules on a bland background?

Table 1.2 Strategies to achieve protein-resistant (non-fouling) surfaces [CR02]

Surface strategy	Comments	Reference
PEG ^a	Effective but dependent on chain density at the surface; damaged by oxidants	[M92]
PEG-like surfaces by plasma deposition	Applicable for the treatment of many substrates and geometries; highly effective	[MRY99]
PEG oligomers in self-assembled monolayers	Highly effective; applicable for precision molecularly engineered surfaces; durability to elevated temperature is low.	[PW93]
PEG-containing surfactants adsorbed to the surface	A simple method for achieving non-fouling surfaces; durability may be low and high surface densities are hard to reach	[LC96]
PEG blocks in other polymers coated on the surfaces	May provide a relatively low density of surface PEG groups	[KVE&00]
Polysaccharides	Nature's route to non-fouling surfaces; some successes but much territory remains explored	[DSB&00], [MC99]
Choline headgroups (phosphatidyl choline)	Has shown good success in many applications	[ISN&99]
Hydrogen bond acceptors	Possibly, this principle imparts non-fouling properties to PEG surfaces; this is leading to new discoveries of surface functional groups for non-fouling	[COT&00]
Adsorbed protein layer	A pre-adsorbed protein layer resists further adsorption of proteins; this approach, long used by biologists, is easy to implement but of low durability	[CBO80]
Hydrogels in general	PEG is in this class; many other hydrogels have shown non-fouling behavior	[LRR&93]

^a Also called poly(ethylene oxide) (PEO).

§ 1.2 Capabilities of Techniques Commonly Used in Biomaterials Development

A number of experimental techniques have been applied to the study of surfaces in general, and specifically to biomaterials. The ultimate goal for biomaterials surface science would be to provide an understanding of how the surface chemistry and structure of a material can be used to control the biological reactivity of bio-macromolecules and ultimately a cell interacting with that surface. To accomplish this goal requires understanding the cell reactivity and characterizing a complex, protein-covered surface [CR02]. *“A layer of adsorbed proteins mediates the interaction of cells with a biomaterial when that biomaterial is placed in the biological environment. In order to*

mimic that environment, future multilayered engineered surface-biology constructs may have a synthetic material, a hydrogel-like support, a SAM (self-assembled monolayer), a variety of tethering hooks and a number of oriented, organized biomolecules. Thus, it is especially important to develop surface analysis methods that can fully characterize these complex layers containing proteins and other biomolecules” [CR02]. Table 1.3 summarizes the principles, depth sensitivity, spatial resolution and analytic sensitivity of some of the most commonly used techniques. Note that table 1.3 by no means includes all surface science techniques available, but it does give an overview of the main techniques used in studies of biological interfaces. The first nine techniques are mentioned in [R93b], the following three are discussed in [BN00], AFM is discussed in [R93b] and [BN00], and the last 2 methods described in this table are described in detail in this thesis.

Some of the main criteria of techniques useful for the study of biomaterials are chemical sensitivity, molecular quantification, imaging with good spatial resolution, and appropriate depth sensitivity. The level of chemical sensitivity that is required for the study of biomaterials necessitates that the technique(s) be able to differentiate all the components at the interface of the material, be it the substrate's components (metals, polymers, SAMs, hydrogel, etc.) or the biological species adsorbed on the substrate (various proteins, lipids, cells, etc.). Also, not only should the species be qualitatively differentiable, but in order to understand the nature of the interactions between the adsorbates and substrate, the technique(s) should also be able to quantify the amount of the species present on the surface at the molecular level.

Table 1.3 Methods to Characterize Surfaces, *bold italic* methods were used in this thesis

Method	Principle	Depth Analyzed (nm)	Spatial Resolution (nm)	Analytic Sensitivity	Environment
^a Auger	X-rays or electron beam causes the emission of Auger electrons	5-10	10	0.1 at. %	UHV ^b
XPS	X-rays cause the emission of electrons of characteristic energy	1-25	1×10^4 - 1.5×10^5	0.1 at. %	UHV
SIMS	Ion bombardment leads to the emission of surface secondary ions	1 – 1000 ^c	50	High	UHV
FTIR-ATR	IR radiation is absorbed in exciting molecular vibrations	1000-5000	1×10^4	1 mol %	UHV, air, or water
STM	Measurement of the quantum tunnelling current between a metal tip and a conductive surface	0.5	0.1	Single atoms	UHV
SEM	Secondary electron emission caused by a focused electron beam is measured and spatially imaged	0.5	4	High, but not quantitative	UHV
<i>Contact angles</i>	Liquid wetting of surfaces is used to estimate the energy of surfaces	0.3-2	1×10^6	Low/high depends on chemistry	air
<i>Radiolabeling Surface Analysis</i>	Relates the amount of adsorbed protein to the solution concentration of protein	< 3	none	0.002 $\mu\text{g}/\text{cm}^2$	air
<i>AFM</i>	Measurement of the attractive or repulsive force between atoms in a surface and in a tip	0.5 ^d	0.3	single molecules	air or water
Brewster Angle Microscopy	Reflectivity of light at interfaces	0.5	1×10^4	monolayer	In water
Imaging Ellipsometry	Polarization changes occur upon reflection at oblique incidence of a polarized monochromatic plane wave.	0.5	5×10^3	monolayer	In water
Neutron reflection	Reflectivity of a neutron beam at interfaces.	2	None	Sub-monolayer	air or water
<i>STXM</i>	Detection of transmitted soft X-rays; spatial resolution obtained via Fresnel zone plate optics	~min. 5 ^e	~ 40	High	air or water
<i>X-PEEM^f</i>	Upon exposure to X-rays, detection of secondary electrons imaged via electron optics	3-20	~30-100	Signal of 10 Fg proteins has been detected	UHV needed

^a Auger electron spectroscopy is damaging to organic materials and used for inorganic; ^bUHV is ultra high vacuum; ^cStatic SIMS \approx 10 Å, dynamic SIMS up to 1 μm ; ^dThe depth sensitivity and spatial resolution depend on the type of AFM mode employed and the nature of the substrate; ^e5 nm protein layer on top of 100 nm thick film, under \sim 2 μm water; ^fThe depth sensitivity and spatial resolution is material dependent; the best spatial resolution obtained for polymers is \sim 100 nm.

The various species that adsorb on surfaces, which themselves can be patterned, come in different size scales (for example, proteins, nm; cells, μm). One must be able to image these features with a spatial resolution that is at least on the nm scale. One further requirement of the ideal biomaterials surface science technique(s) is that it must have sufficient depth sensitivity to obtain signal from the adsorbates as well as the substrate, with sufficient analytical sensitivity to detect the thin layer of adsorbate on the thick substrate.

Out of all the techniques detailed in table 1.3, most of the ones which offer adequate spatial resolution and depth sensitivity require an ultra high vacuum (UHV) environment. This can be a disadvantage because the UHV environment may alter the biological activity of molecules which normally live in an aqueous, buffered environment. Thus, of great significance for STXM, is the fact that measurements can be made *in situ*, ie, in the presence of an overlayer of the protein solution [HMH&02].

§ 1.3 Role of X-Ray Spectromicroscopy in This Field

Soft X-rays have several basic attractions for the microscopist. First, since the wavelength is much shorter than that of visible light, one can hope for higher resolution than is possible with optical microscopy. Second, the interaction of soft X-rays with matter strongly depends on both wavelength and on atomic number. As a consequence one has unique contrast mechanisms, a sensitivity to elemental constituents, and one may accommodate specimens with a wide range of thicknesses. These properties have been appreciated for a long time ([L36], [LT36], [H61]). During the period between 1945 and

1961 a considerable amount of attention was paid to the development of various forms of X-ray microscopy ([H61], [CN60], [KP57], [E66], [HRS72]), but the excitement and enthusiasm died away due to instrumental problems and the successful development of powerful electron microscopy and microanalysis techniques [KR85]. In the 1980's, the availability of synchrotron radiation sources, the development of high resolution zone plates, efficient multilayer reflectors, and high resolution X-ray resists have all contributed to renewed interest ([G78], [KS80], [P80], [S81], [SDN82], [S83], [AU84], [HK84], [SR84], [W84]).

The first scanning X-ray microscope was built in 1972 by Horowitz and Howell ([HH72], [H78]). They used synchrotron radiation focused onto a 1-2 μm diameter pinhole to define the microprobe, and formed images of a variety of specimens detecting either the X-ray fluorescence from the specimen or the transmitted X-rays. The $\sim \sqrt{\lambda d}$ blurring due to Fresnel diffraction limits the probe-to-sample distance to $< 1\mu\text{m}$ for soft X-ray wavelengths; (λ is the wavelength of the light, d is the distance between the probe and the sample) [KJH95]. Thus, to reach submicron resolution while maintaining a finite working distance with soft X-rays, it is necessary to use a focusing element. The first scanning transmission X-ray microscope (STXM) to use a zone plate objective was built in 1982 by Rarback [R83]. It used a bending magnet beamline with a grating monochromator at the 0.7 GeV ring at the National Synchrotron Light Source at Brookhaven National Laboratory. A small pinhole placed near the monochromator exit slit defined the beam to illuminate the zone plate, which focused the beam to a spot of about 300 nm [KJH95]. The basic scheme of STXM has not changed over the years,

although every subsystem has been dramatically improved with respect to instrumentation components (zone plates, detectors, scanning motors, etc), quality of the synchrotron light, data acquisition and analysis methods, and sample preparation methods. One of the very latest implementations of STXM, STXM 5.3.2 at the Advanced Light source, will be described in chapters 2 and 3.

Table 1.4 highlights a review of the literature of the past decade or so, on soft x-ray microscopy techniques and their applications in biology and polymers. The main techniques discussed are transmission X-ray microscopy (TXM), X-ray microtomography (XMT), scanning photoemission electron microscopy (SPEM), and emphasis is placed on scanning transmission x-ray microscopy (STXM) and photoemission electron microscopy (X-PEEM). The publications derived from this thesis work are in *bold italics*.

Table 1.4 Summary of selected literature in soft X-ray microscopy (page 1 of 5)

Ref Code	Technique	Edge or energy	Sample	Problem/Comment
[JWA&91]	STXM	340 eV	Gold test object	Resolution of 36 nm features
[A92]	SPEM	Si2p	Al/Si and PP/PS blend	Review of instruments and applications of MAXIMUM and X1-SPEM at NSLS
[BBF&92]	STXM/ SFXM/ XMT	Ca2p	Human articular cartilage	Mapping of calcium mineral deposits
[FPF&92]	TXM	380 eV	Unicellular algae <i>Chlorella</i>	Examination in TEM of damage caused by TXM
[LTJ92]	TXM	280 - 550 eV	Bacteria, cells (type unspecified)	Use of colloidal gold to reduce dose in microscopy and holography
[AH93]	STXM	C1s	Kevlar	Rotate sample; first chemically specific linear dichroism X-ray microscopy
[D94]	X-PEEM	Al2p	Various brain model systems, neural cell cultures	Review, applications to neurobiology, 100 nm spatial resolution
[KKA&94]	SPEM	280-800 eV	none	Instrument and beamline description for an instrument that combines XPS and zone plate microfocusing
[DDT&95]	X-PEEM	Al2p, Fe3p, Cr2p	Purkinje neurons	Visualization by subtraction imaging and NEXAFS spectra from microscopic areas.

Table 1.4 Summary of selected literature in soft X-ray microscopy (page 2 of 5)

Ref Code	Technique	Edge or energy	Sample	Problem/Comment
[KJH95]	STXM	Various	various	Soft X-ray microscopes and their biological applications. Review that deals with: the interaction of soft X-rays with matter, soft X-ray microscopes, and biological applications.
[MHT&95]	STXM/ XMT	345 eV	test object with two gold patterns on Si ₃ N ₄ , 4.75 μm apart, 100- to 300-nm-wide and 65-nm-thick features	Scanning soft X-ray microtomography used to obtain high-resolution 3D images. Special rotation stage. Features of the test object were resolved to ~ 100 nm in transverse and longitudinal extent with low artefacts in 3D images rendered from the volumetric set.
[SNG&95]	TXM	516 eV	whole <i>Chlamydomonas reinhardtii</i> cell	Description of cryo-object stage, sample cooling methods, evaluation of radiation resistance of vitrified biological structures embedded in ice at temperatures around 100K.
[WJK&95]	STXM	C1s, P2p	MDI-polyurethane, bull sperm, Kevlar, labelled PS spheres	STXM @ NSLS offers 3 forms of imaging: (1) XANES microscopy; (2) luminescence microscopy at the resolution determined by the size of the X-ray microprobe; and (3) dichroism microscopy.
[ASZ&96]	STXM	C1s	Various industrial polymers	Spectral analysis and single energy images are used to study these materials. Sub-100 nm features are detected.
[JCF&96]	STXM	C1s	Au-labelled fibroblast	Imaging in transmission, spectroscopy, luminescence and dark field of ultrastructure of cell; mapping of DNA and protein in cell.
[KYG&96]	TXM	516 eV	COS-1 cells	Mitochondria, endoplasmic reticulum and plasma membrane were observed.
[ASZ&97]	SPEM/ STXM	C1s	Various polymers	STXM and SPEM provide 50 nm and 250 nm spatial resolution, respectively
[CDA&97]	X- PEEM	C1s, N1s	PS/Poly (vinylmethylether) and PS/PSacrylonitrile	The X-PEEM at ALS has a spatial resolution of 0.2 μm at an accelerating voltage of 12 kV. Tunability of the photon energy used to provide chemical state information using NEXAFS on the sub-micrometer scale. Enrichment of phases is shown spectroscopically and microscopically.
[DM97]	X- PEEM	C1s, Ca 2p, P2p, K2p, S2p	Comparisons of ashed and non-ashed cells of various types	Photon energy is scanned to see various components of the cells shine; instrumental development to allow measurements in transmission.
[FWU&97]	X- PEEM	Soft X-rays	none	Construction of a UHV spectromicroscope: SMART (spectromicroscope for all relevant techniques): (XAS, XPS, UPS, XAES), calculated spatial resolution of better than 1 nm. Maximum energy resolution of about 0.1 eV will be provided by a corrected omega filter.

Table 1.4 Summary of selected literature in soft X-ray microscopy (page 3 of 5)

Ref Code	Technique	Edge or energy	Sample	Problem/Comment
[CDL&98]	X-PEEM	C1s	130 nm thin films of stylized BPDA-PDA; stylizing mimicks the rubbing process.	Try to understand alignment process in rubbed aromatic polyimide films. Samples oriented parallel and perpendicular to the electric field vector. The films oriented by the conventional rubbing method showed lateral inhomogeneities in the orientation of the polymer at the surface.
[JK98]	TXM	516 eV and C1s	frozen hydrated <i>Chlamydomonas reinhardtii</i> (fresh water organisms)	2D imaging, 100 nm resolution of hydrated, unsectioned specimens
[PBA&98]	STXM	C1s	Blend of PET and a liquid crystalline polymer (LCP), Vectra A950	Functionality sensitive X-ray microscopy reveals LCP dispersions as small as 100 nm in diameter. Single energy images.
[WFK&98]	STXM	C1s, N1s, O1s, Fe2p	Kevlar fibres, wet soil samples, Fe films	Design and performance of a STXM at the Advanced Light Source is described (STXM 7.0). This instrument makes use of a high brightness undulator beamline and extends the STXM technique to new areas of research. Acquisition modes are point spectra, linescan, single energy images and image sequences (stacks).
[AWS&99]	STXM	C1s	PS:PMMA	Observation of microdomains in both phases
[UAS&99]	STXM	C1s, O1s	polyurethane polymers made from 4,4-methylene di-p-phenylene isocyanate (MDI) and toluene diisocyanate (TDI) isocyanate monomers	At X-1A STXM (NSLS) and 7.0 STXM (ALS). NEXAFS spectra illustrate the spectroscopic fingerprints for distinguishing between MDI-based and TDI-based polyurethane polymers. MDI and TDI polyurea and polyurethane spectral models show that the urea and carbamate (urethane) linkages in these polymers are distinguishable. Differences between the spectra of MDI and TDI polyurethanes synthesized with polyether polyols of different molecular composition and different molecular weight are presented.
[AUS00]	STXM	C1s, N1s, O1s	natural and synthetic polymers	Book chapter describing NEXAFS spectroscopy and microscopy with applications in surfaces and thin films, bulk morphology and composition of multicomponent, multiphase polymers, fibers, organic geochemistry, meteorites and interplanetary dust particles, soils and environmental studies, etc
[JWF&00]	STXM	C1s	layered polymer, micro-meteorite, interplanetary dust particle section.	First image sequence alignment, selection of NEXAFS spectra from large irregular regions, and from small regions (as small as the spatial resolution of the microscope (~40 nm)).

Table 1.4 Summary of selected literature in soft X-ray microscopy (page 4 of 5)

Ref Code	Technique	Edge or energy	Sample	Problem/Comment
[HKT&01]	STXM	C1s, N1s, O1s	styrene-acrylonitrile-based (SAN) copolymer and polyisocyanate polyaddition product-based (PIPA) reinforcing particles in a copolymer polyol-polyurethane	Morphology, size distributions, spatial distributions, and quantitative chemical compositions of co-polymer polyol-reinforcing particles in a polyurethane. Spatial resolution is 50 nm. Quantitative analysis of the chemical composition of individual reinforcing particles is achieved by fitting C1s spectra to linear combinations of reference spectra. Regression analyses of sequences of images recorded through the chemically sensitive ranges of the C1s, N1s and O1s spectra are used to generate quantitative compositional maps.
[KHL&01]	STXM	C1s	Core-shell polymer microspheres of polydivinylbenzene-cores coated with wide shells of poly(DVB55-co-EDMA), ethylene glycol dimethyl acrylate (EDMA).	The chemical composition, core-shell morphology, and porosity of these structured microspheres have been studied quantitatively with (STXM) at a spatial resolution of 100 nm. Images recorded at selected energies through the C1s absorption region were analyzed using singular value decomposition (SVD) to obtain quantitative maps of the components.
[LSH&01]	TXM	400 eV, 413 eV, 516 eV	exocrine pancreas sections embedded in glycol methacrylate (GMA) polymer	GMA embedding and sectioning, widely used in other forms of microscopy, is applicable to X-ray microscopy essentially without modification. This sample preparation demonstrates good radiation tolerance at the doses used for imaging, with little mass loss and no appreciable distortion.
[MIT&01]	STXM/ PEEM/ AFM	C1s	<i>Various films of PS:PMMA blends, unannealed and annealed</i>	<i>Comparison of AFM, STXM and X-PEEM to study thin film polymer blends before and after annealing.</i>
[HMH&02]	STXM	C1s, N1s	<i>Various polyurethane microtomed sections exposed to blood proteins</i>	<i>STXM can detect proteins on soft X-ray transparent polymer thin films with monolayer sensitivity. Of great significance is the fact that measurements can be made in situ, i.e. in the presence of an overlayer of the protein solution.</i>
[HMT&02]	STXM	C1s	<i>various</i>	<i>Examples are given from recent studies of: phase segregation in polyurethanes and polymer blends, protein adsorption on polymers relating to biomaterial optimization, and metal mapping in biofilms.</i>

Table 1.4 Summary of selected literature in soft X-ray microscopy (page 5 of 5)

Ref Code	Technique	Edge or energy	Sample	Problem/Comment
[KHM&02]	STXM	C1s	poly(acrylic acid) in a microporous polypropylene support membrane	SVD analysis of images recorded at carefully selected photon energies was used to obtain quantitative maps of the two components. The sample was studied fully hydrated. Optimum strategies of data acquisition for quantitative X-ray microscopy analysis of radiation sensitive materials are discussed.
[WAK&02]	STXM	C1s, N1s, O1s	various	A new bend-magnet beamline (5.3.2) for STXM at the Advanced Light Source is described.
[YS02]	TXM	280 eV-540 eV	Hydrated macrophage cells	Application of two X-ray microscopes types: one use laser-produced plasma X-rays, the other, synchrotron radiation. Both types show the network of fine fibrillar surface structures.
[BFF&03]	STXM	Various	Bones, cells	Review of STXM at NSLS. Mapping of calcium in bone; imaging of cellular and subcellular structures, studies of radiation damage limitations in biology, absorption spectromicroscopy for studies of polymers, and biomedical specimens.
[CBM&03]	STXM	C1s	oriented single crystals of N,N'-ethylenebis(N'-2-methylphenyl)-urea	NEXAFS comparison to the single-crystal structure of this material. A strong polarization dependence (linear dichroism) is interpreted with the aid of the single-crystal structure and crystal alignment. Ability of STXM to determine molecular orientation on a sub- μ m scale.
[KTS&03]	STXM	C1s, N1s, O1s	Test patterns, DOW Chemicals polyurethanes	Interferometer-controlled STXM microscopes at the Advanced Light Source; FIRST of its kind in the world. See section 2.3.2.2 for a list of advantages of this design.
[LSL&03]	STXM	C1s, N1s, Ca2p	Biofilms from river water supplemented with methanol	Confocal laser scanning microscopy (CLSM), (TEM), and (STXM) used to map distribution of macromolecular subcomponents. STXM provided compositional mapping without the addition of probes. By examining exactly the same region of a sample with combinations of these techniques (STXM with CLSM and STXM with TEM), multimicroscopy analysis can be used to create a detailed correlative map of biofilm structure and composition.
[LL04]	Cryo-TXM	510 eV	Yeast <i>Sacharomyces cerevisiae</i>	3D imaging; density only, no chemical analysis, 60 nm resolution
[MHC&04]	X-PEEM	C1s, N1s, O1s	<i>Fg (water) and Fg (buffer) on PS:PMMA</i>	<i>First demonstration of protein adsorption on (phase segregated) polymers, investigated by X-PEEM with 120 nm spatial resolution</i>

At present, implementations of full field TXM do not provide chemical speciation in as precise a manner as STXM and X-PEEM where NEXAFS spectroscopy can be used to obtain chemical mapping of components in a mixture. Most TXM beamlines do not have energy resolution better than 1.0 eV, which is inadequate for NEXAFS spectroscopy. The chemical differentiation in TXM relies on immunogold-labelling of proteins and elemental speciation of the other components of a biological cell in order to generate 2D or 3D maps of the components within the cell. SPEM provides excellent surface sensitivity and chemical speciation but the spatial resolution of current instruments does not exceed ~300 nm.

For these reasons, and due to best information per unit radiation damage, STXM and X-PEEM have the best combination of chemical speciation and spatial resolution. However, one of the important messages of tables 1.3 and 1.4, and figure 1.1, which compares the performance of STXM and X-PEEM to that of a number of other analytical microscopy techniques [HMT&02], is that no single technique can provide all the information needed to understand biomaterial surfaces. Some give excellent spatial resolution, but poorer chemical information; others have very high chemical content but have poorer spatial resolution. X-ray microscopy in general, and also STXM and X-PEEM, already provide very high spatial resolution (~ 30-100 nm) and information pertaining to the chemical nature of a specimen based on NEXAFS. With improvements in instrumentation, data acquisition and data analysis methods, and sample preparation, both spatial resolution and chemical content will be improved even further.

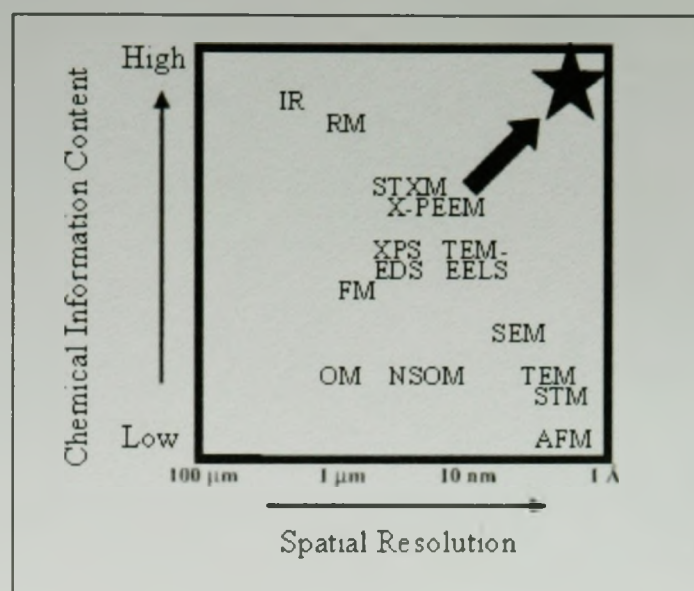


Figure 1.1 Qualitative comparison of the relative performance of various microanalytical techniques applicable to soft matter. Chemical information refers to speciation, not simply elemental analysis. Spatial resolution is that typically achieved rather than the absolute state-of-the-art.

With respect to the challenges of biomaterial optimization, although there was no evidence in the XRM literature of protein detection on surfaces, based on the scientific progress of X-ray microscopy before the start of my PhD thesis (2000) with respect to spatial resolution and chemical sensitivity, STXM and X-PEEM showed promise in being able to identify the adsorption of proteins on polymeric substrates and also the possibility of imaging cells on such protein decorated surfaces. Although the initial goal of the project was to extend from protein decoration to applications in control of subsequent adsorption of cells, the development of X-ray microscopy for the first stage, protein detection, turned out to be a significant challenge and thus became the focus of my thesis. STXM and X-PEEM were working, but they had not yet been applied to biomaterial surfaces. They had potential of chemically identifying the proteins and the substrate on a

spatial scale correspondent to biological species (100 nm – 2 μ m), however, these spectromicroscopy techniques, and our understanding of them, were in their early infancy stage. Cell adsorption and competitive protein adsorption were not tested over the course of my PhD because the techniques needed further development for their application to organic, polymeric and biological materials. Limitations of the experimental techniques lead to the choices of model surfaces that also had to be designed and tested. In the near future, competitive protein adsorption will be investigated either on the PS:PMMA model surface used for much of this thesis, or on other, more relevant biomaterials. Cells and cell-environment interfaces are being extensively studied by STXM ([HMT&02], [LSL&03], [HMZ&04]), so extension to cell-biomaterial interactions will be straightforward.

§ 1.4 Outline of Thesis Chapters

Chapter 2 outlines the fundamental principles of synchrotron radiation, near edge X-ray absorption fine structure (NEXAFS), spectromicroscopy (scanning transmission x-ray microscopy, STXM, and photoemission electron microscopy, X-PEEM) and atomic force microscopy (AFM).

Chapter 3 describes in detail how STXM and X-PEEM measurements were performed. For X-PEEM, methods were developed to acquire data with minimal damage and maximal statistical information by exploration of the beamline and microscope parameters, and development of various corrections for the two CCD cameras that were used. The principles of data analysis for spectromicroscopy are introduced and methods

applied to specific data sets are detailed. In the final section of chapter 3, the sample preparation used for STXM and X-PEEM studies of proteins on phase segregated polymers is outlined.

Chapters 4 to 6, inclusive, are the results and discussion chapters, where each chapter is a publication shown here in published form. These chapters are not presented in chronological order of publication, but in a methodological fashion where the substrates are tested and characterized (4) followed by protein detection on two different types of substrates, PS:PMMA (chapter 5) and microtomed polyurethane sections (chapter 6), using different spectromicroscopy techniques, X-PEEM (5) and STXM (6).

Historically, the reasons that lead to these experimental choices are outlined below. From July 1999 to November 1999, in the early months of this project, we wished to study real life biomaterials in the STXM and X-PEEM instruments. The substrates that were investigated at the time were polyurethane materials that were either a) spun cast or, b) microtomed.

The former were PTMO-ED-MDI (polytetramethylene oxide - ethylene diamine - methylene diphenyl diisocyanate) and PTMO-ED-MDI-PIPA (PIPA: a (MDI)-based hard segment-like material). These polymers were dissolved in dimethylformamide (DMF). The latter microtomed materials were all provided by The Dow Chemical Company. They consisted of a compressed polyurethane foam, with a TDI (toluene diisocyanate) hard segment and a butane oxide (BO) soft segment. One substrate (code #355) contains poly(styrene-*co*-acrylonitrile) (SAN) and poly-isocyanate poly-addition product (PIPA), both referred to as copolymer polyol (CPP) filler particles.

One of the difficulties encountered with the spun cast polymers was that the intrinsic phase segregation of these materials was too small (~10-30 nm) to be detected by the limited spatial resolution of the microscopes (at the time, STXM: 60 nm, X-PEEM: 150 nm). As for the PIPA modified PTMO-ED-MDI polymer, even though the ~200 nm wide PIPA particles were detected in STXM, the films did not cover the substrate (Au/Si₃N₄) uniformly and the protein selectively adsorbed on the gold patches rather than on the polymer film. In addition, the films were very corrugated as the AFM results showed 100 nm root-mean-square (rms) roughness over a 10 µm x 10 µm area. Such corrugation is sufficient to cause charging in the X-PEEM such that these samples could not be used in that microscope.

Similarly, the microtomed Dow polyurethane sections could not be adequately measured in X-PEEM due to charging caused by the rough topography of the surface; the 1-2 µm wide SAN particles protrude from the surface by ~150 nm.

However, the 355 sample (with domains in the range of ~200-400 nm for PIPA, and 1-2 µm for SAN) could be studied in STXM. Chapter 6 shows the results of human serum albumin (HSA) and fibrinogen (Fg) adsorbed to that surface and to two other Dow polyurethane materials. These experiments have been published in the journal of Biomaterials Science, Polymer Edition (J. Biomater. Sci. Polymer Edn. Vol **13**, No.8, p 919-937, 2002). The author of this thesis contributed to this work by performing the protein adsorption parts of the sample preparation, and in collaboration with the first author of the publication (A.P. Hitchcock), contributed to data acquisition, data analysis and writing.

For adsorption of proteins on patterned polymer films, measured with X-PEEM, a phase segregated patterned polymer film with low topography and covering the whole substrate needed to be developed. One approach was to use microcontact printing of self assembled monolayers. For reasons explained in section 3.2.5, this approach turned out to be inadequate. PS:PMMA films of various compositions were then prepared and measured in STXM, X-PEEM and AFM; the results of these experiments are shown in chapter 4. This work was a collaboration between members of Prof. A. P. Hitchcock's group, Prof. J. L. Brash's group, Prof. H. Ade's group, and beamline scientists Dr. A Scholl and Dr. F. Nolting at the Advanced Light Source. This work has been published in the journal of Electron Spectroscopy and Related Phenomena (J. Electron Spectrosc. **121**, 201, 2001). The publication reviews the literature on the PS/PMMA system as of January 2001. Also, it documents the STXM, X-PEEM and AFM results from a variety of PS:PMMA films, as-made and after annealing. The chemical sensitivities and spatial resolutions of these three techniques are compared.

The author of this thesis contributed to this publication by:

- preparing most of the samples (the high molecular weights (> 25 KDa PS/PMMA films were prepared by me and the low MW ones by Dr. G. Appel)
- acquiring and analyzing the AFM images (with Andy Duft's help), except for figure 10 which is adapted from reference 16 of the publication and was acquired by D. A. Winesett.
- acquiring the data (all of X-PEEM, part of STXM), carrying out data analysis and interpretation

- preparing a first draft which was refined for publication by Prof. A. P. Hitchcock and Prof. H. Ade.

Following this work, some improvements concerning the cleanliness of the samples, choice of polymer molecular weights and annealing methods were required to obtain a substrate appropriate for protein adsorption. These efforts are detailed in section 3.4. Furthermore, learning how to properly use X-PEEM for organic materials was a challenge in itself (see section 3.2). Among these problems, arose the issue of radiation damage to polymers; this is briefly discussed in section 3.2.6. With most sample and experimental problems under control, one could finally address the problem of proteins adsorbed on PS:PMMA, which is the subject of chapter 5.

Chapter 5 documents the X-PEEM and radio-labeling results of various concentrations of fibrinogen adsorbed to PS/PMMA from two different solvents (phosphate buffer saline and deionized water). This work has been published in the *Journal of Electron Spectroscopy and Related Phenomena* (*J. Electron Spectrosc.* **137-140**, 2004, 785-794). The author of this thesis prepared all the samples for this publication, performed all the X-PEEM experiments, analyzed a large portion of the X-PEEM data (in collaboration with Prof. A. P. Hitchcock) and wrote the publication with assistance in later stages by Prof. A. P. Hitchcock and Prof. J. L. Brash. The radio-labeling experiments were performed by Mrs. Rena Cornelius.

Chapter 7 discusses the significance of the results obtained in chapters 4-6 and proposes future work.

Chapter 2

METHODS

This chapter describes fundamental principles of synchrotron radiation, near edge X-ray absorption fine structure (NEXAFS), spectromicroscopy and atomic force microscopy (AFM). Section 2.1 briefly introduces synchrotron radiation, which is the X-ray source used to perform NEXAFS spectroscopy. Section 2.2 outlines the theory of NEXAFS. Sections 2.3 and 2.4 give the general principles of the microscopic implementation of NEXAFS in scanning transmission X-ray microscopy (STXM) and photoemission electron microscopy (X-PEEM). Section 2.5 describes principles of atomic force microscopy (AFM). STXM and X-PEEM are “spectromicroscopy” techniques because NEXAFS spectroscopy (“spectro”) is used in conjunction with the imaging capabilities (“microscopy”) to give chemical mapping. For the two synchrotron based techniques, the beamlines and microscope instruments are described.

§ 2.1 Synchrotron Radiation

Whenever charged particles undergo acceleration they emit electromagnetic radiation. When electrons are subjected to an acceleration perpendicular to their velocity (that is, a centripetal acceleration such as is the case when electrons pass through a magnetic field), their direction is changed – they begin to travel in a circular path. When the electron kinetic energy is low compared with the rest mass energy given by mc^2 (i.e., when the electron velocity is non-relativistic or low compared to the velocity of light) the

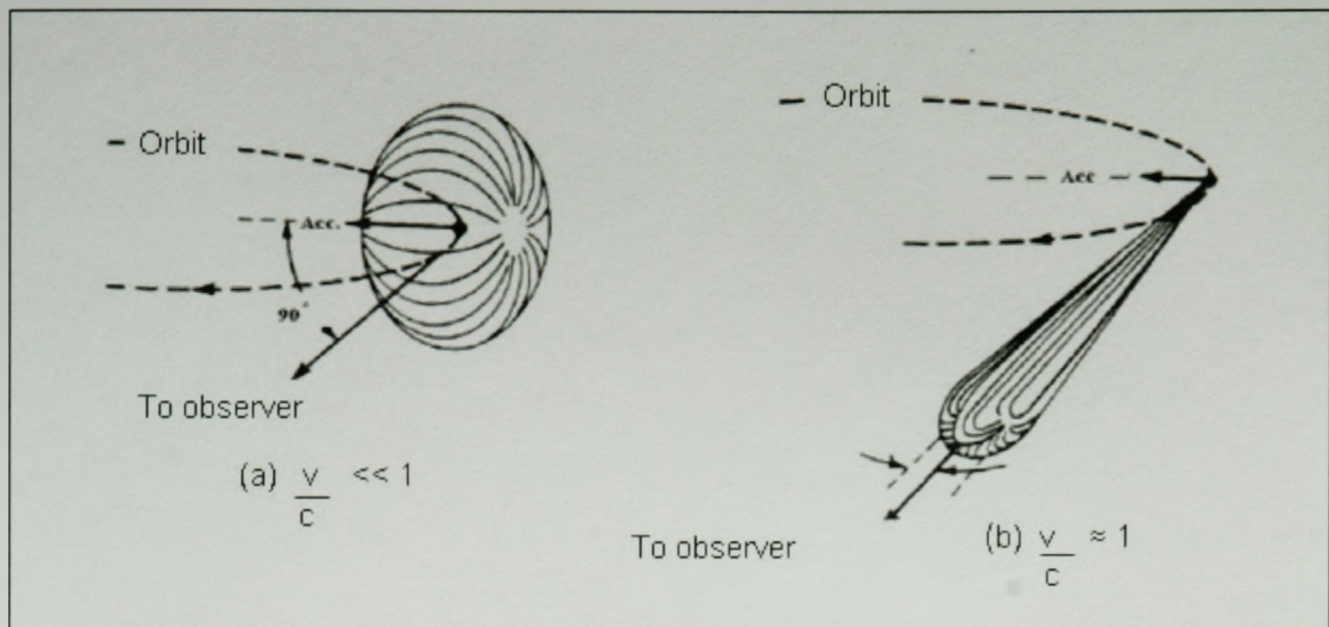


Figure 2.1 Emission patterns of radiation from electrons in circular motion; case (a): at a low velocity compared to the velocity of light; and case (b): approaching the velocity of light.

radiation is emitted in a rather non-directional pattern (called a dipole pattern) as shown in figure 2.1, case (a). However, as the speed of the particle approaches the speed of light, the radiation pattern is distorted by relativistic effects and changes to a narrow cone of radiation with angular spread $\Delta\phi$. The latter type of radiation is called synchrotron radiation, case (b) [W94].

The properties of synchrotron radiation are well known and some of them are described here. For a particle moving at velocity v with a total energy E :

$$\text{Eq. (2.1)} \quad E = \gamma m_0 c^2, \text{ with}$$

$$\text{Eq. (2.2)} \quad \gamma = 1 / \sqrt{1 - v/c^2}$$

the opening of the radiation cone (in steradians) shown in figure 2.1 (b) can be expressed, for high values of γ as:

Eq. (2.3) $\Delta\phi \approx \gamma^{-1}$

Therefore, for high values of γ , a narrow beam of radiation is emitted tangentially to the electron trajectory.

For high-energy electrons curving in the magnetic fields of storage rings, this radiation is extremely intense over a broad range of wavelengths extending from the infrared through the visible and ultraviolet range, and into the soft and hard X-ray parts of the electromagnetic spectrum. The high intensity, high brightness, broad spectral range and other properties (collimation, polarization, pulsed-time structure, partial coherence, high-vacuum environment) make synchrotron radiation a powerful tool for basic and applied studies in biology, chemistry, medicine, and physics, and their many subfields [W94].

First-generation synchrotron sources were originally built for high-energy physics research, in most cases involving the study of reactions that occur when counter-rotating electron and positron beams collide. In many cases, the synchrotron radiation programs started in a parasitic mode.

Second-generation storage rings were designed specifically as dedicated light sources. In general, these rings have a large number of beam lines and experimental stations, primarily from bending magnets, and they serve many users. Third-generation facilities use a combination of bending magnets and insertion devices such as wigglers and undulators. The latter are high field magnetic structures placed in straight sections which make wiggles (long period, high amplitude) or undulations (short period, short

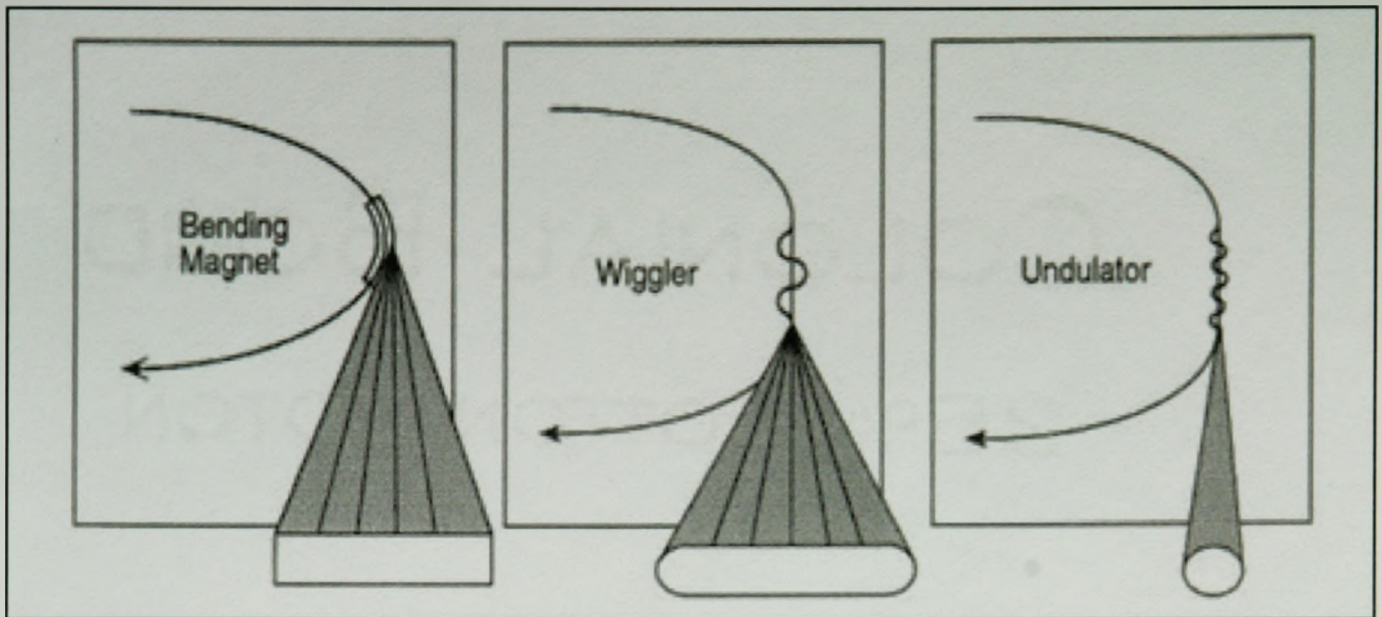


Figure 2.2 Schematic of the three approaches used for synchrotron light generation. Bending magnet light is available at all sources. Wigglers or undulators, which are periodic magnet structures installed in straight sections, provide much enhanced flux and brightness. (Figure courtesy of ALS, LBNL).

amplitude) in the charged particle trajectory which reinforces the light emitted by the accelerated electrons (see figure 2.2).

Both wiggler and undulator magnets deflect the electron beam in alternate directions, producing an angular excursion of the beam. However, the electrons leave the magnet structure in the same way they would if the magnet were turned off- that is, they produce no net deflection or displacement [WBH81].

An undulator is a magnetic structure with many periods in which the angular excursion of the electron beam is less than or of the order of the natural emission angle of synchrotron radiation (as shown in Eq. (2.1), given by $\gamma^{-1} = m_0c^2/E$, the ratio of the electron rest mass energy to its total energy). The undulator preserves the intrinsic brightness of synchrotron radiation in the plane of deflection. Unlike the smooth and

continuous spectral distribution of radiation produced by ring bending magnets and wigglers, interference effects in undulator radiation result in peaks at a few wavelengths. The undulator radiation has high spatial and spectral brightness at these wavelengths, which are tunable by changing the strength of the undulator field, usually by changing the gap.

A wiggler is a magnetic structure with one or a few periods in which the angular excursion of the electron beam is considerably greater than γ^{-1} but less than the angular deviation produced by one ring bending magnet. A wiggler is usually designed so that the angular excursion of the radiation from each pole approximately fills the angular acceptance of the synchrotron light beam pipe. Also, it is usually designed so that the peak magnetic field may be greater than the field in the bending magnets, resulting in a spectrum which may extend to higher photon energies. Thus, a wiggler magnet offers an extended spectral range and overall enhancement of the radiation brightness compared to the ring bending magnets.

The quality of the light produced by synchrotron light sources may be quantified by standard figures of merit, essentially the spectral flux and the brightness. The relevance of each figure of merit depends on the requirements of the experiment. The spectral flux, F , is the number of photons per unit time in a relative bandwidth (BW: $\Delta\lambda/\lambda = \Delta\varepsilon/\varepsilon$) of 0.1% whose units are ph/s/0.1%BW. The other figure of merit is the brightness, B , defined as the number of photons emitted per unit time, 0.1% of bandwidth and per unit phase space, i.e., per unit source area and per unit solid angle (i.e. in units of ph/s/mm²/mrad²/0.1%BW). Brightness cannot be improved by any optical element, and

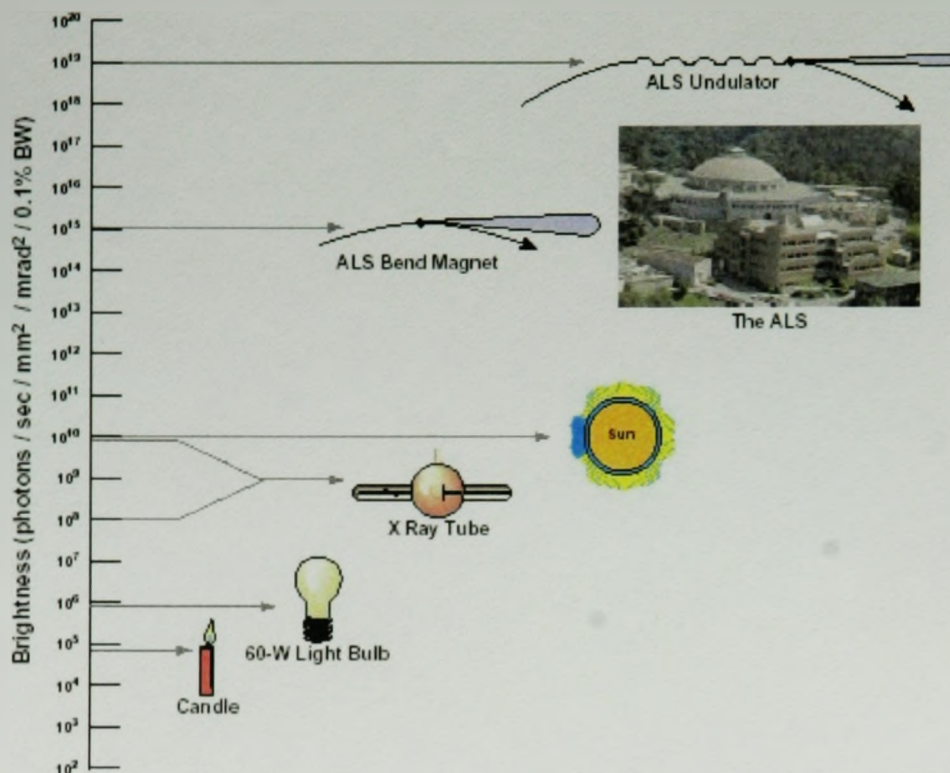


Figure 2.3 Comparison of the brightness of the bending magnet and undulator sources at the Advanced Light Source (ALS) to that of other common light sources.

consequently, it unambiguously predetermines the quality of the synchrotron light. In other words, the physical meaning of brightness is a density of useful photons either per unit area or per unit solid angle.

Figure 2.3 shows a comparison of the brightness available at the Advanced Light Source for bending magnets (10^{15} photons/sec/mm²/mrad²/0.1% BW) and undulator beamlines (10^{19} photons/sec/mm²/mrad²/0.1% BW) to that of other common light sources, such as an X-ray tube which varies between 10^8 and 10^{10} photons/sec/mm²/mrad²/0.1% BW.

§ 2.2 NEXAFS Spectroscopy

§ 2.2.1 History

The near edge X-ray absorption fine structure, NEXAFS, technique was developed in the 1980's with the goals of elucidating the structure of molecules bonded to surfaces, in particular low Z molecules, that are mainly organic molecules containing atoms such as hydrogen, carbon, nitrogen, oxygen and fluorine [S92]. NEXAFS selects a specific atomic species by using photons at the energy of the core excitation edge and probes the electronic structure associated with its bonds to neighbouring atoms. NEXAFS is based on absorption of X-ray photons to cause excitation of the inner shell electrons of the atoms in the substance. These excited inner shell (core) electrons can be promoted to unoccupied energy levels to form a short lived *excited state* or they can be removed completely to form an *ionized state*.

After revealing the shell structure of atoms at the beginning of this century, X-ray absorption spectroscopy was first used in the 1920's for structural investigations of matter. The observed fine structure near the absorption edges was first explained in general terms by a theory of Kossel [K20a, K20b] and for many years was referred to as "Kossel structure". In contrast, the structure extending for hundreds of electron volts past the edge was called "Kronig structure" after the scientist [K31, K32] who proposed an explanation. The latter is what is now called extended X-ray absorption fine structure (EXAFS).

During the 1970's, when EXAFS was developed into a powerful structural tool, the near edge structure which was automatically recorded with every EXAFS spectrum

was largely discarded as too complicated to interpret. One exception was the near edge structure of low-Z molecules which K-shells with binding energies in the 250-750 eV range could be conveniently excited by electron energy loss spectroscopy [B85, H82]. The high quality K-shell excitation spectrum of N₂ recorded with inner shell electron energy loss spectroscopy (ISEELS) [WBV73] served as the input for the first quantitative calculation of the near edge structure of a molecule, performed by Dehmer and Dill in 1975 [DD75, DD76].

The near edge structure has been mostly referred to as the X-ray absorption near edge structure, XANES, [B80] or the near edge X-ray absorption fine structure, NEXAFS [SJ82]. The term XANES is more commonly used for solids and inorganic complexes while NEXAFS is used more in conjunction with molecules, either free or adsorbed on surfaces. Alternatively, one can think of “N” EXAFS as “Not” EXAFS. In the remainder of this thesis, we shall use the term NEXAFS specifically for low-Z molecules, polymers and proteins.

§ 2.2.2 Theory of Inner Shell Excitation Spectra

For details of the theory of NEXAFS spectroscopy, there exists an excellent book on this topic [S92]. Some of the basic principles are given here with examples of the spectra of the materials that were investigated in this work.

Traditionally, X-ray absorption spectroscopy was described in terms of *absorption edges* which are the onset of inner shell ionization (see figure 2.4). There is an absorption edge associated with each inner shell energy level of an atom. All elements have an X-ray

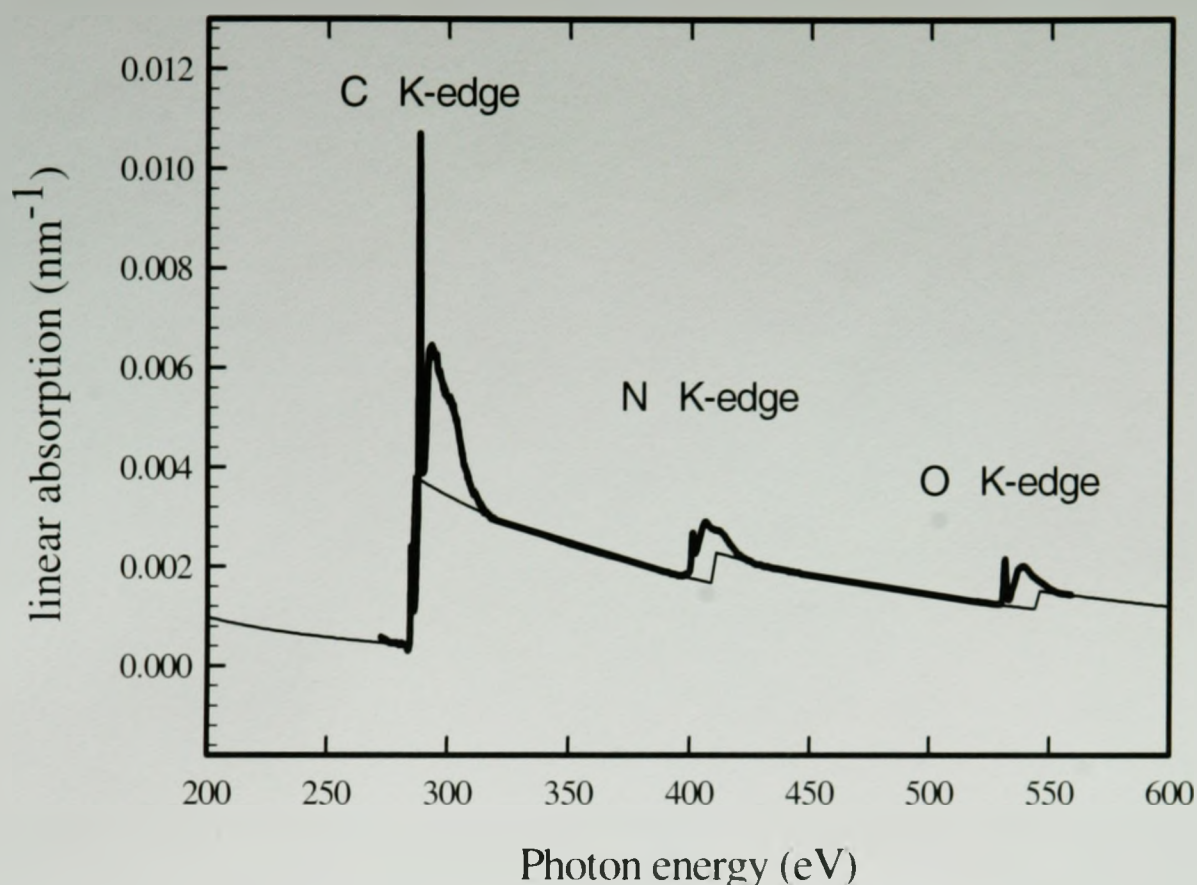


Figure 2.4 X-ray absorption response [HGD93] of fibrinogen, a blood protein, in the region of carbon, nitrogen and oxygen K-edges (thick line) normalized to optical density for 1 nm of protein at its standard density. NEXAFS spectra of fibrinogen recorded by X-PEEM scaled to the predicted elemental response (thin line). A rapid increase of the absorption occurs at the threshold of energy required to excite electrons from these inner shells.

absorption edge in the soft X-ray energy range (100-1200 eV). The amount of a particular element can be determined quantitatively from the difference in the X-ray absorption just above and just below its absorption edge.

While this traditional aspect of X-ray absorption provides the basis for elemental analysis, the modern technique as practiced at synchrotron facilities is much more powerful. It can identify and quantitate chemical structures (i.e. speciation, not elemental analysis) from the fine details of the absorption spectrum that occur at each edge.

§ 2.2.3 Detection methods

In NEXAFS, the X-ray energy is scanned and the absorbed X-ray intensity is measured. NEXAFS spectra can be recorded in different ways. Common methods are total electron yield (TEY), partial electron yield (PEY), partial Auger yield (PAY), transmission and fluorescence yield. The two spectromicroscopy techniques used in this work each illustrate one of these methods: STXM (transmission) and X-PEEM (total electron yield detection, TEY), see figure 2.5.

In transmission, the photons that are not absorbed by the material are detected using an X-ray sensitive detector. The intensity of these photons is proportional to the incident photon intensity, where the proportionality is given by an exponential function dependent on the energy dependent mass absorption coefficient, $\mu(E)$, the sample density, ρ , and the sample thickness, t . This is illustrated by Beer-Lambert's-Law [H48] below:

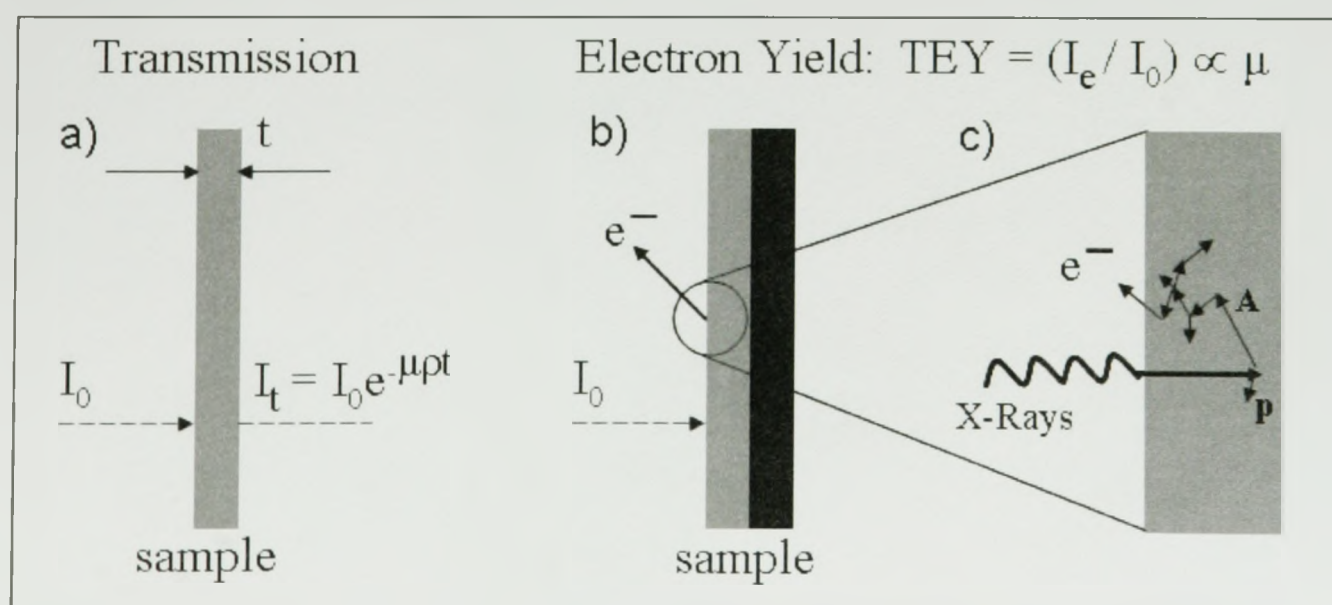


Figure 2.5 Two methods of recording X-ray absorption spectra: a) transmission and b) electron yield. c) A cartoon of electron generation and propagation in the near surface region. A represents an Auger electron and p is a primary electron. See text for further explanation of the figure.

$$\text{Eq. (2.4)} \quad I_t = I_0 e^{-\mu \rho t}$$

Rearranging this equation, one gets:

$$\text{Eq. (2.5)} \quad \text{OD} = \ln(I_0/I_t) = \mu(E)\rho t$$

The optical density, also called absorbance, is the log of inverse transmittance, which is the transmitted intensity over incident intensity.

For transmission detection, the samples must be partly transparent at the X-ray energy of interest, which means a sample thickness of 50 to 200 nm for carbon 1s studies of unit density organic material, ranging up to 1-2 microns thick for higher energy edges or low density samples such as hydrated polymer gels or biological samples.

For electron yield measurements, as long as the sample is conductive, it need not be very thin. The relation between the observed X-PEEM electron yield and the true absorption that occurs in the surface layer that contributes to the signal is a very complicated process that depends on many factors. Some of the most important of these variables are: the incident photon energy, the e^- propagation in the surface layer, the surface work function, the transport of e^- from the surface to the detector and the detection efficiency. Equation 2.6 describes the parameters involved in the X-PEEM signal.

$$\text{Eq. (2.6)} \quad S = G * t * \{[(\text{Flux}) * (\sigma) * (f_{\text{esc}}) * (f_{\Phi}) * (\epsilon_{\text{PEEM}}) - B]\}$$

where:

S = detected signal, G = camera gain (2,4,8), t = exposure time, Flux = photons/s at the sample, σ = photoabsorption cross-section, f_{esc} = e^- escape probability, Φ = work function,

ϵ_{PEEM} = X-PEEM column efficiency (depends strongly on the sample position), B = no-X-ray background and:

$$\text{Eq. (2.7)} \quad \text{Flux} \propto (I\text{-ring}) \cdot (C_{\text{max}} - C) / C_{\text{max}} \cdot (T_{\text{max}} - T) / T_{\text{max}} \cdot (\text{other filters})$$

where:

I-ring = the current in the ALS ring, C_{max} = the maximum opening between the mask and chopper, which together control the polarization and the size of the beam hitting the sample, C = the experimental opening between the mask and the chopper, T_{max} = when no Ti filter is in the beam path, T = when the Ti filter is in the beam path

$$\text{Eq. (2.8)} \quad \epsilon_{PEEM} \propto (\text{magnification})^{-1} \cdot (\text{aperture})^2$$

The incident photon energy influences the resulting signal in that the absorption is energy dependent, as shown on figure 2.4. The maximal absorption, and corresponding photoemission, occurs near the edge of a particular element and follows a decreasing sloped background above the edge.

The way electrons propagate through the surface layer is depicted in Fig. 2.5 c). Electron transport is very material dependent. A typical estimate of the secondary yield in organic materials, is approximately $1e^-$ per 30 eV of photon energy in organic materials but only some of these make it to the surface with a velocity large enough to escape.

The main issue that affects the electron transport in the PEEM is the chromatic aberrations of lenses (both electrostatic and magnetic). Currently, when operating the PEEM2 instrument with the smallest column aperture (12 μm), the column transmission is only a few % (see figure 2.6).

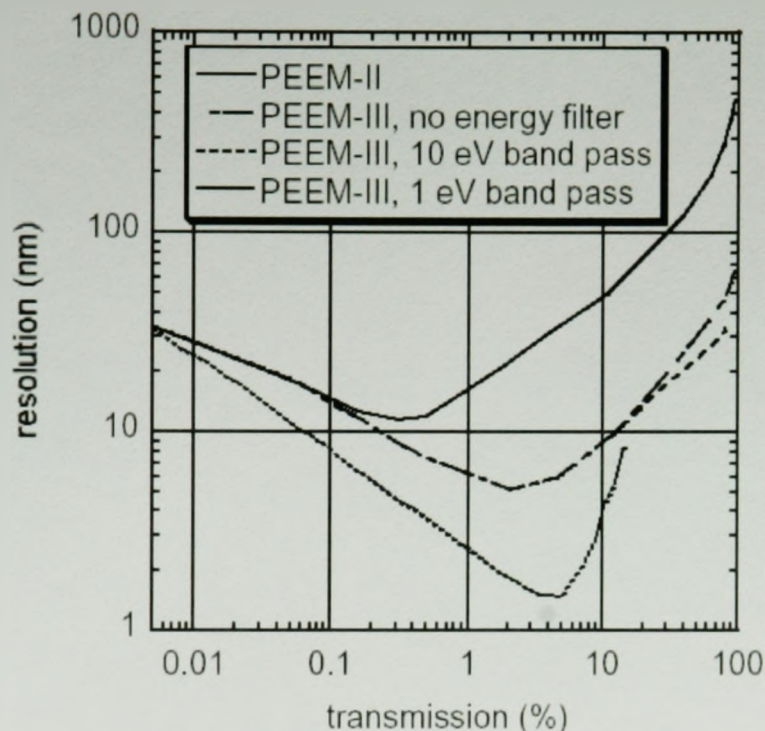


Figure 2.6 PEEM2 and PEEM3 spatial resolution as a function of lens transmission [P].

The detection efficiency is a minor concern since both the phosphor and the CCD are efficient.

§ 2.2.4 Chemical sensitivity

NEXAFS is both element specific and sensitive to the local chemical environment. The former is because the x-ray absorption edges of different elements have different energies, as illustrated in figure 2.4.

As for the bonding environment sensitivity, NEXAFS spectra exhibit considerable fine structure above each elemental absorption edge. Figure 2.7 shows the C1s, N1s and O1s spectra of fibrinogen (Fg), as well as the C1s spectra for polystyrene (PS) and poly(methylmethacrylate) (PMMA), and the O1s spectrum of PMMA. These were obtained from the pure material with the X-PEEM instrument at the ALS.

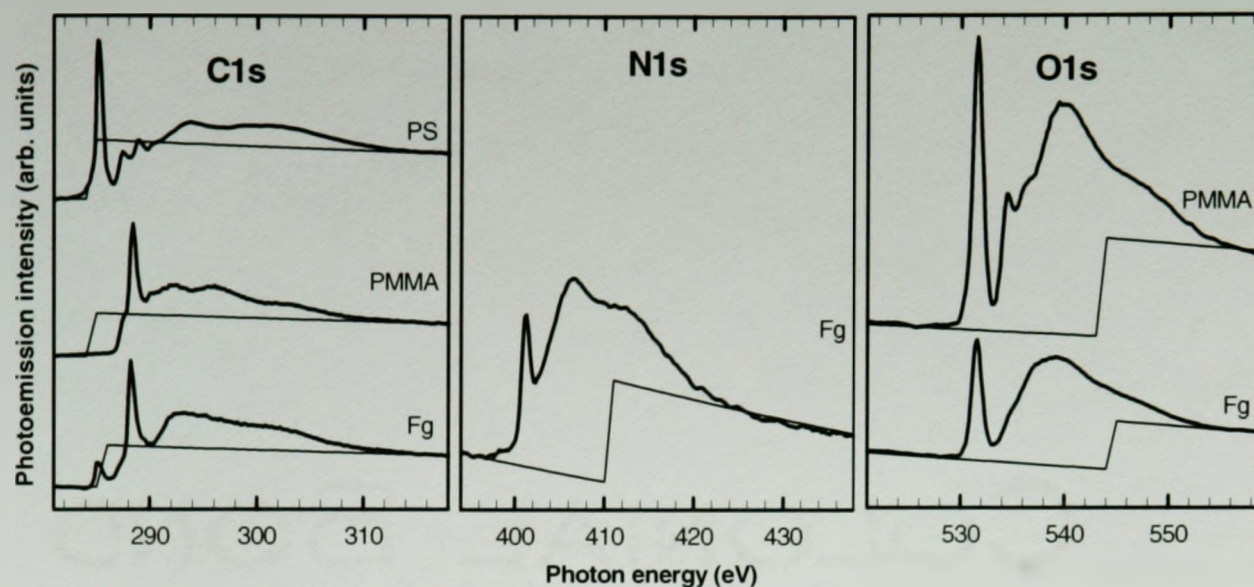


Figure 2.7 C1s, N1s, and O1s NEXAFS spectra of PS, PMMA and Fg recorded as pure materials with X-PEEM. The straight lines indicate the elemental response. The intensities within each panel are on the same scale, although offsets are used for clarity. Different scaling is used for each panel.

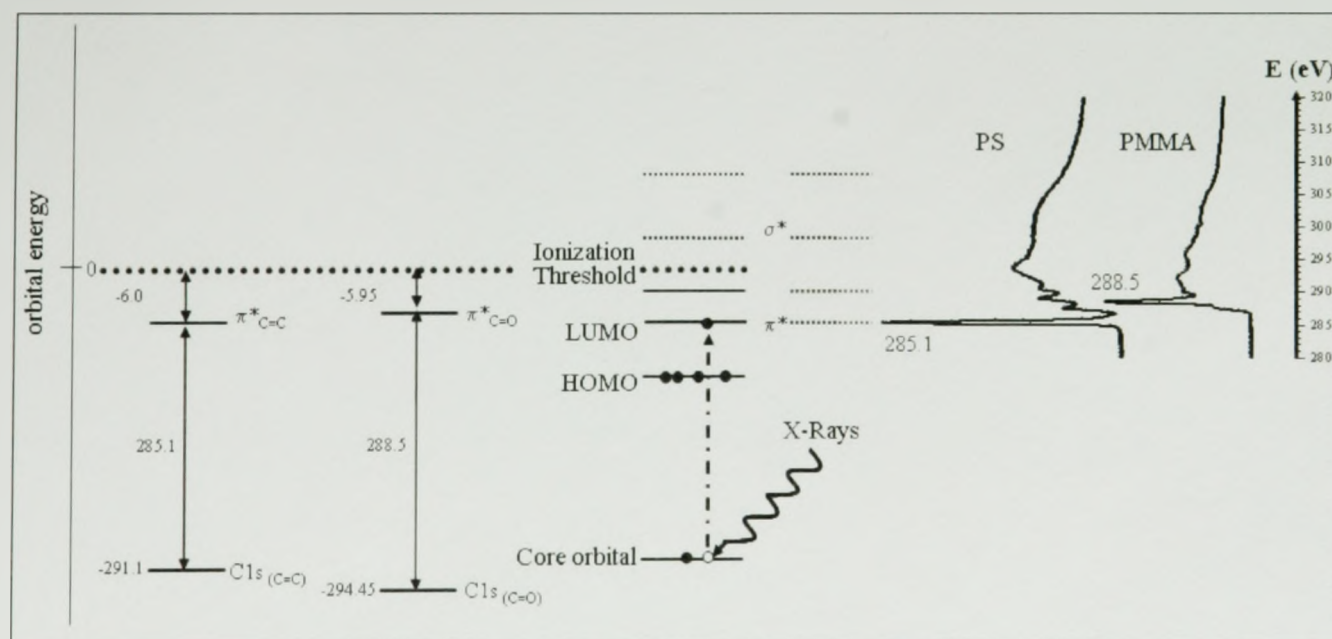


Figure 2.8 Comparison of PS and PMMA C1s energy diagrams and spectra.

Figures 2.4 and 2.7 show that the near edge structures are much more intense than the absorption edge. The fine structure arises from excitations into unoccupied molecular orbitals, as illustrated in figure 2.8. Each molecule has its own distinct electronic structure, which is governed by the different bonds within the molecule. NEXAFS spectra

reflect these differences in bonding due to the following two factors: a) chemical shifts of core levels which are related to the local charge and oxidation state; b) the details of unoccupied molecular orbitals, which are strongly linked to the type of chemical bonding (σ , π) and the local geometry of the excited atom. To illustrate these concepts, figure 2.8 shows the core binding energies of molecules analogous to polystyrene (ie: benzene, 290.4 eV) and to poly(methylmethacrylate) (ie: methyl acetate, 295.85 eV) [BEJ86]. The energies of the $C1s_{(C=C)} \rightarrow \pi^*_{C=C}$ and $C1s_{(C=O)} \rightarrow \pi^*_{C=O}$ transitions are known from the STXM and X-PEEM spectroscopy. Assuming a frozen orbital approximation, in which transition energies are given simply by the difference in orbital energies, one finds that the $\pi^*_{C=O}$ orbital is at a slightly lower energy than that of the $\pi^*_{C=C}$ orbital.

The other features in figure 2.7 can be explained by comparing the C1s spectra of polystyrene, polymethylmethacrylate, and fibrinogen, as well as the O1s spectra of the latter two materials in relation to their chemical structures (figure 2.9).

Starting with the C1s spectrum of polystyrene, the most intense feature at 285.1 eV corresponds to the $C1s_{(C=C)} \rightarrow \pi^*_{C=C}$ transition. This transition is also found (weakly)

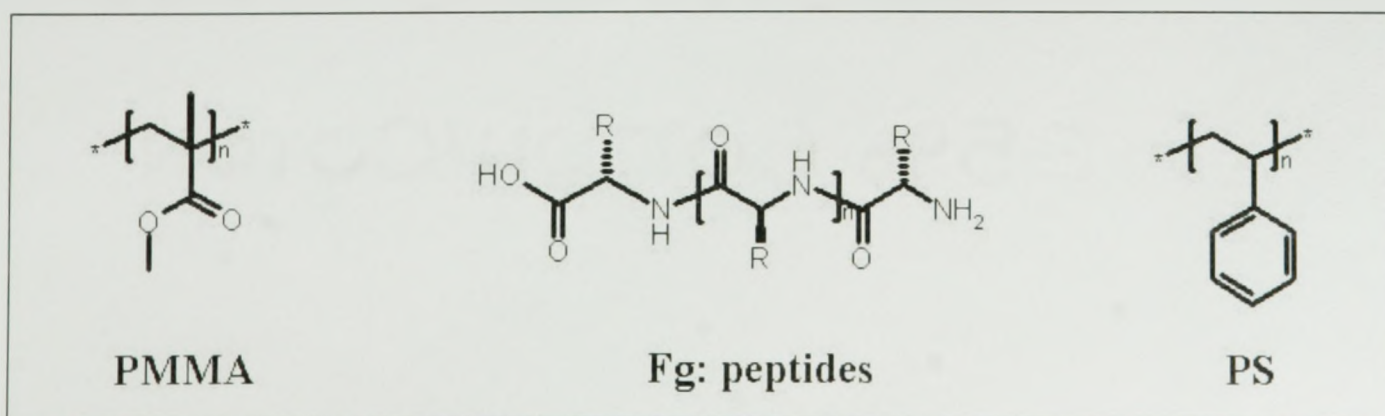


Figure 2.9 Chemical structures representative of PMMA, Fg and PS.

in the fibrinogen C1s spectrum because proteins contain amino acids with phenyl groups (R substituents in figure 2.10). Notice that PMMA does not contain C=C bonds, and thus does not absorb at 285.1 eV.

The intense peak in the C1s spectrum of PMMA arises from the $C1s_{(C=O)} \rightarrow \pi^*_{C=O}$ transition at 288.5 eV. A related $\pi^*_{C=O}$ feature occurs at 288.2 eV in fibrinogen. The difference in energy of the $C1s_{(C=O)} \rightarrow \pi^*_{C=O}$ transitions in these two species is due to the differing environment of the carbonyl group. For PMMA, the C=O is in proximity to an oxygen atom, O-C=O, while the carbonyl group in proteins is bound to a nitrogen atom, N-C=O. Due to the greater electronegativity of oxygen in comparison to nitrogen, the electron density around the C is reduced to a greater extent for PMMA than for Fg, and as a result, the binding energy for the carbonyl carbon 1s level in an amide is smaller than that of an ester (NH₂CHO, 294.45 eV versus H₃CCOOCH₃, 294.85 eV) [IH87]. This is the same as the chemical shift measured in XPS spectra. Thus, the $C1s_{(C=O)} \rightarrow \pi^*_{C=O}$ transition is at a higher energy for PMMA than Fg.

Fibrinogen is the only species amongst these three which contains nitrogen, so it is the only one which shows features in the N1s energy region, 390-440 eV. The main signature of Fg at the N 1s edge is the peak at 401.2 eV, the $N1s_{(N-C=O)} \rightarrow \pi^*_{NC=O}$ amide transition. This arises because there is partial delocalization of the $\pi^*_{C=O}$ orbital on to the amide N atom [IH87].

The right hand panel of figure 2.7 shows the PMMA and Fg O1s spectra. PS is not shown as it does not contain oxygen. Both PMMA and Fg have their main feature at 531.6 eV, corresponding to a $O1s_{(C=O)} \rightarrow \pi^*_{C=O}$ transition. PMMA also has an extra

transition at 535.45 eV which arises from the $O1s_{(OCH_3)} \rightarrow \pi^*_{C=O-OR}$ transition. This feature is analogous to the $N1s_{(N-C=O)} \rightarrow \pi^*_{NC=O}$ feature in Fig, again arising from delocalization of the carbonyl orbital onto the adjacent heteroatom [IH87].

§ 2.3 STXM principles

§ 2.3.1 General Principles

Two STXM instruments were used. From September 1999 until December 2001, the first ALS STXM (without interferometric control) located on beamline 7.0.1 was used [WFK&98]; here, it will be referred to as the “old” STXM 7.0.1. After January 2002, a dedicated STXM [KTS&03], the first in the world with interferometric control, was used on beamline 5.3.2 [WAK&02]. An alternate implementation of interferometer control was installed on beamline 7.0.1; this instrument is referred to as the “new” STXM 7.0.1. In 2003, this latter microscope was modified to use STXM532 type of interferometer control. It is now installed on the molecular environmental science beamline, 11.0.2. The STXM 11.0.2 was not used for the work detailed in this thesis. Differences in the beamlines (5.3.2 versus 7.0.1) and instrument designs (5.3.2 versus “old” STXM 7.0.1) will be highlighted in section 2.3.2.

The use of synchrotron radiation for STXM is necessary because the photon energy must be scanned for NEXAFS and also because a high photon flux in a small spot is required to acquire useful information in a reasonable time. The undulator beamline (7.0.1) provided count rates of the order of tens of MHz at high-energy resolution with photon energies of up to about 1000 eV. Although the brightness of a bending-magnet

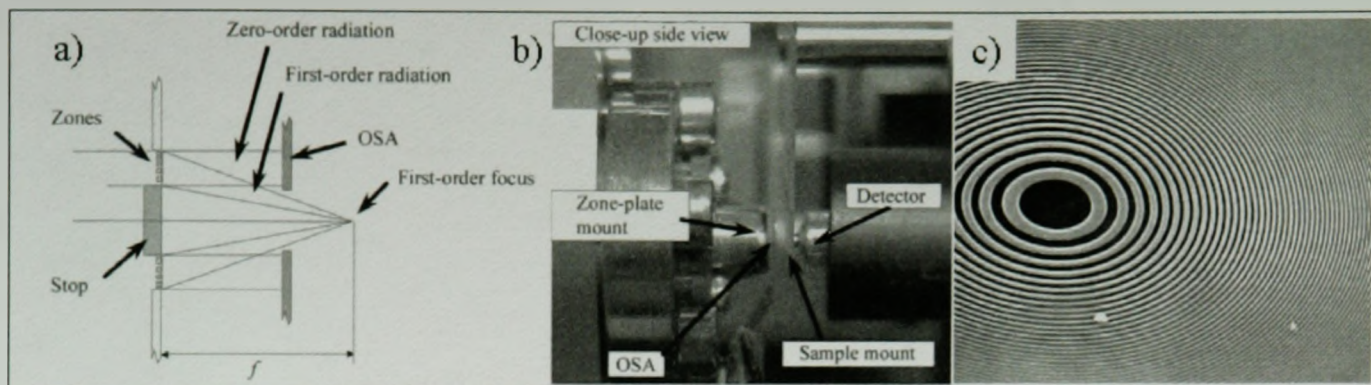


Figure 2.10 Focusing scheme of a STXM: a) in diagram form, b) a picture c) scanning electron microscope image of the inner part of a Fresnel Zone Plate Lens. This lens has 318 nickel zones, a diameter of 45 μm , and the smallest (outermost) zone is 35 nm wide. Courtesy of Center for X-Ray Optics, LBNL.

source is about four orders of magnitude smaller than that of an undulator source, due to inefficiencies of the beamline 7.0 optics, the flux on the sample at the STXM 5.3.2. was smaller by only 1-2 orders of magnitude

In scanning transmission X-ray microscopy (STXM), a soft X-ray beam is focused by a Fresnel zone plate [A99], illuminates the sample and the transmitted X-rays are detected. Transmission images are obtained by a raster scan of the sample through the focal point of the zone plate. Spectra are obtained in point, line or image mode by acquiring signal at multiple photon energies. The primary signal measured in STXM is transmitted intensity (I_t) as a function of energy (spectra), or position (images). This signal, when converted to optical density (OD), is sensitive to sample thickness, density and composition, according to equation 2.5.

Measuring a raster scanned set of pixels and converting with the incident flux (measured through a hole), gives an X-ray OD image at a single photon energy. Changing the photon energy and taking images with other photon energies gives an image

sequence (stack), which includes chemical information as well as topographical information [JWF&00]. Analyzing the data with suitable reference model spectra can provide chemical maps with sub-100 nm spatial resolution.

§ 2.3.1.1 Key concepts in optimizing STXM

The performance of the X-ray microscope can be characterized by several properties, for example, the spatial resolution, and the energy resolution. The latter will be discussed in section 2.3.2.

The spatial resolution is achievable because of the components within a STXM microscope and their precise geometry with respect to one another. Figure 2.10 shows the focusing scheme of a STXM microscope, a) in diagram form, b) a picture, c) scanning electron microscopy image of the inner part of a Fresnel zone plate typically used in full field X-ray microscopy.

The small x-ray spot is produced by a Fresnel zone-plate lens [A99, MB93]. This is a variable-line-spacing circular diffraction grating. The fabrication of zone plate lenses requires state-of-the-art nano-fabrication techniques, because the required structures are sub-micrometer scale and the zones must be positioned with an accuracy comparable to the photon wavelength –typically 2 nm precision over 100 000 nm. Figure 2.10 c) shows an SEM image of a zone plate typically used in full field X-ray microscope. On the figure, the bright areas are gold and the dark areas are Si_3N_4 . The type of ZPs used for STXM are of a different design than those for full field X-ray microscopy; STXM's have a large central stop, as shown on Figures 2.10 a). The purpose of the central stop is to

block the zeroth order light and to suppress unwanted diffraction orders that would degrade spatial resolution. Schematic representations of zeroth and first order light are shown on Figure 2.10 a). The zeroth order light is the light that is not diffracted by the zone plate, and the first order light is the most intense diffracted light. Less intense higher order radiation is suppressed by an order selection aperture, OSA, which is a pinhole slightly smaller than the central stop [KTS&03].

The principles of operation of Fresnel zone plates are well summarized in the CXRO Handbook of synchrotron radiation, versions 1 and 2 [KA86, TAG&01]. The focal length (f) of a zone plate, the distance between the zone plate and the sample, at a given photon energy (E) is given by:

$$\text{Eq. (2.9)} \quad f = D \cdot \delta_{rN} / \lambda$$

where D is the ZP diameter, δ_{rN} is the width of the most outer zone (N th), and λ is the photon wavelength (E (eV) = $1239.9/\lambda$ in nm scale). The value of D and δ_{rN} for the ZP presently used in STXM 5.3.2 are 155 μm and 35 nm respectively. Thus, when scanning across the C 1s edge, from 280 eV to 340 eV, the focal length changes from 1225 μm to 1490 μm . The ZP must maintain a pointing accuracy of 10 nm while moving the ZP by this distance of 265 000 nm; this is achieved by the laser interferometry control system.

The diffraction limited spatial resolution (Δr) is given by [TAG&01]:

$$\text{Eq. (2.10)} \quad \Delta r = 1.22 \cdot \delta_{rN}$$

This equation says the resolution is limited by the ZP outer zone width. However the ultimate resolution of the zone plate can only be achieved if the microscope

is adjusted properly. Thus users have to pay attention to many points about the microscope operational parameters and the beamline settings. In particular, the OSA position, ZP focus, sample-OSA distance, sample focusing, and the accuracy of the energy scale all play a role in getting the highest spatial resolution and keeping it over an extended range of photon energies.

At the 5.3.2. STXM, the diffraction efficiency for first order is about 10%. Most of the light is un-diffracted (zeroth order) and this must be excluded as much as possible since, if it is not blocked, it provides an illumination at reduced intensity of approximately the size of the ZP (~200 μm). Even so there is always an irreducible zero-order contribution which forms a 'halo' of the size of the ZP, with an integrated strength of 1-5% of the focused beam intensity. In addition, depending on the quality of alignment of the OSA and the central stop, there can be some second-order signal (light in the focused spot at twice the photon energy). By aligning the central stop and OSA properly, the non-first order light can be minimized and higher contrast and more quantitative images are obtained. In order to get the minimum amount of zero order light the center of the OSA must be aligned to the center of the ZP to within 5 μm .

§ 2.3.2 Instrumental description, particularities of (7.0.1 and 5.3.2)

§ 2.3.2.1 STXM Microscope

Figure 2.11 shows the 5.3.2 STXM components. The microscope contains the following major system components: zone-plate z stage; OSA x , y stages; sample x , y

coarse stage; sample x , y fine piezo stage; sample z stage; detector x , y , z stage; interferometer system; mounting platform; passive vibration isolation to the floor and vacuum/He enclosure. One of the advantages of the STXM 5.3.2 instrument is the passive vibration isolation to the floor. The instrument is isolated from floor vibrations by styrofoam pads. The microscope is built on a rigid polymer composite base- referred to as polymer granite or polymer concrete (Zanite, Precision Polymer Casting). The large weight resists resonant amplification of floor frequencies. The ALS floor at STXM 5.3.2 is actually quite noisy with resonance modes in 120-160 Hz with > 100 nm amplitudes. The microscope itself is built so that only a small fraction of this amplitude (typically 10 nm) is transferred to the sample or zone plate. The detectors used in the ALS STXMs are phosphors to convert X-rays to visible light. The visible photons are counted by high performance photomultiplier (PMT) systems which can count linearly up to ~ 20 MHz. The 5.3.2 detector is shown in figure 2.12.

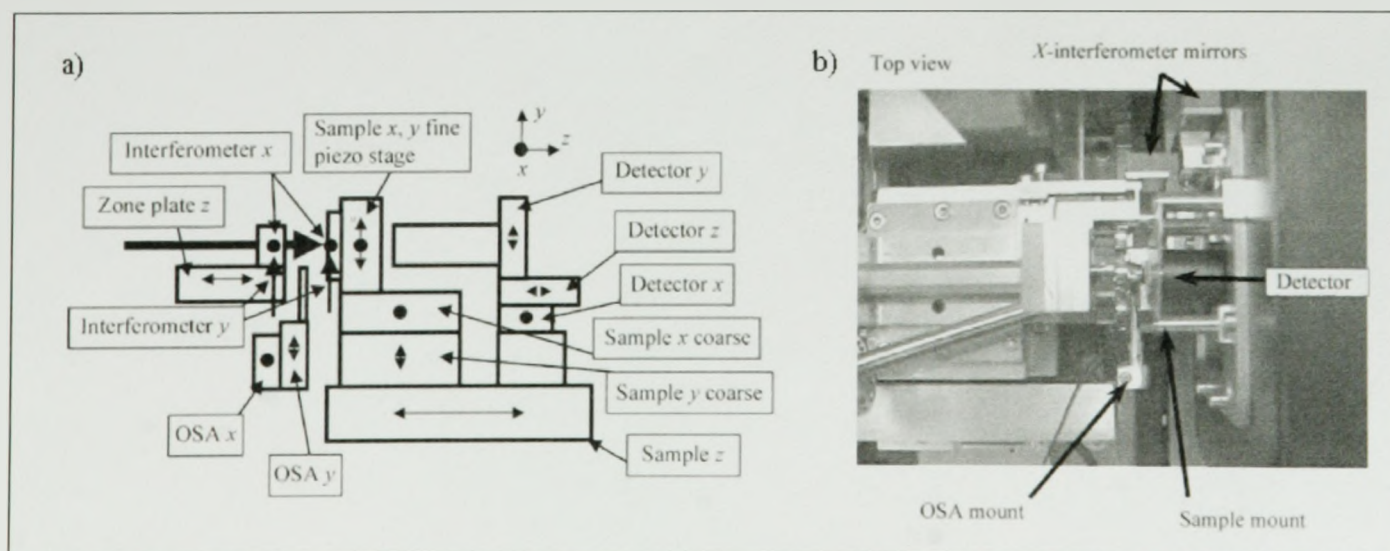


Figure 2.11 5.3.2 STXM components a) schematically, b) top view picture

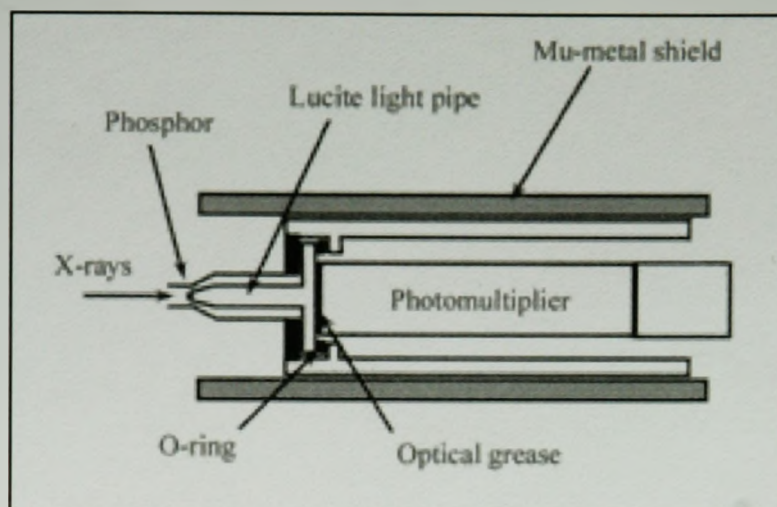


Figure 2.12 Geometry of the 5.3.2 detector for transmitted photons

The front of the Lucite pipe is coated with a very thin layer of a polycrystalline phosphor film. Small single crystals of CdWO_4 (CWO), $\text{YAlO}_3:\text{Ce}$ (YAP) or $\text{Gd}_2\text{O}_2\text{S}:\text{Pr}$ (GSO) are supported directly on a flat Lucite tip. Granular phosphors (P11, P43 and P47) were deposited by sedimentation from a suspension. The granular-phosphor deposition process has to result in a layer that is thin enough to prevent light scattering, and hence loss of signal, yet sufficiently dense to cover the tip. The Lucite tips are carefully shaped to increase the light collection of the granular phosphors by using refraction and critical internal reflection. The cone-shaped Lucite increases the detection efficiency by more than 50% for the same sedimentation procedure. Different phosphors were compared by comparing the system efficiency with that of a silicon photodiode with a very thin oxide layer on the front surface. On average, the diode produces one electron-hole pair for each 3.6 eV of X-ray energy deposited, and the X-rays are always absorbed in the silicon,

except just above the oxygen edge (530 eV). Thus, at a specific photon energy the absolute diode current gives the absolute photon flux.

The main difference from the “old” and the new 7.0.1 design is the implementation of interferometry control which allows the precise measurement of the transverse position of the zone plate relative to the sample. Long-term positional stability and compensation for transverse displacement during translations of the zone plate have been achieved. With the old STXM 7.0.1, it used to be necessary to realign the stacks of images post-acquisition with specialized software [JWF&00]; this typically is no longer the case with the new 5.3.2 and 11.0 microscopes, although minor stack alignment (~ 200 nm versus $1\text{-}2\ \mu\text{m}$ for the old STXM 7.0) is required if the microscopes have not been recently optimized.

The focal length, the distance between the zone plate and the sample, is energy dependent (see Eq. 2.9). In order to keep the sample in focus, the zone plate must move large distances when scanning through an absorption edge (for example, nearly $400\ \mu\text{m}$ at the C1s edge) and during that displacement, the x , y coordinates of the zone plate must remain aligned with that of the sample, ideally to a precision of ~ 10 nm in order to maximize the quality of the spatial resolution. However, over the course of this $\sim 400\ \mu\text{m}$ displacement of the zone plate, its x , y coordinates wobble by up to $\sim 2\ \mu\text{m}$. Thus, the role of the interferometer is to measure and compensate for changes in $(\Delta x, \Delta y)$ of the zone plate and sample position as the zone plate moves in z . It is specifically this “run out” in this motion that caused image mis-alignment.

Some of the advantages of the interferometry system are as follows:

- 1) When the interferometer is operated in a closed-loop mode, vibrations in both scan directions can be reduced to about 10 nm peak-to-peak. Measurements performed in the closed-loop mode showed that the 5.3.2 microscope is ready to use zone plates with spatial resolution better than 20 nm.
- 2) The implementation of a laser interferometer also provides for a continuous absolute coordinate system with a field of view of over 20 mm. This makes the operation and selection of the coarse and fine motion transparent to the operator. The operation is completely under computer control.
- 3) The large-field absolute coordinate system is also integral to a pre-indexing system based on visible-light microscopy. Areas of interest on a sample can be selected with a high-quality visible-light microscope, and the coordinates can be stored under computer control for later use. After sample transfer to an identical sample mount with a transfer accuracy of about 20-30 μm , the areas of interest can be recalled by the operator and easily found.

Another difference between the old 7.0.1 STXM, and the 5.3.2. and “new” 7.0.1 (now 11.0) STXMs is the possibility of evacuating the STXM chambers down to 10^{-6} torr. Already at the old STXM, in order to increase the photon flux at the sample, the microscope could be filled with helium. Compared with air, the He environment provides more photons on account of lower absorption and results in smaller interferometer drifts because of its lower index of refraction; furthermore, the elimination of oxygen from the environment slows the degradation of polymeric materials during soft X-ray exposure [CUA02]. Simultaneously, helium provides a thermally stable environment, once the fill

reaches room temperature. The high thermal transport coefficient of He provides efficient cooling of the stepping motors and other electronic components inside the enclosure. Pumping, rather than pushing the air with He, is used to get faster, cheaper and more efficient removal of air in order to measure at the N1s edge. With further improvement of pumping by use of a turbo pump, it will eventually be possible to use a channel plate for single electron counting detection of surface sensitive TEY detection in STXMs.

§ 2.3.2.2 STXM Beamlines

The improved performance of the 5.3.2 microscope is not solely due to the microscope design and its superior components, the custom built beamline on which the microscope is installed also greatly contributes to the advantageous nature of the instrument. Figure 2.13 shows the layout of beamline 5.3.2.

The STXM zone-plate lens accepts only the coherent fraction of the illuminating beam when focusing at its diffraction limit. This coherent photon flux is inside a volume in transverse phase space (in units of source area and per unit solid angle, i.e. $\text{mm}^2/\text{mrad}^2$) of the order λ^2 , incident on the lens and travelling close to the optical axis. This means that the STXM zone plate lens limits the size of the beam accepted. Photons outside the phase-space acceptance are lost on slits and by overfilling the lens. This leads to a beamline design that is almost paraxial, with small optics and deep foci. The advantages of using small, simple optics are: a) ease of movement of the small optics to obtain a small beam size, b) low cost, much less than for larger, more complicated optics as were

used for BL 7.0.1 (see figure 2.14). The principles of the optical design for BL 5.3.2 have been described in [WPA98].

In order to select a single energy from the fan of wavelengths emitted at the source, the spectrum must be dispersed. A spherical-grating monochromator (SGM) which disperses in the horizontal plane was chosen since it is more efficient for phase-space conservation. The low-dispersion design of the SGM ensures that the grating defocus at the fixed exit slit is negligible over the operational range. This is an advantage of BL 5.3.2 over BL 7.0 where the exit slit had to be moved to accommodate the choice

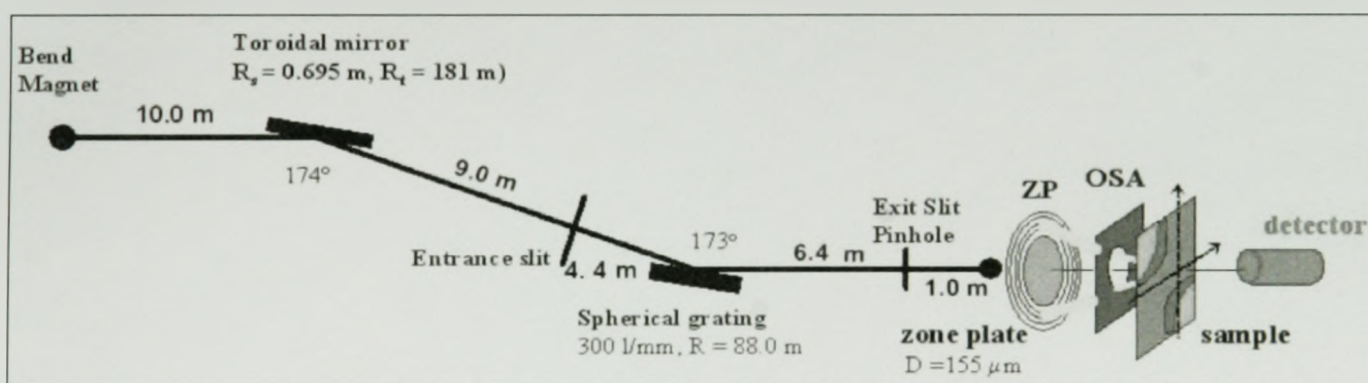


Figure 2.13 Beamline 5.3.2 layout (Plan view)

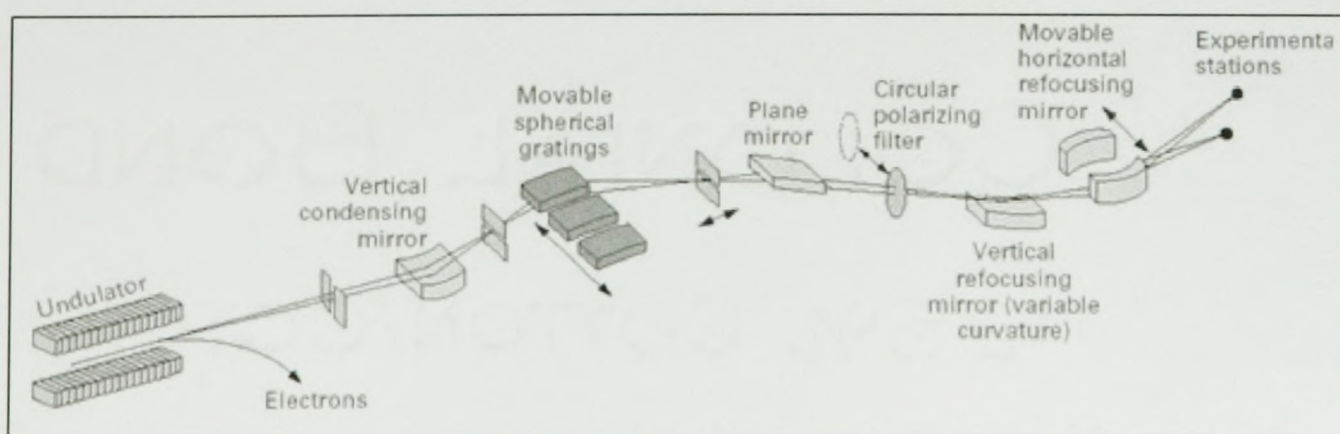


Figure 2.14 Beamline 7.0.1 layout

Table 2.1: Advantages and disadvantages of beamline and microscope 5.3.2

Advantages	Disadvantages
Stable beamline optimized for STXM, good phase preservation	Lower flux than 7.0.1, limited "SGM in focus" energy range (250-600 eV)
Stable STXM due to interferometry	
Good control of exposure due to fast shutter system	
Change of coarse to fine sample stages is transparent to user	
User friendly software	

Table 2.2: Advantages and disadvantages of beamline and "old" 7.0.1 microscope

Advantages	Disadvantages
More intensity	Unstable beamline and monochromator
Larger energy range, 50-1200 eV	Limited access (2 other end stations on the same beamline)
	STXM drifted
	Radiation damage

of movable spherical gratings. Energy resolution is determined by the settings of the entrance slit and the dispersive exit slit.

Another advantage of the 5.3.2 beamline design is the inclusion of the toroidal feedback. It ensures that the zone plate illumination is constant over long periods of time (1-5 hours) and with fast response (100 Hz).

In summary, the advantages and disadvantages of STXM 5.3.2 (beamline and microscope) versus the old STXM set up at 7.0.1 [WFK&98] are given in table 2.1 and table 2.2, respectively.

§ 2.4 X-PEEM principles

§ 2.4.1 Background information

In 1985, Ernst Bauer and his student Wolfgang Telieps published a stunning set of images that abruptly solved a long-debated question in surface science: What is the nature of the phase transition that occurs on the (111) surface of silicon? [TB85] Determining the complex ordered arrangement of atoms, or “reconstruction”, that occurs there had been one of the hottest problems in surface science for nearly 25 years [TTT&85]. One of their images shows a sharply defined coexistence between two structural phases and demonstrates a first-order –rather than a continuous second order – transition between an ordered (bright) and disordered (dark) arrangement of atoms at the surface. Bauer and Telieps’s unambiguous answer about the nature of that disordering transition dramatically introduced a very powerful probe of solid surfaces: low-energy electron microscopy (LEEM).

The desire to add a chemically sensitive imaging mode to the structurally sensitive imaging with slow reflected electrons (LEEM), in turn lead to the development of PEEM. In PEEM, a UV or soft X-ray light source replaces the incident electron beam, and photoelectrons provide the chemical and surface potential contrast. Tonner et al. were the first to use soft X-rays, at a synchrotron, as a means of illumination in the PEEM, thus X-PEEM [TH88], [HHT90], [THK&92].

A principal characteristic of the PEEM is high surface sensitivity which enables the PEEM to be used to study monolayer adsorption at surfaces [REK&91]. The variations in image intensity (contrast) that are seen in PEEM are due to a combination of

topographical features, work function effects, and chemical composition. When the sample is illuminated by UV light, the primary cause of compositional variations in contrast is due to work-function changes between different areas of the surface, which changes the threshold photon energy for electron emission.

With X-rays, the incident photon energy is much larger than the work function, and the contrast depends on the surface composition through the absorption coefficient. The secondary electrons are used to form an image of the surface directly in the X-PEEM. The secondary yield will depend upon the composition both through the absorption coefficient $\mu(E)$ and through the thickness of the film, for thicknesses less than the escape depth of the sample. However, the yield from small areas of the image as a function of photon energy is due only to the variations in absorption coefficient, so that the micro-XANES spectrum is free of structure-induced artifacts.

Chemical imaging with X-PEEM can also be done with photoelectrons instead of secondary electrons. Auger electrons could in principle be used too, but they are less useful than photoelectrons because they contain a convolution of two states, and the peaks are usually broader in energy and are situated on a higher background than the photoelectron peaks [B01]. Secondary electron imaging uses the slow secondaries that are produced in the filling of the core hole created in the primary photoexcitation processes. These processes have a particularly sharp onset in s and p core levels and depend upon the transition probability from the ground state to the unoccupied states above the Fermi level (see figure 2.8).

Whenever photoelectron imaging can be used, it has at least two advantages over secondary electron imaging: (i) a narrow energy distribution ranging from less than 1/2 eV to about 2 eV for useful inner shells and (ii) an easier determination of the bonding via the associated 'chemical' shift of the binding energy of the core level. Secondary electron emission imaging has the advantage that it does not require a band-pass filter. However, because the energy distribution of secondary electrons is wide, usually several eV at FWHM, and because of the chromatic aberration of the objective lens, the spatial resolution is poor without a band pass filter or aberration corrector. The X-PEEM instrument used in this work did not have a band pass filter so the imaging was done using secondary electrons.

The number of secondary electrons produced per incident photon can be much higher than unity, so that the image intensity in the X-PEEM will generally exceed that of a primary photoelectron microscope. The large current of secondary electrons to pursue micro-XANES experiments using bending-magnet x-ray sources [TH88], [HHT90], [THK&92], down to spatial resolutions of 1 μm , with images acquired with integration time constants of 1 s or less.

The work of Tonner and collaborators has led to the construction of PEEMs by several groups ([TDD&95], [WLL&97], [DCL&98], [TR91], [EKR&91], [MBL&97]), including the instrument that was used for this thesis, PEEM2 [APD&99], as well as the introduction of commercial systems, like the one used at SRC since May 2002, the Canadian Photoelectron emission Research Spectromicroscope (CaPeRs), purchased from Elmitec GmbH. The evolution in microscopes and beamline designs has much improved

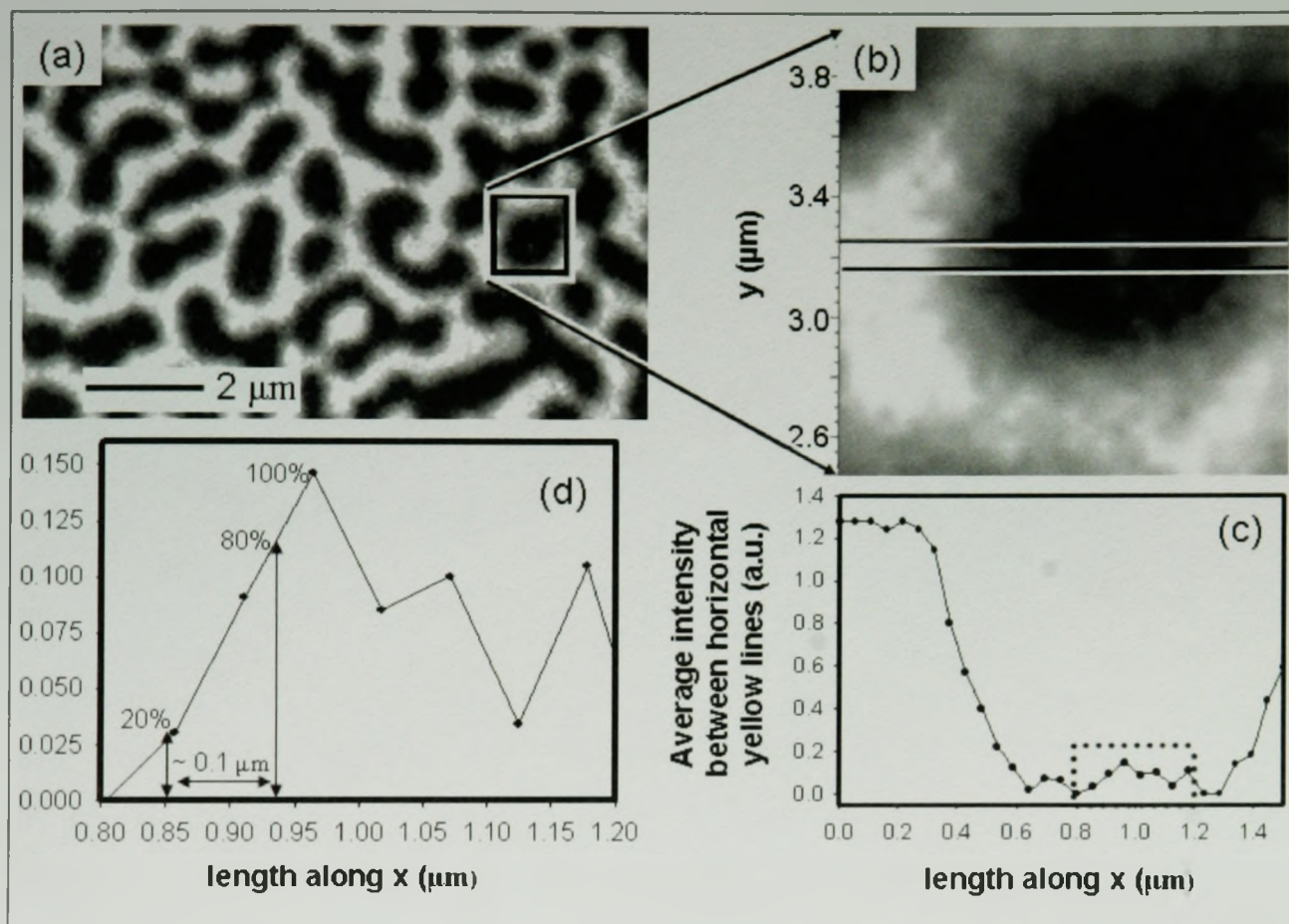


Figure 2.15 The X-PEEM spatial resolution is limited to ~ 100 nm for polymer samples. (a) PS component map from a stack fit analysis of a 30:70 PS:PMMA sample, annealed 8 hours at 160°C . (b) blow up of the black/white box in (a). (c) Line profile from the region between the two black/white lines shown in (b). (d) The blow up from the dotted box in (c) shows that the resolution is approximately 100 nm. This is the distance between 20% and 80% of the maximal intensity where 100% corresponds to the center of the PS microdomain

the spatial resolutions of modern X-PEEM microscopes used at synchrotrons. For polymer samples, PEEM2 can provide ~ 100 nm spatial resolution (see figure 2.15).

Several new X-PEEMs are under development (SMART: [FWU&97], [SGF&02], and PEEM3: [FPW&02]) which will use aberration compensation optics, see figure 2.6 for a theoretical prediction of the spatial resolution in PEEM3 as a function of lens transmission [P]. As depicted on the figure, these microscopes are expected to improve the column transmission by a large amount, enabling higher spatial resolution or higher

efficiency than at present day spatial resolution. Improving detection efficiency will dramatically assist with present day challenges of radiation damage when applying X-PEEM to polymers and biological materials.

§ 2.4.2 Instrumental description (PEEM2)

For a detailed description of the electron optics characteristics of PEEM2, the reader is referred to the publication by Anders et al. [APD&99], the team who designed and built the beamline and microscope.

§ 2.4.2.1 Beamline 7.3.1.1

The X-ray photoemission electron microscope (X-PEEM) on branchline 7.3.1.1 was developed by the ALS in collaboration with the IBM Almaden Research Center (Jo Stöhr). It is designed specifically for X-PEEM micro-analysis of surfaces using near-edge x-ray absorption fine-structure spectroscopy (NEXAFS), x-ray magnetic circular dichroism (XMCD) and x-ray magnetic linear dichroism (XMLD) contrast. Beamline 7.3.1 operates over the photon energy range from 175 to 1500 eV with a spectral resolving power between 1000 and 2000. A spherical-grating monochromator (SGM) with no entrance slit and a low line-density grating (200 lines/mm) is used to obtain high throughput while still achieving the desired spectral resolution.

The schematic of the beamline is given in figure 2.16. The 1.2 m long elliptical refocusing mirror reduces the horizontal source size of 300 μm (FWHM) to an image width of 30 μm (FWHM), while accepting 2 milliradians from the source in the

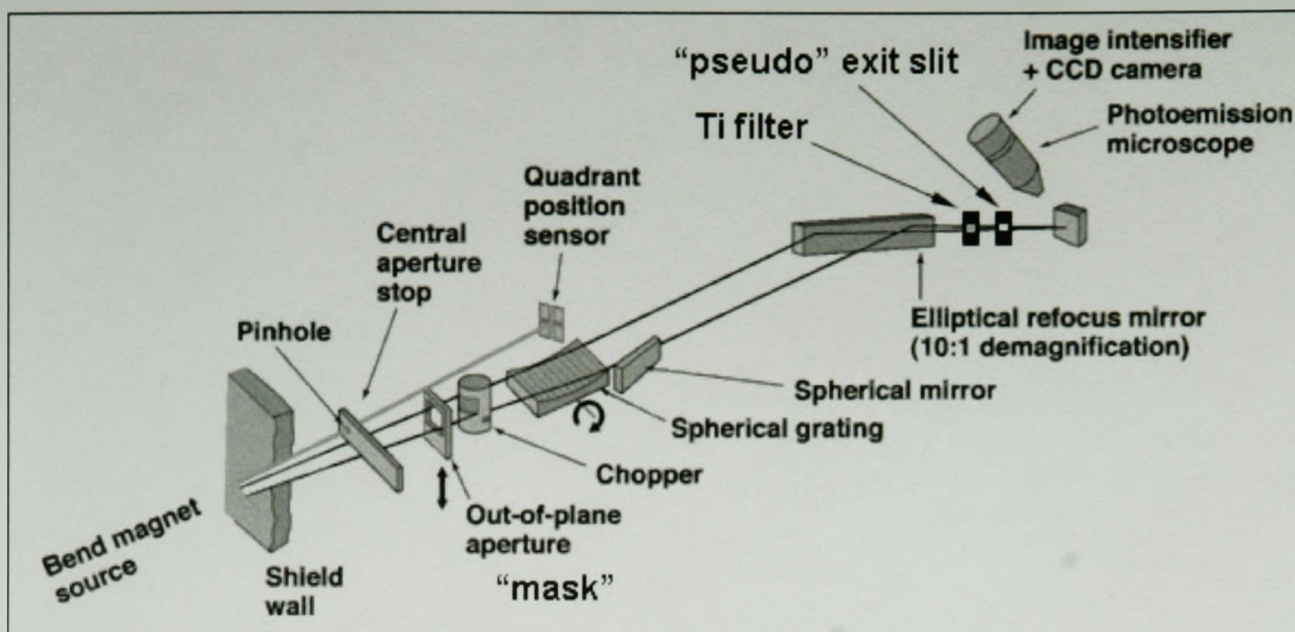


Figure 2.16 PEEM2 beamline layout

horizontal direction. Currently, there is an additional ‘exit slit’ between the elliptical refocusing mirror and the X-PEEM which reduces the beam spot to an ellipse of about $30 \times 50 \mu\text{m}$. The photon flux measured with an x-ray photodiode is 3.3×10^{11} photons/s at 725 eV when the storage ring is operated at 1.9 GeV with a ring current of 400 mA (see figure 3.12). The flux is very high because the minimum number of optical components (2) is used and there is no entrance or exit slit. The storage ring electron beam acts as the entrance slit while the X-PEEM acceptance is the pseudo exit slit. The best achievable resolving power of the beamline is $E/\Delta E = 1800$. For the reduced flux beamline conditions used for studies of X-ray sensitive polymers, $E/\Delta E \sim 500$ at the C1s edge, i.e., $\Delta E \sim 0.6$ eV.

Circularly polarized radiation (from above or below the plane of the storage ring) is obtainable by means of a movable aperture, also called the “mask”. Flux can be controlled by the position of the chopper and the mask. It is essential to use the mask and

chopper to reduce the flux when studying highly radiation sensitive materials like polymers, proteins and some ionic compounds. Mask and chopper together define polarization (linear, elliptical or circular) and flux. They act as two independently moveable knife-edges.

§ 2.4.2.2 X-PEEM Microscope

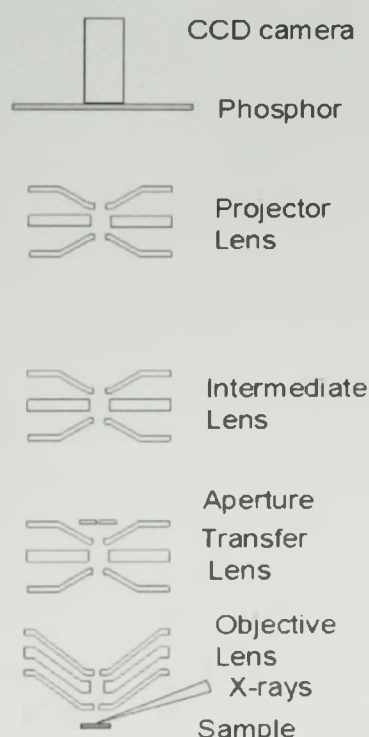


Figure 2.17 Schematics of PEEM2

Figure 2.17 is a schematic of the ALS BL 7.3.1 instrument which is called PEEM2. In X-PEEM, X-ray photons cause photoelectron emission from the surface of the sample. These photo-emitted electrons are extracted into an electron optical imaging system by a strong electric field (~ 10 kV/mm) that is applied between the sample and the objective, the first electrode of the electron optical system. This field is the first lens of the microscope. Several electron-

optical lenses are used to form a full field image of the emitted electrons at a phosphor screen which converts the electrons into visible photons which are detected by a charge coupled device (CCD) camera. The electrostatic optical system of the microscope images photoelectrons at high magnification by means of a three-element high-voltage lens: an objective lens, a transfer lens, an intermediate lens, and a projector lens. The objective

lens of PEEM2 is an electrostatic tetrode lens with a stigmator/deflector assembly located in its back focal plane. It is adjusted to achieve focus and can be operated up to 20 kV; above that, discharges are almost guaranteed.

The transfer lens produces a 1:1 image at the second objective back focal plane outside the lens where an aperture is located. This lens and associated aperture affect both the efficiency and the spatial resolution. The intermediate lens and the projector lens provide additional magnification of the image onto the CCD detector.

The projector lens and intermediate lens are used to control the magnification of the microscope. For large fields of view (from maximum of 200 μm down to 20-25 μm) only the intermediate lens is used. It is slowly increased in voltage to increase magnification, then the projector lens is turned on to magnify even more when fields of view lower than 20 μm are required. In our work, due to the low x-ray flux required to avoid radiation damage, and resultant low electron flux, the experiment remains in a regime where we exhaust our available electron flux through magnification before it is necessary to use the second lens (projector) for further magnification. Using only the intermediate lens produces better images than combined use of the objective and projector or just the projector by itself.

In contrast to most other X-PEEM instruments there is no image intensifier and thus most of my measurements used only the lower 5-10% of the capacity of the CCD. For this reason the camera corrections required for meaningful measurements are very important. Section 3.2.4 describes in finer details properties of CCD cameras.

The combination of high-voltage operation, a small angle-defining aperture (12 - 100 μm), and stable mechanical construction leads to a maximum resolution of ~ 100 nm for polymeric samples when the smallest aperture was used. Figure 2.15 shows 120 nm wide PS microdomain in a PMMA discontinuous phase.

With electron detection, the samples must be adequately conductive, reasonably flat, UHV-compatible solids. The yield of electrons over the entire illuminated area is imaged at high magnification. By recording frames sequentially with incrementally increasing photon energy ('stack acquisition'), one can produce a NEXAFS spectrum for each image point. Section 3.2 describes the various modes of data acquisition at PEEM2.

§ 2.5 Atomic Force Microscopy

§ 2.5.1 Background

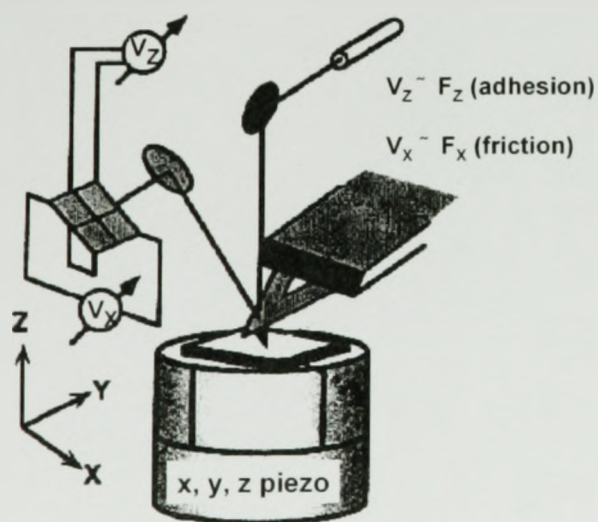


Figure 2.18 Schematic representation of an AFM

surface, a detector that measures the displacement of the cantilever, and feedback electronics to maintain a constant imaging parameter such as tip-sample separation or force [NVL87] (Figure 2.18). The sample rests on a piezoelectric x, y, z translator. A

The atomic force microscope (AFM) was invented by Binnig, Quate and Gerber [BQG86] in 1986. A typical force microscope consists of an integrated cantilever-tip assembly interacting with the sample

laser beam is reflected from the backside of the tip onto a photodiode to measure two types of tip-surface interactions. When the sample approaches, touches, and is withdrawn from the tip, the tip will move up and down in response to surface normal forces F_z , resulting in the vertical deflection signal V_z . The cantilever will also twist in response to friction forces $\pm F_x$, yielding the lateral deflection signal V_x .

§ 2.5.2 Basic AFM Modes

Frommer [F92] identified the two basic modes with which an AFM can be operated: contact mode, and non-contact mode.

§ 2.5.2.1 Contact Mode (CM-AFM)

In this mode, the tip is in constant contact with the surface. This corresponds to the repulsive part of the Lennard-Jones potential which describes the interaction of two bodies as they are brought within several angstroms contact, the model gap for the interface between the AFM probe and the sample surface. The $1/r^{12}$ distance dependence of this repulsion forms the basis for the AFM's ability to detect force gradients over small intermolecular distances. As the tip attached to the end of the cantilever is scanned across the sample surface, the change in cantilever deflection is monitored with a split photodiode detector. A feedback loop maintains a constant deflection between the cantilever and the sample by vertically moving the scanner at each (x,y) data point to maintain a setpoint deflection. This corresponds to a three dimensional measurement of the sample topography. The height is represented by an arbitrary color scale where a

bright feature is high and a dark feature is low. By maintaining a constant cantilever deflection, the force between the tip and the sample remains constant. Binnig and collaborators [BGS87] discovered that this mode can allow atomic resolution by using a very small loading force on the tip, 10^{-7} to 10^{-11} N; this makes the area of contact between tip and sample exceedingly small. Despite the small magnitude of these forces, this mode is not applicable to polymers because the forces are sufficient to plow through the polymers as the probe is scanned over the surface.

Other than topographic information, CM-AFM can also yield the magnitude of intermolecular interactions by performing adhesion and/or friction measurements. Noy, Vezenov & Lieber [NVL87] explained the nature of these measurements. The adhesive interaction between tip and substrate is determined from force-versus-sample displacement (F-D) curves (Figure 2.19).

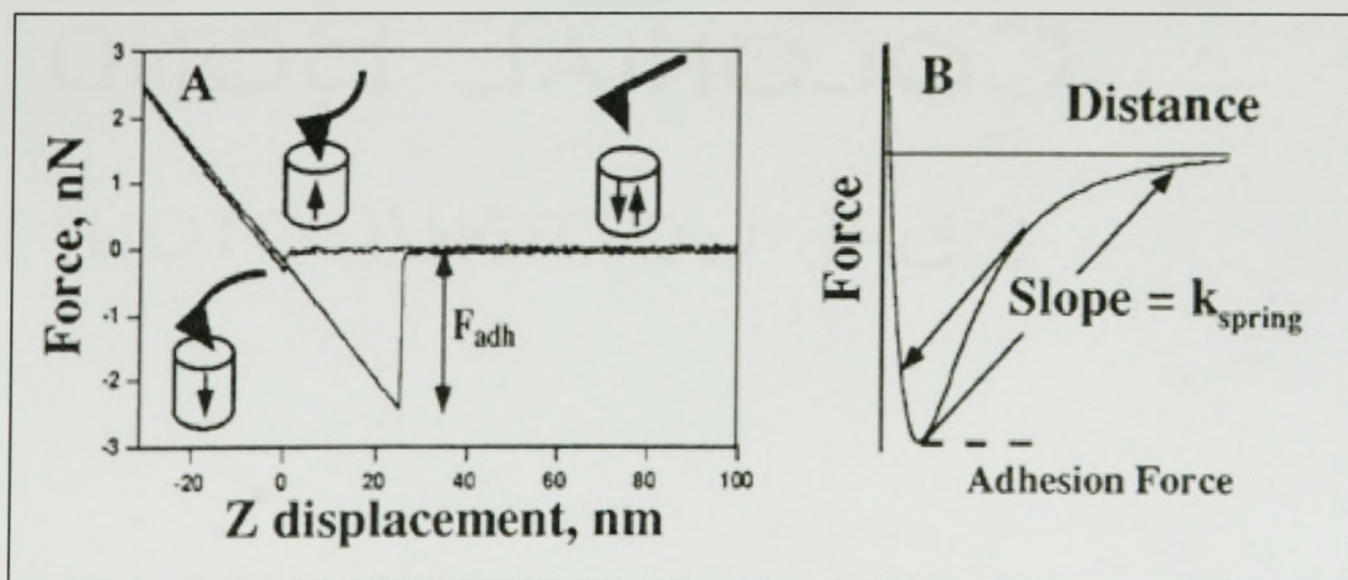


Figure 2.19 (A) Typical force-vs-sample z displacement curve. (B) The cycle in (A) is shown in terms of a schematic potential between the tip-sample functional groups (for a functionalized tip).

At large separations, no force is observed between tip and sample. At short distances, the van der Waals attraction will pull the tip abruptly into contact with the sample (jump into contact point). After that, the deflection of the soft cantilever tracks the movement of the sample (linear compliance regime). Hysteresis in the force between tip and sample is observed when the tip is withdrawn from the sample. The finite force necessary to pull the tip off the sample surface corresponds to the adhesive force between the tip and sample. Whenever the force gradient exceeds the cantilever spring constant, the system becomes mechanically unstable and cantilever jumps occurs.

The deflection of the cantilever is recorded during the sample approach-withdrawal cycle and the observed cantilever deflection is converted into a force using the cantilever spring constant. The pull-off force determined from the jump in the sample retracting trace corresponds to the adhesion between the tip and the sample surface. Clear and Nealey [CN99] described how the forces were obtained from the raw voltage data according to Eq. 2.11:

$$\text{Eq. (2.11)} \quad F_{\text{normal}} = k_n \Delta z = (k_n \Delta V) / S_n$$

where ΔV is the photodiode voltage response, k_n is the normal spring constant and S_n is the normal sensitivity (ratio of photodiode vertical response to the displacement of the piezo electric tube). To quantify the adhesive force, a large number of F-D curves (typically 100) are obtained at various contact points (typically 4-5) such that the parameters of the fit follow a Gaussian distribution with uncertainty $\pm 1\sigma$. Large number of measurements is required because the contact area, which corresponds to the number

of groups interacting with each other, may vary. Thus, the force obtained, F , is a mean pull-off force [WMR&97].

Topographical maps and imaging of friction forces between tip and sample can be acquired simultaneously with contact mode AFM. These forces are determined by the lateral deflection signal V_x (Figure 2.18) as the cantilever twists in response to friction forces $\pm F_x$. As for height images, the brighter regions correspond to greater frictional forces and darker features represent smaller frictional forces. This type of imaging is also referred to as lateral force microscopy (LFM).

Similarly to Eq. 2.11, Hooke's law can be applied to convert the raw voltage data to friction forces, according to Eq. 2.12:

$$\text{Eq. (2.12)} \quad F_{\text{lateral}} = (k_{\text{lat}}\Delta V) / S_{\text{lat}}$$

where k_{lat} is the lateral spring constant and S_{lat} is the lateral sensitivity. S_{lat} is obtained from the initial slopes of the friction loop at the stationary turnaround points for specific scan sizes. A friction loop is obtained by recording the lateral deflection of the cantilever as the sample is scanned in a forward-backward cycle along the direction perpendicular to the cantilever axis [NVL87].

§ 2.5.2.2 Non-Contact Mode

Even though the loading force on the tip is small, 10^{-7} to 10^{-11} N, surface damage is still encountered with 'soft' samples [Q94], i.e. biological samples and polymers. Consequently, the attractive mode, the attractive portion of the Lennard-Jones potential, is

preferred for these samples since there is no contact between tip and sample, i.e. this virtually eliminates lateral shear forces. In non-contact mode (NC-AFM), the cantilever is driven to vibrate near its resonance frequency by a small piezoelectric element. The amplitude of this vibration ranges from 20-100 nm and the tip makes contact with the sample for a short duration in each oscillation cycle. As the tip approaches the sample, the tip-sample interactions alter the amplitude, resonance frequency, and phase angle of the oscillating cantilever. The topographic image is obtained by varying the z position of the scanner such that a constant setpoint amplitude is maintained.

Simultaneously to topographic imaging in NC-AFM, phase imaging is also possible. Because the interaction between the tip and the surface depends not only on the topography of the sample but also on different characteristics (such as hardness, elasticity, adhesion, or friction), the movements of the cantilever to which the tip is attached depends also on these properties [MR97]. In phase imaging, the phase of the sinusoidal oscillation of the cantilever is measured relative to the driving signal applied to the cantilever to cause the oscillation.

§ 2.5.3 Instruments used

Most of the samples measured throughout the course of this PhD work were measured in non-contact mode. I have used three AFM instruments to characterize PS:PMMA samples. From June 2000 until January 2002, and from April 2003 on, a Digital Instruments (now Veeco) AFM was used, DI-Nanoscope IIIA, located in BIMR at McMaster. From February 2002 until June 2002, a contact mode Park-M5 instrument

was employed. The third instrument was a Quesant-350. The latter two AFMs are located at LBNL in Berkeley. Each of these instruments have their own particularities because of the different hardware and operating software, but the principles of operation are standard and will not be detailed here. Although I have generated nearly 1Gb of data, AFM is not the focus of my research and very few of my results will be shown here. Some of the images I acquired are shown in chapter 3 (figures 3.21n, 3.24-3.26). My use of AFM was merely as a check on the PS:PMMA sample preparations and not to develop AFM as a scientific tool.

Chapter 3

EXPERIMENTAL

This chapter describes in detail how STXM and X-PEEM measurements were performed. For X-PEEM, methods were developed to acquire data with minimal damage and maximal statistical information by exploration of the beamline and microscope parameters, and development of various corrections for the two CCD cameras that were used. The principles of data analysis for spectromicroscopy are introduced and methods applied to specific data sets are detailed. The sample preparation used for STXM and X-PEEM studies of proteins on phase segregated polymers is outlined.

§ 3.1. Data Acquisition in STXM

There are various modes of acquisition in STXM. These are: images (single energy) and spectra (point spectrum, line scan, and image sequence). Regardless of the type of data obtained, all can be converted to optical density (Eq. 2.5). This section describes the principles for each of these types of measurements.

§ 3.1.1 Single energy images

For the acquisition of single energy images, there are 4 parameters that need to be specified by the user. These are the photon energy, x , y dimensions of the image, the spacing in each dimension and the dwell time at each pixel. The image sizes depend on which sample moving motors are used: the coarse stepping motor and fine piezo stages.

Table 3.1 Maximum image size available for coarse and fine stages at STXMs 7.0.1 and 5.3.2

Beamline	Coarse scan	Fine scan
7.0.1. (old)	25 mm x 25 mm	60 μm x 60 μm
7.0.1. (new)	25 mm x 25 mm	100 μm x 100 μm
5.3.2.	12 mm x 25 mm	140 μm x 140 μm

The latter offers higher scan speed and greater stability over small distances. Table 2.1 summarizes the maximum image size available for each stage at STXMs 7.0.1 and 5.3.2.

Figure 3.1 shows an example of fine scan images on 5.3.2. The sample used as an example is a polystyrene:poly(methyl methacrylate) (PS:PMMA) film made of PS:PMMA (30:70 w/w), IMDa:310KDa, 1% polymer weight in toluene, spun cast on mica, then floated onto a Si_3N_4 window. The polymer film on Si_3N_4 was annealed for 8 hours at 160 °C. On figure 3.1 a), an image acquired at 285.15 eV, the white areas are those that transmit photons more, or absorb less, corresponding to PMMA (see spectra in figure 2.7). On figure 3.1 b), which is the figure in 3.1 a) converted to optical density, the contrast is reversed because a larger OD corresponds to stronger absorption. Figures 3.1 c) (transmission) and d) (optical density) are higher resolution images which show the presence of micro domains (~100-300 nm) in both phases. On the OD images, these appear as bright spots (PS) in the dark discontinuous domains (PMMA) and dark spots (PMMA) in the bright continuous domains (PS).

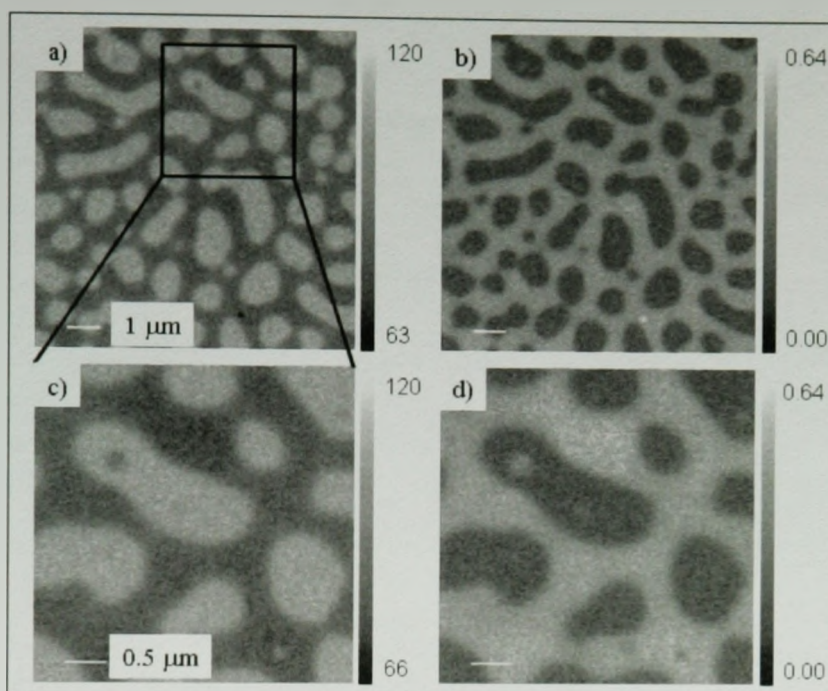


Figure 3.1 Images of PS:PMMA floated on Si_3N_4 a) $10\mu\text{m} \times 10\mu\text{m}$ at 285.1 eV, in transmission; b) Figure a) converted to optical density (OD); c) $4\mu\text{m} \times 4\mu\text{m}$ at 285.1 eV in transmission, showing the presence of micro domains in both phases; d) OD of c).

This sample is used later to describe STXM data analysis procedures, while a similar sample, where the solution was spun cast on native oxide silicon wafer (denoted SiO_x) instead of mica, is used to discuss X-PEEM data analysis.

§.3.1.2 Point spectra

Once a feature of interest is detected from a single energy image, it is possible to acquire a spectrum from a spot that is approximately the size of the focused beam. Typically, the user can specify a number of spectral regions with varying increments of energy and fixed dwell time per energy point. The old STXM 7.0.1 allowed only 1 spectrum at a time, while STXM 5.3.2 allows the spectra up to 10 points to be acquired “simultaneously”, i.e., the sample stage moves from one point to the next, acquiring the signal at each point, before the monochromator moves to the next photon energy. One of

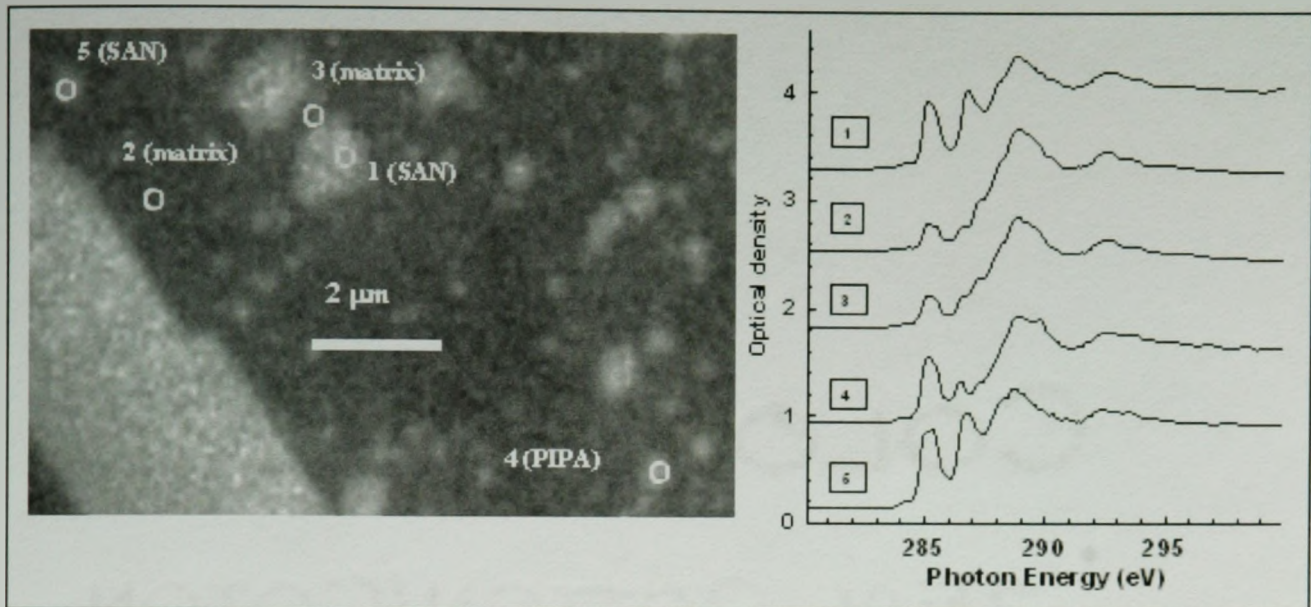


Figure 3.2 (left) location of points where the spectra were acquired, (right) spectra derived from point signals and hole signal (out of image range) recorded at same time.

the advantages of this multi-point mode is the “simultaneous” acquisition of I_0 spectra. This is advantageous because the photon flux has a strong spectral structure which must be corrected. Also, the incident flux decreases with the natural ring current decay, so simultaneous acquisition of the sample and I_0 region ensures greater accuracy. Figure 3.2 gives an example of point spectra of multiple regions recorded simultaneously on a Dow#355 sample. This material is used as a substrate for protein adsorption; results are shown in chapter 6.

§ 3.1.3 Linescan

Linescans consist in moving the sample along a line (selected by the user by drawing on a single energy image) while varying the photon energy. The user can select the length of the line, the number of pixels along the line, and similarly to the point spectrum mode, the user can select the energy ranges of interest with specified dwell

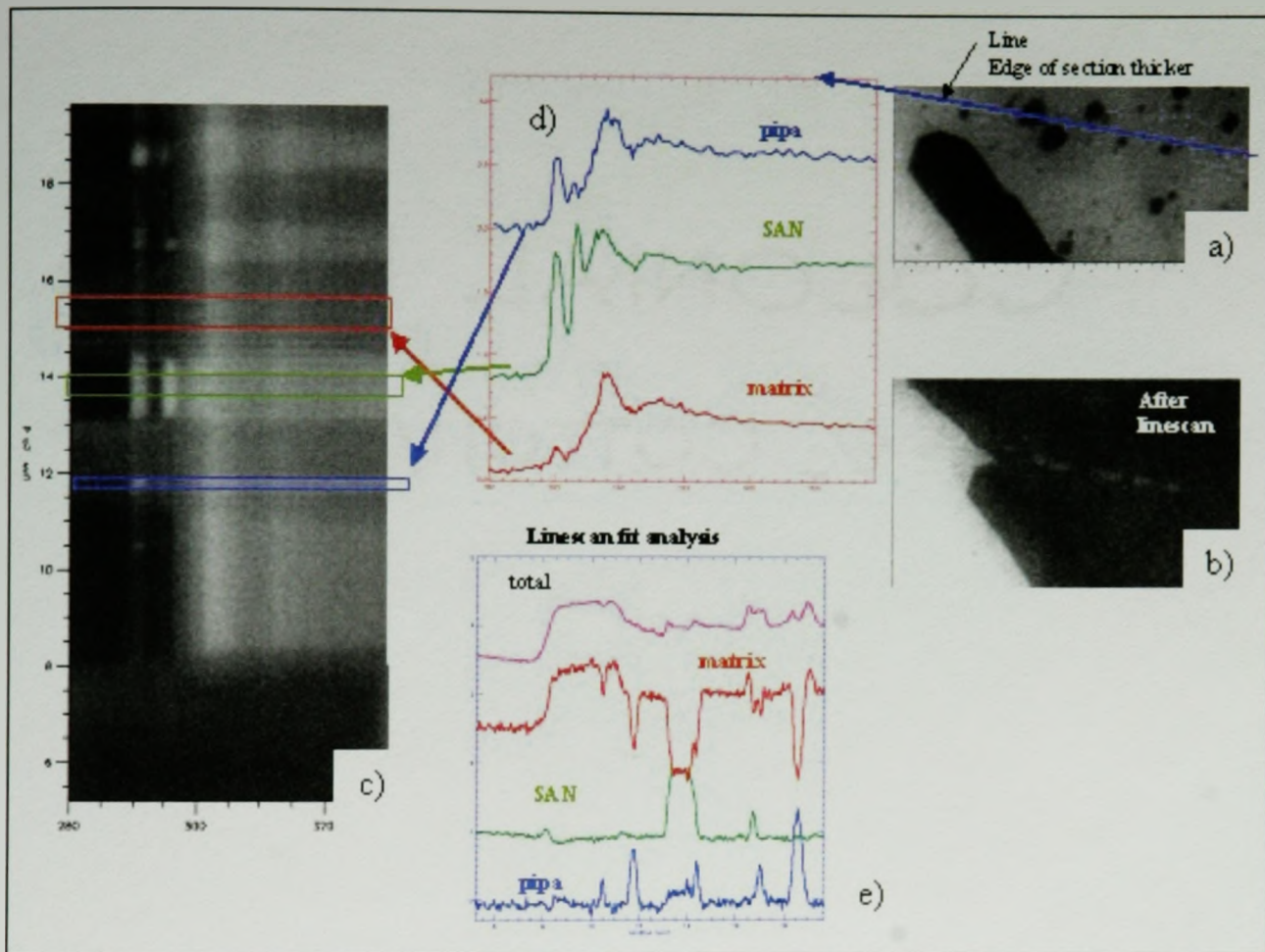


Figure 3.3 Example of a linescan and subsequent analysis (see text for detail).

times at every pixel along the line. The result of a linescan is a “line-spectral image” where the vertical axis is the distance along the line in μm , and the horizontal axis is the scanned energy range. The physical width of the line is usually determined by the spot size and the radiation damage spread. Figure 3.3 shows the steps involved in a linescan acquisition and its analysis. Figure 3.3 a) is an image of the region where the linescan was acquired, shown by the blue arrow; b) is the image after the linescan, showing the effect of radiation damage which is much greater in the aliphatic polyether matrix than in the aromatic filler particle; c) is the “line-spectral image” which contains coloured boxes that correspond to different sections of the line; d) is the spectra for sections shown in c); e) is

the curve fit analysis of the linescan. The latter method is used to visualize and quantify chemical composition along a line.

§ 3.1.4 Image sequences (stacks)

An image sequence, usually referred to as “stack” [JWF&00], consists of acquiring a set of images of one or more regions over a user-defined set of energies. As for single energy images, the user can select the size of the image, the number of pixels and the dwell time at each pixel (per energy point). In addition, the user can specify a number of spectral regions with varying increments of energy. As is the case for single point spectra, STXM 5.3.2 allows acquisition of up to 10 spatial and 10 energy regions “simultaneously”.

Figure 3.4 shows selected images from a stack made up of 67 energies between 280-306 eV of dimensions, $x \times y$, $8 \mu\text{m} \times 8 \mu\text{m}$. The sample is the same as the one shown

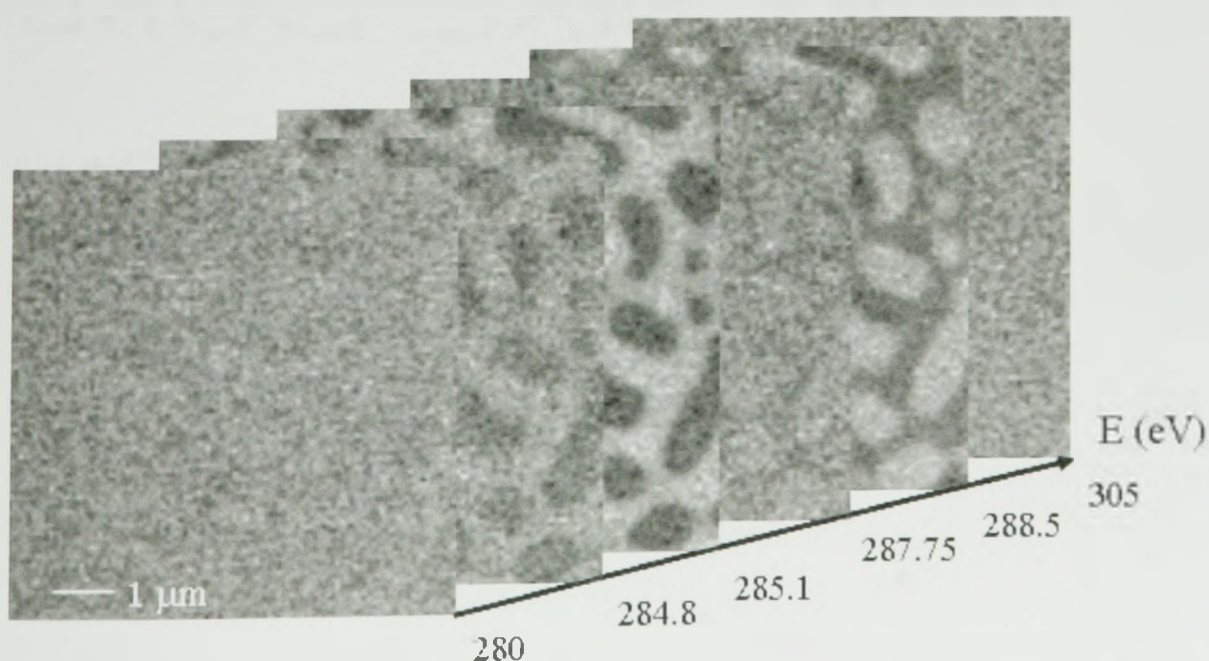


Figure 3.4 Representation of a “stack”, or image sequence. Same sample as figure 3.1

on figure 3.1. The image contrast changes throughout the absorption edge as the PS and PMMA components absorb at different energies. Section 3.3 will detail how to extract quantitative information from such a sequence of images.

§ 3.2 Data Acquisition in X-PEEM

There are three modes of data acquisition in X-PEEM: single energy images, spectra and stacks. The latter two modes record a sequence of images over a range of photon energies, with simultaneous processing and discarding of the images in the case of spectra, and saving all images in the case of stacks. Since X-PEEM is a parallel detection instrument, all modes of acquisition are similar with the main differences being in terms of what data are saved, and whether a single energy or a whole spectrum is scanned.

§ 3.2.1 Images

Typically, single energy images are acquired at energies that correspond to strong transitions of a particular material within the sample to highlight the spatial distribution of that material. In order to obtain adequate statistics (high signal-to-noise ratio) these images are usually acquired with a longer dwell time (10-60 seconds) than is typically used for a “stack of images” (2-5 seconds/image). The acquired images are corrected for camera artifacts either automatically as part of the acquisition, or post acquisition. Since there is no raster scanning of the sample in X-PEEM, the size of the image is determined by drawing a box, or area-of-interest (AOI), onto a larger field-of-view image, by carefully positioning that box where the maximum illumination occurs. The physical size

of the image depends on the magnification given by the objective and intermediate voltages when the sample is in focus.

There are two ways to identify the size of an image. One is to physically measure the field of view (FOV) using a micrometer to measure the displacement as one feature of the sample is moved from one end of the screen to the other. This gives the size of the FOV, and knowing the number of pixels on a line, one can derive the pixel size.

An approximate FOV can also be obtained from figure 3.5, using the voltages of the microscope. The y -axis of the graph is the field of view in microns for the whole face of the CCD. Provided that no binning of the image was selected and that the full 1k x 1k CCD was read, 1000 pixels of an image equal the corresponding number of microns. If less than the full 1k x 1k chip was read, then the FOV is divided by a corresponding fraction.

The bottom x -axis represents the voltage of the magnification (intermediate) lens as a fraction of the sample voltage. That is, if the sample was at 15 kV, and the intermediate lens was at 12 kV, then $12 \text{ kV}/15 \text{ kV} = 0.75$ would be the x -coordinate of the graph, for a field of view of about 80 microns, or 80 nm per pixel.

The two plots on the graph represent the high and low magnification operational modes of the microscope. The higher curve is used if the transfer lens is turned off, and the x -axis represents the value of the intermediate lens as a fraction of the sample voltage. The lower curve is used when the intermediate is set at a fixed value (0.833 of the sample voltage) and the transfer lens is used to magnify more. In this case the x -axis then represents the value of the transfer voltage as a function of the sample voltage. The lower

graph is simply a magnification of the lower portion of the upper graph, that is, it is simply a re-scaling of the y-axis to better see the details down at the small FOV's.

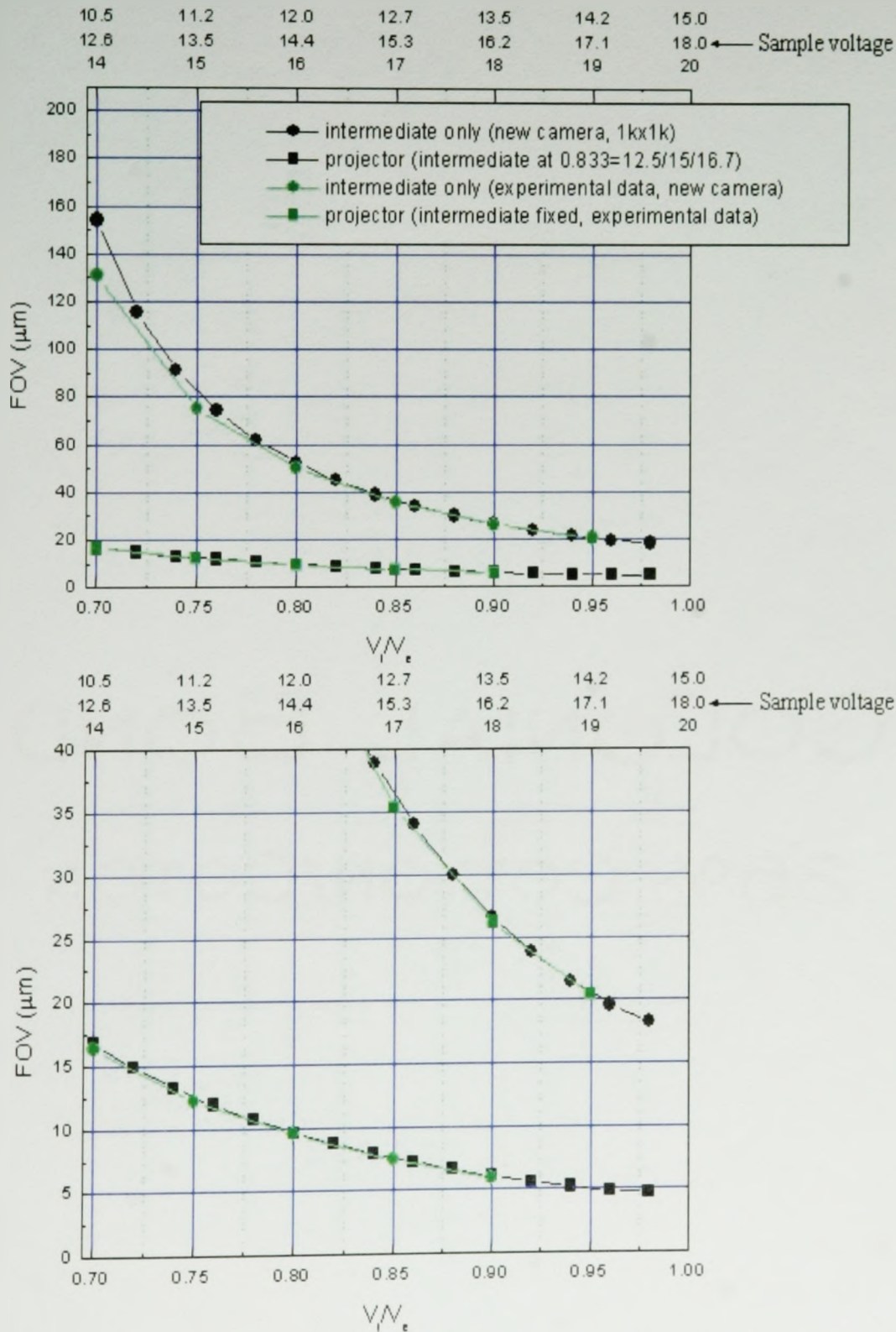


Figure 3.5 PEEM2 FOV as a function of voltages.

§ 3.2.2 Spectra

X-PEEM spectra correspond to the relative intensity of detected photoemitted electrons in a user defined area of the sample as a function of incident photon energy. For spectra, images do not get saved so disk space is saved; a 50 energy stack can vary between 50-150 mega bytes (Mb) while the corresponding spectrum is only ~ 4 kilo bytes.

§ 3.2.3 Stacks

Stacks (image sequences) are acquired over a selected area of the sample and consist in the acquisition of a set of images over a user specified set of energies. All images of the stack are acquired with the same dwell time (~2-5 seconds/image), and all come from the same physical area of the sample (AOI) so they have the same spatial resolution and field of view (FOV). The actual acquisition time, which is also the amount of time that the sample is exposed to x-rays, can be up to 2 seconds longer per image than the dwell time. There are two sources for this additional time. One is the read-out time of the camera which scales approximately linearly with the size of the region of interest (ROI) downloaded from the camera. For example, reading 1k x 1k (10^6) pixels of the camera takes about 1s whereas reading 1/4k x 1/4k (6.2×10^4) pixels takes about 0.3 s. In addition the time of the monochromator motion (0.5- 2s) adds to the deadtime. In total the deadtime is about 1-2s depending on the camera ROI and on the version of the beamline software. However, the area of interest (AOI) (i.e.: physical region of the sample) does not influence the readout-time but reduces the file size.

The spectral energies sampled are defined by the user. Typically, for radiation sensitive polymer samples only the finest spectral features of interest are recorded with small energy steps (0.2 eV is the minimum because of the limited energy resolution of the beamline), with coarser steps (0.5 or 1.0 eV) used to provide signal away from the sharp spectral features. The latter energy regions are needed to define continuum intensities to assist quantitation.

Although these modes of acquisition were already implemented when this thesis work was started, due to issues such as camera noise, proper normalization of signal for organics and polymers, effects of second order radiation on the shape of C1s NEXAFS spectra and the high sensitivity to radiation damage of polymers, many challenges were overcome to optimize adequate data acquisition methods for radiation sensitive polymers. These issues will be detailed throughout sections 3.2.4 to 3.2.6.

§ 3.2.4. Camera Issues

The electrons that are photoemitted from the surface of the sample and which make their way through the electrostatic lenses of the X-PEEM column are collected onto a phosphor screen that converts electrons into visible light, which is detected by a charge-couple-device (CCD) camera. A CDD camera uses a silicon integrated circuit rather than a piece of film to receive incoming light. The CCD chip is segmented into an array of individual light-sensitive cells called “photosites”. Each photosite is one element or “pixel” of the whole picture that is formed. For the two cameras that have been used on PEEM2 only the centre 1024 pixels wide by 1024 pixels high were used. The CCD

photosites accomplish their task of sensing incoming light through the photoelectric effect, which is a characterization of the action of certain materials to release an electron when hit with a photon of light. The electrons emitted within the CCD are trapped within nonconductive boundaries. As long as light impinges on a photosite, electrons accumulate in that pixel. Under external command electronic circuitry transfers the charges in the CCD array, through an analog-to-digital conversion to a set of digital numbers which are transferred to a computer and displayed on a computer screen.

CCD cameras suffer from a number of artifacts, on an individual pixel basis, including background (or dark) signal and variable gain (or flatfield). These artifacts stem from: 1) since they are electronic components, CCDs are sensitive to heat within the camera as well as light from the object of interest, and 2) the individual photosites in the CCD array may vary significantly in their sensitivity to both heat and light. First, this means that the electrons generated by heat rather than by light need to be subtracted from the final tally of electrons in each pixel so that a truer image can be rendered. This is called "dark subtraction". Second, the variance in electron depth across the CCD array due to inherent differences among the pixels needs to be leveled by dividing by a patterned image "white" or "flat field", reflecting gain variation from pixel to pixel. This is called "flat fielding".

The two cameras used at PEEM2 throughout the course of this research have different amounts of background and flatfield noise. The last camera used (from Roper Scientific), which was installed in May 2002, will be referred to here as the "new" camera. It performed much better than the "old" one (Coolview 12 from Photonic

Science) and required less corrections. With new software (written by Dr. A. Scholl), the dark and flat field corrections are automatically performed during data acquisition if the user desires.

The old camera was more problematic and new data acquisition and analysis methods had to be developed. Some of the issues encountered with the old camera are described here:

1) Background ("dark")

Due to a negative offset on the analog side of the analog-to-digital (A/D) converter, the background in many pixels read 0 if there is a light tight enclosure. In order to have an average zero signal when no light hits the camera, the camera electronics displays negative pixels so that about 50% of the pixels are at negative output. Any negative signal is registered as "0" by the unipolar A/D conversion. This is an artifact which had serious consequences for low intensity signals which were often the regime used in low X-ray exposure to radiation sensitive polymer samples. A flashlight bulb was

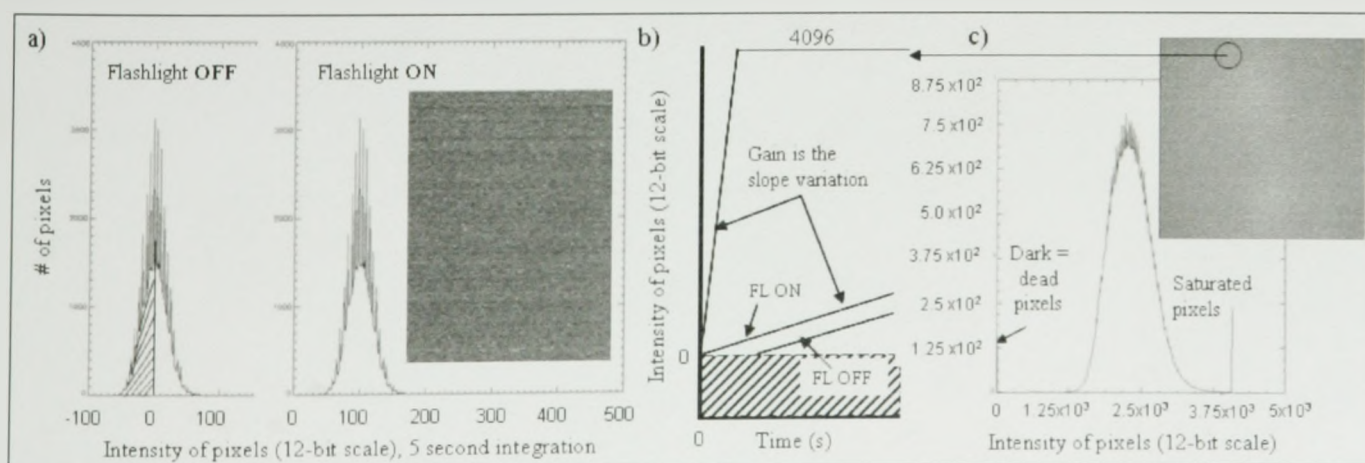


Figure 3.6 a) Histograms of dark noise for the flashlight (FL) OFF and ON, showing the shift in pixel intensity with FL ON, and an example of a dark image from the old PEEM2 camera; b) Intensity of pixels for dark and gain as a function of time; c) histogram of a gain image, the circle shows a saturated pixel with intensity 4096, 2^{12} .

used to ensure that all pixels had some non-zero value. Thus, for low signal intensity measurements, the flashlight was used to add a small signal (~20/sec) to raise the dark signal in all pixels to a (small) positive value (see figure 3.6 a).

The background with the flashlight on had to be recorded and subtracted from the X-ray illuminated images. This corrected for both the additional flashlight signal and the intrinsic background from leakage. This dark signal subtraction also provided a large portion of the gain correction since the hot pixels were also present in this image. The flashlight intensity level had to be set so there was the minimum light needed to get all positive pixels in the image for the desired dwell time.

2) Gain (“noise” or “flat fielding”)

Every pixel has its own gain. Some pixels are ‘bad’ – they go to saturation immediately. The dark-corrected image must be divided by the ‘gain’ image in order to remove this artifact. Gain correction requires division by an image with the pattern reflecting pixel-to-pixel variation in gain. The gain of each pixel changes slightly depending on the amount of stored charge (the signal intensity) and thus the gain correction image needed to be selected to have a similar degree of filling of the important pixels, rather than the same integration time.

The gain-correction image was *noise.xxx.tif*, where *xxx* was the time closest to the time which gives the same average filling (2048) of the camera pixels. For example, if an image had an average signal of 500 for a dwell of 5 sec, then one would use *noise025.tif* (25 seconds exposure to white light) so that the gain profile is appropriate for the extent to which the camera pixels are filled.

The data acquisition method depended on whether one wished to perform camera corrections (dark and gain) “post acquisition” or “on-the-fly”. The advantage of doing post acquisition is that the raw data were preserved and could be tweaked at will to correct for background levels.

§ 3.2.5 I_0 Corrections

A flat conductive substrate, such as Si for polymer spun cast films, or metal, such as Au on Si for self-assembled monolayers, is required both to avoid charging of insulating polymer or organic films and to physically support the thin film. Figure 3.7 schematically shows that the electrons that contribute to the signal do not come from the sample alone. This is due to the substrate’s larger photoabsorption cross-section (σ), e^- escape probability (f_{esc}) and lower work function (Φ).

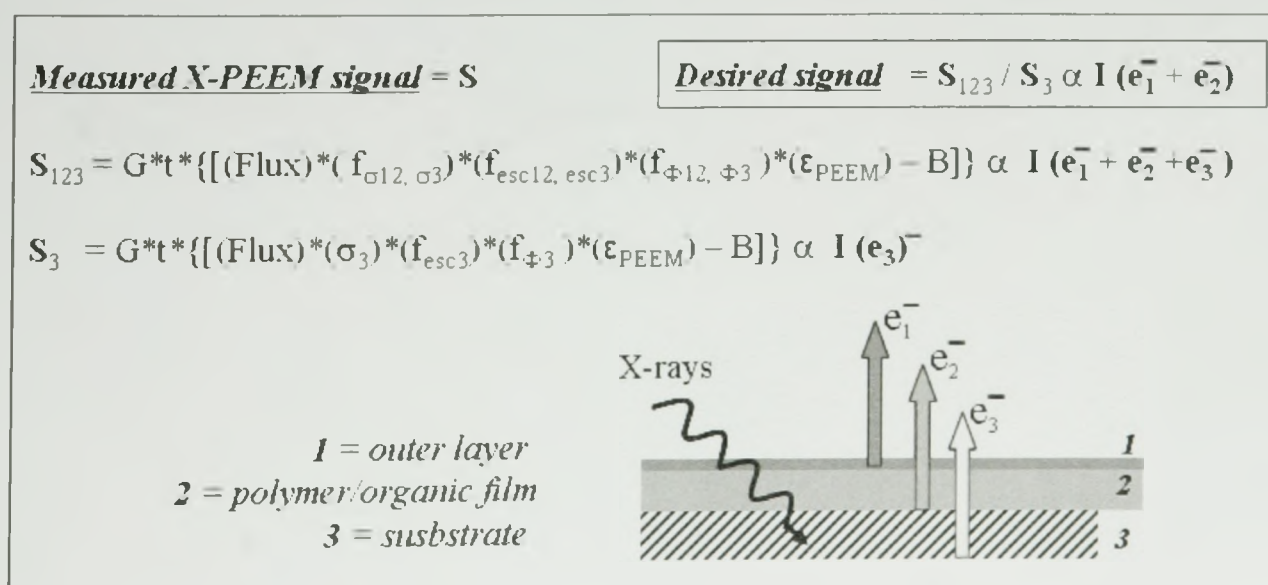


Figure 3.7 The measured X-PEEM signal consists of several variables which are described in equations 2.6-2.8. Consequently, it is a function of the sum of the electrons that are emitted from the outer layer of the surface of the material, the polymer or organic film and the substrate on which the film is adsorbed. The desired signal is that from only the electrons emitted from the sample.

Figure 3.8 gives two examples of samples where the substrates contribute, to different extents because of their respective thicknesses, to the sample's signal. The first example, figure 3.8 a) and b), shows that for this 40 nm thick PS:PMMA film (details of the preparation are highlighted in table 1 of chapter 4), the signal from the stack prior to normalization (thin curve) with the internal I_0 shows a strong C1s signal; the spectral shape is corrected by dividing by the Si spectrum (medium thickness curve). The second

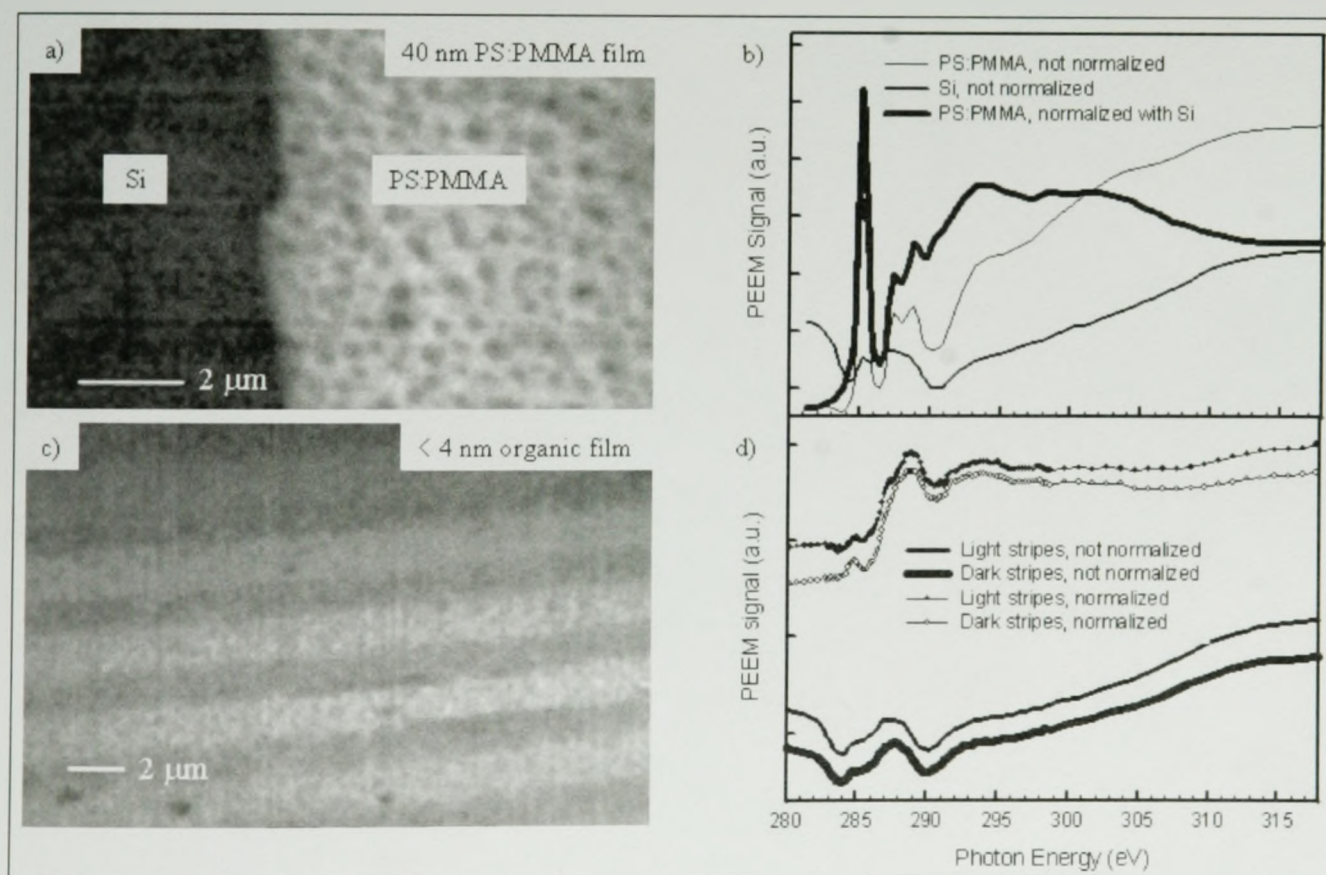


Figure 3.8 Comparison of strong signal (40 nm PS:PMMA) versus weak signal (patterned SAM). a) 285 eV image of a 66:33 PS:PMMA film (40 nm); b) spectra of internal Si- I_0 and PS:PMMA region, from stack not normalized, and from stack normalized with internal I_0 ; c) 280 eV image of a patterned film (< 4 nm) made of streptavidin (SA) stamped into 2 μm x 2 μm lines, backfilled with thiolated polyethylene glycol (PEG-SH), exposed to a biotinylated-ferritin (BFe) solution; d) Rescaled spectra of light and dark stripes: lower curves, before normalization with an external I_0 , upper curves, after normalization

example shows a very thin patterned organic film of streptavidin (SA) stamped into $2\ \mu\text{m}$ x $2\ \mu\text{m}$ lines, backfilled with thiolated polyethylene glycol (PEG-(CH₂)₁₁-SH), exposed to a biotinylated-ferritin (BFe) solution. The spectra in the lower part of figure 3.8 d) are from the light and dark stripes, prior to normalization of the stack with an external I_0 . In this case, the signals are “ I_0 -like”. Division by an I_0 is necessary for the “true” SAM signal to appear (upper curves).

Although the purpose of figure 3.8 is not to show a detailed analysis of these samples, but rather the difference in signal strength for two regimes of sample thicknesses, it is worth mentioning that for the patterned SAM sample, these data and others at different absorption edges, corroborated to show that the back-filling procedure covered the whole surface with PEG-SH. The weak C 1s signal looks like the sample is mostly saturated hydrocarbons (PEG-SH). The strong Fe 2p signal showed mostly globs of BFe with some hint of shadowing preferentially on one side of the thin lanes. The N1s signal was negligible indicating that very little SA adsorbed or perhaps was washed off by the PEG-SH back-filling preparation. These types of samples were abandoned in mid-year 2001 because most showed faulty preparations and much needed to be learnt about proper X-PEEM data acquisition.

The assumption in choosing an appropriate I_0 is that if the substrate is the same for I_0 and I , and if the overlayer (1 and 2 on figure 3.7) is thin, then it may be that the substrate's shape approximately cancels, which is shown in figure 3.8 b) and d). Equations 2.6 to 2.8 described the parameters involved in the X-PEEM signal. When acquiring an adequate I_0 spectrum, most of the variables in these equations should be the

same as for the conditions used for acquisition of the sample of interest such that the contributions from the underlying substrate can be eliminated without altering the true sample signal as a function of incident energy.

The consequences of using different parameters are detailed below for some of these parameters:

A) Camera gain and exposure time: As suggest the equations shown on figure 3.7, the camera and exposure time are proportionate to the intensity of detected photoemitted electrons. An example of the effect of differing exposure times is shown in figure 3.9 where two C1s NEXAFS spectra of freshly HF-etched Si were acquired under the exact same conditions other than for the dwell time.

In order to eliminate the photoelectron contribution of layer 3 (the substrate, in figure 3.7) for a sample that was acquired with exposure time, t , the same exposure time should be used for the clean, polymer-free, substrate. If a different exposure time were used for the substrate spectrum, it could be rescaled before using it to correct the sample's signal, but for the sake of simplicity, the same dwell times were usually used for the sample and the substrate.

B) X-PEEM column efficiency, ϵ_{PEEM} : This parameter is proportional to the magnification of the microscope (controlled by the interplay of the voltages of the electrostatic lens and the sample-objective lens distance) and to the square of the size of the aperture (located between the transfer and intermediate lenses, see figure 2.17). There are four sizes of apertures available: 12 μm , 20 μm , 50 μm and 2 mm. The smallest one gives the best

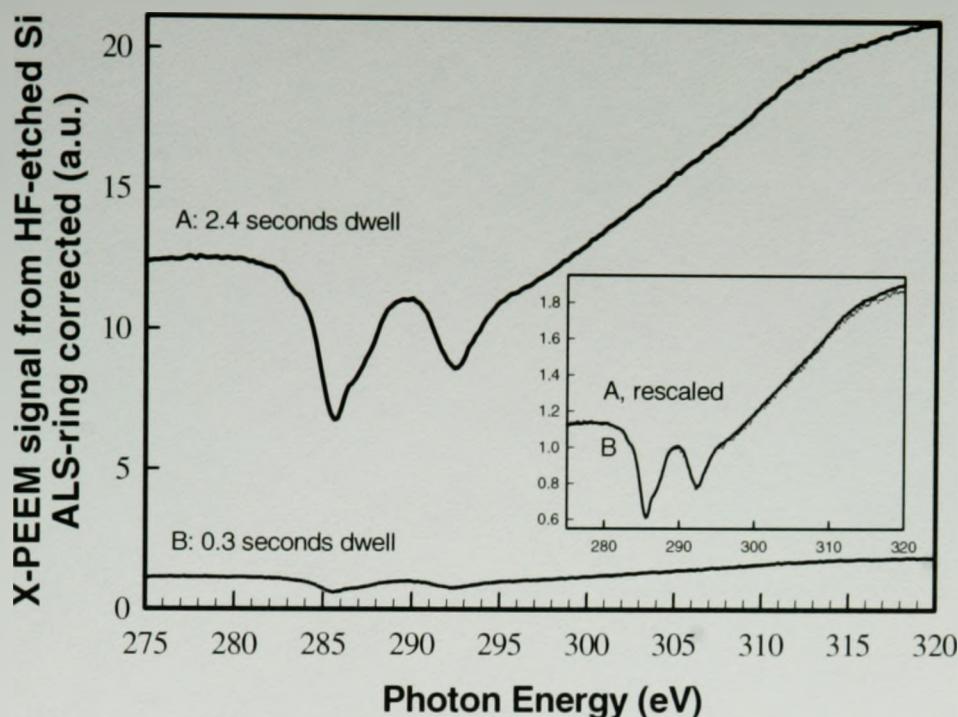


Figure 3.9 HF-etched Si C1s NEXAFS spectra acquired in sequence under similar beamline and microscope conditions, except for the dwell time. A: 2.4 seconds, B: 0.3 seconds. The rescaled spectra in the inset show that their shapes are similar.

spatial resolution, but also rejects a larger portion of the electrons going through the column, thereby resulting in a weaker signal for a same photon flux.

The sample position affects the magnification. The same voltages are only reproducible if the sample-objective lens distance is such that the sample is in focus at the same objective lens voltage and the magnification depends on the combination of the voltages of the objective lens and the intermediate lens. Also, the sample must be tilted such that the plane of the substrate be normal to the column and the x , y positions be centred under the centre of the objective lens such that the maximum number of electrons can go through the column (see figure 3.10 a) for an illustration of the case of ideal sample alignment).

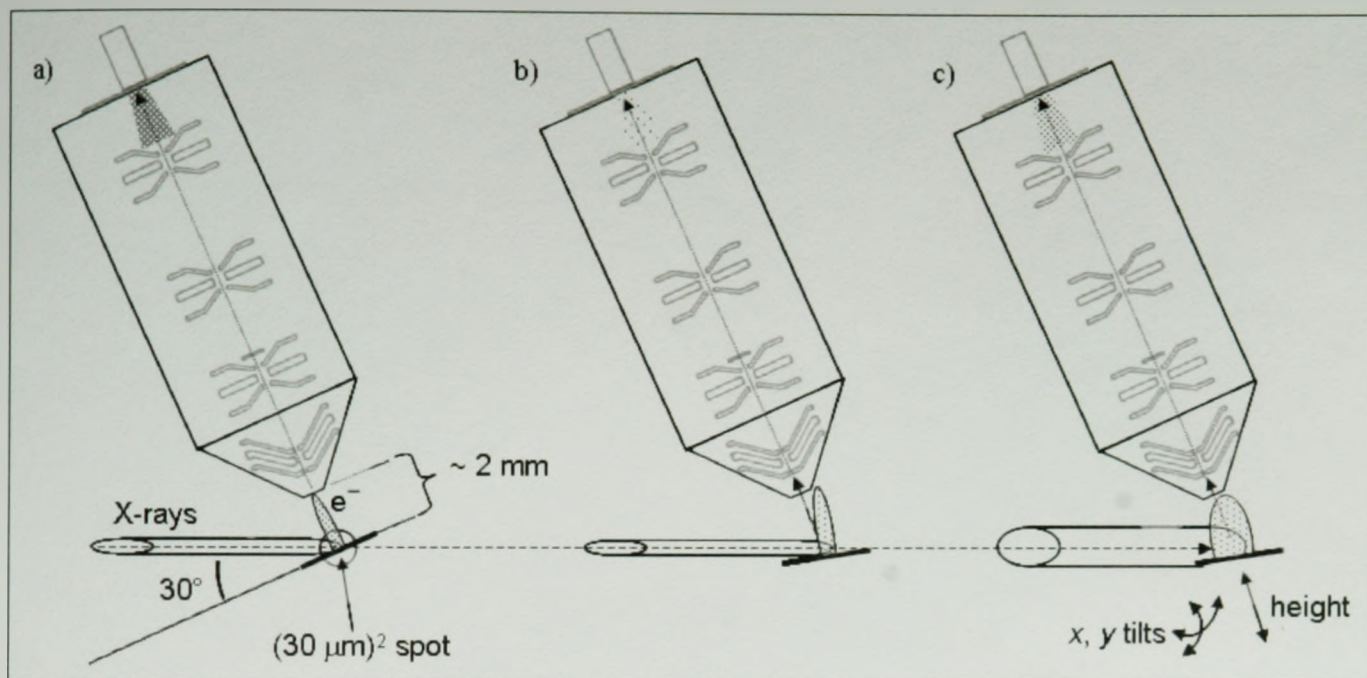


Figure 3.10 Schematic representations of sample alignment and its effect on illumination on the CCD. a) ideal case: the sample is perfectly aligned, large number of photoemitted electrons are detected on the CCD; b) the sample is misaligned, very few photoelectrons reach the camera; c) the sample is misaligned, but the larger X-ray spot size, from the opened exit slit, allows to see more electrons at the detector and the sample position may be better optimized by adjusting the sample tilt and height.

As a result of these effects, the X-PEEM column efficiency affects the choice of an I_0 in the following ways:

i) One of the ways of getting an I_0 signal with the exact same experimental conditions as the sample's data is to make a scratch through the polymer film using a clean piece of wire. This way, the sample and the Si can be in the same FOV during the acquisition of a stack (figure 3.8 a). The only inconvenience with this method of recording an I_0 is that sometimes the scratch contains residues of the polymer film (see figure 3.11) which can later distort the true sample's signal.

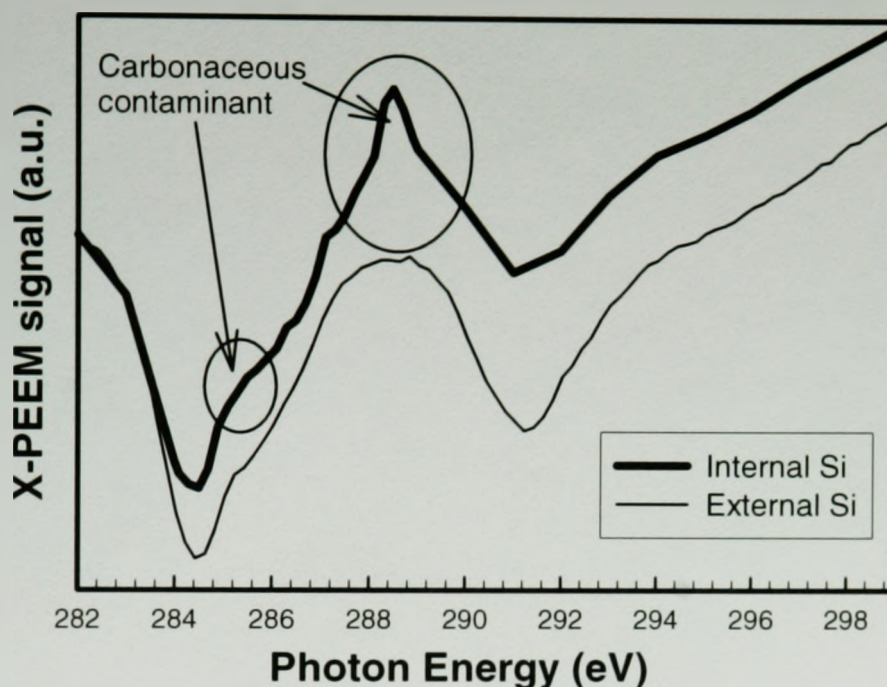


Figure 3.11 Example of C1s NEXAFS spectra of an internal I_0 signal through a scratched polymer film and an external (HF-etched Si) I_0 spectrum. These were acquired at different times under different beamline and microscope settings, so their shapes are expected to be different. The sharp feature between 288-289.5 eV, and the shoulder between 284.9-285.8 eV in the internal spectrum are from a carbonaceous contaminant which is likely from remaining polymer film. These spectra were arbitrarily energy calibrated so that their dips would coincide, and their intensities were rescaled.

ii) Using an HF-etched piece of Si for an external I_0 avoids the problem of contamination, but it is very difficult to position two different samples with the exact same coordinates in space. Sometimes, the sample and the HF-etched Si were put side-by-side on the same sample puck. This made the problem of realigning the sample (HF-etched Si) easier than if another sample puck had to be put in because the sample height and tilt were relatively unchanged for two different samples on a same puck. However, the edges where the two pieces of Si meet sometimes lead to charging and unstable currents in the microscopes; the resulting spectra are then very noisy.

Also, the energy calibration depends on the position of the exit slit (located between the elliptical refocusing mirror and the sample on figure 2.16) with respect to the height of the sample. The slit reduces the size of the beam from $\sim 300 \mu\text{m}$ high $\times 30 \mu\text{m}$ wide to a nearly circular spot of $\sim 30 \mu\text{m} \times 30 \mu\text{m}$. So, when using two different pucks with the exit slit in, it can be very difficult to realign the sample (i.e. find the sample's x,y,z coordinates that give maximum illumination, see figure 3.10), so opening the exit slit to broaden the beamspot on the sample becomes necessary, thus changing the energy calibration when the exit slit is closed again.

C) Flux: This parameter is not only determinant for the choice of parameters for an adequate I_0 , it also plays a distinctive role in the minimization of damage incurred to polymers by their exposure to X-rays. Indeed, one of the struggles of learning how to use X-PEEM was to develop ways to acquire data below a certain radiation damage threshold while maximizing the signal statistics for optimal imaging. Section 3.2.6 briefly describes the methods that were used to measure samples in X-PEEM with minimal radiation damage. One of the important parameters in evaluating the dose absorbed by a material is the incident photon flux (photons/second). There are four main factors that affect the flux that impinges on the samples: the current in the storage ring, the opening of the chopper and mask (see beamline diagram, figure 2.16), the presence or absence of a titanium foil in the beam path and finally, the variation of intensity with incident photon energy. The effects of the latter three factors, which also affected the way I_0 parameters were chosen, are depicted in figure 3.12.

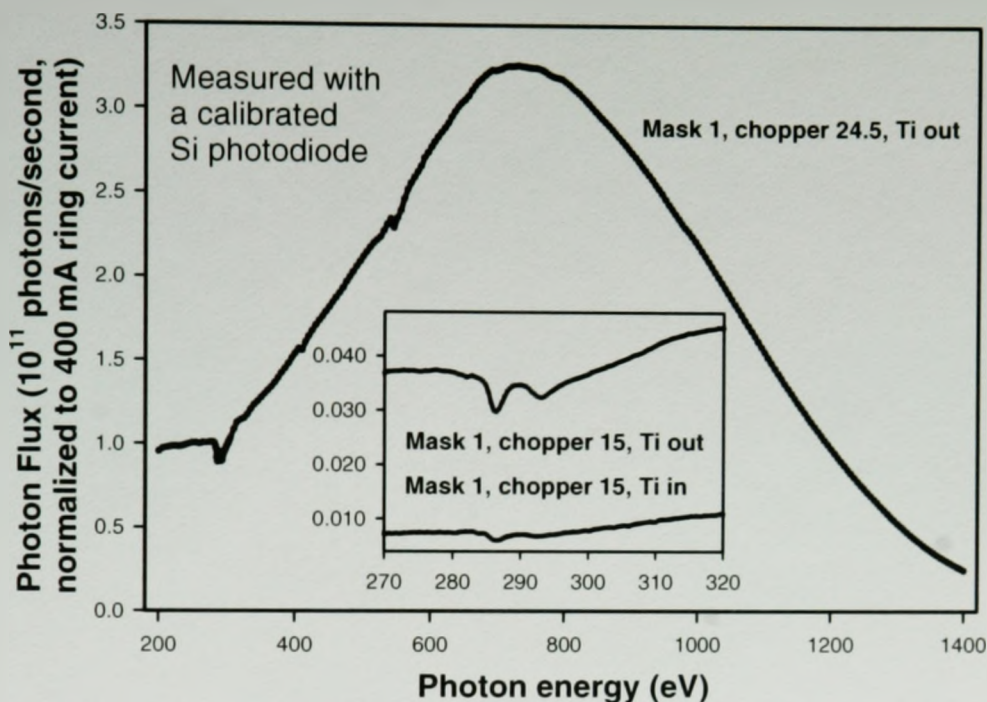


Figure 3.12 Photon flux (in photons/second normalized at 400 mA ALS ring current from 7.3.1.1 monochromator measured by an X-ray photodiode. The insert shows the effect of a Ti filter on the relative shape and flux at the C1s edge

The spectra shown on figure 3.12 were acquired by Andrew Doran, assistant beamline scientist at PEEM2, using an X-ray photodiode to obtain the absolute flux. The number of photons that hit the measured portion of a sample in the X-PEEM is about 10% that of the full flux that reaches the Si photodiode.

Over the course of one spectrum, or stack, at a single absorption edge, the ring current has a negligible effect on the photon flux since the current only decays by about ~3 mA within 100-200 seconds of acquisition and it decays from 400 mA to ~200 mA over the course of an 8 hour fill. However, every data point of the curves shown on figure 3.12 was normalized to correspond to a 400 mA ring current because there was significant ring decay over the course of these spectral acquisitions.

This figure shows the large change in flux that is incurred by closing the chopper from the nearly maximum value of 24.5 (main curve from 200-1400 eV) to the nearly minimal value of 15 (top curve in the inset). As the numerical difference between the mask and chopper values gets smaller, they get closer together and the size of the illumination on the grating is reduced. This does not only decrease the flux (at the C1s edge, the flux is ~25 times smaller for the “completely closed” conditions -mask 1, chopper 15- versus “completely open” -mask 1, chopper 24.5-), it also changes the energy resolution due to the limited number of grating grooves being illuminated. Thus, in order to avoid different flux and energy resolutions, the sample, I, and I_0 signals must be acquired with the same mask and chopper values.

The effect of the Ti filter is seen by comparing the two inset curves, which were

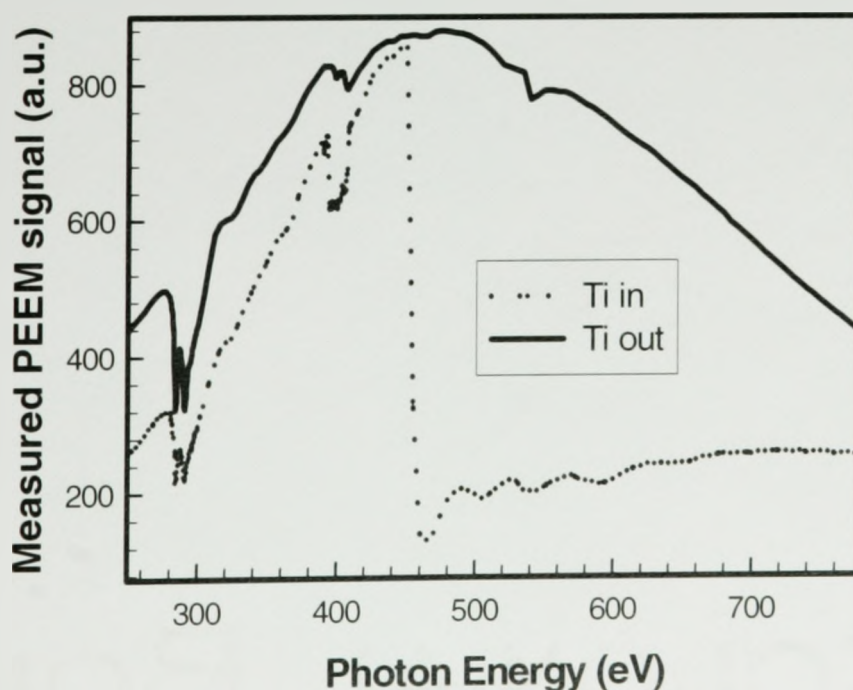


Figure 3.13 I_0 spectra measured off an HF-etched piece of Si, with and without Ti.

both acquired with mask 1 and chopper 15 at the Cls edge (270-320 eV). For the curve with the Ti out, the flux is about 5 times larger than for Ti-in; the resulting I_0 curves also have slightly different shapes. The difference in shape is caused by the reduction of second order light from oxygen, which occurs at ~ 270 eV, with the presence of Ti which absorbs at 450 eV (Ti 2s), below the O1s edge (see figure 3.13).

The curves on figure 3.12 were generated after all the data for my thesis were acquired. Even though I did not measure a specific photon count, I made numerous measurements to gauge the effect of how different mask and chopper settings affected the relative flux on the sample. Also, early on, it was observed that the spectral shape was changing with chopper value when the mask was kept at a constant position. The approach used to test the extent of radiation damage of different materials was to keep the mask and chopper constant, but vary only the dwell time, see section 3.2.6.

Figure 3.14 shows the relative intensity of light hitting a sample in the X-PEEM

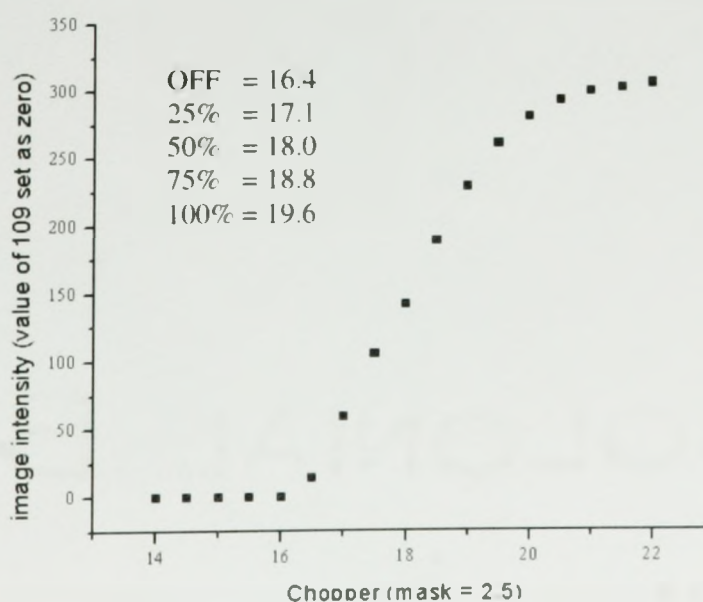


Figure 3.14 Curve of the relative intensity of light hitting a sample in PEEM2 as a function of the chopper value for a fixed mask value of 2.5 with Ti-in.

as a function of the chopper value, with a constant mask value of 2.5. A chopper value of 17 was chosen to perform all the measurements described in chapter 5. At this setting the flux was equivalent to approximately 25% of “full flux”.

§ 3.2.6 Evaluation of Radiation Damage

Samples of the pure materials, PS, PMMA and Fg, were used to derive a maximum time for which these materials could be exposed to X-rays under specific beamline conditions.

The samples were prepared in the following manner. PMMA (MW = 312 K, $\delta = 1.01$) and PS (MW = 1.07 M, $\delta = 1.06$) were dissolved in a 1 weight-% toluene solution. A 50 μl drop was spun cast (4000 rpm, 30 s) onto clean, 1 cm^2 , native oxide Si wafers which had previously been degreased with trichloroethylene, acetone and methanol, then rinsed under running milli-Q water. The PMMA and PS thin films on Si were annealed at 140°C for 4 hours in a vacuum oven with pressure $\sim 10^{-2}$ torr [non-oil based rotary pump]. Non-contact mode atomic force microscopy (AFM) (Quescant, Q-scope 350 instruments) was used to characterize the polymer films. A sharp tweezer tip was used to scratch through the polymer film. Profiles across the scratch showed the polymer films are 40-50 nm thick with 2-5 nm rms corrugation. For the Fg sample, 50 μl of a 1.0 mg/ml plasminogen-free human plasma fibrinogen solution in deionized water was spun cast (4000 rpm, 30 s) onto clean, 1 cm^2 , Si wafers (same origin and cleaning protocol as for PS and PMMA).

Several aspects of the X-PEEM lead to un-necessary sample exposure (and thus

damage). One of these is the time it takes to transfer each image from the CCD camera to the acquisition computer. This time varies with the size of the image collected. The camera and software used in this work allow the user to select an area of interest (ROI) corresponding to either the full field-of-view (1K x 1K pixels), or only the center $\frac{1}{2}$ K x $\frac{1}{2}$ K, or the center $\frac{1}{4}$ K x $\frac{1}{4}$ K. Typically, reading a 1K x 1K image takes about 1 second whereas reading $\frac{1}{4}$ K x $\frac{1}{4}$ K takes about 0.3 seconds. The camera has two hardware controls: binning and region of interest (ROI), which both influence the read-out time. The area of interest (AOI) is the software area that is selected in ImagePro, which does not influence the readout-time but reduces the file size. In addition to the image transfer time, monochromator motion requires a finite time (~ 1 s). Overall the dead time per image (time the sample is exposed to photons but no acquisition is occurring) is about 1-2 seconds. The X-PEEM data used to determine the maximum time before considerable radiation damage occurs were acquired in spectral mode. In this mode an image is acquired for a predefined integration time, a selected portion of the image is transferred to the acquisition computer, and the total signal in that image is reduced to a single value according to:

$$\text{Eq. (3.1)} \quad I = (\sum (I_{ij} - B_{ij})/F_{ij})/n$$

where I_{ij} , B_{ij} and F_{ij} are respectively, the as-recorded image, the background (signal with no X-rays), flat-field correction (recorded separately, using a uniform CCD illumination) and n is the number of pixels summed. The camera parameters were selected to obtain spectra with many energy points (thus a well-defined spectral shape) in a relatively short exposure time. The camera ROI was set to $\frac{1}{4}$ K x $\frac{1}{4}$ K, the binning parameter was 3x3, and

Table 3.2 Maximal exposure times for PS, PMMA, Fg with mask 2.5 and chopper 17

Material	Absorption edge	Exposure time (seconds)
PMMA	C1s	150
	O1s	510
Fg	C1s	700
	N1s	290
	O1s	>2000
PS	C1s	>4000

the dwell time was 0.3 s. The actual exposure time per data point was ~ 2 s.

The beamline parameters were set for minimum flux, by selecting constant values of mask 2.5 and chopper 17, which result in 25% of “full flux” which, for a mask value of 2.5, is obtained when the chopper is set at 19.6 (see Figure 3.14). The times that were derived for each sample at each of the absorption edges where the materials show a spectral signature are shown in table 3.2. These times were obtained by acquiring multiple spectra over the same region of the sample. The spectra were then overplotted to observe the appearance and/or disappearance of spectral features indicative of radiation damage. An example of this is shown in figure 3.15 where appended C1s PMMA spectra show that even by the second spectrum, the $C1s_{(C=O)} \rightarrow \pi^*_{C=O}$ transition, at 288.5 eV, has already decreased significantly and there is an increased intensity at 285.1 eV, arising from $C1s_{(C=C)} \rightarrow \pi^*_{C=C}$, indicative of x-ray damage to PMMA where C=C bonds form in the backbone of the PMMA polymer chains upon loss of the C=O moiety due to removal of CO₂. By the 12th spectrum, the $C1s_{(C=O)} \rightarrow \pi^*_{C=O}$ transition has disappeared and the

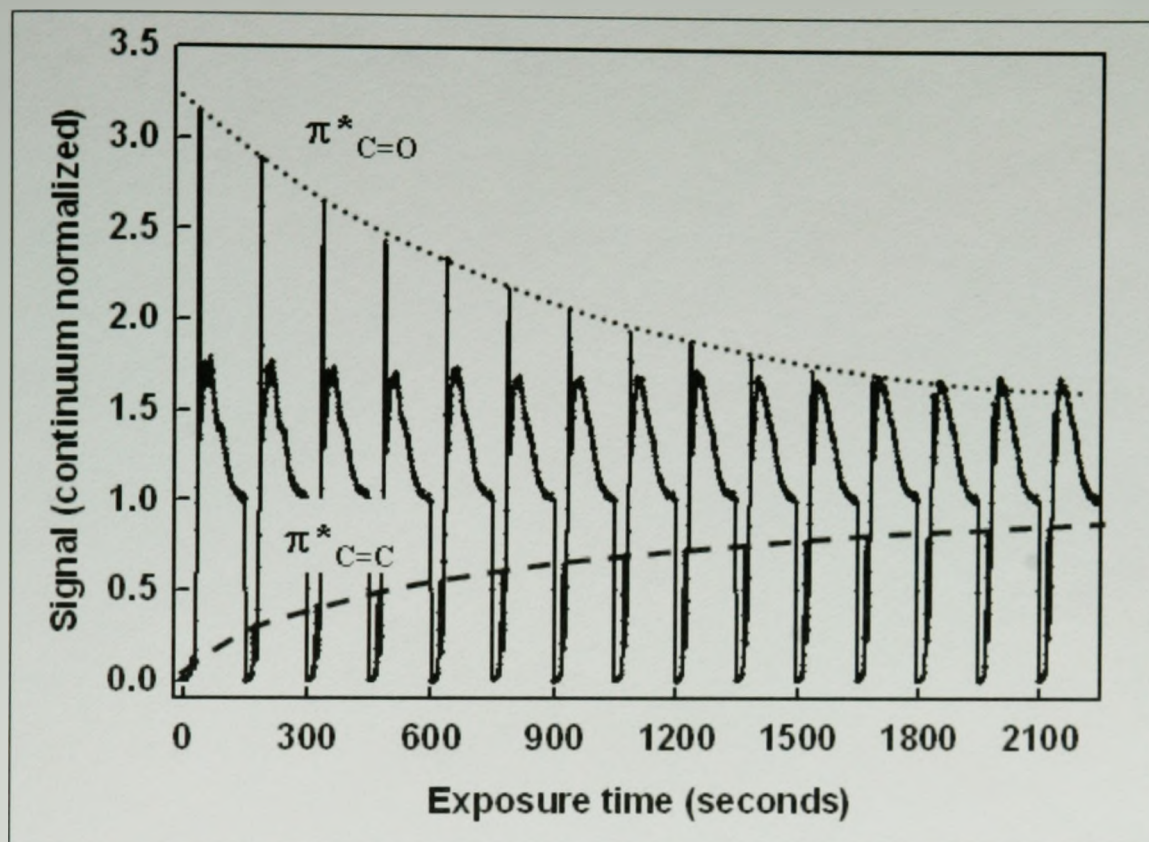


Figure 3.15 Appended C1s PMMA spectra show the effect of radiation damage on the PMMA C1s NEXAFS spectrum. The exposure time for each spectrum was 150 seconds (see text for more details).

intensity of the $C1s_{(C=C)} \rightarrow \pi^*_{C=C}$ has saturated. Thus, a maximal exposure time, at the C1s edge, for PMMA was selected to be no more than the exposure that was incurred to the first spectrum, that is, 150 seconds.

Similarly for the other materials and absorption edges, the time at which such a feature would appear, or disappear, was then chosen as a marker of the maximal exposure time allowed to study the PS:PMMA and Fg/PS:PMMA substrates while keeping the radiation damage to a minimum. This rule of thumb was used for the acquisition of the PEEM data shown in chapter 5.

Figure 3.16 compares the spectra of undamaged and heavily damaged PMMA, Fg and PS. Radiation damage of Fg is dominated by loss of the $C1s \rightarrow \pi^*_{C=O}$ transition at

288.2 eV, In this case, CO_2 is not likely to be a dominant radiation product since there is

no oxygen atom adjacent to the carbonyl. More likely is formation of $\text{C}=\text{N}$ double bonds and loss of the $\text{C}=\text{O}$ double bond. The formation of $\text{C}=\text{N}$ bonds is deduced from the growth of signals at 398-299 eV ($\text{C } 1s \rightarrow \pi^*_{\text{C}=\text{N}}$ transitions) and at 287 eV ($\text{N } 1s \rightarrow \pi^*_{\text{C}=\text{N}}$ transitions) [AHG93].

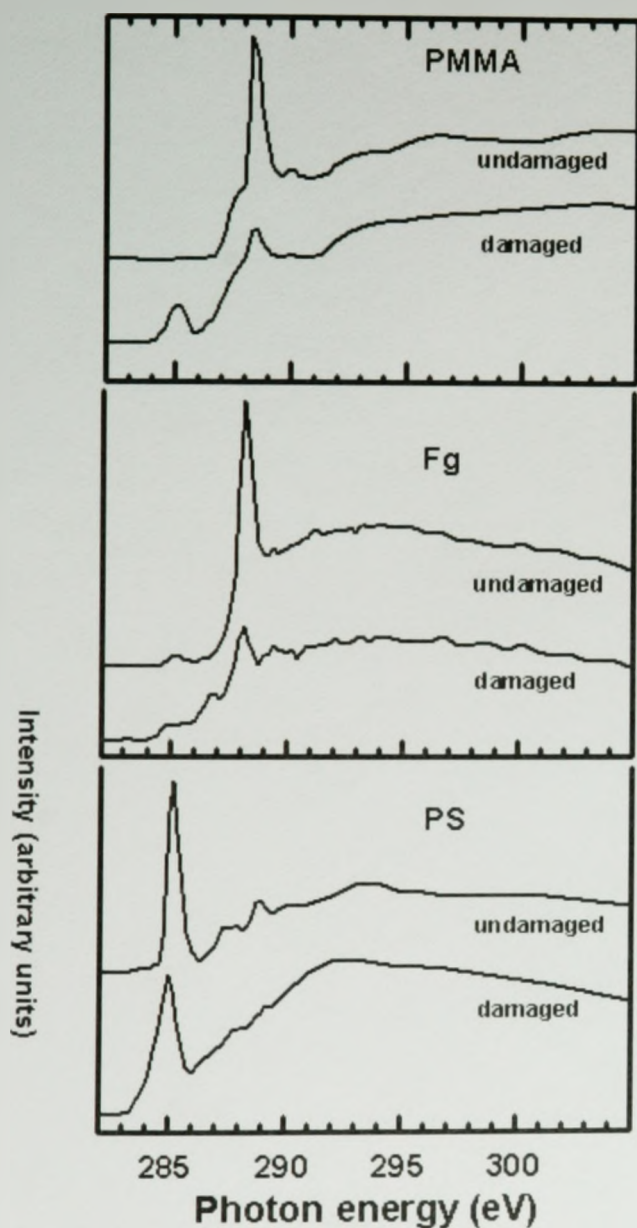


Figure 3.16 C1s spectral changes in PMMA (X-PEEM), Fg (STXM) and PS (STXM) with radiation damage. The spectral changes with damage are the same in the two microscopes.

continuum signals (283, 303 eV) [HSH&85].

Radiation damage in PS takes the form of loss of intensity of the 285.1 eV $\text{C } 1s(\text{C}=\text{C}) \rightarrow \pi^*_{\text{C}=\text{C}}$ transition, and simultaneous increase in signal at 284 eV. The latter is attributed to reduction of the saturated backbone chain. The destruction of aromatic rings is also indicated by loss of the characteristic $2\pi^*$ (289 eV) and double peaked

Figure 3.17 compares the N 1s spectra of damaged and undamaged Fg, and the O

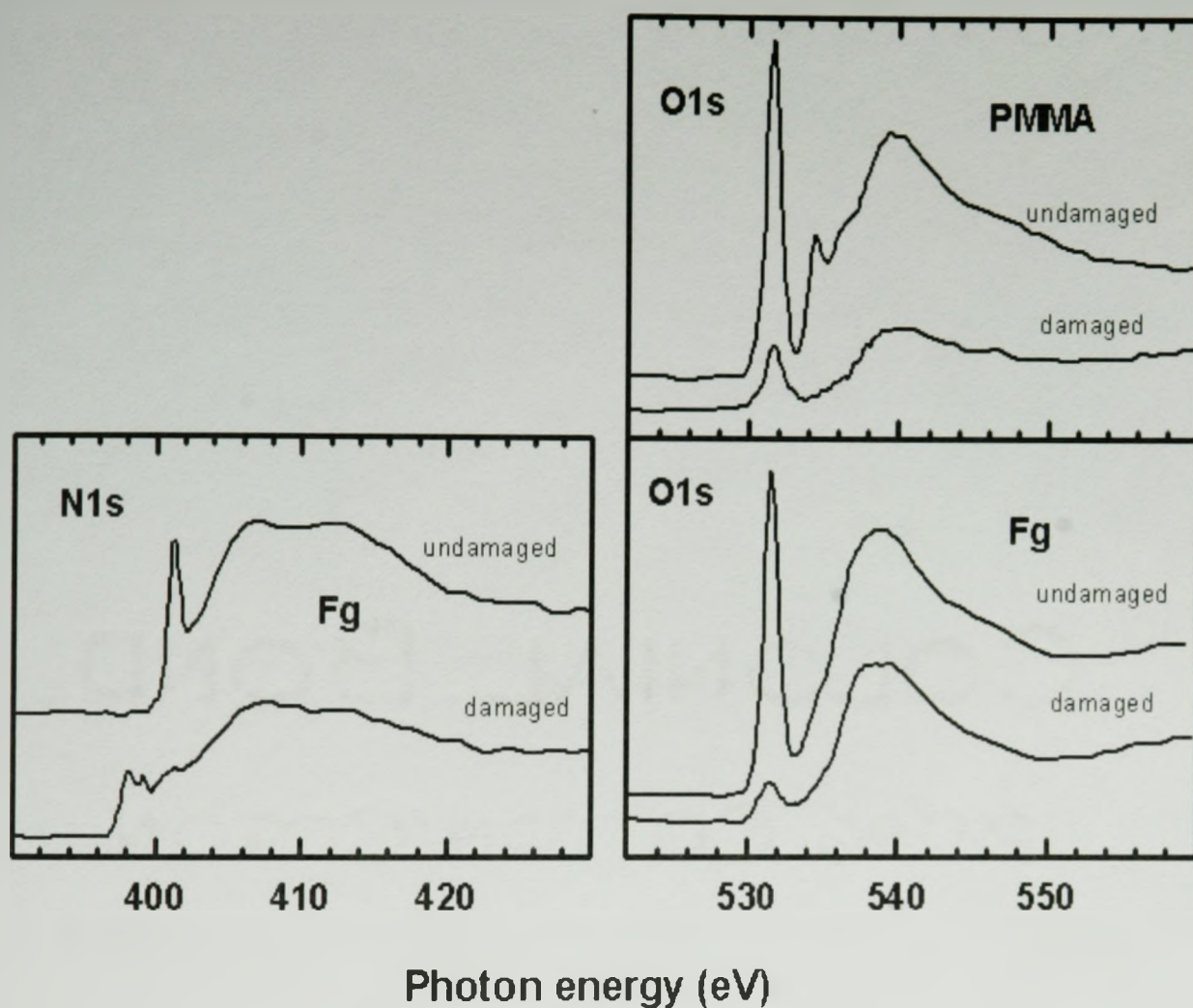


Figure 3.17 N1s and O1s spectral changes in PMMA (X-PEEM) and Fg (X-PEEM).

1s spectra of damaged and undamaged Fg and PMMA. The signature of damage to Fg at the N 1s edge is the decrease of the 401.2 eV peak ($N\ 1s \rightarrow \pi^*_{NC=O}$ amide transition) [CGT&04] and a rise in two sharp signals at 398 and 399 eV. The latter is attributed to formation of C=N bonds. At the O 1s edge the $O\ 1s \rightarrow \pi^*_{C=O}$ transition is selectively lost, and there is large loss of oxygen atoms, as indicated by the decrease in the O 1s continuum signal.

The damage observed in the O 1s edge for PMMA parallels that seen in the O 1s edge. In particular, the $O\ 1s\ (C=O) \rightarrow \pi^*_{C=O}$ transition decreases in intensity, as does the

O 1s (O-H) $\rightarrow \pi^*_{C=O}$ transition at 534 eV.

We are currently pursuing studies to quantitatively describe the damage of these materials both in X-PEEM and in STXM [MHL&xx].

§ 3.3 Spectromicroscopy Data Analysis

The stack data analysis procedures in STXM and PEEM both follow the general scheme depicted in figure 3.18. The samples used to illustrate the methodologies are PS:PMMA films made of 1% w/w polymer (30:70 w/w PS:PMMA, 1MDa:310KDa) in toluene, spun cast on Si (used in X-PEEM) or spun cast on mica, then floated onto a Si₃N₄ window (used in STXM, see figure 3.4). The PS:PMMA films on Si and on Si₃N₄ were annealed for 8 hours at 160 °C.

Following the acquisition of a stack (**STEP 1**), there are a number of steps to execute, sometimes performed in an iterative fashion, before quantitative information about the sample may be obtained from the raw data.

STEP 2 consists in the acquisition of an external I_0 when the acquisition of an internal one was not possible. Sometimes, the area of the stack is selected to include the I_0 region; this method is the most precise one. There are two methods of acquiring an external I_0 in STXM. The first, which is equally precise as the internal method, is easily done in the new interferometer-controlled STXMs by selecting multi-region stacks where one of the regions is an area of the sample where there is no polymer but the substrate is the same (ie: the “ I_0 ” for PS:PMMA floated on Si₃N₄ is a polymer free area on Si₃N₄).

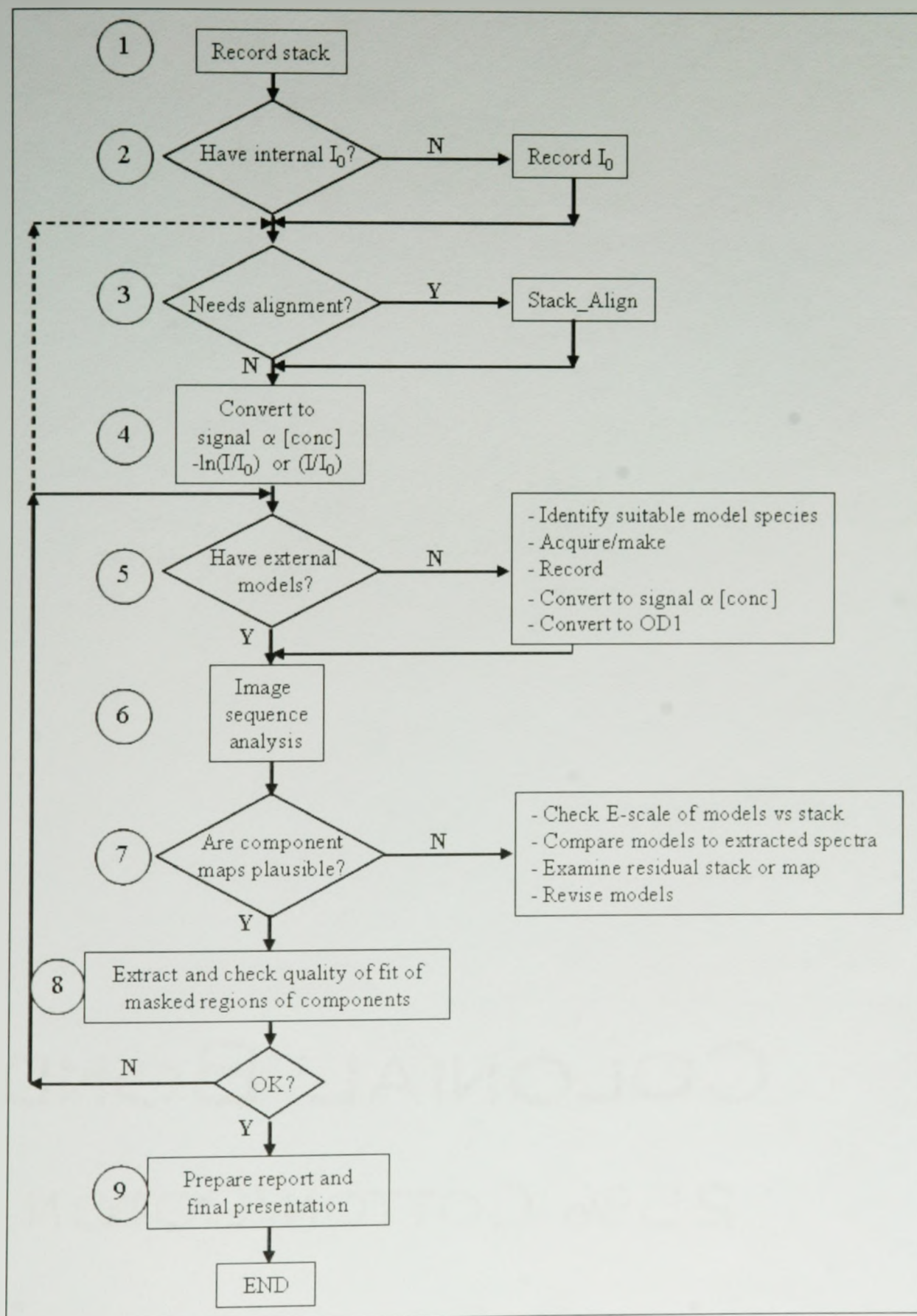


Figure 3.18 Scheme of the general methods used to analyze an image sequence in STXM and X-PEEM.

In other cases, where the Si_3N_4 window is completely covered by the polymer film, the I_0 must be acquired before or after the stack, preferably on a blank window, or else one must make corrections for the Si_3N_4 absorption; this I_0 transmitted signal must be adjusted for the different ring currents, and dwell time if it is the case.

For X-PEEM normalization, as mentioned in 3.2.5 B), there are two methods used to acquire an I_0 , each with their own advantages and disadvantages. The internal I_0 method, though inclined to spectral distortions due to possible residual polymer film, was usually the one chosen because it is easier, faster, and, since all other uncertainties of the external method accounted for (i.e. recalibration of the energy scale and optimal alignment of sample-objective lens), generally the most accurate. The I_0 is used to convert every pixel of the stack data from its raw form to intensities that reflect the concentration of the material (**STEP 4**).

STEP 3, the `stack_align` procedure, which can equally be performed after **STEP 4**, ensures that every spatial feature in all the images of a stack maintains the same x , y coordinates at all energies. The `stack_align` widget offers a variety of options, shown on figure 3.19 where a C1s stack of the PS:PMMA/Si (X-PEEM) sample is used as an example. Note that for this example, the stack was already very well aligned, as shown by the thin curves centred about 0 on figure 3.19 c), which are the x (green) and y (red) displacements in nm. Most of the shifts are less than the size of one pixel (70 nm). A simulated alignment file, with shifts as large as 5 pixels (~ 300 nm), is represented by the thick curves on figure 3.19 c). This simulation was done to show the effects of a misaligned stack which appear in the quantitation of the materials within the substrate.

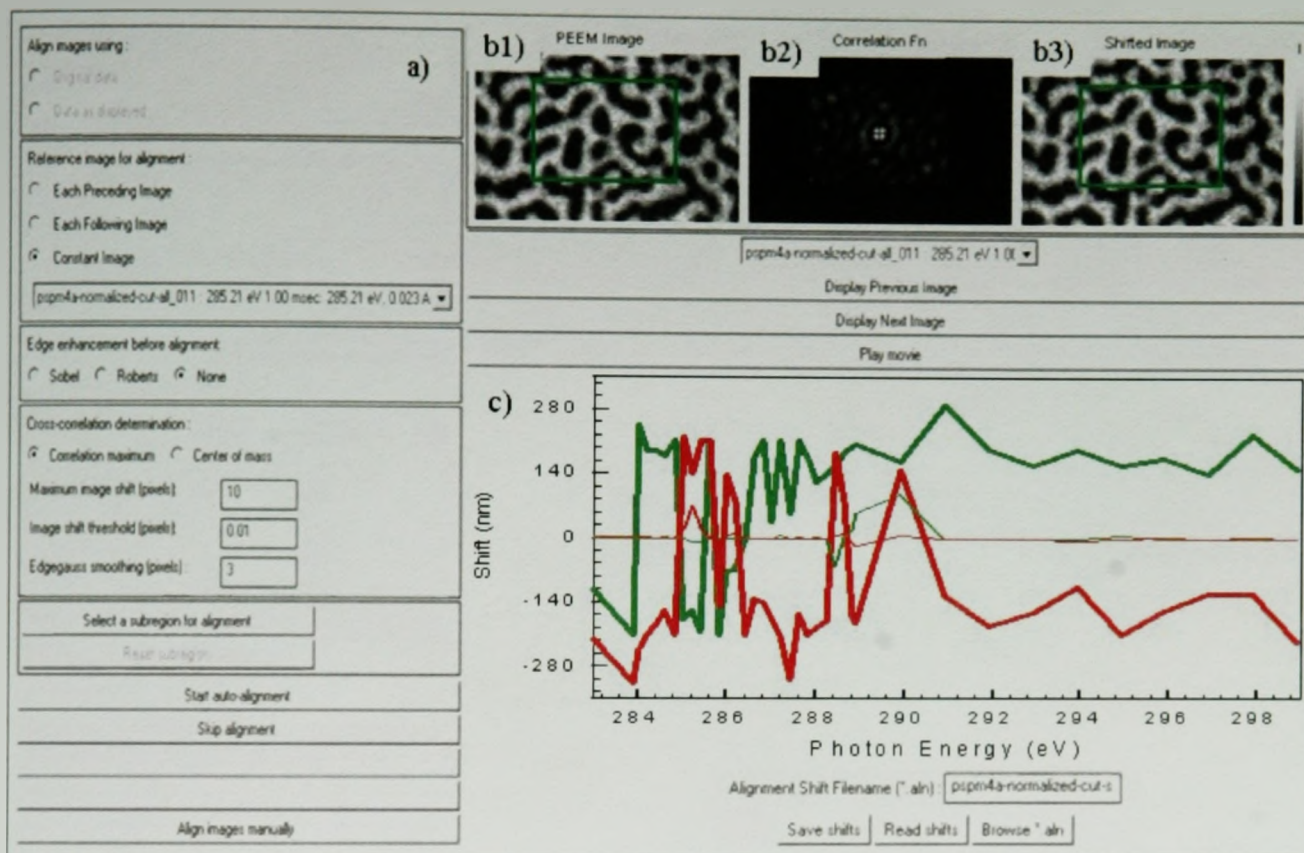


Figure 3.19 Zstack_align widget (see text for details).

Examples of these effects will be shown after **STEP 7** for the results of the properly aligned stack (figure 3.22) versus this misaligned stack (figure 3.23).

The left panel of figure 3.19 a) allows the user to choose the parameters and the options which affect the two dimensional Fourier transform based cross-correlation alignment procedure [JWF&00]. The top row of images (figure 3.19 b) corresponds to, on the left (b1), the original images of the stack, on the right (b3), the shifted images resulting from the alignment process, and in the centre (b2), the correlation function. In a good alignment the correlation image should be an intense single peak with the alignment cursor located at the maximum. In cases where alignment fails the correlation image is usually multi-peaked (see figure 3.19 b2). Experimentation with the various parameters

(region; reference image; correlation maximum versus centre of mass; etc) is often needed to find the combination that works best for any given stack.

In STXM, the jittering of the images is caused by a misalignment of the sample and zone plate as the zone plate moves in z . This has been very rarely seen with the interferometer-controlled STXMs. In X-PEEM, image movement is caused by charging; when the electrons are released from the surface, their trajectories are altered and the whole image “moves”. However, for the data shown in this thesis, there was essentially no charging and the stacks were very stable, as is the case for this example.

STEP 4: Conversion of the raw data into a signal that is proportional to the concentration of the material. The STXM and X-PEEM methods will be treated separately. A) STXM: All data in STXM can be converted from transmission intensity into optical density (see equation 2.5). When the spectra in OD units are normalized to the expected elemental response, $\mu(E)$ (see the straight lines on figure 2.7), which is normalized for 1 nm of material at its standard density, the resulting component maps have their z -scale in units of nm thickness. Figure 3.4 shows some of the 67 images of a Cls stack. The images shown were converted to optical density in the `stack_analyze` widget of aXis2000 using an I_0 spectrum recorded separately.

B) X-PEEM: As explained in section 3.2.5, normalizing the X-PEEM data with an I_0 is not as straight forward as it is in STXM. The approach that was adopted for the stack shown on figure 3.22 and the data described in the publication of chapter 5, Fg on PS:PMMA, is the following. The I_0 was selected from the scratch through the polymer film. Before using this spectrum to normalize the stack, it was first divided by a generated

Si spectrum (Si-SF-mas.txt) which gives the right shape to the I_0 spectrum. This in turn gives the appropriate shape to the resulting PS:PMMA spectrum from the normalized stack. One further normalization factor was introduced by adjusting the intensity of the stack to match the intensity of the model spectra, that is, the expected response for 1 nm of the material at its standard density

Step 5: External models on linear absorption OD scale. In order to generate quantitative information from a stack, it is necessary to have adequate model spectra, on a linear absorption scale.

A) STXM: The raw spectra for PS and PMMA were acquired respectively in point spectrum mode and “defocused” stack mode. The former is faster, but also tends to induce greater radiation damage. The defocused stack mode takes longer, but the photon intensity is less intense as the beam is scanned over a larger area of the sample. In a defocused stack, the radiation dose is further reduced by using a zone plate-sample distance longer than the focal length. As for stacks, the OD spectrum is obtained using as I_0 a spectrum acquired over the same energy range, but in a position of the sample where there is no polymer. The latter OD spectrum is scaled so that its pre-edge and post-edge intensities match the expected response for 1 nm of the material at its standard density. Figure 3.20 shows the PS and PMMA C1s normalized spectra acquired in STXM (thick lines) and in X-PEEM (medium thickness lines). The non-structured curves are the elemental response for each species.

B) X-PEEM: Figure 2.7 shows the X-PEEM acquired normalized spectra for PS, PMMA, and Fg at the three absorption edges of interest, C1s, N1s, and O1s. The C1s spectra for

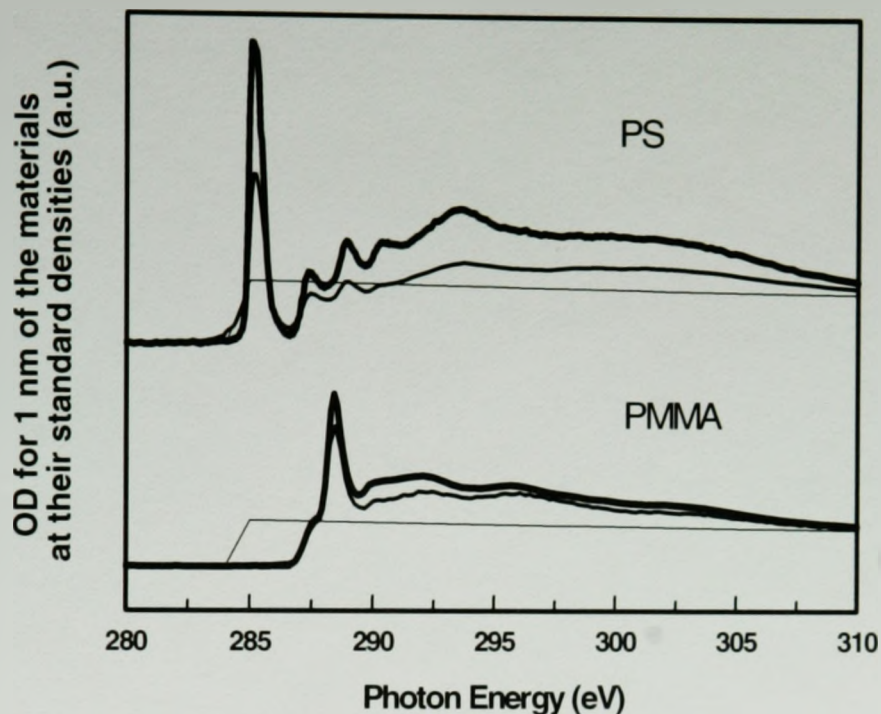


Figure 3.20 C1s NEXAFS spectra of PS, PMMA recorded as pure materials with STXM (thick lines) and with X-PEEM (lines of medium thickness). The straight lines indicate the elemental response. The intensities are on the same scale, although an offset is used for clarity.

PS and PMMA are reproduced in figure 3.20 with the corresponding STXM spectra. The PS and PMMA model spectra were acquired from a spun cast film of the pure material. In this case, the I_0 was obtained from an HF-etched piece of Si, under the same experimental conditions as the PS and PMMA spectra. As for the stack normalization, the I_0 spectrum was divided by a generated Si spectrum to give the expected shape of a Si spectrum. The raw polymer spectra were then divided by this modified I_0 spectrum, and subsequently, this (raw polymer spectrum/ I_0 HF-etched Si/Si-SF-mas) spectrum was in turn adjusted so that the pre-edge and post-edge intensities match the expected response for 1 nm of the material at its standard density (see thin lines on figure 3.20). The sample and the HF-etched Si were put side-by-side on the same sample puck and great care was taken so as not to change the sample height and tilt so as to maintain the energy scale and

illumination constant (see figure 3.10). The camera parameters were selected to obtain spectra with many energy points (thus a well-defined spectral shape) in a relatively short exposure time. As described in section 3.2.6, the camera ROI was set to $\frac{1}{4}K \times \frac{1}{4}K$, the binning parameter was 3×3 (such that each pixel read is 9 times more intense), and the dwell time was 0.3 s. The actual exposure time per data point was ~ 2 s, for a net duty cycle of about 15%.

STEP 6: Image sequence analysis:

There are three types of image sequence processing available in aXis2000: “stack-fit”, “SVD” (singular value decomposition) ([AZC&92], [ZBM&96], [KHM&02]) and “CGO” (conjugate gradient optimization) [LP01]. All three compute a least squares fit of the intensity at each pixel - $S(j,k)$ - to a linear combination of reference spectra for each component (S_i , each on a quantitative linear absorption scale).

Eq. (3.2)
$$S(j,k) = a_0(j,k) + \sum_i a_i(j,k) * S_i$$

For STXM data, the fit coefficient, a_i , is the equivalent thickness (in nm, if the reference spectra are in linear absorption format with units of nm^{-1}), of the i^{th} component at the (j,k) pixel and the concentration at that point is given by $a_i / \sum_i a_i(j,k)$. For X-PEEM data, the fit coefficient is a relative contribution of the component's model spectrum to the detected photoemitted yield, normalized to reflect the contribution from the sample only (without the substrate). The actual thickness is not obtained because of uncertainties in the materials photoabsorption cross-section (σ), e^- escape probability (f_{esc}) and work function (Φ), see figure 3.7. The inversion of the image sequence to component maps - the set of $a_i(j,k)$ values - is conveniently carried out using matrix techniques available as

part of aXis2000. In the stack fit approach, an energy independent term, (a_0), is included, which accounts for energy independent offsets (backgrounds) in the reference or the image sequence spectra. In the SVD approach, there is no a_0 term. In the conjugate gradient optimization (CGO) approach, there is no constant and a non-matrix algorithm is implemented on a pixel-by-pixel, iterative curve fit basis, using a novel method to control convergence.

It is usually a good idea to compare the results from each method. In a robust analysis the component maps derived from the three approaches are very similar, and the map of the constant term is featureless, with a histogram centered about 0.

In addition to the component maps, aXis2000 provides several other useful tools to assist the analyst. A map of the chi square values (the least squares measure of the mismatch between the actual spectrum and the fit at each pixel) is generated. It is also possible to save an image sequence of the residuals which, in favorable cases, allows one to identify missing chemical components by examination of the spectrum of the regions of poor fit.

Figure 3.21 shows the comparison of the three types of image sequence analysis (SVD, stack-fit and CGO) for the stack shown in figure 3.4, STXM data. This analysis was performed with the model spectra shown on figure 3.20, acquired with STXM, on a properly aligned stack.

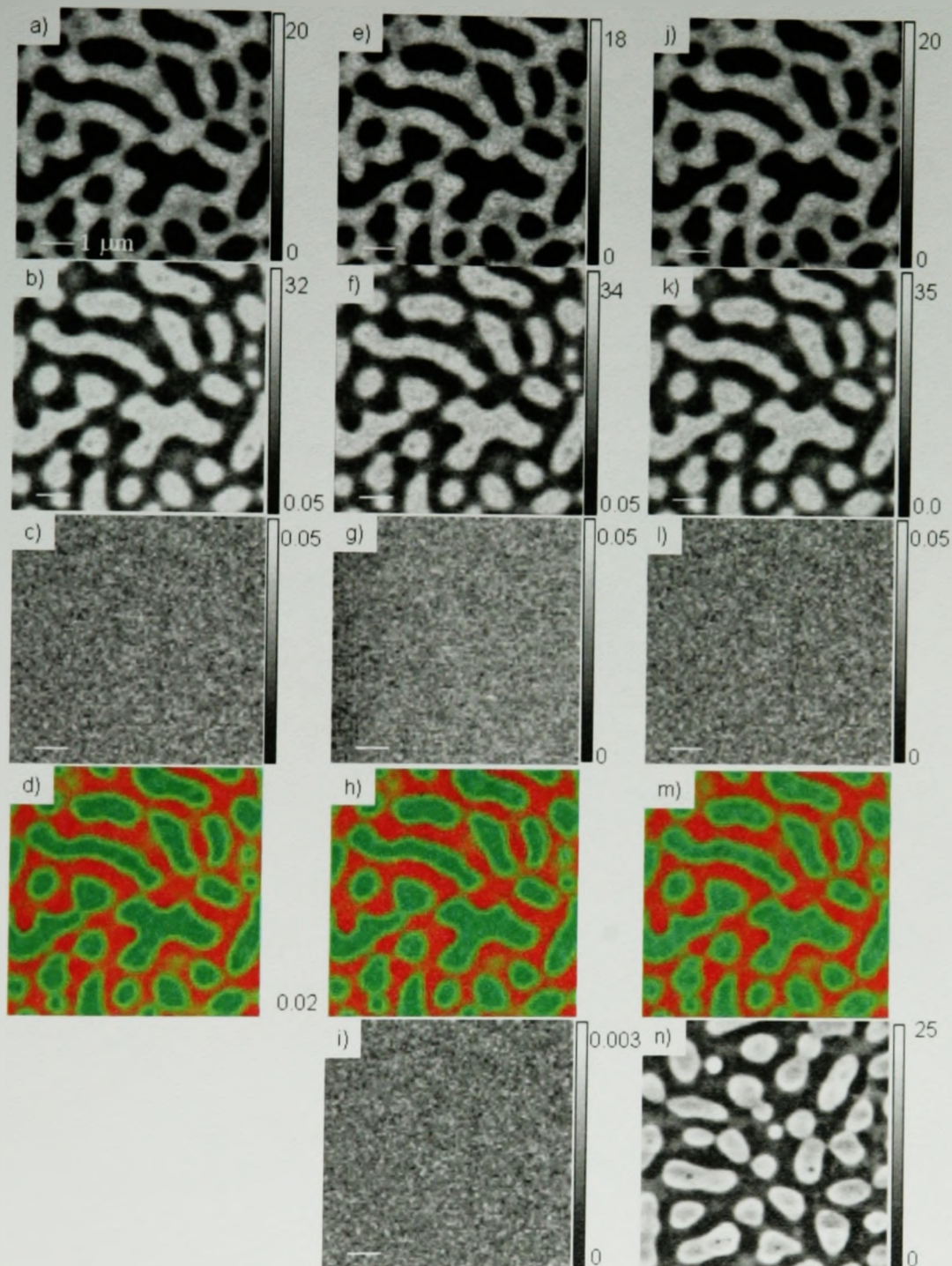


Figure 3.21 Evaluation of three stack fitting routines for a STXM C1s stack of PS:PMMA: a) to d) were generated using “SVD”; a) PS component map; b) PMMA component map; c) chi square map; d) rescaled color-coded composite map: R = PS, G = PMMA; e) to i) were generated using “stack-fit”; e) PS component map; f) PMMA component map; g) chi square map; h) rescaled color-coded composite map; l) constant map; j) to m) were generated using “CGO”; j) PS component map; k) PMMA component map; l) chi square map; m) rescaled color-coded composite map; n) Non-contact mode height AFM images of the same sample.

The results of the SVD analysis are depicted in figures 3.21 a-c, where a) is the PS component map, b) the PMMA component map, and c) the map of chi square values. The very small magnitude of the chi square scale and the absence of structure in the map, demonstrate the quality of the fit.

The stack fit results on figure 3.21 e-g, and i give an equally excellent fit, where both the chi-square map, g), and constant map, i), are featureless, with very small values corresponding to about 0.2% residual in comparison to the strength of the average image signal in the stack. Similarly, the CGO results j) to l), gave nearly identical maps to the SVD and stack-fit analysis methods.

Figures 3.21 d), h) and m) show the “RGB” color coded composite maps generated using the component maps of the SVD, stack fit, and CGO routines, respectively. All three are similar, reinforcing the similarity of the results from the three methods. In general, a “RGB” composite map is generated by taking images in up to 3 buffers and assigning them to red, green and blue color components of a single image. The user is given the option to use a common scale for all three images (thus preserving information about relative intensities of components), or autoscaling each image independently, which will give equal visibility to each component. The latter scaling option was chosen in this case.

When the stack is properly aligned (figure 3.21) and the models are adequate, much can be learnt about materials using this image sequence analysis. For example, the component maps show that the PS domains are continuous with a thickness of ~20 nm, while the PMMA domains are discrete with a thickness of ~ 33 nm. The dark PMMA

domains on the PS component maps (figure 3.21 a, e, j) show small (~ 100 nm) bright spots which correspondingly appear as dark spots in the bright PMMA domains of the PMMA maps (figure 3.21 b, f, k). These micro domains are PS microballs trapped inside of PMMA. Higher resolution images (3.1 c-d) show that there are also PMMA microdomains in the PS continuous phase.

These microdomains are also clearly observed in the non-contact mode AFM height image, figure 3.21 n). Moreover, the thicknesses generated using SVD, stackfit and CGO are corroborated with AFM. This latter image shows the topography of the sample, and not the full film thickness as obtained via STXM data analysis. Nevertheless, maps (a, b), (e, f) and (j, k) on figure 3.21, show that there is a ~ 10 nm thickness difference in the PS continuous phase, and the protruding PMMA discrete domains. A depth profiling analysis of the AFM image revealed a maximum depth of 9.3 nm.

STEP 7: Are component maps plausible? In this case, it is fair to say that the component maps shown on figure 3.21 are plausible given that all three SVD, stack-fit and CGO results are so similar, with featureless chi-square maps, and a featureless constant map for stack-fit. However, if the constant and chi-square maps had contained a lot of features, while the stack seemed properly aligned, then one would need to investigate further. For instance, the E-scale of the models and the stack should match, and the models should have the proper shape.

Using the maps generated in **STEP 6**, one can then continue to **STEP 8**: Extract and check quality of fit of masked regions of components. **STEP 8 a)** Generating masks. Indeed, STXM and X-PEEM are more than imaging techniques, they are also a powerful

spectroscopic tool. With the aid of the aXis2000 software, it is possible to identify pixels with user specified properties (i.e. those in a component map that exceed a certain value which correspond to regions of high concentration of that component). The action of selecting these pixels is referred to as “generating a mask” such that all the pixels including and above the user defined value are given a new value of 1, all others are 0. This “region of interest” (ROI) mask is used to generate spectra from these pixels of the image sequence. Those extracted spectra can then be curve fit to examine in greater detail the spectral match of the unknown and the set of weighted reference spectra.

Step 8b: Curve Fitting. Curve fitting in aXis2000 is processed using the conjugate gradient optimization (CGO) approach [LP01].

To demonstrate **STEP 8**, the C1s X-PEEM data of PS:PMMA/Si (last entry of tables 3.5 and 3.6) is used. The SVD analysis on the aligned stack with model spectra acquired with X-PEEM (see figure 3.20) is shown in figure 3.22 a)-d). The mask values are described in the image caption. Obviously, a higher mask value corresponds to a smaller number of pixels, where a greater proportion of the photoemitted signal was assigned to that particular component by the SVD analysis. This is seen in figure 3.22 h) and i) where some of the highest pixels of the PS and PMMA component maps are shown. Figure 3.22 g) and k) show the rims of the PS and PMMA domains, respectively, which were generated by taking the difference of masks shown in (e and f) and (i and j), respectively

Table 3.3 shows the corresponding curve fit results for the various masked regions shown on figure 3.22. The percentages are derived by dividing the individual fit contribution by the sum of the contributions of both PS and PMMA. This same procedure

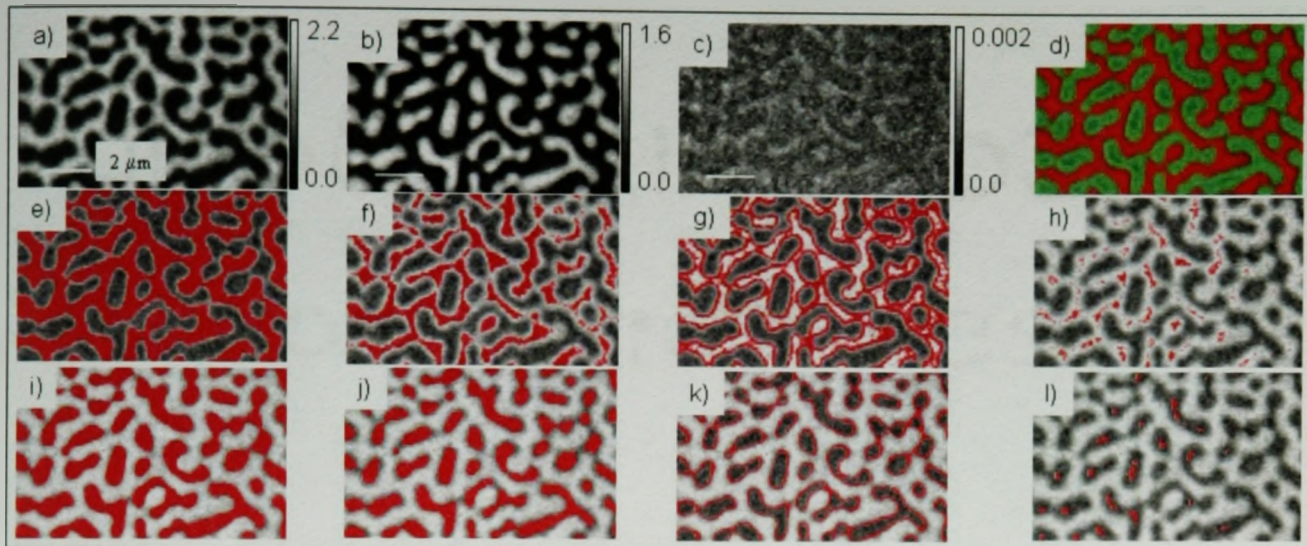


Figure 3.22 SVD analysis of PS:PMMA/Si (last entry of table 3.4), C1s aligned stack and ROI images shown at 285.1 eV; a) PS component map; b) PMMA component map; c) chi-square map; d) rescaled color-coded composite map; e) PS 1.01; f) PS 1.5; g) PS 1.01-1.5; h) PS 1.8; i) PMMA 0.7; j) PMMA 0.95; k) PMMA 0.7-0.95; l) PMMA 1.4

Table 3.3 Curve fit results of PS and PMMA masked regions from figure 3.19 (aligned C1s PS:PMMA/Si X-PEEM stack)

Region and mask	PS contribution / %	PMMA contribution / %	Standard Deviation
PMMA 1.4	0.23 / 14%	1.46 / 86%	0.0007
PMMA 0.95	0.30 / 20%	1.19 / 80%	0.0008
PMMA 0.7	0.36 / 25%	1.08 / 75%	0.0008
PMMA 0.7-0.95 (rims)	0.49 / 37%	0.85 / 63%	0.0008
PS 1.8	1.83 / 99%	0.02 / 1%	0.002
PS 1.5	1.62 / 96%	0.07 / 4%	0.002
PS 1.01	1.40 / 90%	0.16 / 10%	0.002
PS 1.01-1.5 (rims)	1.23 / 85%	0.22 / 15%	0.001

was repeated for a simulated misaligned stack with shifts up to 320 nm (or 5 pixels, 70 nm each), shown on figure 3.19 c). The SVD results and masked ROIs are shown in figure 3.23 while the corresponding curve fit results are found in table 3.4.

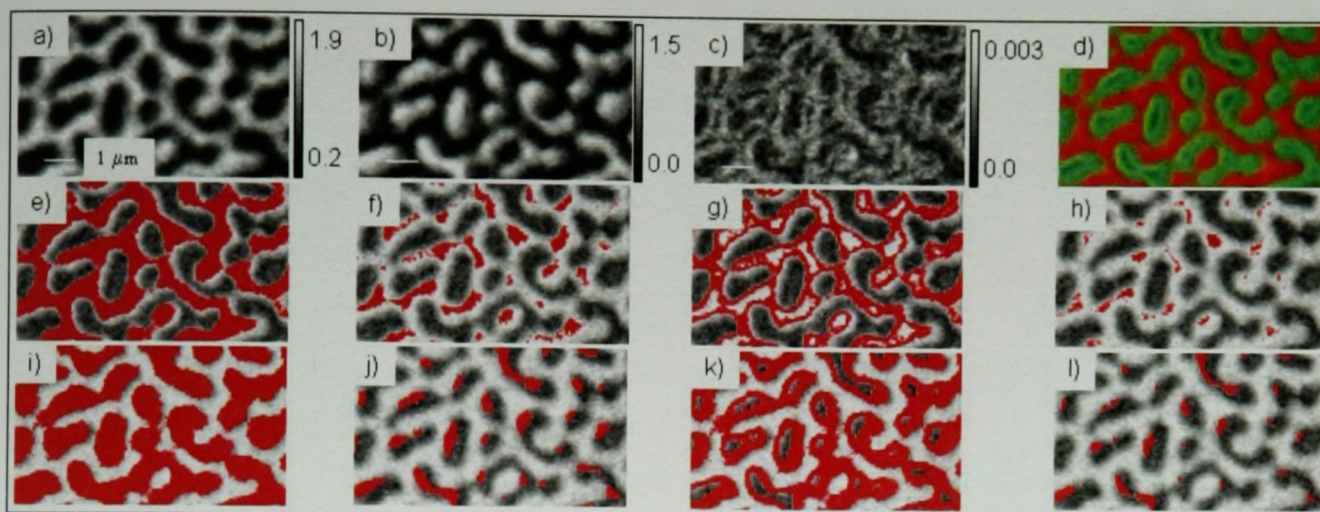


Figure 3.23 SVD analysis of PS:PMMA/Si (last entry of table 3.4), C1s simulated misaligned stack and ROI images shown at 285.1 eV; a) PS component map; b) PMMA component map; c) chi-square map; d) rescaled color-coded composite map; e) PS 1.05; f) PS 1.45; g) PS 1.05-1.45; h) PS 1.6; i) PMMA 0.45; j) PMMA 1.1; k) PMMA 0.45-1.1; l) PMMA 1.2

Table 3.4 Curve fit results of PS and PMMA masked regions from figure 3.19 (simulated misaligned C1s PS:PMMA/Si X-PEEM stack)

Region and mask	PS contribution / %	PMMA contribution / %	Standard Deviation
PMMA 1.2	0.32 / 20%	1.28 / 80%	0.0009
PMMA 1.1	0.34 / 22%	1.21 / 78%	0.0009
PMMA 0.45	0.64 / 37%	0.82 / 63%	0.0009
PMMA 0.45-0.9 (rims)	0.70 / 49%	0.74 / 51%	0.0009
PS 1.6	1.67 / 99%	0.02 / 1%	0.0009
PS 1.45	1.56 / 95%	0.09 / 5%	0.0009
PS 1.05	1.32 / 85%	0.24 / 15%	0.0009
PS 1.05-1.45 (rims)	1.24 / 81%	0.29 / 19%	0.0009

The differences in a well-aligned stack (shifts shown as thin lines in figure 3.19 c) and a misaligned stack (shifts shown as thick lines in figure 3.19 c) can sometimes be very subtle. Indeed, the percent contribution of each component in a specific region are very similar even though the misaligned stack contains shifts by up to 300 nm, or half the

width of a PS or PMMA macrodomain. However, the results in table 3.4, for the misaligned stack, are worse than in table 3.3, for the aligned stack. These effects are especially seen in the PMMA masks where the high PMMA pixels contain 14% PS (aligned) and 20% PS (misaligned). In the aligned stack, this large contribution of PS could be due to some radiation damage or unresolved PS microdomains, and in the misaligned stack, the extra 6% could result from the intermixing of signals as the images are displaced from their optimal coordinates.

In the “rims” masked regions (figures 3.22 g and k, and figure 3.23 g and k), the curve fit results show a considerable amount of the other component in the rim of one component. These rims correspond to the grayish contours shown in all 4 component maps of figures 3.22 and 3.23, though they are larger in the misaligned stack. For the misaligned stack, the presence of microdomains in both phases also does not appear as readily as it does in the aligned stack results, figure 3.22. It is because of these subtle differences that a very good alignment is necessary.

§ 3.4 Sample preparation

§ 3.4.1 Why PS:PMMA?

The PS/PMMA system was selected as an appropriate substrate for the study of protein adsorption on patterned polymers by soft X-ray spectromicroscopy techniques.

This system was chosen for three reasons. First, these two materials are immiscible and readily phase separate in the bulk [C94] and this phase segregation was

expected to continue to the surface [W70] to form patterns at the surface. Background theory and experimental results are given in chapter 4.

Second, surface phase separation of PS and PMMA, if it occurs, would then provide a substrate which has two different materials at its surface and may, if of a suitable size scale, be appropriate for selective protein adsorption studies. Intrinsically, these two materials have different polarities (PMMA > PS). In the presence of an aqueous or buffered protein solution, PMMA could form hydrogen bonds with thiol groups on the surface of the protein. One, or a combination of these physical and chemical properties, could lead to preferential adsorption of the protein to one polymer over the other. Protein adsorption results on PS:PMMA substrates are discussed in chapter 5.

Third, PS and PMMA have very different C1s NEXAFS spectra; this facilitates imaging and chemical differentiation. The main feature that highlights the two materials is their respective highest intensity transitions. The intense $C1s_{(C=C)} \rightarrow \pi^*_{C=C}$ transition of the phenyl rings characterizes PS while the intense $C1s_{(C=O)} \rightarrow \pi^*_{C=O}$ of the ester group characterizes PMMA.

The following sections describe the sample preparation methods for the samples discussed in this thesis. §3.4.2 focuses on the historical perspective of the methods used to prepare the PS:PMMA thin films sample. The development of a cleaning protocol and the optimization of parameters for the samples used in chapter 5 (Fg on PS:PMMA) are detailed in §3.4.3. The PS:PMMA samples used in the STXM experiments are described

in §3.4.3.3. §3.4.4 explains the protein adsorption procedures for the different types of samples, whether they are to be used in a STXM or a X-PEEM microscope.

§3.4.2 Historical perspective

In the very beginning of the sample preparations, the group of Prof. John Dutcher at the University of Guelph, Ontario, provided us with some PS and PMMA polymers and basic methodologies for preparing thin film polymer blend samples. This substrate was used for one of the very first X-PEEM experiments conducted. Our expectations of sample morphology, evaluation of parameters for appropriate PS:PMMA X-PEEM samples, and X-PEEM instrumental procedures and data analysis methodologies were very naïve. Nevertheless, a first step was needed.

The molecular weights used for the first preparation were 2.24 mega Dalton for PS and 150 kilo Dalton for PMMA. They were dissolved in a 66:33 ratio, 0.8 % weight-by-weight in toluene. The Si wafers were “cleaned” by spin coating several drops of toluene right before spin coating with the polymer solution which was dispensed through a Teflon fluoropore filter screwed on at the tip of a syringe. The samples were annealed at 123 °C for 55 hours with a pressure of 100 millitorr in an untrapped vacuumline. Through trial and error, it was found that most of these parameters were far less than optimal! The X-PEEM results of this sample indicated that there was an overlayer of polystyrene covering the whole surface made of a PS matrix embedded with spherical lenses of PMMA ranging in size between 300-500 nm (see figure 3.8 a). Such an

overlay was not desirable for the investigation of first sites of adsorption of proteins on a polymer phase segregated surface.

In order to better understand this system, a collaboration was started with the group of Prof. H. Ade at North Carolina State University. Several MW's and % ratio of each polymer were investigated, using STXM, X-PEEM and AFM. These results were the subject of a publication, inserted *verbatim* in chapter 4.

Following the publication of this work, it was clear that we needed to improve our sample preparation methods in order to get rid of the impurity signal that was found in the STXM and X-PEEM data, and perhaps find the parameters (outlined on page 204 of the publication in chapter 4) that would minimize the number and size of PS microdomains in the PMMA macrodomains, while maintaining a very smooth surface (< 5 nm rms) and create domain sizes that are easy to work with in the X-PEEM, that is between 0.5 and 2 microns. A smooth surface was needed for two reasons. First, with the goal of using this substrate for protein adsorption, the substrate must be flat so that any possible preferential adsorption would indeed be due to the chemical properties of the individual domains in the materials and not to the 3D structure of the material at the surface.

These steps to improve the sample preparation procedures and results are outlined below. The introduction and experimental sections of chapter 4 explain the principles of spin coating and the polymer physics of the PS:PMMA system.

§ 3.4.3 Evolution of PS:PMMA substrates

The work that followed had three goals. The first was to improve the purity and cleanliness of the sample preparation. Intensive testing of the sample preparation procedures was performed. X-ray photoelectron spectroscopy (XPS), AFM and X-PEEM measurements were used. AFM provided a visualization of the amount and size of the debris left on the SiO_x wafers after different stages of the SiO_x cutting and cleaning processes, and after spin coating in different ways. The best method found is outlined below. X-PEEM was used to identify the chemical nature of the remaining impurities on the annealed spun cast polymer film, as well as the extent of phase separation as evidenced by the purity of the NEXAFS spectrum from the PMMA domains.

The second goal was to improve the extent of phase separation while obtaining an appropriate morphology of the polymer films. Various parameters were optimized including different molecular weights (MW) of PS and PMMA (100K:100K, 300K:300K, 1M:310K), different proportions of the two polymers, different spin casting rates, and different annealing temperatures and cycles.

The third goal was to improve the X-PEEM system and acquisition procedures. A better detection system in X-PEEM (new camera, as of May 2002) and development of a minimal X-ray exposure methodology (July 2002, described in section 5.2) allowed the measurement of a low damage PMMA spectrum in PS/PMMA (Dec 2002), see figure 6.1.

§ 3.4.3.1 Cleaning protocol

It was found that the best method to clean the substrates is to sonicate the Si chips for 10 minutes in each of these three successive solvents (trichloroethylene, acetone and methanol or ethanol), followed by rinsing each Si chip individually with running deionized water, then drying by either flushing the surface with a flow of helium or simply by touching the edge of the wafer chip with lens paper while holding the chip vertically. Following this drying step, it was found that spin coating with toluene, without the use of filters which were used in the preparation of the samples measured in the publication of chapter 4, gave best results. The syringe used to spin cast the toluene was cleaned with detergent, rinsed abundantly with DDI water, dried with He, immersed in a 400 ml beaker of toluene, sonicated for 15 minutes with a glass cover on top of the beaker filled with toluene, the syringe is then rinsed with DDI water and as much of the water droplets as possible are removed with He. The beaker filled with the 400 ml of toluene was cleaned by scrubbing with detergent, rinsed generously with DDI water,

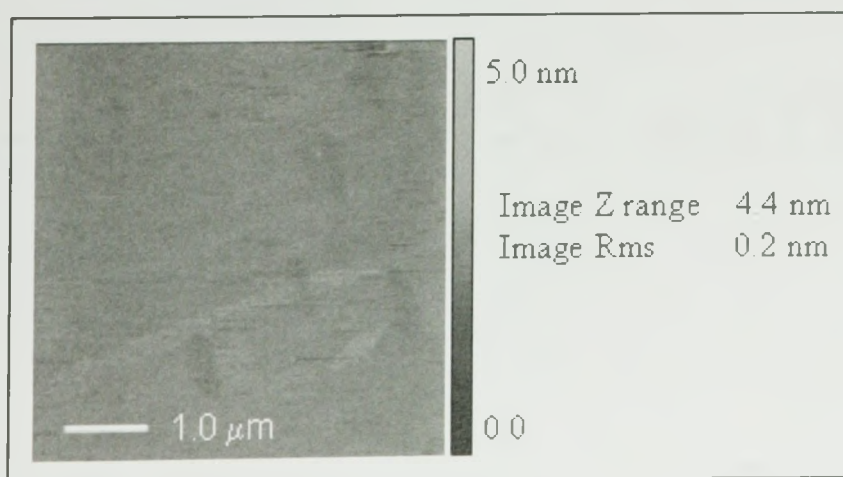


Figure 3.24 $25 \mu\text{m}^2$ non-contact mode AFM image of a clean Si wafer chip (see text above).

dried with He, rinsed with toluene and then filled with toluene. Using another cleaned beaker filled with toluene, the syringe was rinsed twice before it was filled with the solution to be spun cast. One of the resulting AFM images is shown in figure 3.24.

Since there were so many instrumental problems to overcome in the early days of our X-PEEM experiments (camera noise, uncontrolled radiation damage, understanding the beamline and microscope parameters and the effect they have on signal intensity and imaging quality, Io corrections, etc.), a lot of the results that were obtained prior to the installation of the new camera in May 2002 and low X-ray exposure method developed in July 2002 may not be reliable to probe the level of purity of the sample.

§ 3.4.3.2 Choice of MWs and annealing method

The samples prepared were all 1% w/w in toluene, spun cast on SiOx or HF-etched Si. MWs, ratios, spin rates and annealing methods varied. Table 3.5 details the samples that were investigated by AFM and prepared for X-PEEM experiments; the samples prepared for STXM experiments will be discussed in section 3.4.3.3.

Table 3.5 AFM investigation of all PS:PMMA samples explored in X-PEEM (Page 1/3)

Date made	MWs	Ratio	Spin rate	Substrate	Annealing	Results
Jan. 01	100K: 100K	3:7	4000	SiOx	none	PMMA domains (higher) vary in shapes and sizes from 50 nm circular domains to snakes 2µm long by 150 nm
Jan. 01	100K: 100K	3:7	4000	SiOx	2 hrs at 140 °C, cool down to 30 °C in 12 hrs, pressure: 3 x 10 ⁻⁵ torr	Height difference is much decreased; AFM is not "clean"

Table 3.5 AFM investigation of all PS:PMMA samples explored in X-PEEM (Page 2/3)

Date made	MWs	Ratio	Spin rate	Substrate	Annealing	Results
Jan. 01	1.1M: 317K	3:7	4000	SiOx	none	PMMA domains (higher) vary in shapes and sizes from 60 nm in diameter balls to snakes 1.5 μm long by 400 nm
Jan. 01	1.1M: 317K	3:7	4000	SiOx	2 hrs at 140 $^{\circ}\text{C}$, cool down to 30 $^{\circ}\text{C}$ in 12 hrs, pressure: 3×10^{-5} torr	PMMA domains (higher) vary in shapes and sizes from 60 nm in diameter balls to snakes 1.5 μm long by 300 nm
Apr. 01	100K: 100K	2:8	4000	HF-Si	none	Continuous phase is PMMA; discrete domains are 200 nm wide x $\sim 4 \mu\text{m}$ long. PEEM PMMA spectra have large amounts of 285 eV
Apr. 01	100K: 100K	2:8	4000	HF-Si	50 hrs at 140 $^{\circ}\text{C}$, cool down to 110 $^{\circ}\text{C}$ in 20 minutes, leave at 110 $^{\circ}\text{C}$ for 12 hrs, cool down to 30 $^{\circ}\text{C}$ in 30 minutes, pressure: 3×10^{-5} torr	No change from unannealed
Aug. 01	100K: 100K	3:7	4000	SiOx	22 hrs at 180 $^{\circ}\text{C}$, pressure: 6.5×10^{-7} torr	PMMA "balls" of 1-1.5 μm diameter, height of 180 nm

POST "PROPER" CLEANING PROTOCOL:

Oct. 01	100K: 100K	3:7	2000	SiOx	none	Thickness = 42 nm, rms = 3.9 nm, Z-range = 20 nm, largest of small domains = 2.7 μm x 0.64 μm , high density of PS microdomains
	100K: 100K	3:7	4000	SiOx	none	Thickness = 33 nm, rms = 2.7 nm, Z-range = 14 nm, largest of small domains = 2.0 μm x 0.57 μm , high density of PS microdomains
	100K: 100K	3:7	6000	SiOx	none	Thickness = 35 nm, rms = 2.5 nm, Z-range = 15 nm, largest of small domains = 1.21 μm x 0.37 μm , high density of PS microdomains
Oct. 01	100K: 100K	3:7	2000	SiOx	160 $^{\circ}\text{C}$ for 5 hrs, pressure: 8×10^{-7} torr	3 layers of domains Thickness = 46 nm and 38 nm, rms = 21 nm, Z-range = 134 nm
	100K: 100K	3:7	4000	SiOx	160 $^{\circ}\text{C}$ for 5 hrs, pressure: 8×10^{-7} torr	3 layers of domains Thickness = 44 nm and 33 nm, rms = 15 nm, Z-range = 88 nm

Table 3.5 AFM investigation of all PS:PMMA samples explored in PEEM (Page 3 of 3)

Date made	MWs	Ratio	Spin rate	Substrate	Annealing	Results
Oct. 01	100K: 100K	3:7	6000	SiOx	160 °C for 5 hrs, pressure: 8×10^{-7} torr	3 layers of domains Thickness = 36 nm and 22 nm, rms = 14 nm, Z-range = 93 nm
Jan. 02	100K: 100K	3:7	4000	SiOx	none	Round PMMA domains, all about 600 nm in diameter
Jan. 02	100K: 100K	3:7	4000	SiOx	140 °C for 2 hrs	After annealing, the round domains agglomerate into 2-5 μm long snakes by 400 nm wide
Feb. 02	100K: 100K	3:7	4000	SiOx	none	similar to the 1 st entry in this table
	100K: 100K	3:7	4000	SiOx	2 hrs at 120 °C	similar to the 1 st entry in this table
Feb. 02	100K: 100K	3:7	4000	SiOx	2 hrs at 130 °C	similar to the 2 nd entry in this table
	100K: 100K	3:7	4000	SiOx	2 hrs at 140 °C	similar to the 2 nd entry in this table
May 02	300K: 300K	3:7	4000	SiOx	2 hrs at 140 °C	vary in shapes and sizes from 360 nm in diameter disks to snakes 7 μm long by 700 nm; NOTE: this was measured with Park M5 AFM, the quality of the image is doubtful because no microdomains could be detected so the smallest PMMA macrodomains in the PS matrix could have been much smaller than 700 nm
July 02	1.1M: 317K	3:7	4000	SiOx	4 hrs at 140 °C, pressure: 30 mm Hg	Mostly PMMA round domains about 1 μm diameter with few (~ 2-3) 80 nm diameter PS microdomains in PMMA, but also some ~ 50 nm diameter PMMA balls on PS
Oct. 02	1.1M: 317K	3:7	4000	SiOx	6 hrs at 160 °C, pressure: 30 mm Hg	Mostly PMMA round domains about 1 μm diameter with few (~ 2-3) 80 nm diameter PS microdomains in PMMA, but also some ~ 50 nm diameter PMMA balls on PS
Dec. 02	1.1M: 317K	3:7	4000	SiOx	8 hrs at 160 °C, pressure: 30 mm Hg	PMMA domains are ~ 2 μm long by 0.5 μm wide, smallest PMMA domains are 1 μm diameter disks containing very few (~2-3 at most) 80 nm diameter PS microdomains in PMMA; the PS snakes are ~ 1 μm wide.

Observations of AFM images, with regards to domain sizes and amount of microdomains within macro-domains, are useful for accepting/rejecting plausibly appropriate samples for X-PEEM. The high MW combination of 1M:310K PS:PMMA with long annealing times at high temperatures (6-8 hours @ 160C) gave the best phase separation, as well as large micron sized PMMA domains. The latter is needed because of the limited spatial resolution in X-PEEM. AFM shows that there are very few PS microdomains in PMMA (see figure 3.25) and measurements with low X-ray radiation exposure in X-PEEM corroborates with an amount of about 5% PS area in the PMMA macrodomains (see figure 6.1). For the purpose of using this system for protein adsorption, these conditions seem to be the best. This substrate was the one used for protein adsorption where the results are shown in chapter 5.

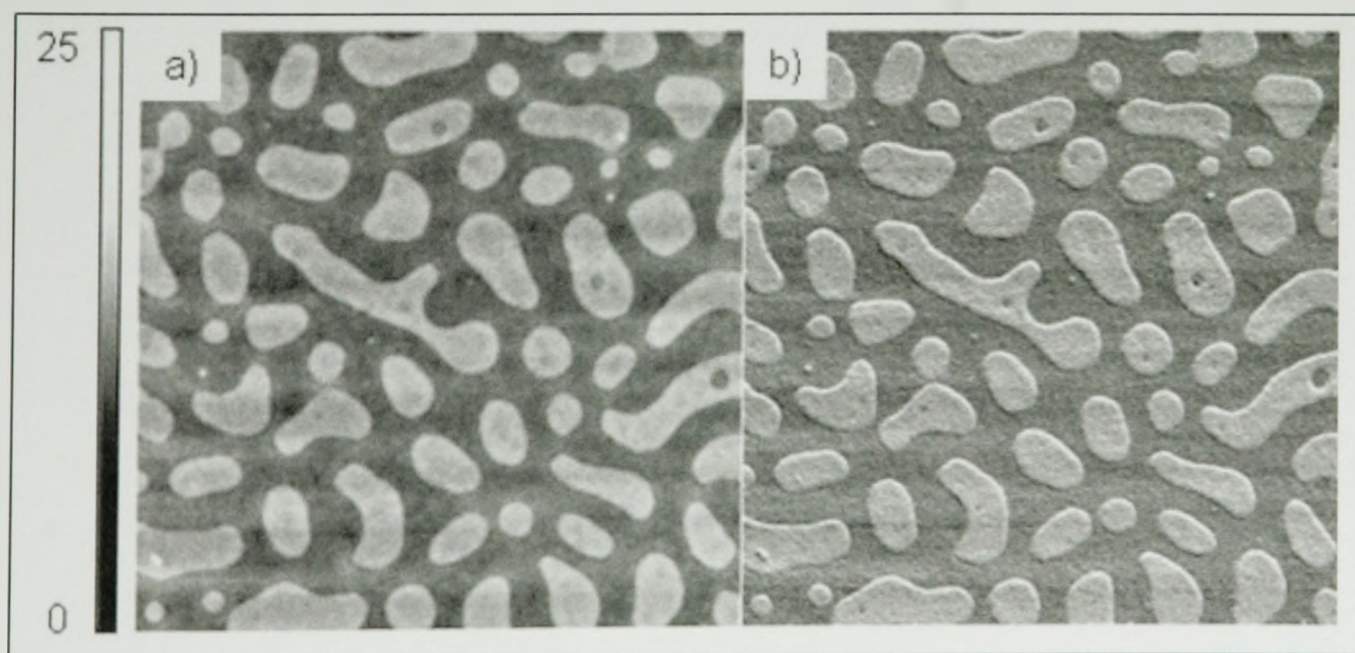


Figure 3.25 (a) AFM height image ($10\ \mu\text{m} \times 10\ \mu\text{m}$) of 30:70 PS:PMMA (1M:310K), 1% w/w in toluene spun cast on SiO_x at 4000 rpm, annealed 8 hours at 160 °C, (b) phase mode, simultaneous acquisition. Last entry of table 3.5.

X-PEEM evaluations

Before the PS:PMMA films could be used for protein adsorption, it was necessary to ensure that X-PEEM could provide C1s NEXAFS spectra from the PS and PMMA domains of the PS:PMMA films that were equivalent to the pure PS and PMMA reference spectra. There were many parameters in the X-PEEM experiment that were not well understood until the period of July-December 2002, as outlined in this chapter, sections 3.2.4-3.2.6. Thus, the X-PEEM data were at times very confusing in so far as being able to determine accurately the extent of phase separation of the PS:PMMA spun cast system. Most of the issues involved were: learning how to generate proper camera corrections for low X-ray exposure measurements, learning how to make adequate I_0 corrections, and determining the beamline and microscope conditions for minimal X-ray damage.

Simultaneously, various parameters of the PS:PMMA sample preparation were tested in an effort to obtain large PS and PMMA macrodomains with as few as possible microdomains, while maintaining a low corrugated (< 5 nm) surface topography. The flatness of the sample is important to avoid charging artifacts in the X-PEEM, and also to address the question of possible preferential first sites of adsorption of proteins on a phase segregated polymer blend, based on the chemical differentiation of the domains at the surface of the substrate, as opposed to the topography of the sample. Table 3.6 summarizes the results of the PS:PMMA X-PEEM measurements.

Table 3.6 PS:PMMA samples explored in X-PEEM

Date	Sample (refer to table 3.5)	X-PEEM conditions	Results
June 01	as-made (made Apr. 01)	OLD camera: camera and I ₀ corrections - dark data collected systematically; HF-etched-Si measured on 2 days Software development required to complete this aspect.	At acceptable dose for PMMA, the 20/80 PS/PMMA signals are poorly defined. Even so, observations made are: snake morphology; PMMA is the continuous phase; relative areas are about 50:50; PMMA regions show large PS signal (285 eV is ~50% of 288.4 eV)
Jan 02	2 hours @ 140 °C (made Jan. 02)	OLD camera: obtained pixel intensity for fixed mask (0.9), varying chopper X-PEEM: dust particle on the objective lens	Both PS and PMMA rich spectra have strong spectral features of one another, probably due to BAD pulsing during acquisition; does not give true information of sample chemistry
Feb 02	2 hours @ 130 °C (made Feb 02)	ALS: 2-bunch mode OLD camera: re-measure set of camera correction images, re-measured pixel intensity as a function of chopper for fixed mask (0.9) under 4 different sets of conditions	Even with dark and noise corrections, pattern is blurry and the PMMA rich pixels contained a huge amount of PS Tested "on-the-fly" and post camera corrections; work equally well. "struggles" to get low damage PMMA.
May 02	3:7, 2 hours @ 140 °C (made May02)	Beamline: has been realigned NEW camera!!!! re-measured pixel intensity as a function of chopper for fixed mask (2.5)	For stack: 260s, chopper 17, PMMA rich spectrum has 285 eV peak ~ 25% of 288 eV peak. We now know (after July 2002) that under these conditions, the PMMA is heavily damaged, so this sample MAY have been appropriate for protein adsorption, but the AFM image (Park-M5) was also unclear.
July 02	(made July 02)	Stack acquired under low PMMA dose conditions (from pure PMMA, July 02)	For stack: 158s, chopper 17, PMMA rich spectrum has 285 eV peak ~ 25% of 288 eV peak.; even though the sample current was very low, the stack's images are moving a lot: grainyness of images looks like X-PEEM was not well aligned. As indicated in AFM, micro PMMA-in-PS appear.
Dec. 02	(made Dec 02)	Stack acquired under low PMMA dose conditions (from pure PMMA, July 02)	- the sample was VERY clean, the extra ~5% of π^* C=C could easily correspond to PS-in-PMMA (as seen in AFM), - there is no gain to reduce the total exposure time below 165 seconds as the spectral quality is degraded. - C1s data shows PS microdomains in PMMA!! - the Si scratch was not 100 % polymer free

§ 3.4.3.3 PS:PMMA sample preparation for STXM

The PS:PMMA samples spun cast on Au/Si₃N₄ that were measured with the old STXM 7.0.1, which results are shown in the publication of chapter 4 (AFM images in figures 3 and 4 of the publication), were never again reproduced adequately until April 2003 when the PS:PMMA film was spun cast on mica first, then floated onto Si₃N₄. This latter suggestion was given by Dr. Kari Dalnoki-Veress (Physics Department at McMaster) and the film was floated by his M.Sc. student, Lun Si.

After the initial successful preparation of October 2000, on most other attempts to spin coat directly onto the Si₃N₄ membrane, or Au-coated Si₃N₄, the films were always very non-uniform, with thick deposits of polymers in the center of the window. These deposits affected the film morphology such that either no pattern was observed in AFM on the window (even though the film's morphology on the wafer part of the Si₃N₄ was identical to "on SiOx spin coating"), or when there was a pattern, only very few of the thinner regions of the films (figure 3.26 c) showed a pattern indicative of a morphology similar to "on SiOx spin coating".

The presence of these thick deposits was hypothesized to come from the effects of the vacuum from the spin coater chuck on which the Si₃N₄ membranes were deposited for coating, ie: by deforming the thin 75-100 nm thin Si₃N₄ window where the polymer solution could be trapped into a "puddle". However, even after attaching the ~200 µm thick Si₃N₄ wafer chip (with double-sided tape) onto a piece of Si prior to spin-coating, these "puddles" were still found, regardless of the polymer concentration or spin casting rates.

Figure 3.26 shows a montage of AFM images which shows typical morphologies of “successful films” (a, b, c) versus some of those that contained puddles of polymer deposits (d, e, f). The smaller domain sizes on figure 3.26 c) in comparison to figure 3.26 a) and b) is because the molecular weights used for c) were 100KDa:100KDa, as opposed to 1.1MDa:310KDa for a) and b). Even though the same molecular weights were used for a) and b), different domain sizes and morphologies resulted. The main reason for this is that different annealing cycles were used (b was found to be optimal for the PS:PMMA samples spun cast on SiOx, see figure 3.25). Also, it is possible that the film in a) also

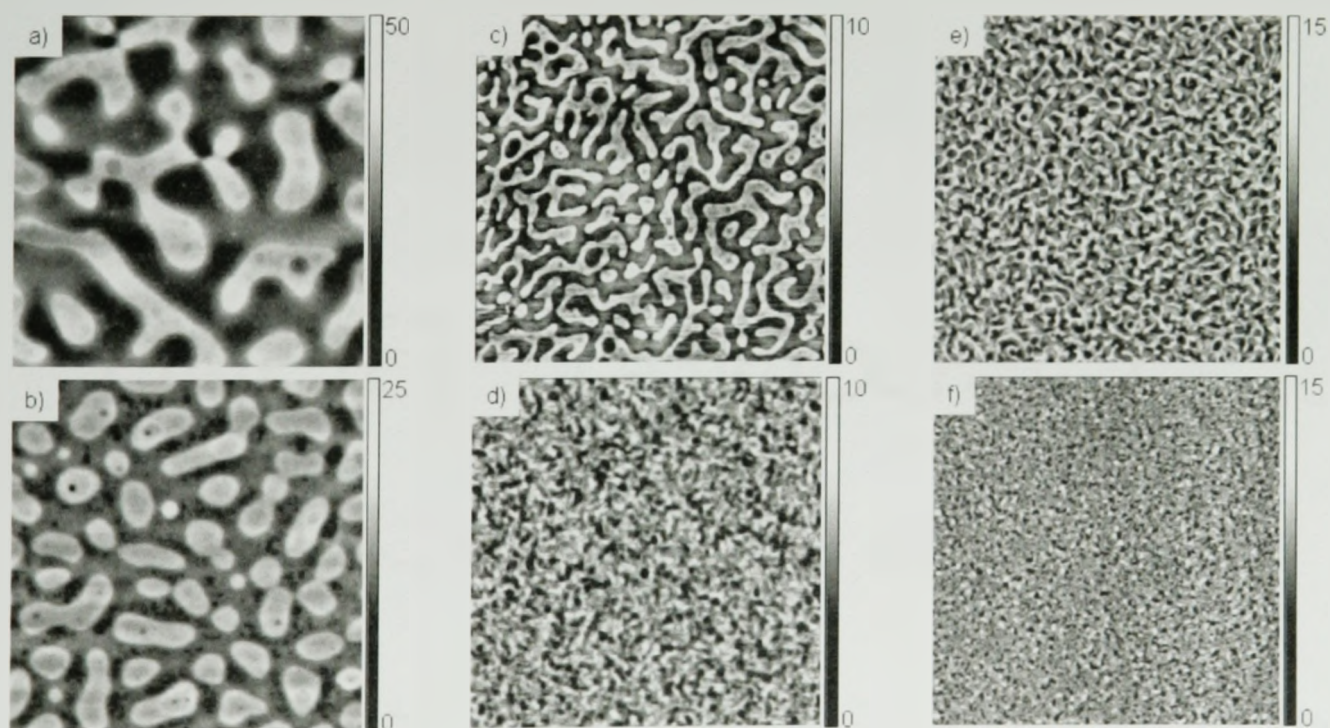


Figure 3.26 AFM images (non-contact mode, height, 10 μm x 10 μm) of 30:70 PS:PMMA films in toluene, 1%, spun cast at 4000 rpm: a) 1.1M:317K on Au/Si₃N₄, annealed 2 hours at 140°C (October 2000); b) 1.1M:317K on mica floated on Si₃N₄, annealed 8 hours at 160°C (April 2003); c) 100K:100K on thin region of 250 μm wide Si₃N₄ window, annealed 2 hours at 140°C (January 2002); d) 100K:100K on thick region of 250 μm wide Si₃N₄ window, annealed 2 hours at 140°C (January 2002); e) 100K:100K on thin region of 2 mm wide Si₃N₄ window, annealed 2 hours at 140°C (January 2002); f) 100K:100K on wafer off of 2 mm wide Si₃N₄ window, annealed 2 hours at 140°C (January 2002).

suffered from deformation of the Si_3N_4 window.

For these reasons, and because other experiments at the ALS took priority over this, the preparation of thin PS:PMMA films on Si_3N_4 was abandoned until April 2003, when help from Dr. Dalnoki-Veress' group was offered.

§ 3.4.4 Protein adsorption methods for STXM and X-PEEM samples

The proteins used in this work, and their origin, are detailed in publications of chapters 5 (Fg on PS:PMMA) and 6 (human serum albumin (HSA) and fibrinogen (Fg) on polyurethane microtomed sections). The methods used to adsorb these proteins to the substrates are different depending on whether the sample is to be measured in STXM or X-PEEM. Figure 3.27 is a schematic representation of the methods used for both types of samples.

In X-PEEM, for the results shown in chapter 6, the Fg/PS:PMMA samples were prepared by 10 min incubation of the PS:PMMA substrate in ~2 ml of Fg solution contained in a Fisher multi-well plate (1 cm diameter wells), followed by continuous dilution of the overlayer solution with running deionized water for ~3–5 min. The Fg/PS:PMMA substrate was then removed from the well. This rinsing method was used to avoid depositing protein or buffer salts from the air–solution interface.

In STXM, because the detected signal comes from the transmitted photons through the full thickness of the film, the sample cannot be immersed into a protein solution. Instead, a small drop of protein solution is deposited on the polymer surface and the sample is kept in a humid environment. At the end of the adsorption time, the

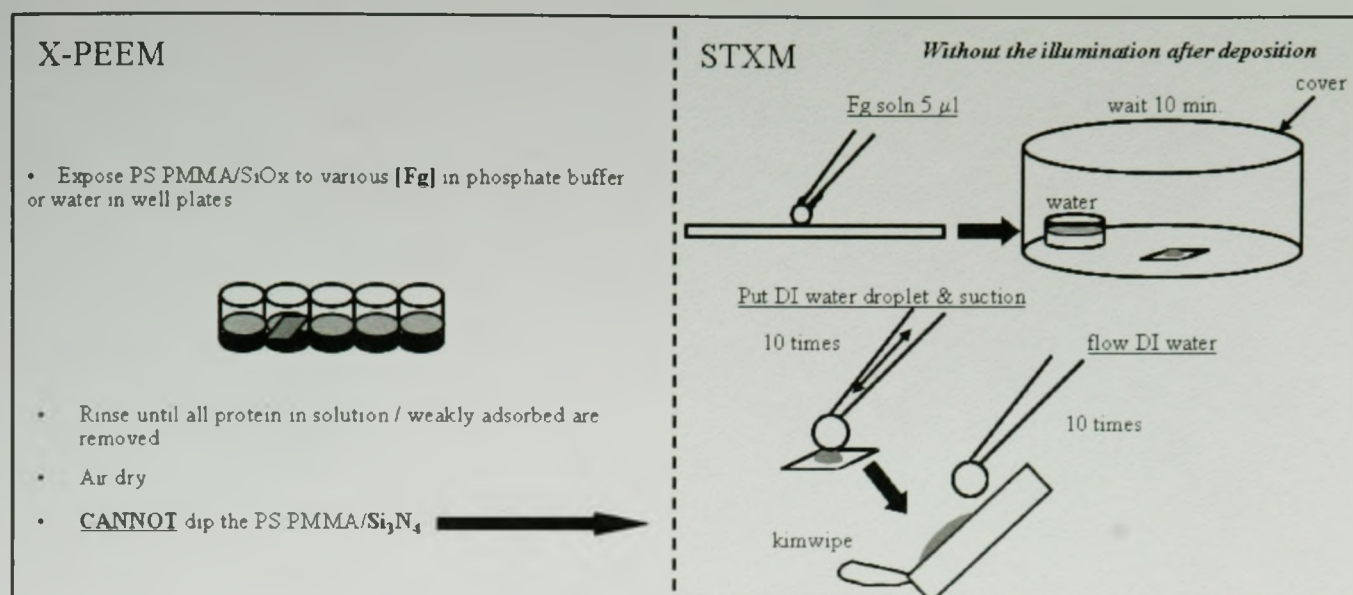


Figure 3.27 Schematic representations of the protein adsorption procedures for X-PEEM and STXM samples.

remaining portion of protein solution on the sample is rinsed by sucking in and out the drop with fresh volumes of deionized water. On pages 924-925 of the publication in chapter 6, deviations from this method are noted.

Chapter 4

X-RAY SPECTROMICROSCOPY OF IMMISCIBLE POLYMER BLENDS: POLYSTYRENE/POLY(METHYL METHACRYLATE)

This chapter consists of a publication which is a three-instrumental methods comparison of PS:PMMA thin films: X-ray spectromicroscopy of immiscible polymer blends: polystyrene–poly (methyl methacrylate). This work has been published in the Journal of Electron Spectroscopy and Related Phenomena (J. Electron Spectrosc. 121 (2001) 203-794) and is presented here in published form. The contributions from the author of this thesis were detailed in the introduction.



24 September 2004

Our Ref: HG/jj/Sept04/J445

Your Ref:

Cynthia Morin
McMaster University/Chemistry Department
1280 Main Street West
Hamilton, Ontario
Canada L8S 4M1

Dear Cynthia Morin

JOURNAL OF ELECTRON SPECTROSCOPY & RELATED PHENOMENA, Vol 121, No 1-3, 2001, pp 203-224, Morin et al: "X-ray spectromicroscopy of ..."

As per your letter dated 23 September 2004, we hereby grant you permission to reprint the aforementioned material at no charge **in your thesis** subject to the following conditions:

1. If any part of the material to be used (for example, figures) has appeared in our publication with credit or acknowledgement to another source, permission must also be sought from that source. If such permission is not obtained then that material may not be included in your publication/copies.
2. Suitable acknowledgment to the source must be made, either as a footnote or in a reference list at the end of your publication, as follows:

"Reprinted from Publication title, Vol number, Author(s), Title of article, Pages No., Copyright (Year), with permission from Elsevier".
3. Reproduction of this material is confined to the purpose for which permission is hereby given.
4. This permission is granted for non-exclusive world **English** rights only. For other languages please reapply separately for each one required. Permission excludes use in an electronic form. Should you have a specific electronic project in mind please reapply for permission.
5. This includes permission for the National Library of Canada to supply single copies, on demand, of the complete thesis. Should your thesis be published commercially, please reapply for permission.

Yours sincerely

Helen Gainford
Rights Manager

Your future requests will be handled more quickly if you complete the online form at www.elsevier.com/wps/find/obtainpermissionform.cws_home/obtainpermissionform

The following pages have been removed.
Please use the citation below to access them.

Morin C, Ikeura-Sekiguchi H, Tylliszczak T,
Cornelius R, Brash J, Hitchcock A, Scholl A, Nolting F,
Appel G, Winesett D, Kaznatcheyev K, Ade H. 2001.

X-ray spectromicroscopy of immiscible polymer blends:
polystyrene-poly(methyl methacrylate). Journal of
Electron Spectroscopy and Related Phenomena.
121(1-3): 203-224.



ELSEVIER

Journal of Electron Spectroscopy and Related Phenomena 121 (2001) 203–224

**JOURNAL OF
ELECTRON SPECTROSCOPY**
and Related Phenomena

www.elsevier.com/locate/elspec

X-ray spectromicroscopy of immiscible polymer blends: polystyrene–poly(methyl methacrylate)

C. Morin^a, H. Ikeura-Sekiguchi^a, T. Tyliczszak^a, R. Cornelius^a, J.L. Brash^a,
A.P. Hitchcock^{a,*}, A. Scholl^b, F. Nolting^b, G. Appel^c, D.A. Winesett^c, K. Kaznachejev^c,
H. Ade^c

^a*BIMR, Department of Chemistry, McMaster University, 1280 Main St. W., Hamilton, Ont., Canada L8S 4M1*

^b*Advanced Light Source, Berkeley Laboratory, Berkeley, CA 94720, USA*

^c*Department of Physics, North Carolina State University, Raleigh, NC 27695, USA*

Received 5 February 2001; received in revised form 6 April 2001; accepted 9 April 2001

Abstract

Spun cast thin films of blends of low and high molecular weight mono-disperse polystyrene (PS) and poly(methyl methacrylate) (PMMA) with nominal compositions ranging from 66/33 wt.%/wt.% (w/w) up to 10/90 w/w PS/PMMA have been studied, as-made and after annealing. Two synchrotron-based X-ray microscopies — scanning transmission X-ray microscopy (STXM) and X-ray photoemission electron microscopy (X-PEEM) — as well as several variants of atomic force microscopy (AFM) were used to probe the composition and morphology of the bulk and surface of these blends. The chemical sensitivities and spatial resolutions of these three techniques are compared. All samples are observed to have a PS signal in the C 1s X-ray absorption spectrum of the surface of the PMMA-rich domains as measured in the X-PEEM. A continuous thin PS layer is not expected at a PMMA surface since neither polymer should wet the other at thermodynamic equilibrium. The likely origin of this PS surface signal is from a bimodal distribution of PS domain sizes with the PS signal arising from domains at the surface which are smaller than the ~200-nm resolution of the X-PEEM. High resolution AFM and STXM provide direct evidence for this explanation. © 2001 Elsevier Science B.V. All rights reserved.

Keywords: Soft x-ray microscopy; NEXAFS; DS; PMMA; Polymer blends; Phase segregation; Quantitative chemical mapping

1. Introduction

Polystyrene (PS) and poly(methyl methacrylate) (PMMA) are immiscible polymers which readily phase separate in the bulk [1]. Typical annealing temperatures correspond to a deep quench into the two phase region of the phase diagram. The phases

in even low molecular weight (MW) blends are nearly pure at temperatures below 200°C, e.g. PS and PMMA with MW=21K each have >99.5% pure phases at 165°C [1]. Since the interfacial tension between the polymers is larger than the difference in their surface tensions [2], it is expected that the two materials will have a strong tendency to extend the bulk phase segregation right to the surface. Indeed dewetting studies indicate that neither polymer is able to wet the other polymer [3]. PS/PMMA blends and copolymers are classic model systems for poly-

*Corresponding author. Tel.: +1-905-5259-1450; fax: +1-905-521-2773.

E-mail address: aph@mcmaster.ca (A.P. Hitchcock).

mer phase segregation studies, but they also have direct technological relevance. The bulk and surface immiscibility is important in nanoscale patterning. For example, thin films of PS-*b*-PMMA diblock copolymers are currently being investigated for possible use in the fabrication of high density magnetic storage media [4], while phase separated PS/PMMA blend thin films have been proposed as antireflection coatings [5]. This work was initiated as part of a biomaterials study for which we required flat, thin films of PS/PMMA blends with a surface consisting of pure PS and pure PMMA in adjacent micron-scale domains, to be used as substrates for competitive protein adsorption studies. To aid development of these substrates, we are using two types of soft X-ray microscopy, scanning transmission X-ray microscopy (STXM) and X-ray photoemission electron microscopy (X-PEEM), as well as atomic force microscopy (AFM), to investigate aspects of morphology formation and evolution in PS/PMMA polymer thin film blends. The near edge X-ray absorption fine structure (NEXAFS) [6] spectra of PS and PMMA are very different, which make this a relatively convenient polymer system to study with NEXAFS microscopy.

Heterogeneous PS/PMMA polymer thin films are typically formed from a homogeneous solution by spin casting, followed by thermal annealing. The kinetics and mechanisms of the phase separation process in the thin film; surface roughening; and the relationship between equilibrium morphology and the fabrication and materials parameters are of considerable academic and technological interest. During the initial stages of the spin casting process most of the solution is cast off leaving a thin layer on the substrate. As the layer thins due to fluid flow, the evaporation of the solvent becomes important. The effect of evaporation is to increase the concentration of the polymer in the solution. This slows the shear thinning of the film. Phase separation of the polymers can occur in the presence of the increasingly lower concentration of solvent and a wide range of initial morphologies have been observed in numerous studies of PS/PMMA thin films [3,5,7–13]. Morphologies can be produced in which one phase is encapsulated in the other with either PMMA or PS as the matrix phase, or as primarily bilayers with either PS or PMMA exposed at the surface interface. The

morphology adopted depends on the solvent, surface, and spin-casting parameters (T , spin rate, volume, concentration . . .) and subsequent annealing. The following bullet list itemizes and briefly describes the factors which play a role in determining the initial morphology of the as-formed film, the kinetics and mechanism of its thermal evolution, and the final equilibrium morphology.

- Molecular weight (MW) of the polymers. Differential solidification rates can lead to stratification and different matrix formation during spinning; longer chains will be less mobile and metastable structures may be more important during annealing. Above a critical molecular weight, the viscosity of polymers scales with $MW^{3.4}$ [1].
- Polydispersity ($\delta = M_w/M_n$ where M_w and M_n are the weight and number averaged MW, respectively). This has a complex influence and should be kept as close to 1 as possible (i.e. monodisperse).
- Composition ratio. In bulk materials, the majority component has a tendency to form a continuous matrix phase. In thin films, the interface and surface energies need to be considered [14].
- Substrate surface energy. This can vary dramatically depending on the substrate used and has a strong effect on morphology, especially for very thin films (<100 nm) [9]. In general one would expect vertical segregation of the components within a blend film with that component with the greater affinity for the substrate being more prevalent at the substrate interface.
- Choice of solvent. This affects evaporation characteristics and relative solubility, both of which can lead to inhomogeneous vertical or even lateral distributions of components in spun-cast polymer blend films [9].
- Temperature of substrate during spin casting. This affects solubility of polymers and the evaporation rate of solvent.
- Spinning rate. This mainly affects film thickness, although losses by preferential evaporation or solubility could be affected by rate of flow across the surface.
- Annealing procedure. Temperatures above the glass transition temperature (T_g) are required for the polymer chains to become mobile. The time

required to approach equilibrium increases at higher MW and equilibrium may never be achieved (in a human time scale at least) for sufficiently high MW systems. The kinetics of polymer phase transformations are linked to MW, film thickness, and possibly the annealing atmosphere.

- **Impurities.** These may act as surfactants or compatibilizers, thus changing the intrinsic phase separation processes of a given film.

PS prefers hydrophobic substrates such as H-terminated Si, whereas PMMA prefers hydrophilic substrates such as the Si–O and Si–OH terminated native oxide layer of a Si wafer (denoted SiO_x). Thus, when thin films of PS/PMMA are deposited on a Si wafer with a native oxide surface, we expect the PMMA tends to segregate to the substrate. This preference exerts its influence both during spin casting, and even more so during annealing. Tanaka et al. [8] examined PS/PMMA films up to 25 μm thick spun cast from toluene (PS: MW=90K, δ=1.05; PMMA: MW=69K, δ=1.06) on silicon, gold and a siliconized substrate. They found considerable dependence of the phase segregation morphology and surface composition on the substrate as well as the film thickness. Walheim et al. [9] investigated PS/PMMA blends spun from toluene, tetrahydrofuran, and methyl ethyl ketone onto SiO_x, Au, and a low surface energy organic monolayer. Winesett et al. [10] have also investigated the effect of different substrates (Si, Au and Co) on PS/PMMA morphologies and their annealing behavior. In all studies, the type of substrate and solvent utilized had a pronounced effect on the as-cast morphology. For PS and PMMA, the balance of surface attractiveness can be controlled carefully and neutral surfaces can be created and selectively tuned with the use of random PS-*r*-PMMA copolymer brushes [14].

The air interface composition and morphology appear to be equally complex and might furthermore be dependent on the polymer substrate interaction in ultra thin films (<100 nm). During spin casting either polymer can separate preferentially to the air interface. This is primarily a function of the solvent and molecular weight utilized [9]. Tanaka et al. [8] reported a continuous surface layer of PS in 25-μm thick PS/PMMA films spun cast from toluene (PS:

MW=90K, δ=1.05; PMMA: MW=69K, δ=1.06), but noted that a mixed surface results for films of 100 nm or smaller thickness. Thon-That et al. [11,12] have explored the surface morphologies of PS/PMMA blend films spun cast from chloroform solution onto mica. In contrast to the observations of Tanaka et al. [8], the as-cast films studied by AFM and XPS by Thon-That et al. [11,12] have a PMMA enriched surface. On Au surfaces, Walheim et al. [9] have found PS surface enrichment for toluene and tetrahydrofuran (better solvents for PS than for PMMA), but a surface layer of PMMA for methyl-ethyl ketone, which is a poor solvent for PS. Almost a complete bilayer with PMMA on top was observed when PS/PMMA was cast from methyl-ethyl ketone on a low surface energy organic monolayer [9]. The evidence to date suggests that the surface composition of as-cast films is not so much dominated by a 'segregation' or preference of one polymer to the surface, as by the strong preference of one polymer for the substrate as well as the relative solubility of the two polymers in the chosen solvent.

During annealing, the blends should evolve towards thermodynamic equilibrium. The surface tension of pure PS and pure PMMA is almost the same. According to Wu [2], 3K PMMA and 44K PS have surface tensions of $\gamma_{\text{PMMA}} = 41.1$ dyn/cm and $\gamma_{\text{PS}} = 40.7$ dyn/cm at 20°C, while $\gamma_{\text{PMMA}} = 32.0$ dyn/cm and $\gamma_{\text{PS}} = 32.1$ dyn/cm at 140°C. This suggests there should be very little thermodynamic driving force for surface segregation at annealing temperatures above 135°C, temperatures typically used as they are well above the glass transition temperature of both polymers ($T_g(\text{PS}) \sim 110^\circ\text{C}$, $T_g(\text{PMMA}) \sim 120^\circ\text{C}$ for the MWs used [1]), yet deep within the two phase region of the phase diagram. Hence, the interfacial energy may be more important in establishing the surface morphology than the surface energies themselves, and the systems try to minimize interfacial area rather than the surface area of a particular polymer. Wu [2] calculated the interfacial tension (γ_{AB}) and spreading parameters $\{S = \gamma_{\text{B}} - (\gamma_{\text{A}} + \gamma_{\text{AB}})\}$ for PS and PMMA as a function of temperature (γ_{A} and γ_{B} are the surface free energies (surface tensions) of A and B, respectively, and γ_{AB} is the A–B interfacial energy). The interfacial tension for 44K PS and 3K PMMA [2] is 3.2 dyn/cm at 20°C and 1.7 dyn/cm at 140°C. A dewets B for a negative spreading param-

ter. Since the interfacial tension γ_{AB} is larger than the absolute value of the surface tension difference over the entire temperature range considered ($|\gamma_{PS} - \gamma_{PMMA}| < 0.8$ dyn/cm), the spreading parameter, S , is negative for all annealing temperatures, irrespective of whether PS (or PMMA) is phase A or phase B. Thus neither polymer should wet the other polymer. Since γ_{AB} increases with increasing MW, S should be even more negative for the higher MW polymers which are typically used in many experiments.

Some experiments seem to directly confirm the implications of the spreading parameter as calculated by Wu [2]. In an investigation of a 28-nm thick PS film floated on top of a 90-nm PMMA film cast on Si, Qu et al. [3] found that PS dewets PMMA. The PMMA films were spun cast from toluene onto Si wafers and annealed at 160°C in vacuum to remove any solvent. Because various MW were used, the thickness was maintained at ~90 nm by varying the polymer concentration. The PS films were spun cast on Si, then these as-made films were floated on water, then transferred on top of the PMMA film. The bilayers were annealed at 162°C to initiate dewetting. As the annealing time was increased, increasingly larger holes formed in the PS layer.

Kumacheva et al. [15] used confocal fluorescent microscopy to study a 90:10 (w/w) PS/PMMA blend, prepared by a very slow and controlled evaporation of a 4 wt.% toluene solution (PS: MW = 234K, $\delta = 6.3$; PMMA: MW = 306K, $\delta = 2.3$). This preparation, which has many factors different from those involved in spin coating, resulted in 135-nm thick PMMA lenses on top of a PMMA-depleted PS subsurface layer, and regularly distributed PMMA dispersions in a PS matrix further away from the surface.

Ade et al. [16,17] characterized films of 50:50 (w/w) PS/PMMA blends spun cast from toluene onto Si substrates with a native oxide layer (PS: MW = 27K, $\delta = 1.05$; PMMA: MW = 27K, $\delta = 1.10$). The 140-nm thick films were annealed at 180°C for varying times. In this case, the equilibrium system consisted of a PMMA matrix and substrate interface layer which supported PS droplets within a rim of PMMA.

In contrast to all of the above results, Thon-That et al. [11,12] concluded from angle resolved XPS data

that PS/PMMA blend films develop a PS film on top of the PMMA rich domains during annealing. The results on PS/PMMA blend films described below indicate that there are finely dispersed PS domains on top of the PMMA domains. With insufficient spatial resolution, this PS dispersion could be mistaken as a thin PS film. Other recent studies of the surface structure of polymer thin film blends include those of PS/poly(vinyl methyl ether) [18], PS/poly-(bromo-styrene) [13,19] and PS/poly(*n*-butyl methacrylate) [20]. On the silicon substrates used, PS encapsulates poly(vinyl methyl ether) [18] and poly-(bromo-styrene) [17] unless the films are too thin [13], while poly(*n*-butyl methacrylate) encapsulates PS [19].

While much of the literature is consistent, there are some apparently conflicting observations in the literature for materials which deal with the phase segregation phenomena in this or similar systems. This is probably because there are many different parameters playing a role in thin film polymer blend morphology and phase separation phenomena. Thus the actual film that results is quite dependent on the exact details of the formulation, surface composition, and annealing protocol. In order to better understand polymer blend morphology and surface properties, one needs to apply experimental techniques with good spatial resolution, high chemical sensitivity, and variable depth sensitivity to carefully selected and prepared polymer blend systems. While there are many experimental techniques to visualize morphologies of thin films of polymer blends, very few are able to provide quantitative chemical analysis at high spatial resolution, and fewer still which can examine the surface with an appropriate sampling depth. For bulk structure studies, transmission electron microscopy (TEM) has the highest spatial resolution, and in principle one can obtain chemical sensitivity through selective staining or by electron energy loss spectroscopy. However staining may introduce artefacts, and radiation damage in many polymer systems is too rapid to achieve the quality of energy loss signal needed for chemical analysis at high spatial resolution. Atomic force microscopy (AFM) is excellent for surface visualization and provides indirect chemical sensitivity through phase mode or adhesion force measurements. However it does not provide direct chemical identification and it

is extremely sensitive to the outermost layer, which in polymer systems may be unrepresentative of the relevant near-surface region due to low MW contamination. Soft X-ray spectromicroscopy (also known as NEXAFS microscopy) [21–23], in a number of variants, provides a powerful complement to TEM and AFM. In NEXAFS microscopy, inner-shell electronic excitation is used as a chemically sensitive image contrast mechanism. Scanning transmission X-ray microscopy (STXM) measures the absorption through a thin film and thus is a bulk technique. X-ray photoelectron emission microscopy (X-PEEM) measures the absorption indirectly by detecting photo-ejected electrons, and is a near-surface technique (10–15 nm estimated sampling depth). Both STXM and X-PEEM are finding increasing use in the analysis of complex polymer systems, on account of their ability to perform chemical mapping at a relevant spatial scale. In both techniques NEXAFS spectra can be acquired on a small region down to the spatial resolution limit of the instrument ('microspectroscopy'), and images can be acquired at photon energies selected for their chemical sensitivity ('analytical microscopy'). In many recent applications the full power of the combined spatial–spectral domain is exploited by automated acquisition of image sequences, which produce a three-dimensional data set which can be analyzed to extract extensive chemical information from the region studied ('spectromicroscopy'). Efficient acquisition [24] and data analysis procedures [25,26] are under active development. We refer the reader to recent reviews for full details of the rapidly growing field of soft X-ray spectromicroscopy and its applications to biology [21] and polymer science [22,23].

Here we describe some of our own recent studies on PS/PMMA thin film blends. The goal has been the preparation of samples which are fully phase segregated at the surface and which have domain sizes larger than 0.3 μm . Such samples are of interest for biomaterials-related studies of competitive protein adsorption on a surface with hydrophilic and hydrophobic domains [27]. For this we have used PMMA-rich blends made from high MW components. Some of us (Ade) had previously studied a variety of relatively low molecular weight PS/PMMA thin films with NEXAFS microscopy

techniques [16,17]. The combination of the prior low molecular weight studies and the present high molecular weight studies, carried out over a range of compositions and with various sample preparation conditions, has provided a relatively coarse sampling of the available parameter space. Although the bulk had the expected phase segregated morphology, both high MW and low MW blends were found to have a measurable PS signal in the NEXAFS spectra from regions of the presumed pure PMMA domains and, at least according to the X-PEEM results, pure PMMA could not be exposed at the surface under any of the annealing conditions employed. A main goal of this paper is to explain this initially puzzling observation, which is in apparent contradiction to the general understanding that PS on top of PMMA will dewet, and thus should consist of pure PS and PMMA domains at the surface.

To clarify some issues raised by these results, new blends prepared from low molecular weight PS and PMMA were also studied. Given the many parameters that influence morphologies in PS/PMMA thin films, perhaps it is not surprising that the various PS/PMMA polymer blends we have investigated in this study exhibit a variety of different surface and bulk morphologies. Our intent here is to use these results (i) as an illustration of X-ray microscopy as a complementary tool to AFM for studies of phase segregation phenomena in polymer thin films, and (ii) to identify the approaches which might allow preparation of fully surface differentiated PS/PMMA surfaces which we are seeking as substrates for competitive protein adsorption studies.

2. Experimental

2.1. Sample preparation

All high molecular weight polymers used for these studies were obtained from Polymer Source and used without further purification. The 66/33 (w/w) PS/PMMA sample (PS: MW=2.2M, $\delta=1.1$; PMMA: MW=150K, $\delta=1.1$) (w/w is wt.%/wt.%) was prepared by spin casting a 0.8% solution (total polymer in toluene). The details of the starting polymers and sample annealing are summarized in Table 1. A small volume of this solution ($\sim 50 \mu\text{l}$)

Table 1
Details of fabrication and AFM characterization of the PS/PMMA blend samples

Sample (PS/PMMA)	PS		PMMA		Spin casting (%) ^a	Vacuum anneal	Thickness (nm) ^b	rms Surface roughness (nm)
	MW	δ	MW	δ				
66/33	2.2M	<1.1	150K	<1.1	0.8	120°C, 55 h	32 (SiO ₂)	4.5
40/60	21K	1.02	22K	1.03	1.4	165°C, 24 h	50	–
50/50	27K	1.02	27K	1.03	1.4	180°C, 1 h	60	12
30/70	1.06M	1.06	312K	1.01	1	140°C, 2 h	61 (SiO ₂)	4
							82 (Si ₃ N ₄)	6
10/90	1.06M	1.06	312K	1.01	1	180°C, 30 min	5.8 (SiO ₂)	3.2

^a All spin casting was done from toluene solutions of the indicated total wt.% polymer.

^b Measured by AFM from height between the polymer surface and the bottom of an adjacent scratch, which exposed the substrate.

was passed through a teflon micropore filter to remove particulate impurities and dropped onto the spinning substrate at 4000 rpm. Spinning was continued for ~5 s. The 66/33 samples were vacuum annealed at 120°C for 55 h then cooled to 40°C over a period of 5 h. The 10/90 (on Si) and 30/70 PS/PMMA samples were made from a different set of polymers (PS: MW=1.07M, δ =1.06; PMMA: MW=312K, δ =1.01). Thin films of the 10/90 and 30/70 samples were spun cast from toluene (1% by weight solution) onto native oxide Si (for X-PEEM) and gold-coated Si₃N₄ membranes (for STXM). The 10/90 sample was vacuum annealed at 180°C for 2 h then cooled to 30°C over 8.5 h. The 30/70 samples were vacuum annealed at 140°C for 2 h, followed by slow cooling over 12 h. During annealing the samples were pumped continuously using an untrapped diffusion pump with silicone fluid. The samples were transferred to the microscope in air, in a protected enclosure.

The low molecular weight 40/60 w/w PS/PMMA samples were prepared by spin coating from toluene (1.4% solution) (PS: MW=21K, δ =1.02; PMMA: MW=22.65K, δ =1.03; Polymer Laboratories) on SiO₂ and annealing at 165°C for 24 h in a vacuum oven (<10⁻⁴ Torr), followed by a sudden quench to room temperature. For STXM investigations the low MW films were floated from the silicon substrate and mounted on TEM grids.

2.2. X-PEEM and STXM

Scanning transmission X-ray microscopy (STXM) was performed at beamline 7.0.1 of the Advanced Light Source (ALS) [28] and at the Stony Brook

instrument on X1A at the National Synchrotron Light Source (NSLS) [29–31]. The STXM optical layout is depicted in Fig. 1a. In STXM, a Fresnel zone plate (ZP) is used to focus monochromatic X-rays ($\Delta E \sim 0.15$ eV) to a small spot, which is 50 nm if the ZP is operated at the diffraction limit (coherent illumination). Images are acquired by raster scanning an X-ray translucent sample in the focal spot while detecting the flux of transmitted X-rays. The sample is in a He atmosphere. Spectra are obtained by successively stepping the X-ray energy through a spectral region while recording point, line, or image data. In the ALS studies, image sequences¹ have been used to provide detailed chemical mapping. At the NSLS, high resolution images at chemically sensitive energies were obtained. Fig. 1b plots the C 1s spectra of PS and PMMA on a quantitative linear absorption scale. These spectra were extracted from ALS STXM image sequences recorded on the 30/70 PS/PMMA sample (PS taken from the as-made, and PMMA taken from the annealed data set). The vertical scale was derived by normalization to computed linear absorption coefficients for PS and PMMA outside of the structured NEXAFS region, using the tabulated elemental X-ray absorption response [32] and the known bulk densities (PS = 1.05 g/cm³, PMMA = 1.19 g/cm³ [33]). For each species, prior to conversion to the quantitative linear absorption scale, a fraction of the other component has been subtracted since all regions of the bulk have some PS and some PMMA (the raw and subtracted

¹Examples of the STXM and X-PEEM image sequences for the annealed 30/70 sample have been deposited as supplementary material with the journal (WEB ACCESS details).

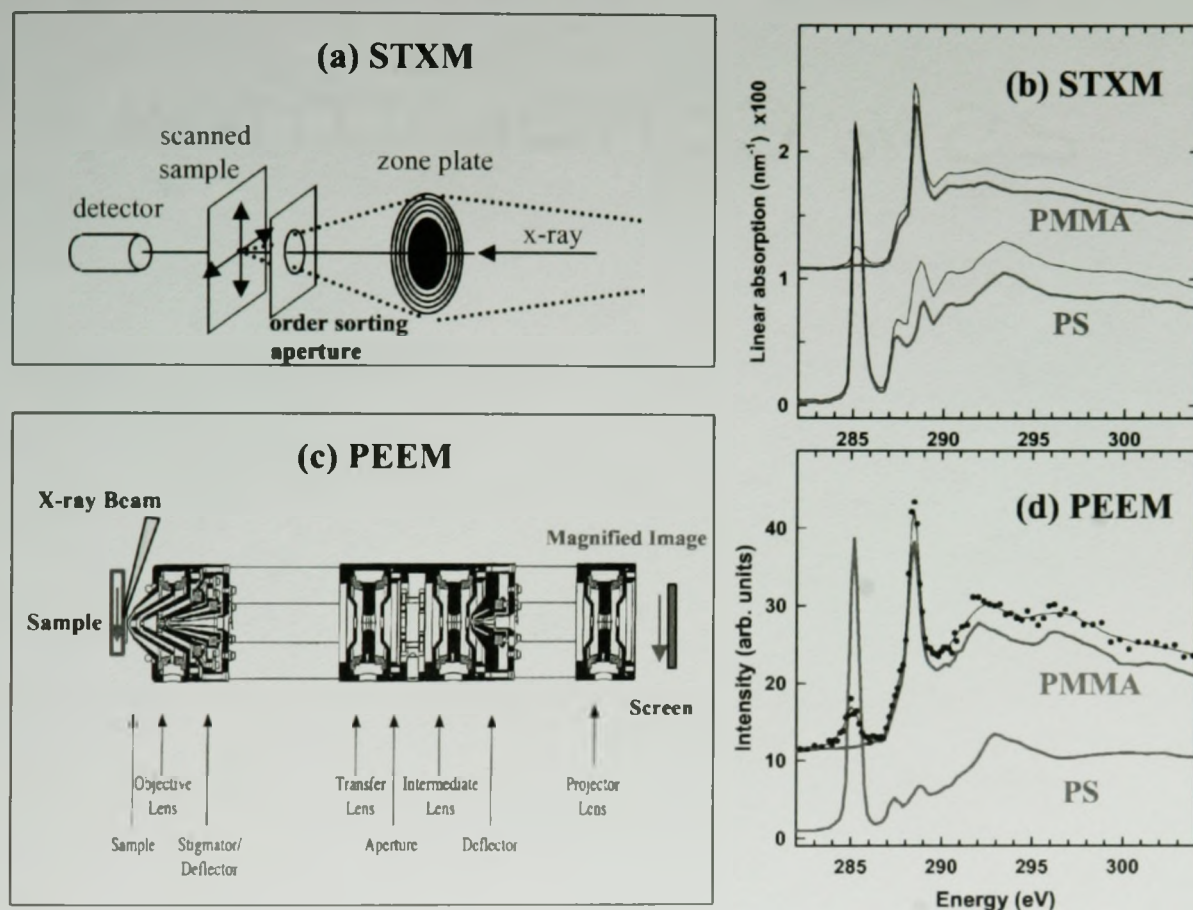


Fig. 1. (a) STXM optics. (b) C 1s NEXAFS spectra of PMMA and PS derived from STXM image sequences. The as-recorded spectra are indicated by the thin lines, while the estimated pure material response are the thick lines (see text). The measured OD intensities have been converted to linear absorption coefficient by normalization below 284 and above 300 eV to the linear absorption for pure PS and PMMA computed from elemental absorption parameters [32] and the known densities. (c) ALS X-PEEM optics. (d) C 1s NEXAFS spectra of PS and PMMA derived from X-PEEM image sequences. A portion of the PS signal has been subtracted from the PMMA signal to reduce the intensity of the 285-nm signal to baseline. In (b) and (d) the PMMA spectrum has been offset by 1 and 10 units, respectively.

spectra are shown in Fig. 1b). The amount removed was selected by requiring the resulting spectrum to have a shape similar to the spectra of pure PS and PMMA recorded with the NSLS STXM. In order to have the same energy point sampling and spectral resolution, we prefer to use the reference data taken from the same instrument as that used for a given study, even though these corrections are needed. The signal contrast in STXM arises exclusively from the X-ray absorption coefficient and the transmission signal, after conversion to optical density, provides accurate quantitation [22,23].

Surface sensitive X-ray microscopy was performed at the photoelectron emission microscope

(X-PEEM) on ALS beamline 7.3.1 [34]. The X-PEEM optical layout is depicted in Fig. 1c. Here, a $300 \times 30\text{-}\mu\text{m}$ spot impinges the sample surface at a 30° incident angle and the photo-ejected electron distribution is imaged using an electrostatic column. Polymer samples for X-PEEM must be ultra high vacuum compatible, flat, and sufficiently thin to provide enough conductivity to avoid extensive charging. The C 1s spectra of PS and PMMA extracted from X-PEEM image sequences recorded on the as-prepared 30/70 PS/PMMA sample are plotted in Fig. 1d. The PS spectrum is the as-recorded signal taken from regions where there is only PS in the sampling depth of the X-PEEM.

Because of the ubiquitous surface PS signal, a small amount of the PS spectrum has been subtracted from the as-recorded PMMA signal to get the PMMA reference spectrum used in further analyses. The raw data, and thus the amount of PS in this optimal PMMA region, is indicated in Fig. 1d. In contrast to STXM, the signal in X-PEEM is determined not only by X-ray absorption, but also by many other factors — topography, shadowing, work function, and charging. As a consequence, procedures for quantitative chemical analysis are much less developed for X-PEEM than for STXM. The vertical scales of the X-PEEM reference spectra are set by adjusting the difference in intensity at 308 and 280 eV to an arbitrary value of 10.

3. Results

3.1. High molecular weight PS/PMMA thin films

3.1.1. Bulk versus surface morphology

Although we present in detail only the results for 30/70 blends made from the high MW components,

similar results (not shown here) have been obtained for 90/10 and 66/33 PS/PMMA blends. For STXM the PS/PMMA blend was spun cast on a Au-coated X-ray transparent silicon nitride window, whereas for X-PEEM the substrate was a Si wafer, without removal of native oxide. Thus the surfaces relevant to preferential adhesion of the two components were SiO_x in the case of X-PEEM, and Au, in the case of STXM. From other work [8,10], it is known that SiO_x has a lower water contact angle than Au and thus it would be expected that the attraction for PMMA would be greater for the SiO_x surface than the Au surface. Other than the different substrate, the details of preparation of the STXM and X-PEEM samples are identical (solution composition, spin casting, annealing procedures). AFM was recorded from each type of sample.

Fig. 2 plots STXM and X-PEEM images of the annealed 30/70 PS/PMMA recorded at the $\pi^*_{\text{C}=\text{C}}$ transition in PS (285.1 eV), the $\pi^*_{\text{C}=\text{O}}$ transition in PMMA (288.4 eV), and in the C 1s continuum (300 eV). A common grey scale for these images (0–1.4 OD for STXM, 0–110 arbitrary units for X-PEEM) is used so that the image intensity reflects the actual

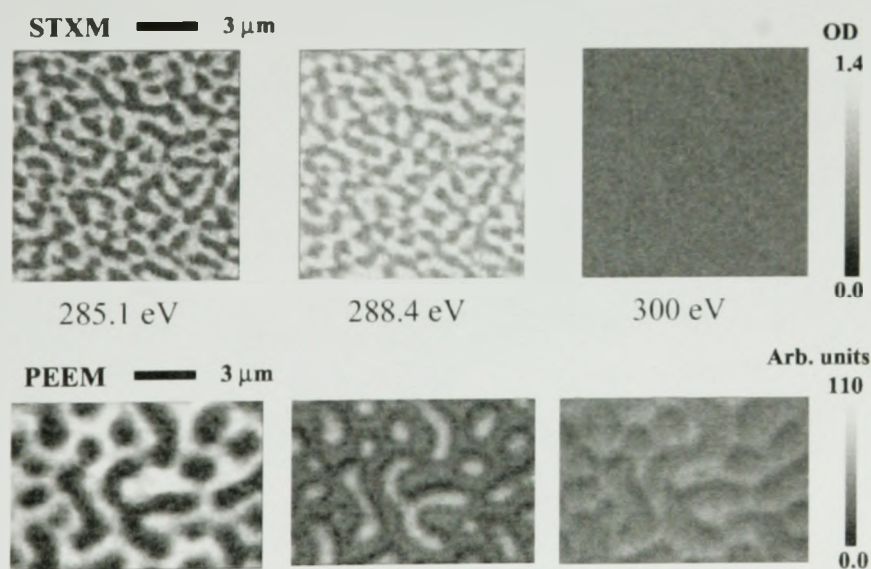


Fig. 2. STXM (upper) and X-PEEM (lower) images of annealed 30/70 (w/w) PS/PMMA recorded at 285.1, 288.4 and 300 eV. The images are presented on the same spatial scale. The sample for STXM was spun cast on Au-coated silicon nitride, while that for X-PEEM was spun cast on an oxidized silicon wafer. The STXM images are displayed in optical density using a common gray scale ($B=0$, $W=1.4$ OD units). The X-PEEM images have been normalized to incident flux (recorded independently from an HF-etched Si wafer) and are plotted on a common gray scale ($B=0$, $W=110$ arbitrary intensity units). In each case lighter pixels indicate stronger X-ray absorption (and/or, in case of X-PEEM, higher probability of electron emission). (ALS X-PEEM, ALS STXM).

signal level at each pixel at each energy. The spatial scale is identical in each of the images displayed in Fig. 2. The apparently finer scale of the microstructure in the STXM may reflect contributions of domains at different depths through the ~80-nm thin film. The sensitivity to the chemical identity through the complete contrast reversal between 285.1 and 288.4 eV is very clear. The PS domains are those regions which are bright at 285.1 eV and dark at 288.4 eV. The absence of contrast in the STXM image at 300 eV provides a useful constraint on the film structure. From atomic X-ray absorption factors [32], it is known that PS has ~60% larger optical density (OD) than PMMA at 300 eV ($OD(PS)/OD(PMMA)=1.62$ at 300 eV). Even for the annealed sample the PS and PMMA domains do not appear to extend completely through the film so each pixel has some admixture of PS and PMMA. Thus, in order for the contrast to disappear at 300 eV the difference in linear absorption coefficients has to be compensated by differences in the relative amounts of PMMA and PS.

Like the STXM results, the X-PEEM images at 285.1 and 288.4 eV have reversed contrast, clearly identifying the domains. The contrast at 288.4 eV is lower than that at 285.1 eV in both STXM and X-PEEM, since PS has strong absorption whereas PMMA has negligible absorption at 285.1 eV, while both PS and PMMA absorb at 288.4 eV. In contrast to STXM, the X-PEEM image at 300 eV has the same pattern as that at 285.1 eV (PS domains strong), although of lower contrast. The residual contrast in the X-PEEM image at 300 eV is notable, and again places important constraints on the film structure within the near surface region sampled. Another notable feature of the X-PEEM results is the existence of a shading at the boundaries of the light features in the 288.4- and 300-eV images which is absent in the 285-nm image. This may arise from sample topography in which case it would reflect an altered efficiency of electron collection from a sloped surface. However, the angle is actually rather shallow: from the AFM studies of this surface, the difference between high and low regions is only 10–20 nm, while the domains are more than 1 μm in size. Also, one would expect a topography derived signal to contribute at all photon energies. A more plausible origin is a contaminant which partially

segregates to the PS-PMMA interface. Two possibilities are siloxane (ubiquitous) or silicone (diffusion pump oil from the vacuum annealing). The detailed analysis of the NEXAFS spectrum from the shadow region is consistent with the presence of ~20% contamination in the surface region sampled by X-PEEM. A similar signal is also detectable at a few percent in the bulk STXM results (vide infra). The component maps for this contaminant signal indicate that it occurs over the whole surface, with greater amounts at the interfaces between the PS-rich and PMMA-rich domains. While clearly we would prefer to have uncontaminated samples (and are revising procedures to achieve this), the detection and mapping of this signal is a good example of how NEXAFS microscopy can probe sample details missed by chemically insensitive probes such as AFM.

Maps of the PS and PMMA bulk and surface domains were obtained by recording and analysing image sequences in both STXM and X-PEEM. Analysis using all of the images allows the full spectral variation to be used in deriving quantitative spatial distributions (maps) of the PS and PMMA components. A pixel-by-pixel linear regression procedure [26] was used to derive the component maps presented in the remainder of this manuscript. For STXM, where quantitative reference standards exist, this analysis provided a quantitative picture of the film structure. For X-PEEM, only a semi-quantitative picture of the near surface region is obtained.

Fig. 3 compares component maps derived from X-PEEM and STXM with AFM images for the annealed 30/70 PS/PMMA sample. Fig. 4 presents the PS and PMMA maps in comparison to AFM for the as-made 30/70 PS/PMMA sample. In each case, two height-mode AFM images are displayed, to check for sensitivity of the surface morphology to the type of substrate used. On both SiO_2 and $\text{Au/Si}_3\text{N}_4$ substrates the continuous phase in the AFM image has slightly larger area. The relative amounts, and the continuity, would suggest that the majority PMMA component is the continuous phase. In Figs. 3 and 4 the chemical analysis derived from the X-PEEM and STXM image sequences is presented as a single color-coded composite map while the maps of the individual PS and PMMA components of the annealed 30/70 PS/PMMA are presented in

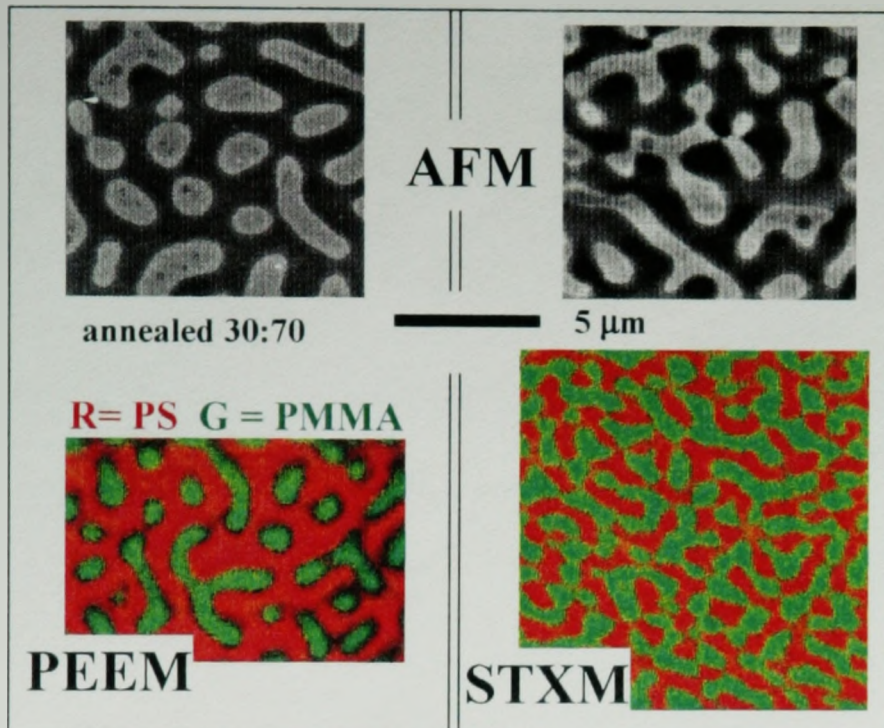


Fig. 3. Comparison of AFM, X-PEEM and STXM results for annealed 30/70 (w/w) PS/PMMA. The STXM was measured from a film spun cast on a Au-coated silicon nitride window, whereas the AFM and X-PEEM were recorded from the blend spun cast on a Si wafer covered with native oxide. The AFM height-mode images located above each X-ray micrograph are for samples prepared on the same substrate as the corresponding X-ray micrograph. Ex-situ vacuum annealing was carried out as indicated in Table 1. The X-PEEM and STXM are color coded composite images derived from the individual PS and PMMA component maps obtained by linear regression analysis of the C 1s spectrum at each pixel (Figs. 5 and 6). The color intensities in STXM are independently scaled to better represent spatial relationship, although at the cost of relative intensities. A third, impurity component was not included in this composite (see spectral fits in Figs. 7 and 8). The thickness of the sample was ~ 60 nm as determined by AFM from the step height at a scratch. (McMaster AFM, ALS X-PEEM, ALS STXM).

Fig. 5 for X-PEEM and in Fig. 6 for the STXM results. For both the annealed and as-made samples, the X-PEEM result clearly indicates that the continuous phase is predominantly PS. Thus X-ray microscopy shows immediately that a simplistic interpretation of the AFM — namely that the continuous phase is the majority PMMA species — is incorrect. In contrast to X-PEEM, the STXM images shows phases that are about equally continuous, with perhaps a small preference for PMMA domains to be encapsulated by PS domains. The value of the direct chemical sensitivity of NEXAFS microscopy to clarify the interpretation of AFM is well illustrated by this example. This has been noted in earlier comparisons of AFM and NEXAFS microscopy of polymers [13,17,19,20].

Table 2 summarizes the quantitative analysis of the surface and bulk composition of the as-made and annealed 30/70 blend. X-PEEM indicates that in each case, $\sim 2/3$ of the surface is PS-rich while $1/3$ of the surface is PMMA-rich, based on pixel counting, using a threshold of $\sim 50\%$ of full range intensity in each component map. This is consistent with the AFM which indicates $\sim 60\%$ of the surface is the continuous, PS domain. It is clear that the surface region of these samples is highly enriched in PS relative to the 30/70 w/w starting composition (note that a wt.%/wt.% of 30/70 corresponds to a mol.%/mol.% composition of 29/71 (mol/mol) and a vol.%/vol.% composition of 33/67 (v/v) so the units used to express the composition do not play a significant role in this system). In contrast, the

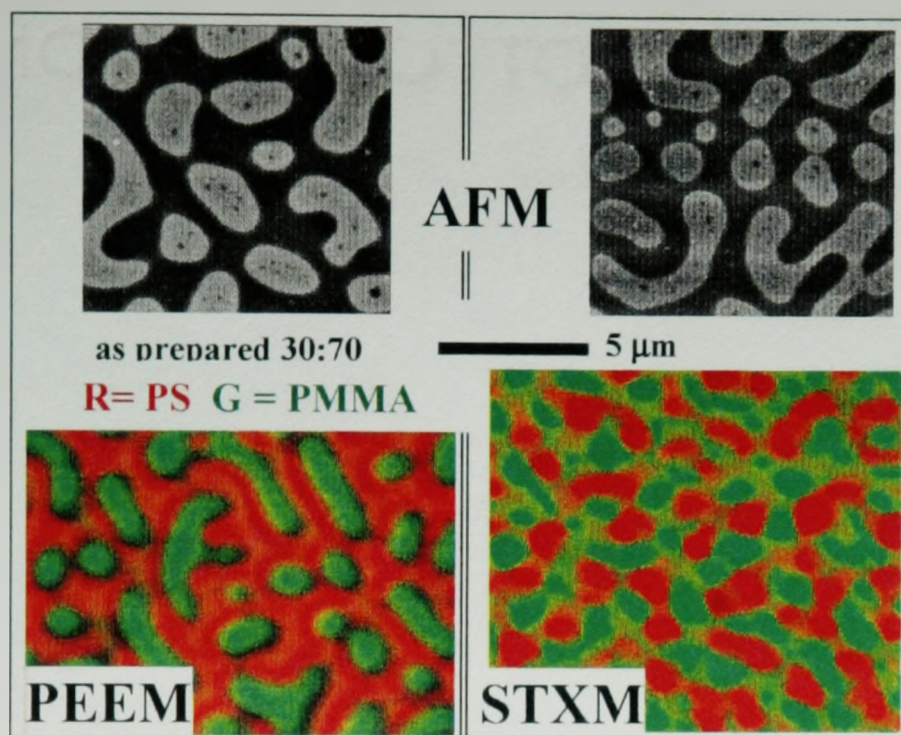


Fig. 4. Comparison of AFM, X-PEEM and STXM results for as-prepared 30/70 (w/w) PS/PMMA. Details as indicated in the caption of Fig. 3. (McMaster AFM, ALS X-PEEM, ALS STXM).

STXM analysis indicates a composition of 28(4)/72(4) PS/PMMA for the annealed sample, and 24(3)/76(4) PS/PMMA for the as-made sample. Both values are in good agreement with the starting composition suggesting that differential solubility did not modify the polymer composition through preferential loss in the spin cast process (only a small portion of the drop deposited forms the actual thin film, most of the polymer is flung off the substrate). The STXM quantitation is based on the average thickness of each domain type in the maps generated using the OD models. Both the X-PEEM — STXM comparison (Fig. 3), and the quantitative analysis of the annealed sample, indicate that, even after annealing, the surface structure does NOT extend through the full film but rather reflects some mechanism leading to an enrichment in PS at the surface of this sample. This could arise from depletion of PMMA due to a PMMA wetting layer on a SiO_2 surface, repeatedly observed in prior studies, that would enrich the surface in PS. Alternatively there could be

PS surface segregation as suggested by some [8,9]. A third possibility could be that the surface structure is the result of a kinetic factor and incomplete annealing.

The surface morphology of the as-prepared 30/70 PS/PMMA as revealed by AFM and X-PEEM is rather similar to that of the annealed sample (compare Figs. 3 and 4). In contrast, the STXM chemical map of the as-prepared 30/70 sample is qualitatively very different from that of the annealed sample. In particular, there are three main intensity levels in the STXM of the as-made sample. The bright regions are columns of mainly PS, the dark areas are columns of mainly PMMA, and the intermediate grey level indicates regions in the sample where both PS and PMMA are present in the column being sampled. Variable angle STXM tomography [35] would be required to determine unambiguously the three-dimensional relationship among the domains. Another difference is the presence in the as-prepared sample of many small domains of PS embedded in the

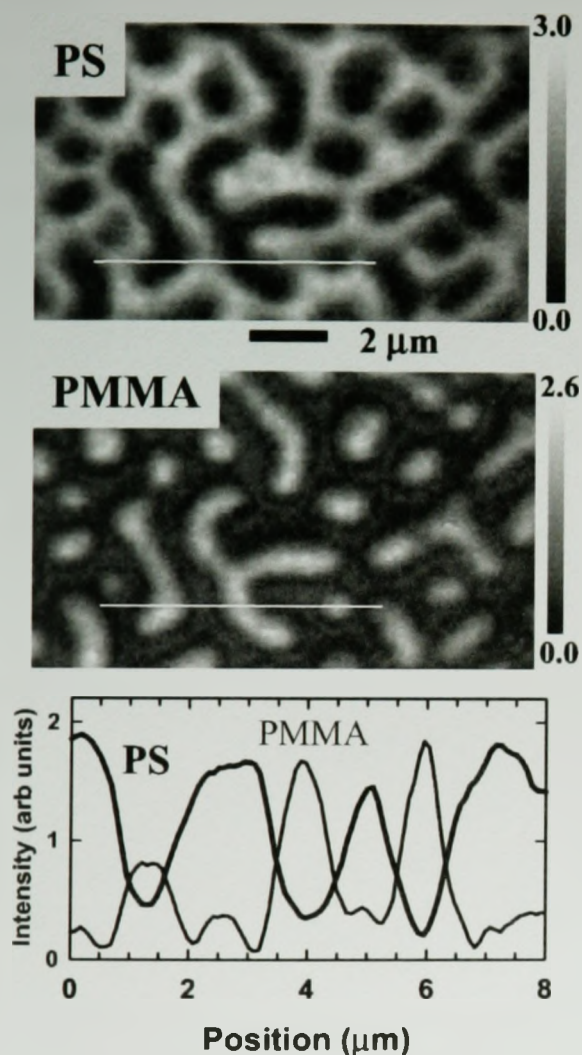


Fig. 5. PS and PMMA component maps derived from X-PEEM for annealed 30/70 (wt.%/wt.%) PS/PMMA. The vertical scales are in units of normalized response derived by setting the 300–282-nm intensity jump in the PS and PMMA reference spectra to 10. The lower plot is the intensity profile along the line indicated in the component maps. Note that the PMMA signal goes close to zero in the PS-rich regions but the PS-signal always is offset from zero. (ALS X-PEEM).

PMMA domains. In the AFM height mode image of the as-made sample, the PMMA domains (white) contain a large number of holes (likely small PS domains), which are absent in the AFM image of the annealed sample. Larger examples (>100 nm) of these embedded PS domains can be seen when the X-PEEM data is examined carefully. In the AFM

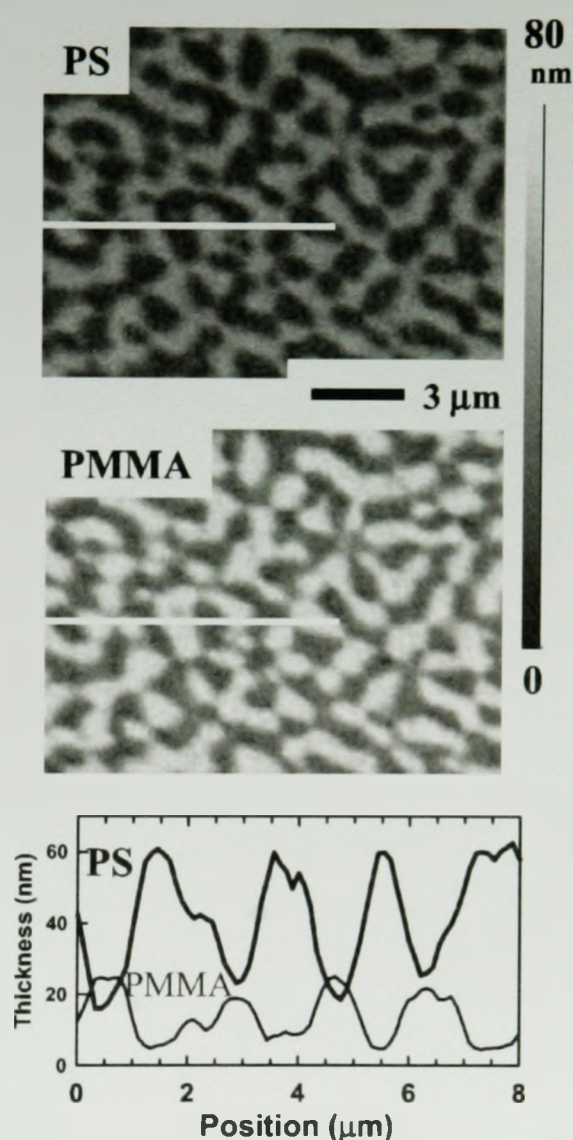


Fig. 6. PS and PMMA component maps derived from STXM for annealed 30/70 (w/w) PS/PMMA. The vertical scales are thickness in nm, derived by using the PS and PMMA reference spectra calibrated in linear absorption coefficient. The lower plot is the intensity profile along the line indicated in the component maps. (ALS X-STXM).

height image of the annealed 30/70 PS/PMMA sample (Fig. 3) there are some larger PS domains which appear to be coalesced versions of the smaller domains. In some cases shading in the AFM height image suggests these 'enclosed' PS domains lie below the surface.

Table 2

Composition of as-prepared and annealed bulk and surface of 30/70 PS/PMMA films as determined by STXM, X-PEEM and AFM

Sample	Anneal	STXM (vol.%/vol.%) ^a	X-PEEM (area/area) ^b	AFM (area/area) ^b
30/70 on Au	N	24(3)/76(4)	–	50/50
30/70 on Au	Y	28(4)/72(4)	–	60/40
30/70 on SiO ₂	N	–	62(5)/38(5)	56/44
30/70 on SiO ₂	Y	–	62(5)/38(5)	60/40

^a Based on the average thickness of component maps for the same area.^b Based on thresholding at a level that separates the X-PEEM or AFM maps into the two dominant domains, then counting pixels.

3.1.2. Surface composition analysis: origin of PS in PMMA domains

When the NEXAFS spectrum of PMMA-rich regions is extracted from X-PEEM image sequence data for the annealed 30/70 sample, a peak is invariably observed at 285 eV, suggesting there is PS in the surface (and possibly bulk) of the PMMA domains in the film. An example of this is presented in Fig. 7 which plots the average NEXAFS spectrum at selected pixels in PS-rich and PMMA-rich domains of the X-PEEM image, along with a spectral decomposition of the extracted spectra into PS and PMMA components. Assuming no work function effects, the spectral decomposition indicates ~12% of the NEXAFS signal comes from PS in the PMMA region. Note that the sampling depth in X-PEEM is sample dependent (due to different work functions and bulk electron transport properties), but probably of the order of 10–15 nm. Fig. 8 presents the C 1s spectra of the bulk of the PMMA domains of the annealed 30/70 PS/PMMA sample as measured by STXM. Relative to that found in the X-PEEM, there is less 285-eV signal in the STXM data and the shape is less well defined, suggesting possible impurity contributions, as well as some PS. Assuming all the 285-eV signal arises from PS, the amount (~7%) would be equivalent to a uniform ~5-nm thickness of PS over the PMMA domains, or to non-uniform PS domains with 7% volume fraction. The latter is consistent with unresolved small droplets of PS distributed throughout the PMMA domains. Note the ~80-nm film thickness determined from STXM quantitation is in good agreement with that of 80 nm measured by AFM from the jump at a scratch (see Table 1). A uniform thin layer of PS at the surface

would give a strongly enhanced signal in the X-PEEM relative to that seen in STXM, on account of the exponential decay of X-PEEM signals with sampling depth. Even if the sampling depth was 15 nm, a 5-nm thick PS surface layer would result in a much larger PS signal than that found in the X-PEEM analysis (Fig. 7). Since the as-cast film is very far from equilibrium and the high molecular weight PS used in the 30/70 sample can diffuse only slowly during the relatively shallow and short anneal, it is possible that a temporary PS enriched surface gradient layer develops as the PS moves to get out of the PMMA domains. Alternatively, on account of slow diffusion rates, and random break-up of PS domains, it is possible the PMMA domains could end up enclosing small, pure PS droplets.

Based on the STXM/PEEM quantitation and the AFM studies presented below, we believe that the 285-eV signal arises from very small PS domains in the PMMA domains. The size of these domains must be smaller than can be resolved by either X-PEEM (~200-nm spatial resolution) or STXM (~90-nm spatial resolution) but should be observable with AFM (~5 nm). Indeed, the AFM of the as-prepared 30/70 sample shows PS domains below 100 nm with a frequency corresponding to ~20% of the area of the large PMMA domain (Fig. 3), providing support for this interpretation. However these domains are less frequent in the AFM of the annealed 30/70 sample (Fig. 3), somewhat inconsistent with the observation of similar amounts of 285-eV signal in PMMA domains in X-PEEM of both the annealed and as-made samples. If the PS signal in the PMMA domains persists throughout the whole film, then one would expect the PS signal in PMMA domains to be

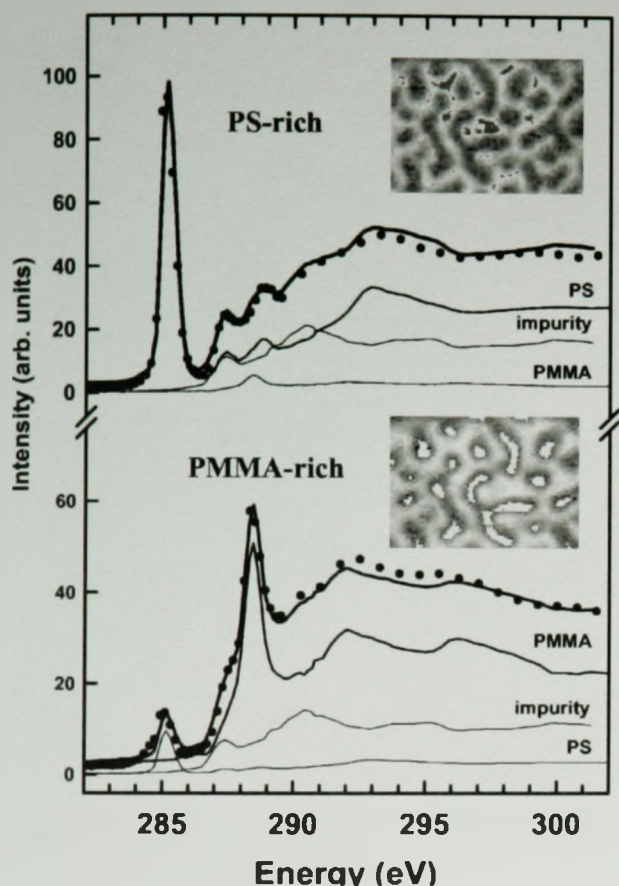


Fig. 7. Spectral decomposition of the C 1s spectra extracted from the PS-rich (2.5*PS, 1.5*impurity, 0.2*PMMA, where the reference spectra are jump-normalized) and PMMA-rich (0.25*PS, 1.0*impurity, 1.8*PMMA) domains of the near surface region of annealed 30/70 PS/PMMA measured by X-PEEM. The pixels contributing to the spectra are indicated in the insert images. In addition to a significant PS component in the PMMA domains and a small but detectable PMMA signal in the PS domains, the fit to the NEXAFS spectra indicates there is a third component ('impurity') at the surface with an aliphatic character. This could be a surface contaminant such as a siloxane or silicone from the preparation. (ALS X-PEEM).

of similar intensity in STXM and X-PEEM. The analysis of the NEXAFS spectra of PMMA domains in the annealed sample recorded by STXM shows that the PS signal averaged throughout the whole thickness of the PMMA domains is similar but somewhat smaller than at the surface, a maximum of 7% by STXM versus 12% by X-PEEM of PS in the PMMA domain spectrum (Figs. 7 and 8). Thus it is

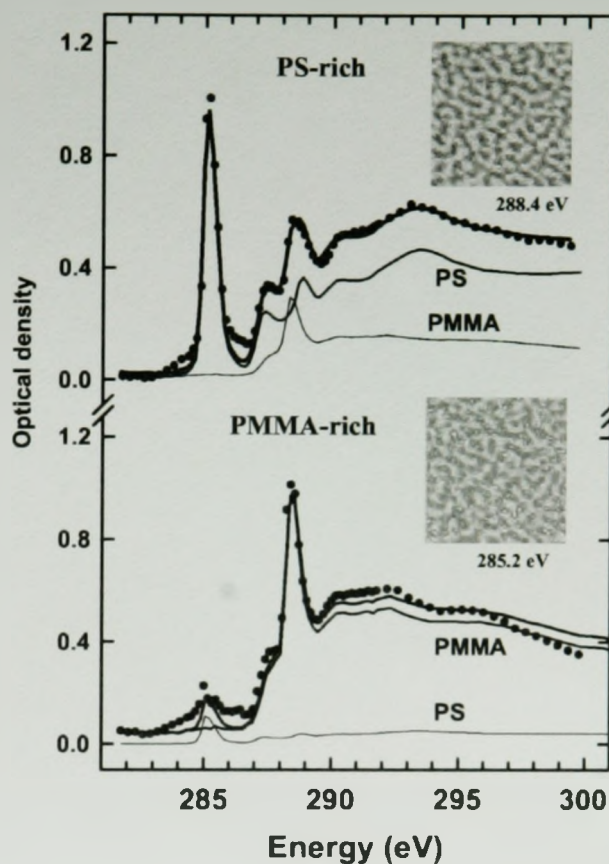


Fig. 8. Spectral decomposition of the C 1s spectra extracted from the PMMA-rich (45 nm PS, 22 nm PMMA) and PS-rich (5 nm PS, 72 nm PMMA) domains of the annealed 30/70 PS/PMMA measured by STXM. The component thicknesses were derived by extracting the sum of the spectra at the indicated pixels (black on upper image, and white on lower image) and fitting to the linear absorption coefficient reference spectra for pure PS and PMMA. The spectra could be fit satisfactorily using only the PS and PMMA components. (ALS STXM).

difficult to say on the evidence at hand if the PS droplets in PMMA domains are uniformly distributed or preferentially in the near surface region.

Two other structural models were considered, but are considered unlikely. One possible explanation is localized subsurface PS. Since the principal domains are very large laterally (1–3 μm), such domains would have to be very sheet-like for the observed PS signal to arise from a PS domain fortuitously underlying a PMMA domain. It seems rather implausible

that such a sheet-like domain would occur at about the same shallow depth below each PMMA domain. A second possible explanation could be the existence of a film of PS over the whole surface. This was the interpretation proposed by Tanaka et al. [8] for films much thicker than examined here. However, as outlined in the introduction, this contradicts the known thermodynamics for this system. Thus it could only exist if the system is far from equilibrium and a surface enriched PS layer formed as a consequence of the kinetics of the film formation and was maintained because there was insufficient annealing. Annealing clearly changes the bulk morphology of the 30/70 PS/PMMA blend (compare the STXM maps in Figs. 3 and 4) as well as the surface (see the AFM in Figs 3 and 4). This is inconsistent with a metastable surface PS layer.

Two alternative explanations of the 285-eV signal detected in the PMMA-rich domains relate to instrumental details of the X-PEEM. While possible, we do not believe they are the correct explanation. At full intensity, the X-PEEM beam line at ALS has a rather high flux ($\sim 10^{11}$ ph/s in the spot on the sample at the C 1s edge) and thus one possible explanation is that the 285-eV signal is not from PS but rather from the products of radiation damage of PMMA [36]. Radiation damage of PMMA leads to loss of the pendant methyl ester with associated reduction in the 288.4 eV $\pi^*_{C=O}$ signal and mass loss. The photoejected electrons can also reduce the saturated backbone to form C=C bonds which would produce signal at 285 eV. Studies of pure PMMA were carried out to understand these effects and identify operational regions where the damage is minimal. In order to rule out the possibility that the 285-eV signal corresponds to a damage product, we also measured the 30/70 PS/PMMA sample as a function of radiation dose, using for each dose a fresh sample area. At high doses the 288.4 eV $\pi^*_{C=O}$ signal is reduced with increasing dose while the 285-nm signal increases, although more slowly. Based on these damage rate studies, we are confident that for all except the data shown in Fig. 11, the dose used was sufficiently low to ensure the 285-eV signal introduced by damage was negligible. Thus we conclude that the 285-nm signal observed in the low dose measurements reported herein is NOT from

radiation damage but rather reflects the original chemistry of the sample.

A second possible instrumental artefact is limited spatial resolution. If the point spread sampling function [30] of the X-PEEM electron optics has low level wings then the 285-eV signal observed at the location of PMMA domains could arise from adjacent PS domains. For this to occur, the spatial sampling would have to extend several microns. Measurements of the point spread function of the X-PEEM using a very sharp, high contrast object indicate the wings extend only a few hundred nanometers from the point sampled under the electron optical conditions employed. There is an intermediate aperture in the X-PEEM (Fig. 1) which controls spatial resolution by restricting the angular sampling of the optical column. Smaller apertures reduce the wings of the point spread function at the expense of signal intensity. We have ruled out this explanation by measuring fresh regions with 12- and 20- μ m diameter intermediate apertures and showing that the 285-eV signal is independent of aperture size. This indicates that the 285-eV signal does not arise from sampling of adjacent domains, at least for the micron scale domains detected in the X-PEEM images (vide infra).

3.2. Low molecular weight PS/PMMA thin films

The results for the high molecular weight PS/PMMA blends described above are difficult to reconcile with our earlier STXM studies of low MW PS/PMMA blends [16,17], which were interpreted in terms of complete phase segregation. One possible origin of different results is the large MW of the PS and PMMA components, as well as the difference in their values (1060K/312K) which may lead to differential mobility. It is likely the high MW systems are very far from thermodynamic equilibrium, even after annealing. In order to gain further insight into the origin of the PS signal in the surface region of the PMMA domains, which is clearly and consistently observed in NEXAFS recorded by X-PEEM, we have used X-PEEM, AFM and STXM to study a low molecular weight blend that has been more aggressively annealed than the 30/70 blend. The much lower molecular weight and the longer,

higher temperature anneal, should lead to a system much closer to equilibrium. In previous studies of 50:50 27K/27K PS/PMMA blends, Ade et al. [16] found via singular value decomposition (SVD) analysis of STXM micrographs that these systems have 'essentially pure domains' after rather short annealing times of 10 min at 180°C. Lateral force microscopy (also known as surface friction microscopy or SFM), providing frictional contrast, also showed that the 10-min annealed samples have a surface morphology that clearly matched that derived from NEXAFS microscopy [16]. However, the topography is smooth and on a much larger length scale, which supports the interpretation of the SFM as being due to differences in composition. To illustrate these findings, we show the SFM image in comparison to the PS, PMMA composition and total thickness maps derived from STXM of the 10-min annealed sample in Fig. 9. This study in particular did not detect PS in the PMMA matrix, except for small droplets. Furthermore, after 1 week of annealing a very different morphology was observed (Fig. 10). The STXM component maps as well as AFM imaging of the cyclohexane washed surface (which preferentially removes PS) clearly showed rims of PMMA around PS droplets sitting on top of a thin PMMA substrate-wetting layer. The height of the droplets was in excess of 500 nm, much larger than the original film thickness of 145 nm. The morphology of the droplets and the lack of significant further morphological evolution for longer anneal times indicated that morphologies close to the thermodynamic equilib-

rium had been reached; the larger PS domains slowly grow at the expense of the few remaining small PS domains via Ostwald ripening [1]. Further details of these results are given elsewhere [17]. The curvature of the PS phase at the air-PMMA-PS intersection at the PMMA rims (Fig. 10) would be difficult to explain if there were a PS surface layer on top of the PMMA matrix. The existence of the rim is a clear indication that the system attempts to balance the Newman equations at the interface [3].

Notwithstanding these unambiguous earlier results, we have investigated low molecular weight samples prepared similarly to the high MW films prepared for the preferential protein adsorption studies. To our surprise, X-PEEM showed that annealed low MW blends also have a PS signal at the surface of the PMMA-rich domains. X-PEEM results for an aggressively annealed 40/60 (wt.%/wt.%) PS/PMMA sample prepared from low molecular weight (21K/22K) components (see Table 1 for sample preparation details) are presented in Fig. 11. Fig. 11a and b shows PS and PMMA component maps derived from X-PEEM image sequence analysis. Spectral decomposition of the C 1s spectra extracted from the PS-rich (Fig. 11c) and PMMA-rich (Fig. 11d) regions are also indicated. These results indicate that: (a) lower molecular weight and more aggressive annealing gives rise to a more regular pattern of domains; (b) the PMMA phase forms the continuous matrix domain; and (c) the PS phase corresponds to elevated droplets. The latter two observations are particularly notable since they

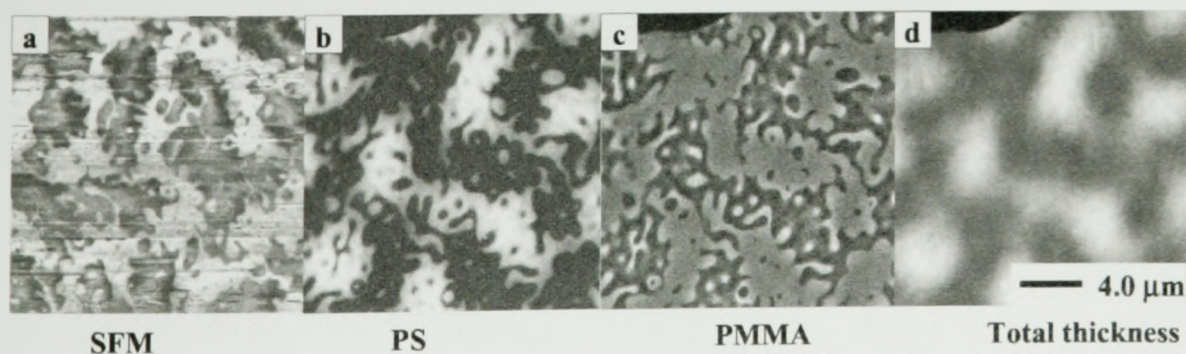


Fig. 9. (a) Surface friction image (SFM); and (b) PS, (c) PMMA and (d) total thickness maps derived by SVD analysis of NEXAFS images recorded with STXM from a 50/50 w/w PS/PMMA (27K/27K) blend annealed for 10 min at 180°C. (NSLS STXM. Adapted from Ref. [16]).

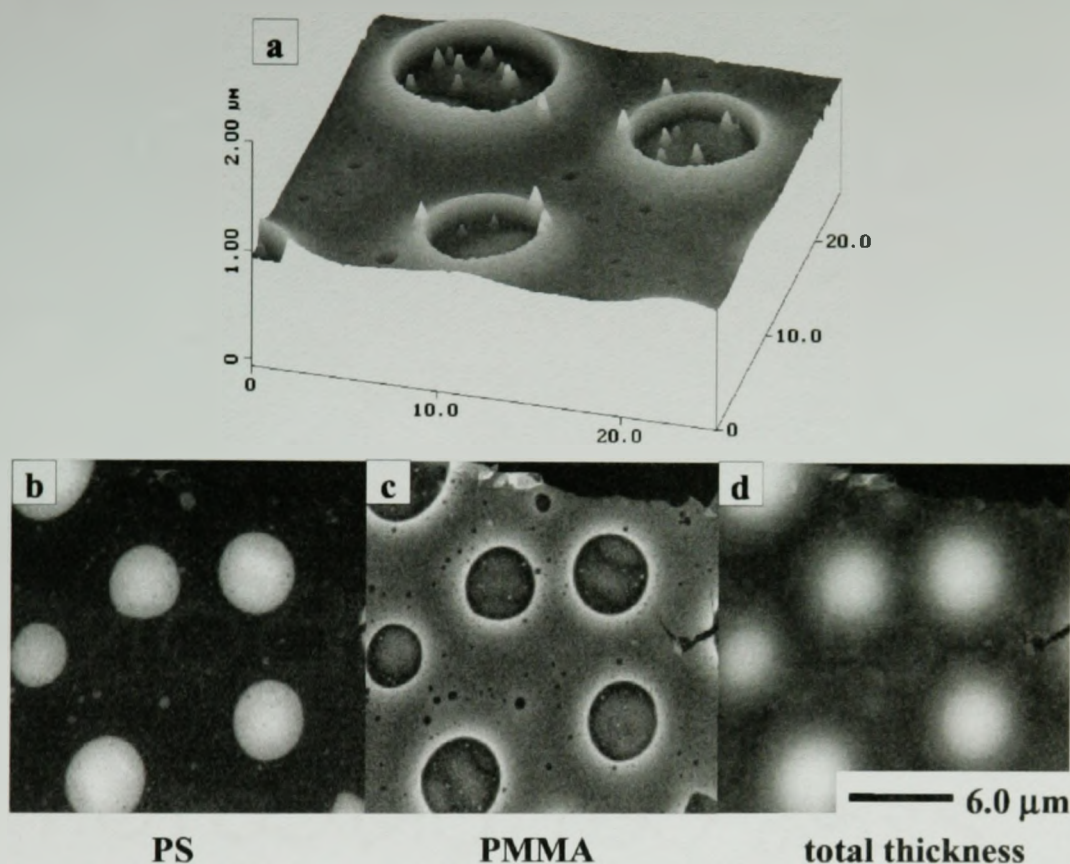


Fig. 10. Morphology of 50/50 w/w PS/PMMA (27K/27K) blend annealed for 1 week at 180°C. (a) AFM topography after preferential dissolution of PS via cyclohexane washing; (b) PS map; (c) PMMA map; (d) total thickness map derived from STXM. (NSLS STXM. Adapted from Ref. [16]).

are totally opposite to the situation with the 30/70 film made from the high MW components, where PS is the continuous phase (in the surface region at least) and it is the PMMA which forms protruding, elevated domains in the 30/70 film. The similarity of the samples shown in Fig. 11 to those in Fig. 10 led us to believe that equilibrium is essentially reached in the sample depicted in Fig. 11 as well. However a very large signal at 285 eV is observed in the NEXAFS of the surface region of the PMMA-rich matrix phase, as with the higher MW samples. Some of the 285-eV signal is associated with beam damage, since this particular data set was taken with too high incident flux, as indicated by the reduced height of the 288.4-eV signal relative to the C 1s continuum. Even so, a large proportion of the 285-eV signal is from PS in the near surface region of this sample.

This is fully confirmed by AFM of the annealed 40/60 low MW PS/PMMA sample after cyclohexane washing (Fig. 12a,b), which shows a bimodal distribution of PS domain sizes with the PMMA matrix containing a large number (~20%) of PS drops which are smaller than the X-PEEM resolution. Fig. 12c,d shows AFM of a 50/50 low MW PS/PMMA blend without the cyclohexane washing. In this case, the sample was annealed less aggressively and there are fewer of the small PS domains decorating the PMMA matrix.

We conclude that the 285.1-eV signal observed consistently in all X-PEEM studies of PS/PMMA blends arises from PS in the surface region, which AFM shows to be in the form of small PS droplets distributed on top of the surface of the PMMA domains. Since the earlier STXM studies [16,17] did

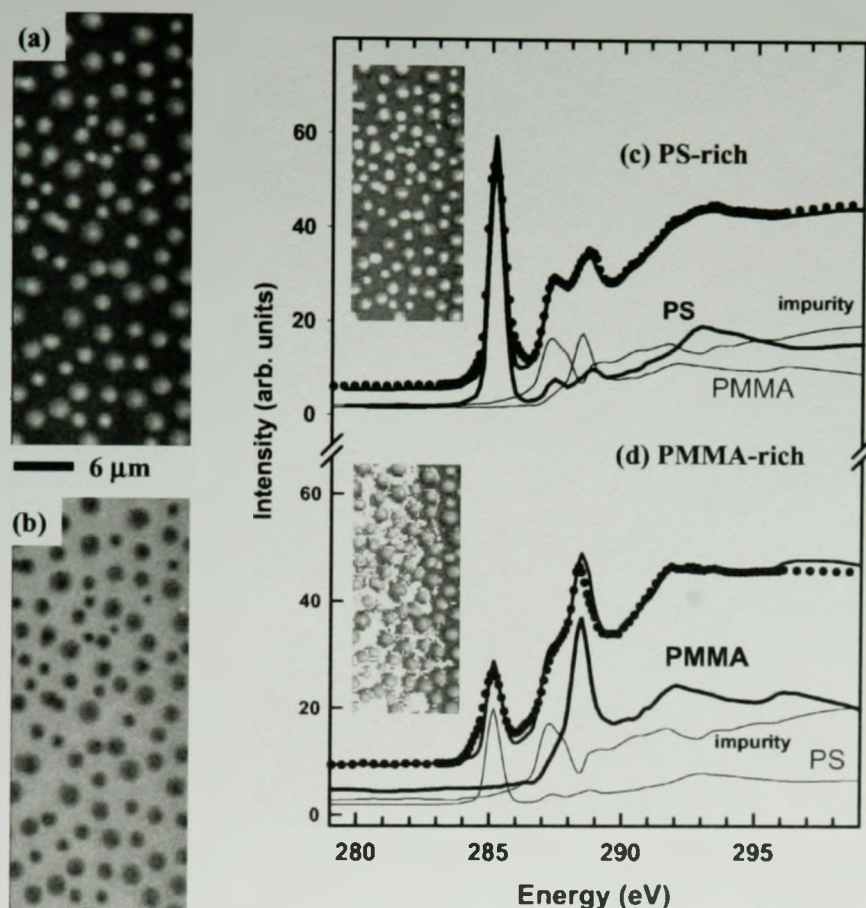


Fig. 11. (a) PS and (b) PMMA component maps derived from X-PEEM of an aggressively annealed low MW 50/50 PS/PMMA blend spun cast on a SiO_2 surface. Spectral decomposition of the C 1s spectra extracted from (c) the PMMA-rich (2.5*PS, 1.5*impurity, 0.2*PMMA) and (d) PS-rich (0.25*PS, 1.0*impurity, 1.8*PMMA) regions, at the locations indicated in the insert images (the reference spectra are edge jump-normalized). For this measurement the flux used was too high and the PMMA was damaged. However only part of the 285-eV signal in the PMMA-rich spectrum arises from beam damage, as can be seen by comparison to the C 1s spectrum of pure PMMA which has been radiation damaged to produce a similar level of reduction of the $\pi^*_{\text{C=O}}$ peak relative to the continuum. (ALS X-PEEM).

not explicitly test for the existence of a surface layer of PS, careful STXM measurements were carried out on the 40/60 low MW PS/PMMA sample. The 40/60 sample was floated from the Si substrate onto a TEM grid. The experiments were designed to minimize the radiation dose given to the samples to prevent the development of a potential 285-eV signal from damaged PMMA. Only two images were acquired: at 281.8 and 285.16 eV. The linear absorption coefficient for PMMA between these two energies is virtually unchanged, while that for PS changes dramatically. PS domains with a wide range

of size distribution were found with STXM. An example of these STXM results is shown in Fig. 13. Many small domains are observed at or below the spatial resolution limit of the X-PEEM. The composition of the PMMA matrix area between the small PS domains was carefully analyzed. The difference in the OD between the images acquired at the two energies in the PMMA region was less than 0.015. For PS, the difference in linear attenuation coefficient at these two energies is $\sim 21 \mu\text{m}^{-1}$. Hence, the upper limit for the thickness of a uniform PS layer would be 0.7 nm, even before taking into account

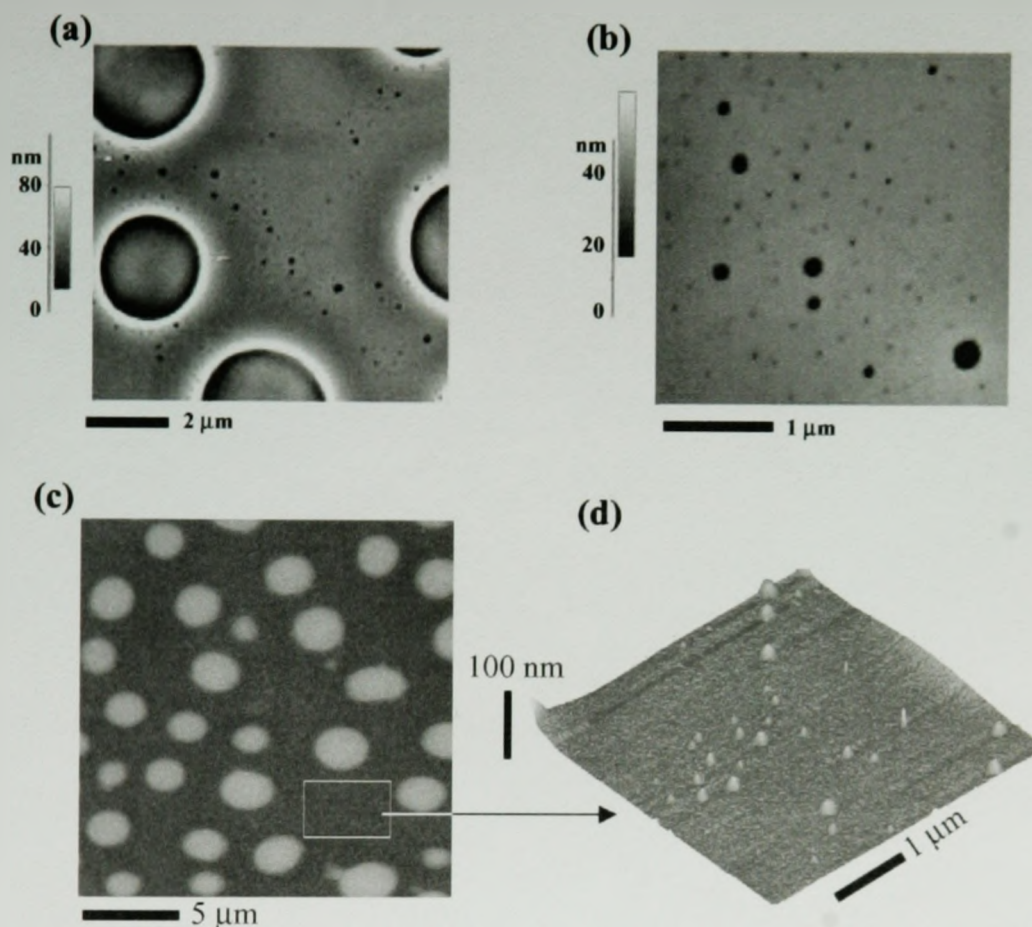


Fig. 12. (a) AFM image of the annealed low MW 50/50 PS/PMMA blend after washing with cyclohexane to remove surface PS. (b) Expanded region of the AFM shown in (a) which shows the pits where small droplets of PS have been removed (NCSU). (c) AFM (height mode) image of a 21K/21K 50/50 w/w PS/PMMA blend spun cast from toluene solution and vacuum annealed for 1 h at 180°C. (d) Expanded perspective view of the PMMA domain showing small PS droplets sitting on the surface (McMaster).

apparent signal due to the finite point spread function of the microscopy [30]. Assuming a sampling depth of 10 nm, a 0.7-nm overlayer would result in a smaller PS signal than that actually observed in X-PEEM. The PS signal seen in the PMMA regions with X-PEEM is thus attributed to small PS domains that can not be resolved in the X-PEEM results, which were recorded under conditions giving ~ 200 -nm spatial resolution. The high spatial resolution NSLS STXM study indicated that these small domains cover about a 20% area of the PMMA matrix in the 40/60 PS/PMMA sample, consistent with the AFM shown in Fig. 12a,b.

4. Discussion

The PS signal observed in the NEXAFS of the surface of the predominantly PMMA domains in all of the PS/PMMA blends is real. However we do not propose that this is experimental evidence that surface segregation to create a homogeneous PS layer on PMMA is thermodynamically preferred. Rather we attribute the signals to the existence of a bimodal size distribution for PS domains which includes a set of PS domains which are unresolved in X-PEEM. In the 40/60 and 50/50 low MW PS/PMMA blend samples, AFM and STXM provided

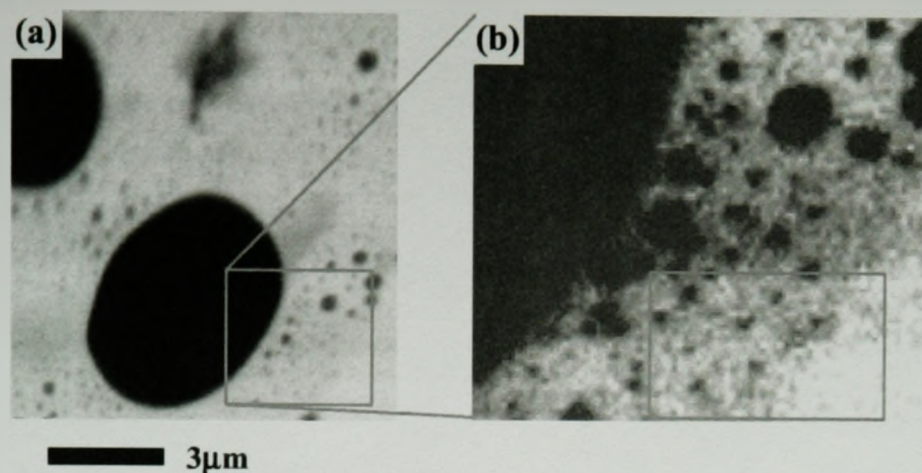


Fig. 13. (a) High resolution C 1s STXM image at 285.2 eV of 40/60 w/w PS/PMMA (21K/22K) blend annealed for 1 day at 165°C. (b) Expanded region of the STXM image shown in (a). Numerous small PS domains are readily visible. The area indicated in the lower part of (b) was used for the quantitative analysis discussed in the text. (NSLS STXM).

direct visualization of these micro domains, which persist due to the slow process of Ostwald ripening, even though these systems are relatively close to equilibrium. For the high MW 30/70 PS/PMMA blend, the system is likely still far from equilibrium, such that small PS domains initially formed at the surface of large PMMA domains have not been able to merge or ripen via diffusion with other PS regions to form a macro-domain.

The presence of small PS droplets in the PMMA domains and the deficit of PMMA in the AFM and X-PEEM of the 30/70 system, could be due to the generally low mobility of the large MW PS. Effectively the sample does not reach equilibrium under the annealing regime used. However it is surprising that the PS in the bulk of the sample has sufficient mobility to re-organize on micron length scales (compare Figs. 3 and 4) whereas the PS at the surface of the sample is immobile. One possible explanation is that when the PS-on-PMMA is in the form of very small isolated domains, they can not coalesce with other PS domains, but have to shrink via Ostwald ripening, i.e. diffusion, and thus overcome the repulsive interactions of the surrounding PMMA domain. In contrast, the large PS domains running through the whole film are areas where a continuous region of PS has initially formed and can rapidly coalesce.

For the 30/70 PS/PMMA system, the continuous regions of PS may arise because the PS comes out of solution more rapidly than PMMA on account of its higher MW (even though PS has a higher intrinsic solubility in toluene than PMMA does, for the same MW). If this is the case, then faster deposition of PS might lead to a structure in which there is a layer of PS near the substrate, with 'puddles' of PMMA embedded. This would explain why PS forms the continuous phase, even though it is the less abundant species. Finally, as indicated by the AFM (Figs. 3 and 4), there are a number of very fine PS domains in the large PMMA domains in the 30/70 sample. These are too small to detect by X-PEEM, but they would contribute to the spectrum.

There is clearly much more work to be done to understand and fully integrate the many aspects of this interesting polymer system, and to extend these results to the preparation of the surface differentiated PS/PMMA blend sample desired for competitive protein adsorption. Currently our strategy to achieve the latter is to use lower MW components (100K/100K), longer annealing (12 h or more at 140°C), and to improve our procedures to avoid impurity contamination. While clearly we would have preferred uncontaminated samples for this study, the detection and mapping of the impurity signal itself is a good example of how NEXAFS microscopy can

probe sample details missed by chemically insensitive probes such as AFM.

The large variety of morphologies and their different thermal evolution reported in the literature (as outlined in the Introduction) reflect the complexity of the PS/PMMA blend system which arises from a very fine balance of the forces controlling morphology and dynamics of phase segregation. We wish to emphasize the need for careful control of key parameters and a full reporting of the sample preparation, annealing and experimental measurements in order to facilitate cross-comparison of results. Further, examination of identical samples by complementary techniques should be used wherever possible.

The results reported here clearly demonstrate many ways in which both X-PEEM and STXM X-ray microscopy can be powerful tools for understanding phase segregation phenomena in blends and in other polymer systems. Although the current STXM and X-PEEM instruments have lower spatial resolution than AFM and TEM/SEM, they are a very useful complement to these higher resolution techniques because they provide direct chemical information. Finally, we note that soft X-ray microscopy can be applied to many problems other than phase segregation in polymers. Other recent studies of polymer properties include investigations of cross-link density in superabsorbent polymers [37], filler particles in polyurethanes [38], composition of core-shell micro-spheres [39], dewetting in PS-BrPS bilayer films [17,20], and pattern formation in free standing confined trilayer films [40].

Acknowledgements

Hitchcock and coworkers are supported financially by the strategic program of NSERC (Canada) and a Canada Research Chair. We thank Jim Garrett for his assistance with annealing the samples, and Andy Duft for his expert operation of the AFM. The samples in Figs. 7 and 8 were made and imaged with AFM by the group of M. Rafailovich from SUNY@Stony Brook. H Ade is supported by NSF (DMR-007143 and Young Investigator Award DMR-9458060). Data were acquired with the Stony Brook STXM at the NSLS developed by the group of Janos

Kirz and Chris Jacobsen at SUNY Stony Brook, with support from DOE (DE-FG02-89ER60858) and NSF (DBI-9605045). The zone plates were developed by S. Spector and C. Jacobsen of Stony Brook and D. Tennant of Lucent Technologies Bell Laboratories, with support from the NSF (ECS-9510499). The NSLS is supported by the Office of Basic Energy Sciences, Energy Research, Department of Energy. X-ray microscopy carried out at the Advanced Light Source is supported by the director, Office of Science, Office of Basic Energy Sciences, Materials Science Division of the DoE under contract DE-AC03-76SF00098 at Lawrence Berkeley National Laboratory.

References

- [1] I.M. Campbell. *Introduction To Synthetic Polymers*. Oxford University Press, New York, 1994.
- [2] S. Wu. *J. Phys. Chem.* 74 (1970) 632.
- [3] S. Qu, C.J. Clarke, Y. Liu, M.H. Rafailovich, J. Sokolov, K.C. Phelan, G. Krausch. *Macromolecules* 30 (1997) 3640.
- [4] T. Thurn-Albrecht, J. Schotter, C.A. Kastle, N. Emley, T. Shibauchi, L. Krusin-Elbaum, K. Guarini, C.T. Black, M.T. Tuominen, T.P. Russell. *Science* 290 (2000) 2126.
- [5] S. Walheim, E. Schäffer, J. Mlynek, U. Steiner. *Science* 283 (1999) 520.
- [6] J. Sohr. *NEXAFS Spectroscopy*. Series in Surface Science, Vol. 25. Springer, Berlin, 1992.
- [7] K. Dalnoki-Veress, J.A. Forrest, J.R. Stevens, J.R. Dutcher. *Physica A* 239 (1997) 87.
- [8] K. Tanaka, K. Takahara, T. Kajiyama. *Macromolecules* 29 (1999) 3232.
- [9] S. Walheim, M. Boltau, J. Mlynek, G. Krausch, U. Steiner. *Macromolecules* 30 (1997) 4995.
- [10] D.A. Winesett, S. Zhu, J. Sokolov, M. Rafailovitch, H. Ade, J. High Perf. *Polymers* 49 (2000) 458.
- [11] C. Thon-That, A.G. Shard, R. Dalay, R.H. Bradley. *Macromolecules* 33 (2000) 8453.
- [12] C. Thon-That, A.G. Shard, D.O.H. Teare, R.H. Bradley. *Polymer* 42 (2001) 1121.
- [13] D. Slep, J. Asselta, M.H. Rafailovich, J. Sokolov, D.A. Winesett, A.P. Smith, H. Ade, S. Anders. *Langmuir* 16 (2000) 2369.
- [14] P. Mansky, Y. Liu, E. Huang, T.P. Russell, C. Hawker. *Science* 275 (1997) 1458.
- [15] E. Kumacheva, L. Li, M.A. Winnik, D.M. Shinozaki, P.C. Cheng. *Langmuir* 13 (1997) 2483.
- [16] H. Ade, D.A. Winesett, A.P. Smith, S. Qu, S. Ge, J. Sokolov, M. Rafailovich. *Europhys. Lett.* 45 (1999) 526.
- [17] H. Ade, D.A. Winesett, A.P. Smith, S. Anders, T. Stämmler, C. Heske, D. Slep, M.H. Rafailovich, J. Sokolov, J. Stohr. *Appl. Phys. Lett.* 73 (1998) 3775.

- [18] A. Karim, T.M. Slawacki, S.K. Kumar, J.F. Douglas, S. Satija, C.C. Han, T.P. Russell, Y. Liu, R. Overney, J. Sokolov, M.H. Rafailovich, *Macromolecules* 31 (1998) 857.
- [19] T. Schmitt, P. Guttman, O. Schmidt, P. Müller-Buschbaum, M. Stamm, G. Schonhense, G. Schmahl, *X-ray Microscopy*, AIP Conf. Proc. 507 (2000) 245, editors: W. Meyer Ilse, T. Warwick and D. Attwood.
- [20] D. Slep, J. Asselta, M.H. Rafailovich, J. Sokolov, D.A. Winesett, A.P. Smith, H. Ade, Y. Strzhemechny, S.A. Schwarz, B.B. Sauer, *Langmuir* 14 (1998) 4860.
- [21] J. Kirz, C. Jacobsen, M. Howells, *Q. Rev. Biophys.* 28 (1995) 33.
- [22] H. Ade, in: J.A.R. Samson, D.L. Ederer (Eds.), *Experimental Methods in the Physical Sciences*, Vol. 32, Academic Press, New York, 1998, p. 225.
- [23] H. Ade, S.G. Urquhart, in: T.K. Sham (Ed.), *Chemical Applications of Synchrotron Radiation*, World Scientific Publishing, Singapore, 2000 (in press).
- [24] C. Jacobsen, S. Wirick, G. Flynn, C. Zimba, *J. Microsc.* 197 (2000) 173.
- [25] I.N. Koprinarov, A.P. Hitchcock, C.T. McCrory, R.F. Childs, *J. Phys. Chem. B* (submitted).
- [26] A.P. Hitchcock, I.N. Koprinarov, H. Stöver, L. Croll, E. Kneidler (in preparation).
- [27] A.P. Hitchcock, I.N. Koprinarov, T. Tyliczszak, C. Morin, Y.M. Heng, R. Cornelius, J.L. Brash, H. Ade, S. Anders, A. Scholl, F. Notling, *ALS Compendium*, 2000, LBNL publication, 47838.
- [28] T. Warwick, K. Franck, J.B. Kortwright, G. Meigs, M. Moronne, S. Myneni, E. Rotenberg, S. Seal, W.F. Steele, H. Ade, A. Garcia, S. Cerasari, J. Denlinger, S. Hayakawa, A.P. Hitchcock, T. Tyliczszak, E.G. Rightor, H.-J. Shin, B. Tonner, *Rev. Sci. Inst.* 69 (1998) 2964.
- [29] C. Jacobsen, H. Ade, J. Kirz, C.-H. Ko, S. Williams, X. Zhang, E. Anderson, D. Kern, *Scanning soft X-ray microscopy*, in (Eds.) P.B. Kenway, P.J. Duke, G.W. Lorimer, T. Mulvey, I.W. Drummond, G. Love, A.G. Michette, M. Stedman, *X-ray Optics and Microanalysis 1992*, Bristol, IOP Publishing, 571.
- [30] D. Sayre, H.N. Chapman, *Acta Crystallogr.* A51 (1995) 237.
- [31] M. Feser, M. Carlucci-Dayton, C. Jacobsen, J. Kirz, U. Neuhausler, G. Smith, B. Yu, *X-ray Microfocusing: Applications and Techniques*, I. McNulty (Ed.), SPIE Proc. 3449 (1998) 19.
- [32] B.L. Henke, P. Lee, T.J. Tanaka, R.L. Shimabukuro, B.K. Fujikawa, *At. Nucl. Data Tables* 27 (1982) 1.
- [33] J. Brandrup, E.H. Immergut, E.A. Grulke (Eds.), *Polymer Handbook*, 4th Edition, Wiley, 1999.
- [34] S. Anders, H.A. Padmore, R.M. Duarte, T. Renner, T. Stammer, A. Scholl, M.R. Scheinfein, J. Stöhr, L. Séve, B. Sinkovic, *Rev. Sci. Inst.* 70 (1999) 3973.
- [35] Y. Wang, C. Jacobsen, J. Maser, A. Osanna, *J. Microsc.* 197 (2000) 80.
- [36] T. Coffey, S.G. Urquhart, H. Ade, *J. Electron Spectrosc.* (in press).
- [37] G.E. Mitchell, L.R. Wilson, M.T. Dineen, S.G. Urquhart, F. Hayes, E.G. Rightor, A.P. Hitchcock, H. Ade, *Macromolecules* (in press).
- [38] A.P. Hitchcock, J. Koprinarov, T. Tyliczszak, E.G. Rightor, G.E. Mitchell, M.T. Dineen, F. Hayes, W. Lidy, R.D. Priester, S.G. Urquhart, A.P. Smith, H. Ade, *Ultramicroscopy* 88 (2001) 33.
- [39] I.N. Koprinarov, A.P. Hitchcock, W.H. Li, Y.M. Heng, H.D.H. Stöver, *Macromolecules* 34 (2001) 4424.
- [40] I.N. Koprinarov, A.P. Hitchcock, K. Dalnoki-Veress, C. Murray, J. Dutcher, H. Ade, *J. Phys. B* (in preparation).

Chapter 5

SELECTIVE ADSORPTION OF PROTEIN ON POLYMER SURFACES STUDIED BY SOFT X-RAY PHOTOEMISSION ELECTRON MICROSCOPY

The following work documents the X-PEEM and radio-labeling results of various concentrations of fibrinogen adsorbed to PS/PMMA from two different solvents (phosphate buffer saline and deionized water). This work has been published in the Journal of Electron Spectroscopy and Related Phenomena (J. Electron Spectrosc. 137-140 (2004) 785-794) and is presented here in published form. The contributions from the author of this thesis were detailed in the introduction.



24 September 2004

Our Ref: HG/jj/Sept04/J442

Your Ref:

Cythnia Morin
McMaster University/Chemistry Department
1280 Main Street West
Hamilton, Ontario
Canada L8S 4M1

Dear Cythnia Morin

JOURNAL OF ELECTRON SPECTROSCOPY & RELATED PHENOMENA, Vol 137-140, Morin et al: "Selective adsorption of ..."

As per your letter dated 23 September 2004, we hereby grant you permission to reprint the aforementioned material at no charge **in your thesis** subject to the following conditions:

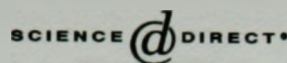
1. If any part of the material to be used (for example, figures) has appeared in our publication with credit or acknowledgement to another source, permission must also be sought from that source. If such permission is not obtained then that material may not be included in your publication/copies.
2. Suitable acknowledgment to the source must be made, either as a footnote or in a reference list at the end of your publication, as follows:

"Reprinted from Publication title, Vol number, Author(s), Title of article, Pages No., Copyright (Year), with permission from Elsevier".
3. Reproduction of this material is confined to the purpose for which permission is hereby given.
4. This permission is granted for non-exclusive world **English** rights only. For other languages please reapply separately for each one required. Permission excludes use in an electronic form. Should you have a specific electronic project in mind please reapply for permission.
5. This includes permission for the National Library of Canada to supply single copies, on demand, of the complete thesis. Should your thesis be published commercially, please reapply for permission.

Yours sincerely

Helen Gainford
Rights Manager

Your future requests will be handled more quickly if you complete the online form at
www.elsevier.com/wps/find/obtainpermissionform.cws_home/obtainpermissionform

Available online at www.sciencedirect.com

**JOURNAL OF
ELECTRON SPECTROSCOPY**
and Related Phenomena

Journal of Electron Spectroscopy and Related Phenomena 137–140 (2004) 785–794

www.elsevier.com/locate/elspec

Selective adsorption of protein on polymer surfaces studied by soft X-ray photoemission electron microscopy

C. Morin^a, A.P. Hitchcock^{a,*}, R.M. Cornelius^a, J.L. Brash^a,
S.G. Urquhart^b, A. Scholl^c, A. Doran^c

^a Department of Chemistry, BIMR, McMaster University, 1280 Main Street West, Hamilton, Ont., Canada L8S 4M1^b Department of Chemistry, University of Saskatchewan, Sask., Canada S7N 5C9^c Advanced Light Source, Berkeley Lab, Berkeley, CA 94720, USA

Available online 28 March 2004

Abstract

X-ray photoemission electron microscopy (X-PEEM) using synchrotron radiation illumination in the C 1s, N 1s and O 1s regions has been used to characterize a phase segregated polystyrene/polymethylmethacrylate (PS/PMMA) polymer thin film, and to map the adsorption of fibrinogen (a blood plasma protein) on this surface from both isotonic, buffered, and low ionic strength, unbuffered aqueous solutions at varying fibrinogen concentrations. The concentration dependence of the coverage correlates with independent, non-spatially resolved measurements using ¹²⁵I-radiolabeled protein. At low concentrations (<0.1 mg/ml) of the buffered solution, adsorption of fibrinogen occurs with strong preference for PS domains. In contrast, adsorption from similar concentrations of unbuffered solution strongly prefers the interface of the PS and PMMA domains. Increasing the solution concentration up to 1 mg/ml of both buffered and unbuffered solutions leads progressively to full surface coverage (close-packed monolayer). These results demonstrate for the first time that X-PEEM with tunable soft X-rays has the sensitivity to locate and detect adsorbed proteins at the submonolayer level, while simultaneously detecting the spatial distribution of phases, and protein distribution relative to the phases, at the surface of an underlying microphase separated polymer substrate.

© 2004 Elsevier B.V. All rights reserved.

Keywords: Photoemission electron microscopy; Protein mapping; Polystyrene; Polymethylmethacrylate blend; Polymer thin films; Biomaterials

1. Introduction

The biocompatibility of a material is believed to be related to the properties of the first protein layer adsorbed on contact with biological tissue or fluids. Initially adsorbed proteins mediate the subsequent interactions of cells with the surface [1]. It is envisioned that novel surfaces that direct the biological healing process would have a well-defined array of bio-recognition sites designed to interact specifically with cells since many of the important functions of cells depend on the type and orientation of molecules at their surfaces. In other cases, such as artificial materials used for blood contact, unfavorable aspects of first-layer protein adsorption can lead to coagulation, complement activation and other adverse responses [2]. Thus, techniques which can map submonolayer amounts of adsorbed proteins at high spatial resolution, and thereby identify preferred sites of protein attachment on het-

erogeneous substrates, are of interest to assist understanding of biocompatibility issues and the development of improved biomaterials.

We are exploring the strengths and limitations of a number of soft X-ray microscopies for this purpose. Earlier we have shown that scanning transmission X-ray microscopy (STXM) can detect protein at near monolayer coverage adsorbed on structured polymers, even in the presence of a few micron overlayer of aqueous buffer [3]. While the ability to study wet systems is very attractive for approximating real world biomaterial–biological interfaces, the sensitivity to the actual polymer–protein interface is limited since the interface is only one part of the signal measured in a transmission experiment. The sampling depth of X-ray photoemission electron microscopy (X-PEEM) is ~10 nm, and thus X-PEEM, while a vacuum technique like XPS, should have significantly higher surface sensitivity than STXM and perhaps be better suited for this purpose. Here, we report first explorations of X-PEEM for studies of protein adsorption. The test substrate is a phase segregated blend of polystyrene (PS) and polymethylmethacrylate (PMMA), spun cast as a

* Corresponding author. Tel.: +1-905-525-9140x24749.

fax: +1-905-521-2773.

E-mail address: aph@mcmaster.ca (A.P. Hitchcock).

thin film on a Si wafer. We recently reported a detailed characterization of spun cast thin film PS/PMMA blends by atomic force microscopy (AFM), PEEM and STXM [4]. The test protein for investigating selective adsorption on this surface is fibrinogen (Fg), a 340 kDa plasma protein that plays a central role in coagulation and thrombosis [5]. Fibrinogen adsorption from blood plasma is unusual in that more fibrinogen is adsorbed on most materials in a short exposure (10 s) than lengthy (1 h) contact times [6]. Also, more fibrinogen adsorbs from intermediate plasma dilutions than from either highly diluted or undiluted plasma. These phenomena, collectively called the “Vroman effect” [5], are intriguing and suggest that fibrinogen molecules, once adsorbed, are eventually displaced from the surface by other adsorbing plasma proteins. While that concentration and exposure time-dependent behavior is specific for fibrinogen adsorption from the complex mixture of proteins present in plasma, it is interesting to measure adsorption from pure fibrinogen solutions as a reference point for the more complex, mixed protein plasma system, which will eventually be the target for study.

Measurements were performed using the electrostatic PEEM at the Advanced Light Source (ALS, Berkeley, CA) [7], and a magnetic PEEM at the Synchrotron Radiation Center (SRC, University of Wisconsin at Madison). Here, we describe only the ALS results due to space limitations. We have recorded images, spectra, and image sequences in the C 1s, N 1s and O 1s regions on annealed PS/PMMA thin films both before and after exposure to fibrinogen. The protein adsorption was carried out from a phosphate buffer (pH 7.2) at concentrations from 0.005 to 1 mg/ml, and from low ionic strength, unbuffered aqueous solutions at 0.05 and 0.1 mg/ml (pH 6.6–6.9 with protein present). Adsorption isotherm studies by ^{125}I -radiolabeling and atomic force microscopy studies were also carried out. Detailed analysis of the PEEM results shows that, in the low concentration limit, fibrinogen prefers the continuous PS domains when adsorbed from a buffer solution, but shows a distinct preference for the PS/PMMA interface when adsorbed from non-buffered solution.

2. Experimental

2.1. Materials and methods

2.1.1. Substrate

PS (MW = 1.07×10^6 dalton, $\delta = 1.06$) and PMMA (MW = 0.31×10^6 dalton, $\delta = 1.01$) were obtained from Polymer Source Inc. and were used without further purification. A 28.72 (w/w) PS/PMMA (1% by weight) toluene (Aldrich, 99.8% anhydrous) solution was spun cast ($\sim 50 \mu\text{l}$ drop, 4000 rpm, 30 s) onto clean 1 cm \times 1 cm native oxide Si (111) wafers (Wafer World Inc.), which had previously been degreased with trichloroethylene (Aldrich, >99.5% pure), acetone (Burdick & Jackson, HPLC grade), and methanol

(Caledon), then rinsed under running Milli-Q water. The PS/PMMA/Si substrates were annealed at 160 °C for 8 h in a vacuum oven with pressure $\sim 10^{-2}$ Torr. Non-contact mode AFM measurements of the PS/PMMA substrate and several Fg/PS/PMMA samples were made in the region of the I_0 normalization scratch. These showed the polymer film is 40–50 nm thick with 5–10 nm (rms) corrugation in the PS/PMMA pattern. The adsorbed fibrinogen could not be reliably detected by our AFM measurements, probably because of the softness of the polymer substrate, combined with a corrugation that is similar in size scale to the size of the adsorbed proteins.

2.1.2. Protein

Plasminogen-free human plasma fibrinogen (Calbiochem) was used; dialysis to remove possible low-molecular-weight impurities was performed for the radiolabeling but not the PEEM samples. It is reported to be >95% clottable by thrombin, and pure as judged by SDS-PAGE. Solutions for exposure to PS/PMMA were made at various concentrations in two different solvents, deionized water and phosphate buffer (Pierce, No. 28372, 0.1 M sodium phosphate and 0.15 M sodium chloride, when a pouch is dissolved in 500 ml deionized water, the pH is 7.2).

2.2. Methods

2.2.1. X-PEEM

X-PEEM of organic materials is challenging on account of potential problems with charging, field emission, and radiation damage. We have worked extensively to optimize our sample preparation, data acquisition, and data analysis procedures [8] to the point where we can measure many systems with minimal artifacts. Aspects important in this work are: keeping the PS/PMMA layer thin (<50 nm) and flat (~ 10 nm rms); using an internal reference (scratch through the film to expose Si for I_0 determination); use of a Ti filter to reduce second order radiation in C 1s region; use of beamline masks to decrease flux on the sample (at ALS beamline 7.3.1, the peak flux is $\sim 10^{10}$ photons/s at 400 eV in a $30 \mu\text{m} \times 30 \mu\text{m}$ spot). We have characterized the radiation damage rates for all three components [9]. As expected, PMMA is the most sensitive. Under the conditions used (masking to $< \sim 5\%$ of full flux), a 120 s measurement time leads to about 1/10th of saturation damage. In order to have sufficient spectral definition and statistical precision, most of these measurements were made with a total exposure time ranging between 120 and 180 s, of which less than 50% of the time is used to acquire ~ 60 images, each with 1 s exposure, the remainder being overhead associated with data transfer and monochromator movement. With the masking conditions used the bending magnet beam is elliptically polarized with 70–80% right circularly polarized light. The electrostatic field at the sample was typically 9 kV/mm, but this sometimes had to be reduced to as low as 8 kV/mm, in cases of mild charging. The intermediate voltage was then

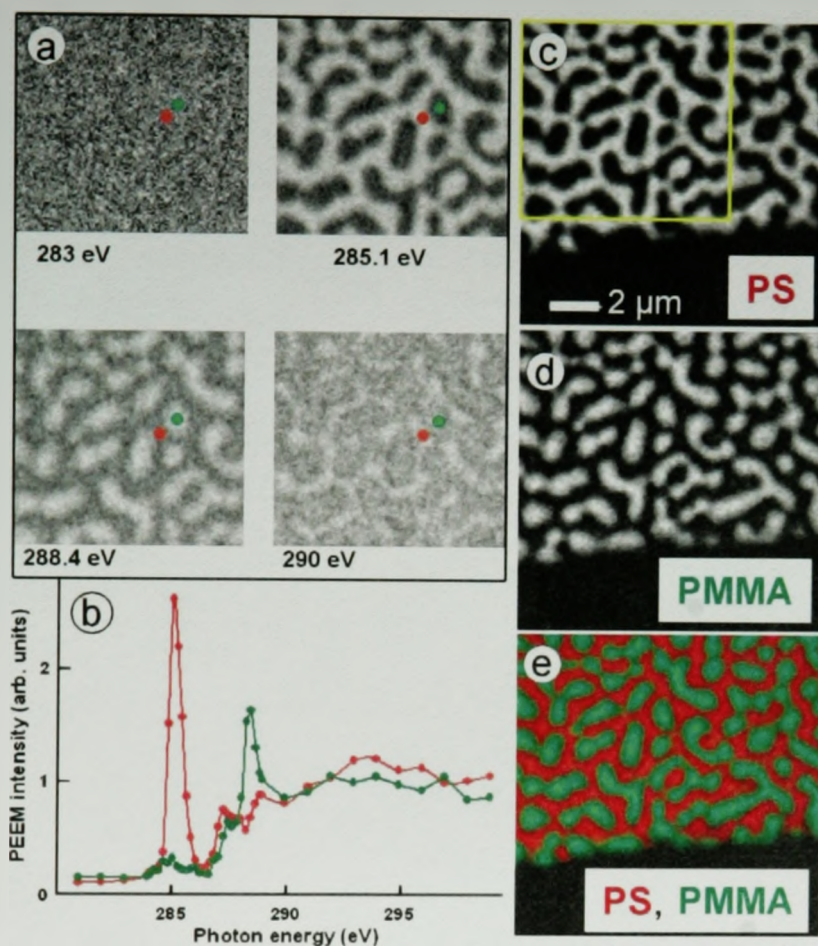


Fig. 1. (a) X-PEEM images at 283, 285.1, 288.4 and 290 eV, 4 of the 40 images in the C 1s region of an annealed 28/72 (w/w) PS/PMMA blend thin film spun cast on native oxide Si (note the actual average surface composition is 57:43; see text). (b) Spectra from the indicated spots. (c and d) Component maps of PS and PMMA derived by singular value decomposition of the C 1s image sequence. (e) Color coded composite map (red: PS; green: PMMA).

adjusted such that the resulting field-of-view was between 40 and 60 μm. The energy scales were calibrated from the known positions of the PS, PMMA and Fg structures [8,13]. The incident flux signal was taken from the region of a scratch through the polymer film (see Fig. 1) for the C 1s and N 1s edges, and from the signal from a downstream Au mesh for the O 1s edge. The I_0 signals were corrected for the elemental photoabsorption response of Si or Au [10].

Image sequences (stacks) were prepared for analysis by: (1) energy calibration, (2) normalization to the elemental-corrected I_0 ; and (3) scaling the intensity to match to the elemental photoabsorption response of the substrate polymer, $C_5H_8O_2$ [10], based on the nominal 30:70 PS/PMMA stoichiometry. Assuming the work function is not strongly affected by the differing amounts of adsorbed protein, this approach should give an approximately quantitative analysis (percent composition of the region sampled) since the model spectra used in the analysis are placed on a linear absorption scale (signal per nm) which is set by matching to the elemental response. Component maps for PS, PMMA and Fg were

then derived from these calibrated, normalized image sequences by either singular value decomposition (SVD) [11] or stack fit [12] fitting routines, within the aXis2000 X-ray microscopy analysis package [13]. Stack fit gave statistically better fits than SVD since it incorporates an additional constant term which accommodates uncorrected backgrounds such as those from camera offsets, and possibly some long escape depth signal from the underlying Si wafer. For the C 1s and O 1s edges, fits were made to three components (PS, PMMA and Fg) while for the N 1s edge, the fit was made only to two components (PS and Fg) since the PS and PMMA are indistinguishable in this energy region.

2.2.2. Protein exposure

For X-PEEM, the Fg/PS/PMMA samples were prepared by 10 min incubation of the PS/PMMA substrate in ~2 ml of Fg solution contained in a Fisher multi-well plate (1 cm diameter wells), followed by continuous dilution of the over-layer solution with running deionized water for ~3–5 min. The Fg/PS/PMMA substrate was then removed from the

well. This rinsing method was used to avoid depositing protein or buffer salts from the air–solution interface.

2.2.3. Experiments with radiolabeled fibrinogen

Fibrinogen was labeled with ^{125}I (ICN Biomedicals, Mississauga, Ont., Canada) using the iodogen technique [14], a standard protocol for radioiodination of proteins by IODO-GEN[®] (Pierce Chemical Company, Rockford, IL) [15]. The labeled protein was dialyzed overnight against isotonic Tris buffer to remove unbound radioactive iodide. Trichloroacetic acid precipitation [16] of aliquots of protein solutions before and after completion of the experiments confirmed that >99% of the ^{125}I remained bound to the protein. The adsorption experiments were carried out in phosphate buffered saline (pH 7.2) with four repeats and in Milli-Q water (three repeats), also for 10 min exposures. For the radiolabeling experiments, the samples were rinsed statically for 2.5 min in a similar volume of buffer solution, and three times more for 2.5 min each in Milli-Q water. Adsorbed amounts were calculated as described earlier [17]. For the blend surface, it was demonstrated that batch rinsing and continuous rinsing gave the same adsorption isotherm.

3. Results

3.1. PS:PMMA substrate

Fig. 1 presents selected energy images and selected region C 1s spectra measured with X-PEEM. The raw images show the PS:PMMA phase segregated pattern only at the energies of strong PS (285.1 eV) and strong PMMA (288.5 eV) absorption peaks, with contrast inversion. Fig. 1 also presents PS and PMMA component maps derived from singular value decomposition analysis [11] of the C 1s image sequence and a color composite map. X-ray damage to PMMA [9] results in loss of C=O bonds, leading to intensity loss at 288.5 eV, and formation of C=C bonds, leading to intensity gain at 285 eV. The C 1s image sequence for PS:PMMA was measured for 140 s, about the time for ~10% of saturation damage, and thus should have a barely detectable signal at 285 eV. In fact the PMMA domains do exhibit a significant 285.1 eV signal. In this particular example very little of the 285 eV signal is from radiation damage; the majority is associated with PS micro-domains embedded in the PMMA macro-domains [4] which, to date, are an unavoidable feature of our sample preparation. Based on analysis of the C 1s spectrum averaged over large areas, the composition in the depth sampled by X-PEEM (estimated as 5–10 nm) is 57(2):43(2) (w/w), significantly enriched in PS relative to the formulation, as found earlier [4].

Table 1 reports the advancing water contact angles for the pure PS, pure PMMA and the PS:PMMA blend surface. Pure PS is more hydrophobic than pure PMMA. The water contact angle for PS:PMMA falls at an intermediate value, one that is consistent with the actual 57:43 surface composition, as opposed to the 28:72 formulation.

Table 1
Advancing water contact angle^a for PS, PMMA and PS:PMMA

Sample	Angle on sample ^b	Literature
PS	77.5(4)	86 [23]
PS:PMMA	74.9(8)	—
PMMA	70.7(3)	62–73 [24]

^a Advancing water contact angles were measured using the sessile drop method. Milli-Q water and a Ramé-Hart (Mountain Lakes, NJ) NRI goniometer were used for these measurements.

^b Error in last digit is based on spread of two measurements.

3.2. ^{125}I -Fg on PS:PMMA adsorption isotherms

Fig. 2 shows isotherms for adsorption of ^{125}I -labeled Fg from phosphate buffer to pure PS, to pure PMMA and to the PS:PMMA blend surface. Across the entire concentration range there is a significantly greater amount of Fg adsorbed to the PS than to the PMMA, while the blend surface adsorbs an intermediate amount. The adsorbed amounts at the higher concentrations are in the range of close-packed monolayers. The higher amounts on PS occur not just at monolayer saturation but also in the low concentration regime. This suggests that, for the 10 min exposure time used, the adsorbed amount on the three different surfaces reflects relative binding affinities rather than any kinetic effect. The adsorption behavior as monitored by ^{125}I -labeling, is also sensitive to the ionic strength of the adsorbing solution. As shown in the inset to Fig. 2, the slope of the isotherm in the <0.1 mg/ml regime for Fg adsorption from buffer is ~1.5× as steep as that for Fg adsorption from water. For adsorption from buffer these

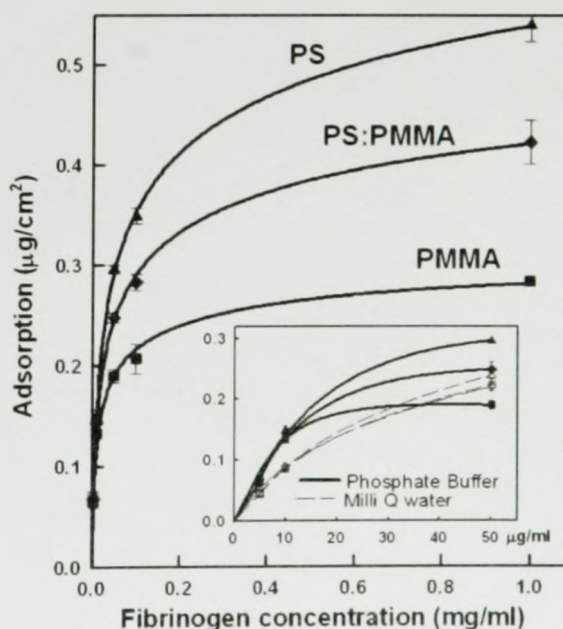


Fig. 2. Isotherms for adsorption of ^{125}I -labeled Fg from phosphate buffer (pH 7.2) to pure PS, pure PMMA and the PS:PMMA blend surface. The inset compares the isotherms at low concentration from phosphate buffer and water.

results suggest that for the PS:PMMA blend, Fg will adsorb preferentially to PS rather than to PMMA domains. However, the data also indicate there is no preference when the solvent is water, at least for concentrations up to 50 $\mu\text{g/ml}$.

3.3. X-PEEM of Fg/PS:PMMA

3.3.1. Reference spectra

Fig. 3 shows the NEXAFS spectra of pure PS, PMMA and Fg spun cast thin films in the C 1s, N 1s and O 1s regions, recorded with X-PEEM. The intensity scales in each panel (core edge) are on the same scale (aside from the offsets introduced for clarity) but the scales are set independently from panel to panel to allow proper viewing of the spectra. The dotted lines are the expected elemental responses [10]. All three materials exhibit distinct C 1s spectra. The Fg and PMMA spectra are each dominated by C 1s ($\text{C}=\text{O}$) \rightarrow $\pi_{\text{C}=\text{O}}^*$ transitions. However, the $\pi_{\text{C}=\text{O}}^*$ peak in Fg occurs 0.3 eV below the $\pi_{\text{C}=\text{O}}^*$ peak in PMMA since the carbonyl carbon is in a less electronegative environment (CONH versus COOR). Due to the small size of this shift and the otherwise similar nature of the Fg and PMMA C 1s spectra, accurate energy calibration is essential for reliable analysis. Addition of signal from the N 1s and O 1s edges significantly enhances the ability of NEXAFS to differentiate these species. Only Fg has a N 1s spectrum, with a characteristic N 1s \rightarrow π_{CONH}^* transition at 401.2 eV, as found in other proteins and peptides [18,19]. At the O 1s edge, PMMA and Fg each are dominated by O 1s \rightarrow $\pi_{\text{C}=\text{O}}^*$ transitions at 531.6 eV, but PMMA has an extra transition at 535.5 eV arising from O 1s ($\text{O}-\text{CH}_3$) \rightarrow $\pi_{\text{C}=\text{O}}^*$ transitions, specific to esters.

3.3.2. Fg(buffer)/PS:PMMA

Fig. 4 presents results of a stack fit analysis of the C 1s image sequence for Fg adsorption from 0.05 mg/ml buffer solution. In the composite map (a), pure red indicates 100% PS, pure green indicates 100% PMMA and pure blue indi-

cates 100% Fg in the region sampled. Due to the finite sampling depth both adsorbed protein and underlying polymer substrate may contribute. If so, this would be indicated by intermediate colors (purple for Fg and PS or turquoise for Fg and PMMA). Fig. 4a shows the continuous PS domains to be purple rather than red, whereas the PMMA domains are pure green with a few isolated blue dots on the PMMA. This indicates that there is a much larger amount of Fg present on the PS domains than on the PMMA domains. The pattern of the main signal in the Fg component map (Fig. 4d) matches that of the continuous PS domains, not the discrete PMMA domains, also indicating that Fg sits preferentially on the PS domains. Note that the smallest regions with detectable protein signal are about 200 nm, ~ 4 times the size of a single protein [20], indicating that with improved signal quality and spatial resolution it may be possible to map single protein molecules with X-PEEM. Fig. 4e, 4f and 4g are spectra of the pixels in the regions indicated by the color outlines in the grayscale component maps (Fig. 4b–d), which were selected using threshold masking of the component maps. Fig. 4e–g also show the results of curve fits of these selected-area spectra to the reference spectra plotted in Fig. 3. This analysis indicates detectable Fg signal in the high-PS pixels, and strong PS-signal in the high-Fg pixels, but very little Fg in the high-PMMA pixels. Thus, the preference for Fg to adsorb on the PS rather than the PMMA domains is fully supported by the spectral analysis.

The numerical results for fits to the spectra of the PS-rich, PMMA-rich and Fg-rich regions for all four Fg(buffer)/PS:PMMA systems studied are presented in Table 2. For the 0.05 mg/ml Fg(buffer) system quantitative spectral analysis indicates that the center of the PS domains contain $\sim 20\%$ Fg. Similarly, the spectrum of pixels with strong Fg components is analyzed to contain 45% PS and negligible amounts of PMMA. Finally, the center of the PMMA domains is dominated by PMMA (70%) with the remaining signal mostly PS (21%), probably associated

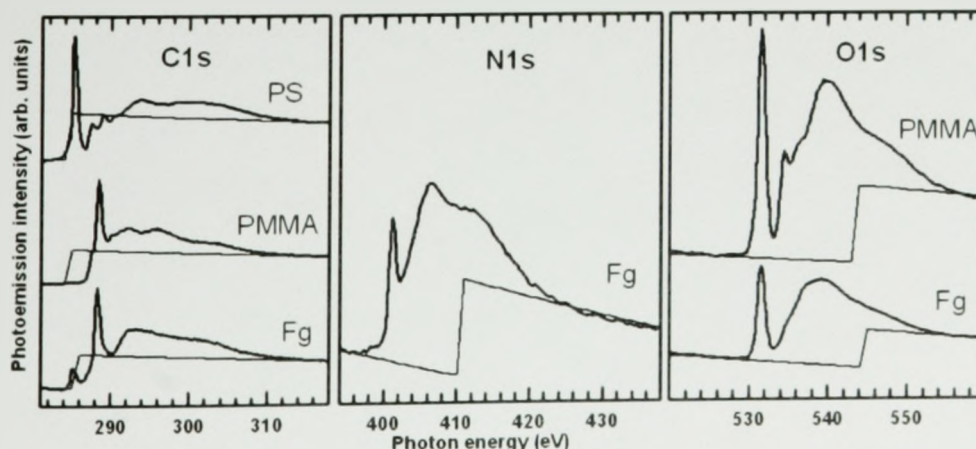


Fig. 3. C 1s, N 1s and O 1s NEXAFS spectra of PS, PMMA and Fg recorded as pure materials with X-PEEM. The dashed lines indicate the elemental response [10]. The intensities within each panel are on the same scale, although offsets are used for clarity. Different scaling is used for each panel.

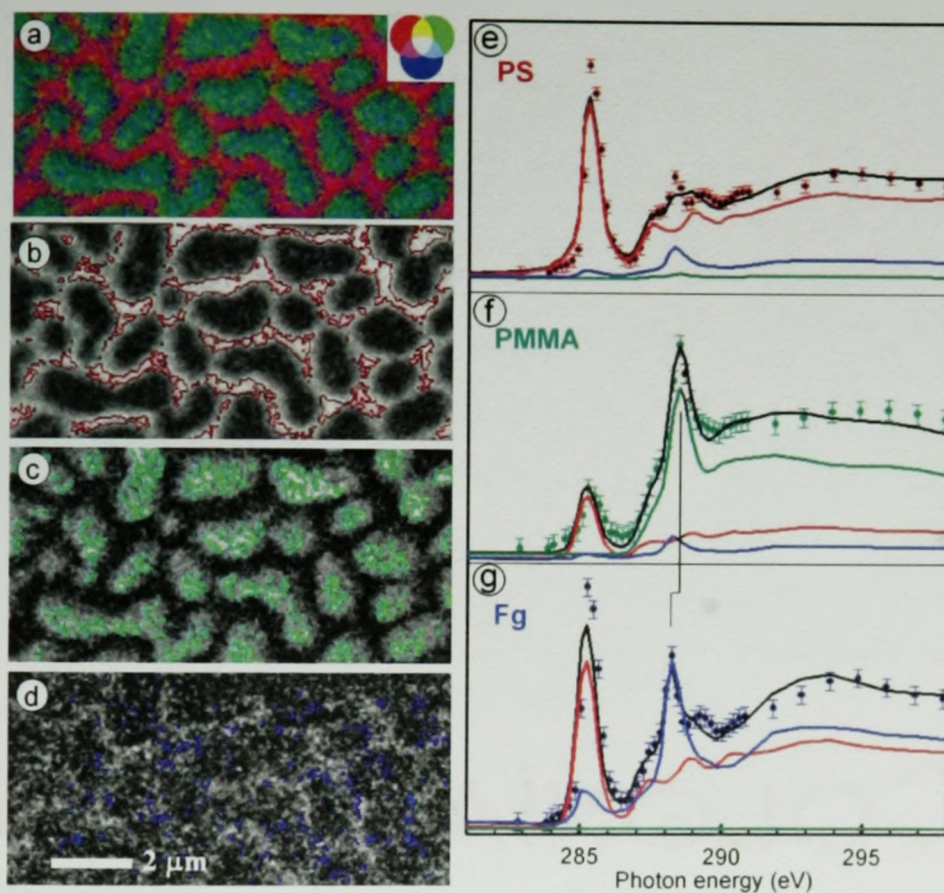


Fig. 4. (a) Composite map (red: PS; green: PMMA; blue: Fg) derived from component maps extracted by stack fit analysis of a C 1s image sequence for fibrinogen (0.05 mg/ml in buffer) adsorbed on the PS/PMMA blend surface. (b–d) Component maps indicating the regions from which spectra of high-PS, high-PMMA and high-Fg signals were extracted and displayed in (e–g) which also plot the curve fits of the extracted spectra (dots: data; black line: sum of component signals; colored lines: component signals). Most of the 285 eV signal in the spectrum of the PMMA-rich pixels comes from radiation damage

with micro-domain PS [4], although possibly also reflecting some radiation damage. One should be careful to differentiate between “first site of adsorption”, “sparse occurrence of Fg on PMMA” and “where most of the protein sits”. The latter is what our analysis is indicating. It is possible there is a preference for the PS/PMMA interface as the first site of adsorption (see further). However, we base our interpretation “Fg prefers PS when adsorbed from buffered solutions” on the dominant site of Fg attachment in the stable, equilibrium system. N 1s and O 1s image sequences were also measured for some of the systems (results not shown) and these results are consistent with a preference for Fg adsorption on PS rather than PMMA at low concentrations.

Fig. 5 shows the C 1s spectra extracted for pixels of high PS (a) and high Fg (b), for four concentrations between 0.005 and 1.0 mg/ml of Fg(buffer). For the lowest protein concentration, the high-PS region spectrum is very similar to that of pure PS, while for the same concentration, the high-Fg has a strong PS signature, consistent with its location on the PS domains, as shown by the mapping in Fig. 4. As the protein concentration increases to 1.0 mg/ml, the high-PS spec-

tra show an increasing 288.2 eV $\pi_{C=C}^*$ peak from the Fg. For adsorption from a 1.0 mg/ml solution, the Fg signal is stronger than that for PS. As expected, the C 1s spectrum of high-Fg pixels becomes progressively more like pure Fg as the Fg concentration increases. Also, the high-Fg pixels are spread over increasingly large areas as the concentration increases, and the high-Fg location changes from “dominantly on PS” for the two lowest concentrations, to nearly full surface coverage at 1.0 mg/ml. The corresponding results for the PMMA-rich pixels are consistent with the conclusion of PS-preference at low coverage, and whole-surface coverage at high concentration. However, the plots are not shown since the high-PMMA spectra for exposure from low concentration Fg(buffer) solutions are significantly distorted by radiation damage.

3.3.3. Fg(water)/PS/PMMA

Fig. 6 presents color composite maps derived by stack fit analysis of C 1s, N 1s and O 1s image sequences recorded for Fg adsorption from 0.05 mg/ml unbuffered, low ionic strength aqueous solution. In contrast to the corresponding

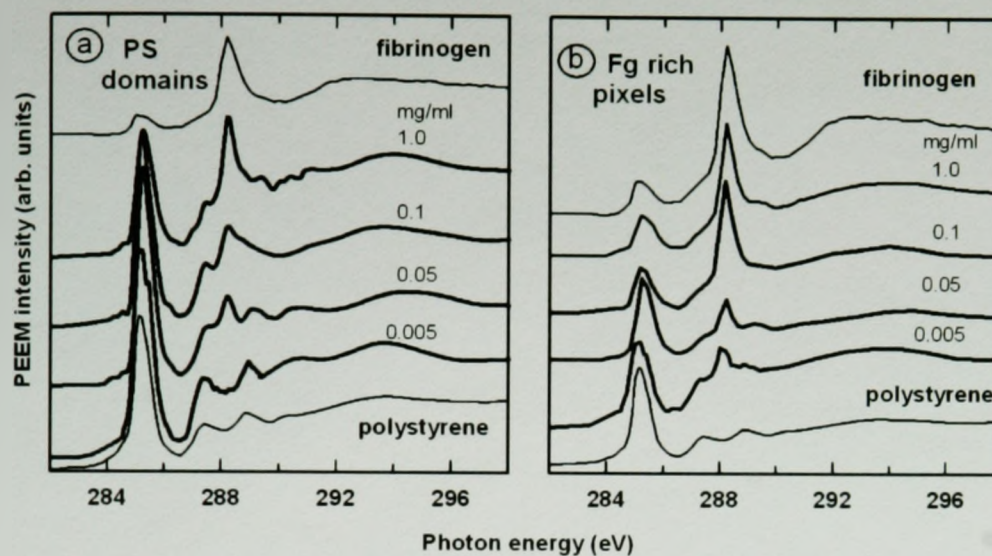


Fig. 5. (a) Spectra from high-PS pixels of the PS component maps generated from stack fit analysis of C 1s image sequences recorded for fibrinogen (0.005, 0.01, 0.05 and 1.0 mg/ml in buffer) adsorbed on the PS:PMMA blend surface. (b) Same for spectra of high-Fg pixels of the Fg component map.

Table 2

Composition^a of selected PS-rich, PMMA-rich and Fg-rich regions from analysis of C 1s image sequences of a PS/PMMA sample exposed for 10 min to phosphate-buffered Fg solution

Region masked	Relative amounts (%) ^b			
	PS	PMMA	Fg	Normalization
(A) 0.005 mg/ml				
PS	87	11	1	1.43
PMMA	28	64	8	1.38
Fg	54	5	41	1.59
(B) 0.05 mg/ml				
PS	79	2	19	1.89
PMMA	21	70	9	2.32
Fg	45	1	55	1.71
(C) 0.1 mg/ml				
PS	58	6	35	1.61
PMMA	21	68	10	1.39
Fg	28	11	61	1.75
(D) 1.0 mg/ml				
PS	37	28	35	1.47
PMMA	25	63	12	1.47
Fg	25	31	43	1.49

^a The values in the table are percentages derived from the average from selected regions (see Fig. 4, for the case of 0.05 mg/ml Fg exposure) of the PS, PMMA and Fg component maps reported by a three-component stack fit analysis (C 1s, O 1s) or a two-component stack fit analysis (N 1s). If the work function of the various parts of the surface, and different systems is the same, the normalization of the intensity of the image sequences (see text) should result in summation of the coefficients to unity. Deviations of that sum from unity indicate systematic errors such as incorrect intensity normalization as well as statistical errors. The normalization factor (right most column) gives a sense of the size of errors.

^b Standard deviations of the curve fits to the selected region spectra are between 5×10^{-5} and 5×10^{-4} .

isotonic buffered system (Fig. 4), the color composite map derived from the C 1s image sequence (Fig. 6a), shows that the PS domains are a relatively pure red color, indicating significantly less Fg present. Instead one sees irregular but fairly intense blue on the PMMA side of the PS/PMMA boundaries. This indicates that, in this unbuffered system, Fg is adsorbed preferentially at the PS/PMMA interface. This interpretation is supported by the O 1s and particularly by the N 1s composite map. We note that the O 1s spectrum of the PS region (in this case, identified by threshold masking the inverted PMMA component map) shows significant Fg signal. This indicates that there is some Fg on the main portions of the PS domains in addition to the strong interface component.

While the color coded composite maps give a compelling visualization of the spatial registry of the components, one can legitimately ask: "is this simply artistry?" To unambiguously demonstrate the origin of these signals, the lower three panels in Fig. 6 are the spectra extracted from the PS-rich, PMMA-rich and Fg-rich pixels which are taken from the color coded regions in the inset images in the spectral plots. These regions were selected by defining a region of interest through a threshold masking procedure applied to the component maps. The interface regions (blue spectra) show a strong Fg signature at each core edge, but with measurable PS and PMMA signals also present, while the spectra of the PMMA (green) and PS (red) domains show negligible Fg signal. The curve fit analysis of these thresholded spectra are summarized in Table 3, along with results from a similar analysis of C 1s, N 1s, and O 1s image sequences for a 0.1 mg/ml Fg/PS:PMMA sample.

Even though fresh areas of the sample were selected for each measurement and the acquisition strategy was designed to stay below 10% modification of the most sensitive PMMA

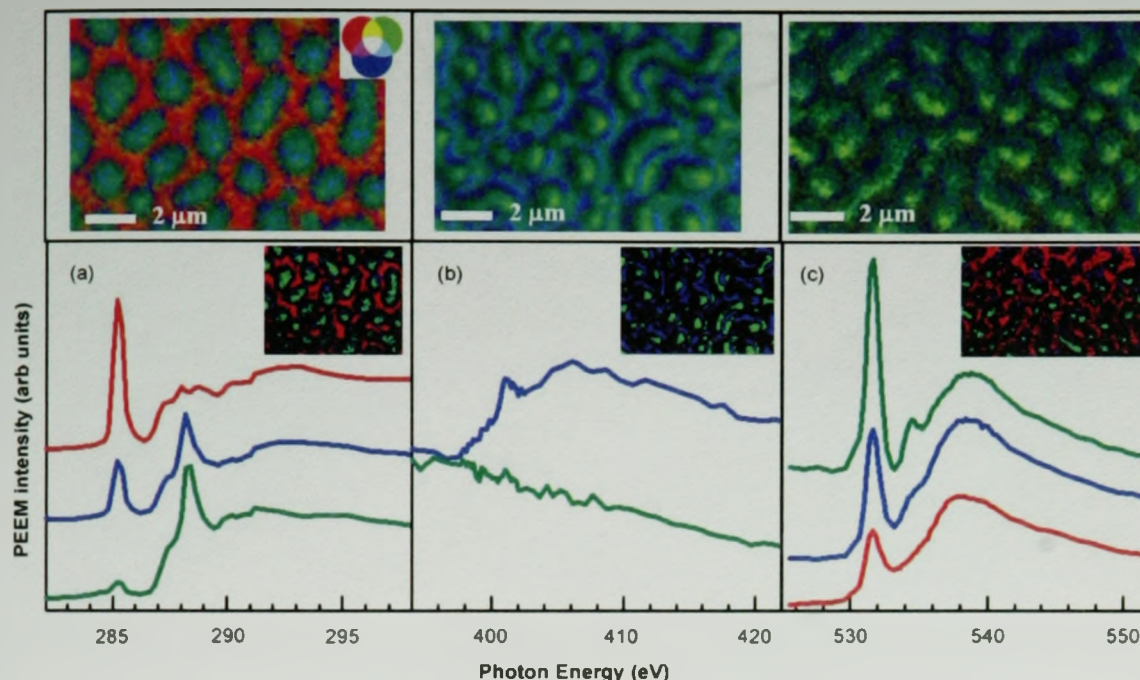


Fig. 6. (a) Color composite map (top) (red: PS; green: PMMA; blue: Fg) and high-PS, high-PMMA and high-Fg spectra derived from a C 1s image sequence recorded for 0.05 mg/ml Fg(water) (bottom). The inset map in the spectral plot indicates the region from which the spectrum was extracted, identified by threshold masking the component maps. (b) Same for N 1s image sequence. In this case, only a two-component fit was carried out (green: PS and PMMA; blue: Fg). (c) Same for O 1s image sequence. The image sequences were collected over three different regions of the sample which is why the domain patterns differ for each core edge study.

component, the radiation dose used was still too high for a damage free analysis. This is indicated by the presence of (excessive) 285 eV signal in the C 1s spectra of PMMA domains and by the intensity of the N 1s $\rightarrow \pi^*$ transition which is lower than in the pure-Fg spectrum (compare Figs. 3 and 6). However, while damage may modify the spectra, the characteristic signatures remain identifiable. The protein is strongly adsorbed (since it could not be washed away) and the sample is dry in the PEEM chamber. Thus, we believe it is very unlikely that the decomposition products would have moved far enough away from the fibrinogen adsorption site to affect the spatial mapping results. In future lower dose conditions will be used to avoid damage artifacts in the spectroscopy.

4. Discussion and summary

This work provides the first demonstration that X-PEEM can map selective adsorption of a protein on the different domains of a chemically heterogeneous polymer surface with a spatial resolution better than 0.1 μm . The data from X-PEEM is shown to provide mapping information that is complementary to the total surface concentration data obtained from radiolabeled protein experiments.

Perhaps the most striking result from this study is that at low protein concentration and low ionic strength in un-

buffered medium, the protein adsorbs preferentially at the interface between the PS and PMMA domains. This observation is not unexpected from the point of view that proteins are highly surface active and "prefer" the interfacial environment to any other. In this case the interface is among three "phases" (water, PS, PMMA) instead of the more usual two. Presumably attachment at this location is the strongest, and results in the lowest free energy of the system.

The interdomainal location is not preferred when the protein is in isotonic buffer at pH 7.2. Instead, adsorption occurs predominantly on the PS domains. Differences in the behavior of fibrinogen in these two media may be expected on the basis of a difference in net charge due both to different pH (although this difference is small in relation to the isoelectric point of 5.5 for fibrinogen) and/or to charge screening effects at high ionic strength. However, since there are no formal charges on either PMMA or PS, charge effects at low surface coverage should be minimal. Fibrinogen is less soluble in water than in isotonic buffer and thus would be expected to adsorb more extensively from water. However, the similarity of the isotherms at low coverage (Fig. 2) suggests that the effects of any small solubility difference may be negligible: indeed, the ^{125}I -radiolabeling shows that adsorption is lower from water than from buffer. For the moment there is no obvious reason for the difference in adsorption patterns from the two media. It may be speculated that conformational effects may play a role in these phenomena.

Table 3
Composition^a of selected PS-rich, PMMA-rich and Fg-rich regions from analysis of C 1s, N 1s, and O 1s image sequences of a Fg(water)/PS/PMMA samples

Region masked	Relative amounts (%) ^b			
	PS	PMMA	Fg	Normalization
(A) 0.05 mg/ml Fg(water)				
C 1s				
PS	77	23	0	1.79
PMMA	9	72	19	1.72
Fg	25	31	44	1.92
N 1s ^c				
PS/PMMA	–	91	9	0.85
Fg	–	29	71	1.03
O 1s				
PS	30	0	70	1.02
PMMA	79	17	4	0.72
Fg	0	19	81	0.82
(B) 0.1 mg/ml Fg(water)				
C 1s				
PS	91	0	9	1.44
PMMA	14	78	7	1.01
Fg	67	13	21	1.59
N 1s ^c				
PS/PMMA	–	91	9	1.03
Fg	–	36	64	1.06
O 1s				
PS	32	0	68	0.88
PMMA	63	32	5	0.68
Fg	19	9	72	0.93

^a See footnote a of Table 2.

^b See footnote b of Table 2.

^c N 1s image sequence was only fit to two components as PS and PMMA are indistinguishable at this edge.

Also, it is possible that the phosphate buffer might play a role in directing Fg to the PS domains. While the beamline used for these measurements did not access the required energies, we intend to measure these types of samples at the P 2p or P 1s core edges in the future in order to rule out co-adsorption with phosphate as the source of the difference in the preferred sites of adsorption. In future studies, the effect of different buffers on adsorption site preference could be investigated.

The present results suggest that, for the 10 min exposure employed, thermodynamic factors (binding affinity) rather than kinetic factors control adsorption. It would be interesting to extend the measurements to shorter exposure times to see if the site preference remains the same or changes in a kinetic-controlled regime.

Using hydrophobicity gradient surfaces, it has been shown convincingly that proteins adsorb more extensively and with greater affinity to hydrophobic compared to hydrophilic surfaces [21,22]. It has also been shown by Rapoza and Horbett [14] that Fg in isotonic buffer adsorbs with greater affinity to hydrophobic compared to hydrophilic surfaces. They found that glassy, rigid polymers (such as PS) showed relatively

high fibrinogen adsorption, regardless of whether the polymer was hydrophobic or hydrophilic. However, the binding strength (as measured by elutability) was much lower on hydrophilic polymers and oxygen-containing hydrophobic polymers (such as PMMA). Our results are in accord with these findings in that our radiolabeling data show more extensive adsorption of Fg on PS than on PMMA, and our X-PEEM data show preferential adsorption to the PS domains in the blends at low coverage.

This work has shown that, due to a significant sampling depth, X-PEEM can simultaneously map the chemical structure of a thin film polymer support and sub-monolayer amounts of adsorbed protein. We believe that this approach to the study of protein adsorption will have important applications in the design and surface characterization of biomaterials, e.g. in sub-micron spatial patterning of proteins at the biological-biomaterial interface. These methods may also be useful in other applications where spatial selectivity of adsorption is important (e.g. protein separation and purification). Future work will explore extension of the technique to competitive adsorption in multi-protein systems (e.g. plasma, tear fluid). For these systems, it is anticipated that heavy atom labeling will be required to differentiate proteins one from another.

Acknowledgements

This research is supported by Natural Science and Engineering Research Council (NSERC, Canada) and the Canada Research Chair programs. X-ray microscopy was carried out using PEEM2 at the ALS (supported by DoE under contract DE-AC03-76SF00098) and the Canadian PEEM at SRC (supported by NSF under award DMR-0084402). The Canadian PEEM was funded by NSERC. Cynthia Morin acknowledges the support of an ALS graduate fellowship during which time most of this work was performed.

References

- [1] D.G. Castner, B.D. Ratner, *Surf. Sci.* 500 (2002) 28.
- [2] M. Tirrell, E. Kokkoli, M. Biesalski, *Surf. Sci.* 500 (2002) 61.
- [3] A.P. Hitchcock, C. Morin, Y.M. Heng, R.M. Cornelius, J.L. Brash, *J. Biomater. Sci. Polym. Ed.* 13 (2002) 919.
- [4] C. Morin, H. Ikeura-Sekiguchi, T. Tyliczszak, R. Cornelius, J.L. Brash, A.P. Hitchcock, A. Scholl, F. Nolting, G. Appel, A.D. Winesett, K. Kaznatcheyev, H. Ade, *J. Electron. Spectrosc.* 121 (2001) 203.
- [5] A.I. Bloom, P.T. Thomas (Eds.), *Haemostasis and Thrombosis*, Churchill Livingstone, New York, 1987.
- [6] S.M. Slack, T.A. Horbett, *J. Biomater. Sci. Polym. Ed.* 2 (1991) 227.
- [7] S. Anders, H.A. Padmore, R.M. Duarte, T. Renner, T. Stammer, A. Scholl, M.R. Scheinfein, J. Stöhr, I. Seve, B. Sinkovic, *Rev. Sci. Instrum.* 70 (1999) 3973.
- [8] C. Morin, A.P. Hitchcock, H. Ikeura-Sekiguchi, A. Scholl, A. Doran, K. Kaznatcheyev, 2001 ALS Compendium, I.B.N.I. Publication, 2002.
- [9] C. Morin, A.P. Hitchcock, L. Li, X. Zhang, T. Araki, A. Doran, A. Scholl, manuscript in preparation.

- [10] B.L. Henke, E.M. Gullikson, J.C. Davis, *At. Data Nucl. Data Tables* 54 (1993) 181.
- [11] I.N. Koprinarov, A.P. Hitchcock, C. McCrory, R.F. Childs, *J. Phys. Chem. B* 106 (2002) 5358.
- [12] A.P. Hitchcock, et al., *Chemical Record*, manuscript in preparation.
- [13] aXis2000 is a freeware program written in Interactive Data Language (IDL), and available from <http://unicorn.mcmaster.ca/aXis2000.html>.
- [14] R.J. Rapoza, T.A. Horbett, *J. Biomed. Mater. Res.* 24 (1990) 1263.
- [15] Pierce Chemical Company, IODO-GEN Iodination Reagent, 1993.
- [16] E. Regoeczi, *Iodine-Labeled Plasma Proteins*, vol. 1, CRC Press, Boca Raton, FL, 1984.
- [17] B.M.C. Chan, J.L. Brash, *J. Colloid Interface Sci.* 82 (1981) 217.
- [18] B.W. Loo Jr., I.M. Sauerwald, A.P. Hitchcock, S.S. Rothman, *J. Microsc.* 204 (2001) 69.
- [19] M. Gordon, G. Cooper, T. Araki, C. Morin, C.C. Turci, K. Kaznatcheev, A.P. Hitchcock, *J. Phys. Chem. A* 107 (2003) 6144–6159.
- [20] J.H. Brown, N. Volkmann, G. Jun, A.H. Henschen-Edman, C. Cohen, *Proc. Natl. Acad. Sci. U.S.A.* 97 (2000) 85.
- [21] H. Elwing, A. Askendal, B. Ivarsson, U. Nilsson, S. Welin, I. Lundstrom, *Am. Chem. Soc. Symp. Ser.* 343 (1987) 468.
- [22] H. Elwing, S. Welin, A. Askendal, U. Nilsson, I. Lundstrom, *J. Colloid Interface Sci.* 119 (1987) 203.
- [23] D.K. Han, G.H. Ryu, K.D. Park, S.Y. Jeong, Y.H. Kim, B.G. Min, *J. Biomater. Sci. Polym. Ed.* 4 (1993) 401.
- [24] R.G. Craig, G.C. Berry, F.A. Peyton, *J. Phys. Chem.* 64 (1960) 541.

Chapter 6

TOWARDS PRACTICAL SOFT X-RAY SPECTROMICROSCOPY OF BIOMATERIALS

The following work documents the STXM results pertaining to the adsorption of two blood proteins (human serum albumin and fibrinogen) to 3 types of polyurethanes which were characterized by STXM only [HKT&01]. The protein adsorption experiments have been published in the journal of Biomaterials Science, Polymer Edition (J. Biomater. Sci. Polymer Edn. Vol 13, No.8, p 919-937, 2002) and is presented here in published form. The contributions from the author of this thesis were detailed in the introduction.

McMaster University
Department of Chemistry
1280 Main Street West
Hamilton, Ontario, Canada
L8S 4M1

Thursday, September 23, 2004

To whom this may concern:

I am completing a PhD thesis at McMaster University entitled "Soft X-Ray Spectromicroscopy of Proteins on Patterned Polymer Films". I would like your permission to reprint the following journal article in my thesis.

"Towards Practical Soft X-Ray Spectromicroscopy of Biomaterials", Journal of Biomaterials Science, Polymer Edition, Volume 13, No. 8, p.919-937, 2002
A.P. Hitchcock, C. Morin, Y.M. Heng, R.M. Cornelius, and J.L. Brash

I am also requesting that you grant irrevocable, nonexclusive licence to McMaster University [and to the National Library of Canada] to reproduce this material as a part of the thesis. Proper acknowledgement of your copyright of the reprinted material will be given in the thesis.

If these arrangements meet with your approval, please sign where indicated below and return this letter to me by fax at 905-521-2773. Thank you very much. I would like to have this form by October 15th, 2004, in time for the submission of my thesis to McMaster University's School of Graduate Studies.

Sincerely,

Cynthia Morin

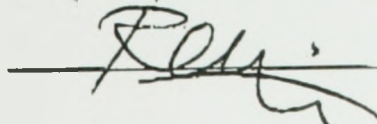
Permission Granted For The Use Requested Above

VSP International Science Publishers

Authorized by: R.E. OTTD ON BEHALF OF DR. M.W.C. WAHLS

Title: SENIOR ACQUISITION EDITOR

Date: 28/9/04

Signature: 

J. Biomater Sci. Polymer Edn, Vol. 13, No. 8, pp. 919—937 (2002)

© VSP 2002.

Also available online.. www.vspub.com

Towards practical soft X-ray spectromicroscopy of biomaterials

A. P. HITCHCOCK*, C. MORIN, Y. M. HENG[†], R. M. CORNELIUS and J. L. BRASH

Brockhouse Institute for Materials Research, McMaster University, Hamilton, ON, Canada, L8S 4M1

Received 21 December 2001; accepted 11 April 2002

Abstract—Scanning transmission X-ray microscopy (STXM) is being developed as a new tool to study the surface chemical morphology and biointeractions of candidate biomaterials with emphasis on blood compatible polymers. STXM is a synchrotron based technique which provides quantitative chemical mapping at a spatial resolution of 50 nm. Chemical speciation is provided by the near edge X-ray absorption spectral (NEXAFS) signal. We show that STXM can detect proteins on soft X-ray transparent polymer thin films with monolayer sensitivity. Of great significance is the fact that measurements can be made in situ, i.e. in the presence of an overlayer of the protein solution. The strengths, limitations and future potential of STXM for studies of biomaterials are discussed.

1. INTRODUCTION

The adverse effects of implanted biomaterials (regardless of intended anatomic location) begin with the selective interactions of blood proteins with the surface of the biomaterial [1, 2], typically a polymer. In the work reported here, soft X-ray spectromicroscopy is being developed to investigate a number of issues related to selectivity in the first contact of biological systems with polymers which are heterogeneous at the surface through patterning or intrinsic surface or bulk phase segregation. Demonstration of the ability to detect and map adsorbed protein at the monolayer level on surfaces with lateral chemical differentiation is our initial target. Eventually we seek to track site selectivity in the adsorption of specific proteins from mixtures, although this is likely to require labeling techniques since soft X-ray spectroscopy cannot readily distinguish different proteins.

*To whom correspondence should be addressed. E-mail: aph@mcmaster.ca

[†]present address: The Hospital for Sick Children, 555 University Avenue, Toronto, ON Canada M5G 1X8.

Soft X-ray spectromicroscopy (also known as near edge X-ray absorption fine structure or NEXAFS microscopy) is finding increasing use in the analysis of soft materials, on account of its ability to probe chemical complexity quantitatively on spatial scales of 50 nm or better, as well as the versatility with which it can be adapted to a wide range of problems. Reviews of soft X-ray spectromicroscopy techniques, instrumentation, and a broad survey of results have been presented recently [3-6]. Inner-shell excitation or NEXAFS spectroscopy [7] is used as the chemically sensitive image contrast mechanism. For the past few years we have been exploring two techniques of soft X-ray spectromicroscopy for the study of biomaterials and the interaction of biomaterial surfaces with biological subsystems, particularly proteins. Scanning Transmission X-ray Microscopy (STXM) uses a focused X-ray probe with sample scanning and synchronized detection of transmitted X-rays to measure the wavelength dependent optical density through a column of material. Although not intrinsically surface sensitive, it is possible to detect, and thus quantitatively map the distributions of surface species such as proteins if the NEXAFS spectrum of a surface species is sufficiently different from that of the bulk biomaterial constituents. STXM in the water window energy range (200—520 eV) can be applied to samples in vacuum, in air or He at atmospheric pressure, and, of greatest importance to biomaterials, to wet samples enclosed in a cell equipped with X-ray transparent windows.

In this paper we describe only STXM results. We are also engaged in a parallel effort for developing X-ray photoelectron emission microscopy (XPEEM) for biomaterial studies. XPEEM uses large area X-ray illumination (50 μm \times 50 μm , at the facility we use) and an electron lens system to record images of the spatial distribution of electrons ejected from a surface following X-ray absorption. Because the electron yield is proportional to the X-ray absorption coefficient, chemical identification and mapping can be derived from the wavelength dependence of the image contrast. The electron lens systems used are most sensitive to the numerous low energy secondary electrons rather than the relatively few primary photoelectrons. Thus the sampling depth is of the order of 5—10 nm, considerably larger than techniques based on energy resolved electron analysis such as X-ray photoelectron spectroscopy (XPS). In addition to chemical sensitivity, XPEEM signals are also very sensitive to topography, local work function variations, and charging, and thus deriving quantitative maps from XPEEM data is much more complicated than with STXM. Finally XPEEM requires a ultrahigh vacuum sample environment, which is not compatible with studies of biomaterials under wet conditions.

2. EXPERIMENTAL

2.1. X-ray microscopy instrumentation and techniques

Soft X-ray scanning transmission X-ray microscopy (STXM), developed by Kirz, Jacobsen, Ade and co-workers at the National Synchrotron Light Source (NSLS)

[3, 8, 9], is now implemented at several other synchrotron facilities (Advanced Light Source (ALS), Pohang Light Source), and instruments are under construction elsewhere (BESSY, Swiss Light Source (SLS), Canadian Light Source). Panel (a) of Fig. 1 is a sketch of the STXM experiment at the undulator beamline 7.0 at the Advanced Light Source, where this study was performed. The undulator produces high brightness X-rays which are passed through a spherical grating monochromator to select a narrow photon energy range (typically ~ 150 meV). The beam of monochromated soft X-rays is then focused to 50 nm or less by a Fresnel zone plate, then passed through an order sorting aperture to select only the first order diffraction of the zone plate. X-rays transmitted through the sample are detected by conversion to visible light by a fast phosphor, followed by photon detection in single photon counting mode. To obtain an image at a given photon energy, the sample is raster scanned through the focal point while recording the intensity of transmitted X-rays (Fig. 1b). Alternatively, the photon energy can be scanned while sitting at a fixed spot on the sample to acquire the NEXAFS spectra of features of interest (Fig. 1c). The most useful mode is to acquire the NEXAFS signal over a whole field of view, by recording image sequences or stacks [10] (Fig. 1d). Post acquisition analysis of image sequence data is used to correct for image misalignment, and to generate chemical maps, as discussed further below.

Typical incident intensities in the 50 nm focused spot of existing STXMs range from 10^6 Hz (NSLS X1A, ALS 5.3.2) to 10^8 Hz (ALS 7.0.1) [11, 12]. High brightness third generation light sources are particularly useful to achieve high intensities on the sample and thus rapid scan rates. With sufficient flux, and suitable control and acquisition interfacing, rapid scan rates (currently, 0.2 to 1 ms per pixel at the ALS), and thus high efficiency analytical microscopy, can be achieved. Radiation damage is a concern, but the damage rate relative to the signal acquisition rate is much smaller than in electron microscopy [13]. In these studies we characterize damage rates, we check for extent of damage after key measurements, and we discard data acquired where excessive damage has occurred. STXM is used analytically by acquiring NEXAFS spectra at one location (point mode), along a line (line mode), or through collection of full image sequences (image mode). All of these modes were employed in these studies and are illustrated below.

The transmitted X-ray intensity (I) is converted to absorbance (optical density) by using the Beer-Lambert law, $A = -\ln(I/I_0) = \mu\rho t = \sigma t$, where I_0 is the incident flux, I is the transmitted flux, μ is the mass absorption coefficient, ρ is the density, t is the thickness and σ is the linear absorption coefficient. The incident flux (J_0) is recorded independently with the sample removed (single beam mode of optical spectroscopy). The measured signal averages over a column of the sample and thus it is generally considered 'bulk'-sensitive. However, thin samples (50—200 nm of organic matter at a carbon density of ~ 1 g/cm³) are needed to achieve adequate

transmission in the 250—1250 eV soft X-ray range. When the sample is this thin, the surface region (outer ~10 nm) contributes significantly to the transmission mode signal and thus large surface species such as adsorbed proteins can be detected, as illustrated below. In this study, the sample thickness is such that absorption saturation is avoided and there is a linear relationship between absorbance and the thickness-density product.

2.2. Data analysis methods

Point spectra, linescan spectra, images, or image sequences are converted to quantitative chemical information (point, line or area compositional maps) by spectral fitting on a pixel-by-pixel basis using linear curve fitting procedures [14-16]. These methodologies, along with many other image and spectral data processing procedures used in this work were accessed by the aXis2000 program [14].

In order to generate quantitative chemical information we fit the spatially resolved NEXAPS signals with reference spectra on a pixel-by-pixel basis. The reference spectra are recorded separately, generally from pure materials. They are placed on absolute linear absorption scales so that the fit coefficient for a given component at a given pixel is the thickness of that component at that position. The ratio of that thickness to the sum of thicknesses of all components fitted is then a measure of the local composition. The array of fitting coefficients for a given component, derived by fitting the individual pixel spectra to linear combinations of reference spectra, is a quantitative chemical *component map*. The fits can be carried out using singular value decomposition [15, 16], linear regression, or a conjugate gradient algorithm. The fit coefficients can be constrained to be positive or they can be treated as freely adjustable parameters. Each methodology provides maps of residuals and a statistical analysis of the errors. Comparison of the results from different algorithms helps build confidence in the significance of weak signals such as those associated with proteins on polymer surfaces. Where vertical scales are provided for the component maps in the figures shown below, these indicate the estimated thickness in nm of that component, if it was pure. Typically a given pixel can have contributions from 3 or more components. Estimated uncertainties are 10 - 15%. Systematic errors are considerably larger than statistical errors (the latter are typically 1 - 3% for the majority components). The uncertainty in the quantitation of the weak signal from surface adsorbed proteins is considerably higher — perhaps as much as 50%. In addition to grayscale maps of individual components, we present color maps where the intensity of the red, green or blue component gives the spatial distribution of that component over the region mapped. In all color maps presented here we have individually byte-scaled each component and thus the intensity of one component relative to the other is not properly represented. This approach provides clearer information of spatial localization of the components, since it makes the weak protein signals visible against the much stronger polymer components. With byte-rescaling one must be careful in interpreting intermediate colors, although they do indicate regions where multiple components are present in the column sampled.

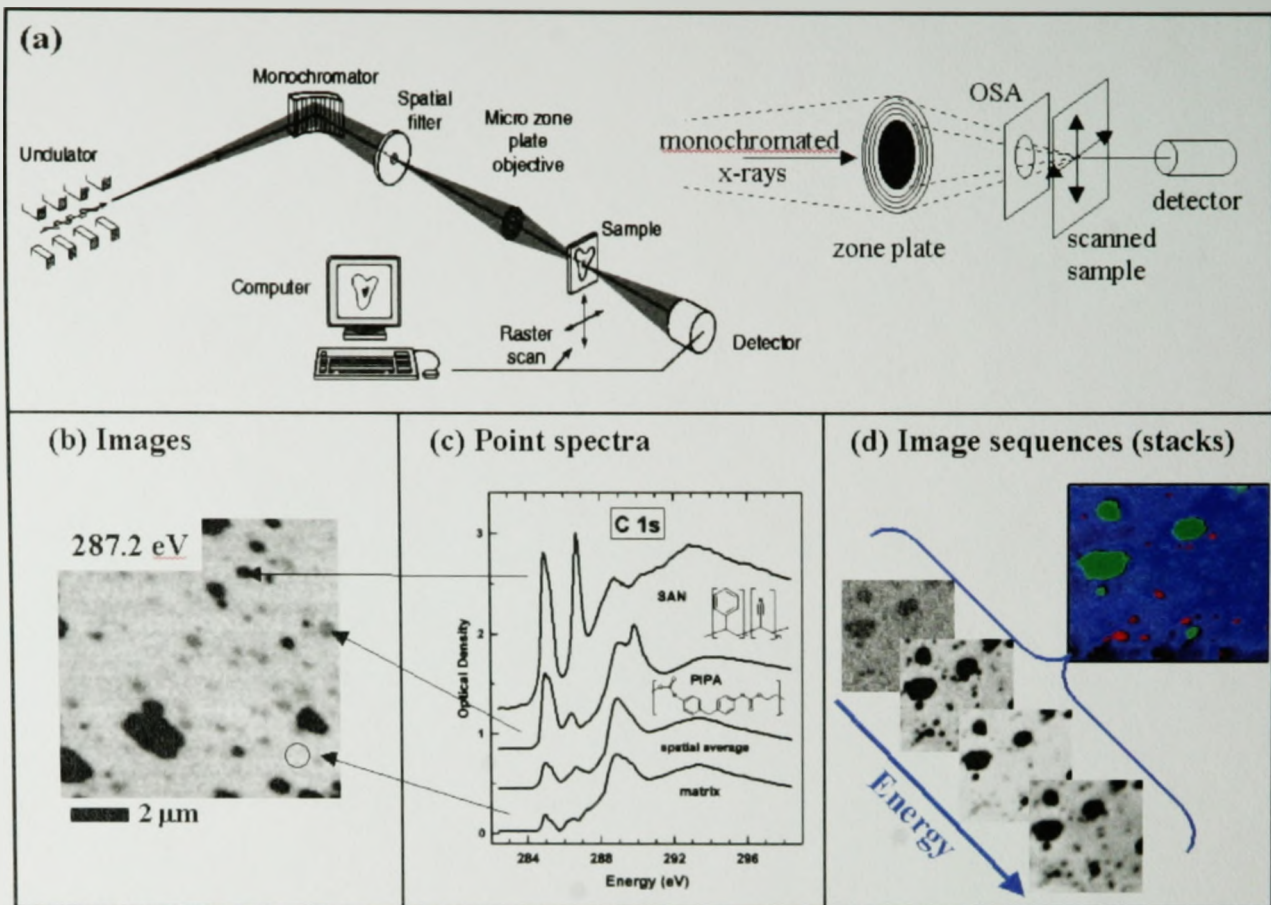


Figure 1. (a) Schematic of undulator beamline 7.0 and the STXM endstation at the Advanced Light Source (ALS) BL 7.0. The inset shows details of the STXM optics. (b) Image of sample #355, a compressed polyurethane foam with styrene acrylonitrile (SAN) and poly-isocyanate poly-addition product (PIPA) filler particles. This image was recorded at 287.2 eV, the energy of the C $1s \rightarrow \pi^*$ CN transition at which the SAN particles selectively absorb. (c) Spectra from spatially selected regions compared to a defocused sample average spectrum. These spectra were actually obtained from an image sequence, but equivalent point spectra can be acquired with the STXM. (d) Illustration of the image sequence (stack) concept. Four of 120 images are displayed, along with a color coded chemical constituent map derived by pixel-by-pixel curve fitting (R = PIPA, G = SAN, B = matrix).

2.3. Substrates and protein exposure methods

2.3.1. Materials.

2.3.1.1. *Substrates.* Three different substrates were used, all provided by Dow Chemical. All three consist of a compressed polyurethane foam, with a TDI (toluene diisocyanate) hard segment and a butane oxide (BO) soft segment. The three differ with regard to types of filler particles. One substrate (code #355) contains poly(styrenecoacrylonitrile (SAN) and poly-isocyanate poly-addition product (PIPA, a methylene diphenyl diisocyanate (MDI)-based hard segment-like material), both referred to as copolymer polyol (CPP) filler particles. The second substrate (code #530) contains only SAN particles. The third substrate (code #529) contains only PIPA particles. The synthesized foams were cryo microtomed to 100 nm thickness and multiple sections were placed either on TEM grids or on 4-pane Si_3N_4 windows (2 x 2 array 1.25 x 1.25 mm membrane, 75 nm thick; frame size is 7.5 mm x 7.5 mm, 200 μm thick Si). The silicon nitride (Si_3N_4) windows were obtained from Silson Ltd. [17] and were rigorously cleaned to semiconductor industry standards by the manufacturer. They were removed from plastic storage capsules and used without further surface preparation.

2.3.1.2. *Deionized water.* From Sigma, HPLC water, residue after evaporation <0.0003%.

2.3.1.3. *Protein.* Human serum albumin (HSA) was from Behringwerke AG, Marburg, Germany, and is reported to be homogeneous as judged by sodium dodecyl sulphate polyacrylamide gel electrophoresis (SDS-PAGE). Fibrinogen (Fg) was from Calbiochem, San Diego, California, USA. It is prepared from human plasma and is plasminogen depleted. It is reported to be >95% clottable by thrombin, and is homogeneous as judged by SDS-PAGE.

2.3.1.4. *Buffers.* The phosphate buffer saline packs were from Pierce, Rockford, IL, USA.

2.3.2. *Sample preparation and mounting methods.* Dry sections of the polyurethanes (#355, #529 or #530) deposited on a TEM grid were exposed for 20 min to 1 ml of 0.1 mg/ml protein solution (albumin or fibrinogen) in deionized H_2O or phosphate buffer. For the sample in Fig. 3, the droplet of solution was allowed to dry out on the surface, thus depositing 0.1 mg over perhaps 0.5 mm^2 . This corresponds to an average thickness of 200 nm (assuming $\rho = 1 \text{ g/cm}^3$) For the sample in Fig. 4, a 5 μl drop of 0.1 mg/ml Fg in saline phosphate buffer was deposited over a #355 section (deposited on a Si_3N_4 window). Such a drop covers an area greater than that of the section itself. At the end of the 20 minute exposure time, the drop had not evaporated. Three consecutive rinses of the remaining drop were done by sucking in and out the drop with 50 μl volumes of deionized water. The sample was then loaded into the STXM. For the sample in Fig. 5 a #355 section was exposed

to fibrinogen as above. It was then extensively washed to remove excess protein, dried and then rehydrated by adding a drop of water on top of the section. A second window was then placed on top of the first one, thereby creating a water layer over the section between the two windows.

For the samples in Figs 6 and 7, a 5 μ l drop of 0.01 mg/ml Fg in freshly prepared phosphate buffer was deposited over a #355 section on a Si_3N_4 window. A second window was immediately placed over it and the sample was placed in the STXM about 10 min after fabrication. Due to instrumental difficulties, the sample was not measured until 2 h after fabrication.

3. RESULTS

3.1. STXM of CPP containing polyurethanes: substrate characterization

The polyurethane substrates used in this study were supplied by Dow Chemical as cryo-microtomed thin sections placed on TEM grids or silicon nitride windows. They consist of a polyurethane matrix with a TDI hard segment and a butane oxide soft segment, in which one or more types of copolymer polyol (CPP) particles are embedded [18]. These CPP particles provide chemically differentiated domains at the surface with sizes in the 0.1 to 2 micron range, which is well suited to the spatial resolution of current X-ray microscopes. In contrast the 'natural' phase segregation in most polyurethanes is at a 10 - 30 nm scale [18] which is too small for current X-ray microscopy capabilities. Both particle materials — SAN and PIPA — are aromatic and hydrophobic in character, while the matrix of the polyurethane is an aliphatic polyether which is more hydrophilic.

In other studies we have shown that C 1s NEXAFS spectroscopy can readily distinguish the urea and urethane linkages present in polyurethanes; determine polyol content; and identify the types of R and R' groups in a given polyurethane [19-21]. NEXAFS signals in STXM have been used to map key functional groups quantitatively — urea, urethane and polyol in native polyurethanes [22], and the types of filler particles [6, 23]. STXM spectromicroscopy is being used to help understand how filler materials affect mechanical properties such as elastic modulus, tear strength and resiliency, and to aid the development of improved fillers [23].

Figure 1 shows the spectral signatures of the SAN, PIPA and polyurethane matrix, and their spatial distributions in the (#355) substrate. The #530 SAN polyurethane substrate was similar except it did not have any of the small PIPA particles and the SAN particles were somewhat larger than in #355. The #529 polyurethane substrate has only PIPA particles and again, the particle size distribution includes larger PIPA particles than found in #355.

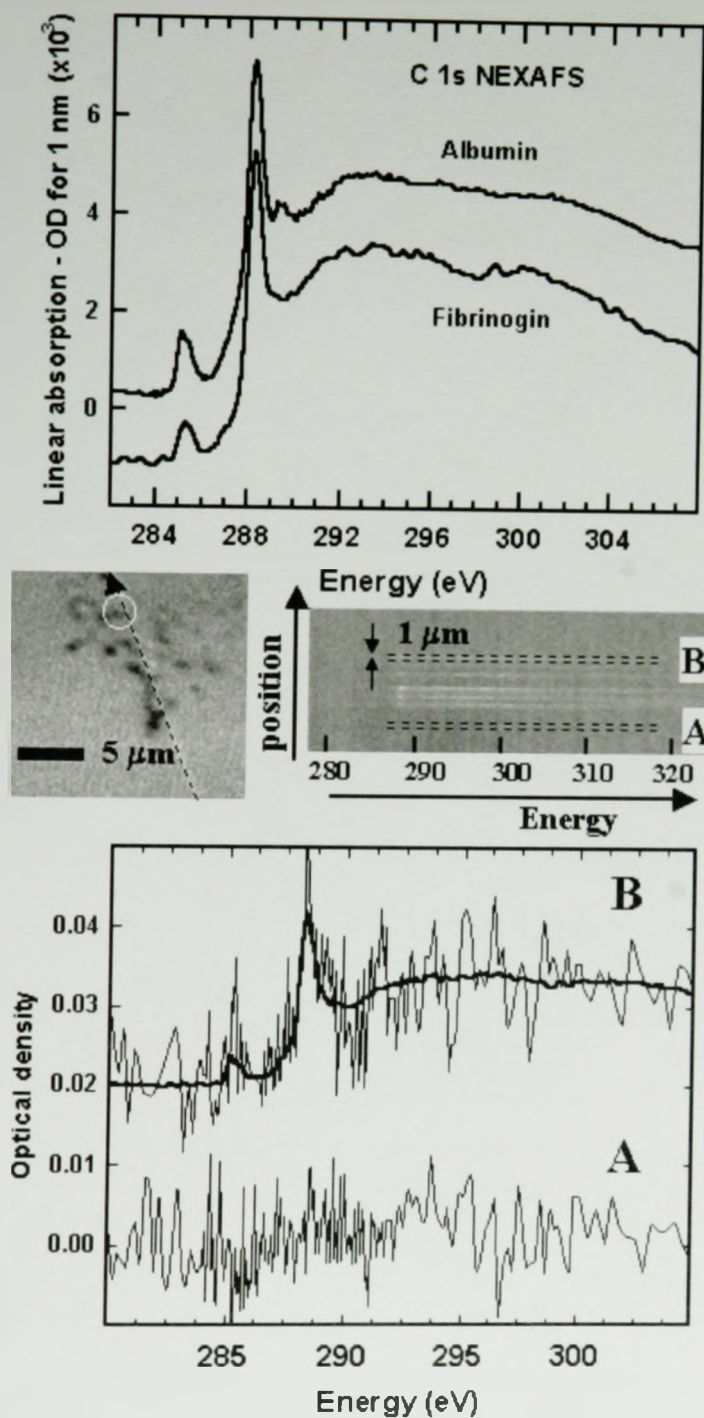


Figure 2. (top) Comparison of the C 1s NEXAFS spectra of albumin and fibrinogen recorded in the STXM. (lower) Illustration of monolayer sensitivity of STXM spectroscopy to pure albumin. The central panel displays an image (288.2 eV) of a deposit of pure albumin on a silicon nitride window (dry), and the signal from a linescan spectrum across the dotted line. The spectra shown in the lower panel were extracted from the linescan by adding signal over less than 1 micron in the areas indicated by dashed lines, labeled A and B. Spectrum B is offset vertically by 0.02 units. The OD of only 0.01 in the C 1s continuum is equivalent to 3 nm protein. An albumin molecule in its standard conformation is 3 x 8 nm, indicating monolayer sensitivity.

3.2. Protein-polymer interaction studies

Eventually we intend to apply our technique to studies of protein decorated polymer samples while they are fully covered with a solution layer that has a composition of that of the relevant biological system, such as blood plasma. At present we are exploring STXM studies of both dry and wet samples to understand and optimize our data acquisition and analysis methods. Results to date indicate that while STXM is essentially a 'bulk' technique, protein monolayer detection is possible, although close to the current limit of sensitivity [6]. In particular, the sensitivity to an adsorbed layer depends on how different the adsorbate spectrum is relative to that of the underlying substrate. We find the most reliable detection of weak protein deposits when we use the full spectral signature in analysis of a full image sequence (40–80 energies) rather than simply imaging at one or a few photon energies.

The upper panel of Fig. 2 presents the C 1s spectra of albumin and fibrinogen. The spectra are rather similar, with each being dominated by the strong peak at 288.2 eV, which is the C 1s(C=O) \rightarrow $\pi^*_{\text{C=O}}$ transition at the amide group of the peptide bond. Each also shows a weak peak at 285.1 eV, associated with C 1s(C=C) \rightarrow $\pi^*_{\text{C=C}}$ transitions at the phenyl groups of aromatic amino acids. One small difference between the spectra of albumin and fibrinogen is that albumin has a weak peak at 289 eV which is not seen in fibrinogen. Since each protein has some of each of the 20 amino acids, it is expected that averaging over such distributions leads to very little differentiation. This is in sharp contrast to the isolated amino acids where it is straightforward to identify the amino acid from the C 1s spectrum [24].

The lower section of Fig. 2 explores the STXM detection limits for pure protein in the absence of any other organic material. The deposit of albumin from a very dilute solution on a clean silicon nitride window shows a readily differentiated C 1s spectrum typical of protein which is three to four times more intense than the noise in a blank (the spectrum from an equivalent length of the adjacent window which does not have deposited protein). The optical density associated with the protein signal in the circled region is equivalent to a sample thickness of 3 nm, approximately the expected thickness of an albumin monolayer.

Figure 3 reports the result of a measurement of a sample consisting of human serum albumin deposited onto the #529 PIPA polyurethane substrate. This sample was prepared by placing a drop of a 1 mg/ml solution onto the microtomed section supported on a 3 mm TEM grid. An uneven distribution of the albumin was left on the surface after solvent evaporation. A region at the edge of a thick deposit was chosen to explore the detection sensitivity. The strength of the protein-like C 1s NEXAFS signal, in the regions where the map indicates the weakest signal which can be attributed to protein (circle in Fig. 3), is approximately equivalent to a monolayer. This sample was not prepared as a controlled biomaterial — protein interaction but it is of historical interest since it was our first demonstration of the surface sensitivity of STXM and thus the viability of the technique.

Figures 4–7 show results from mapping fibrinogen (Fg) adsorbed on a microtomed section of the 2-filler #355 polyurethane system presented in Fig. 1. These

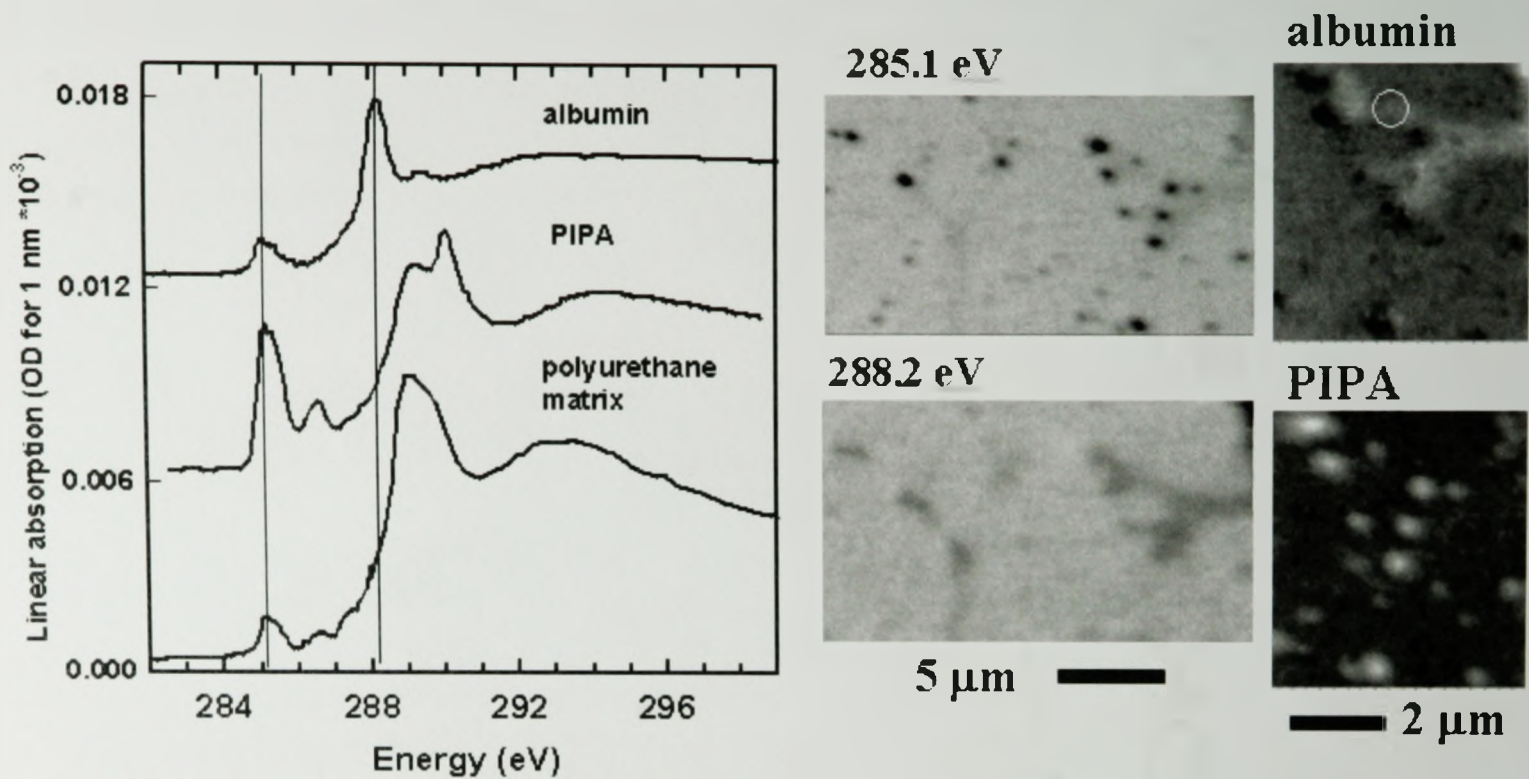


Figure 3 Reference spectroscopy (left), transmission images at 285.1 eV (highlighting PIPA) and 288.2 eV (highlighting protein) (center); and (right) component maps of albumin and PIPA derived from a C 1s image sequence recorded from a thin section sample of #529 (PIPA-in-TDI polyurethane) with deposited albumin, measured in the dry state. In the weakest regions of the albumin 'smear' (e.g. the circled region), the signal is at the monolayer level.

figures exemplify four different steps in the evolution of our ability to detect proteins on polymer surfaces. For the sample shown in Fig. 4, the fibrinogen was adsorbed on the sample by immersion for 20 min in a dilute solution (0.1 mg/ml) in buffer. Excess protein solution was removed by thorough rinsing without taking the sample through the air-water interface. The sample was then dried. The microtomed sample has three classes of chemical constituents exposed at the surface — polyether-rich matrix, SAN and PIPA. The left part of Fig. 4 plots the reference spectra used in the data analysis. The labeled component maps indicate the spatial distribution of the identified components. The residual shows a map of the difference between the fit and the actual image sequence, integrated over the full energy range (54 energies between 282 and 292 eV). The residual map represents deviations between the fit and the measured signal of less than 5%. The spatial distribution of the residuals indicates that the SAN reference spectrum is not a perfect match to the SAN in this sample. While there is some misidentification in these maps associated with limitations of the reference spectra and statistical noise, the high signals in the Fg map indicate positions of preferred adsorption on the surface. The registry of the protein relative to the other components is indicated in the final part of Fig. 4 namely the color coded composite component map in the lower right part. Here the individual SAN, PIPA and protein maps have been combined by assigning red to SAN, green to PIPA and blue to fibrinogen. The intensities within each color have been byte scaled, so that the very weak protein signal can be located relative to the strong SAN and PIPA signals. In this preparation, we find that fibrinogen has a preference to be attached to the matrix beside the SAN particles, with also indication from the orange color of some adsorption on top of the SAN particles.

The sample examined in Fig. 5 was prepared as that for Fig. 4 but, just prior to STXM analysis it was rehydrated with a small drop of deionized water then capped by a second silicon nitride window to form a wet cell. In this measurement we wished to explore the ability of STXM to detect protein adsorbed on a polymer in an environment of reduced contrast caused by the X-ray absorption of an aqueous overlayer of a few micrometers in thickness. The results indicate that STXM can detect adsorbed proteins on polymers in the presence of thin aqueous overlayers. Furthermore the amount of fibrinogen detected is in the monolayer range in some regions. In addition to the color coded composite component map, Fig. 5 shows a fit to the C 1s NEXAFS spectrum extracted from pixels which have high fibrinogen content. These pixels were identified by generating a binary mask based on an intensity threshold for the fibrinogen map (threshold set to 60 nm), and using that mask to define the region of interest for spectral extraction from the full image sequence. The spectrum in the high-Fg region is primarily that of the matrix rather than SAN. We have compared this analysis to that of the adjacent SAN particles (not shown). The quality of the fit is equally good. The amount of Fg determined on top of the SAN particles is only 10 nm, a signal level similar to the residual of the fit.

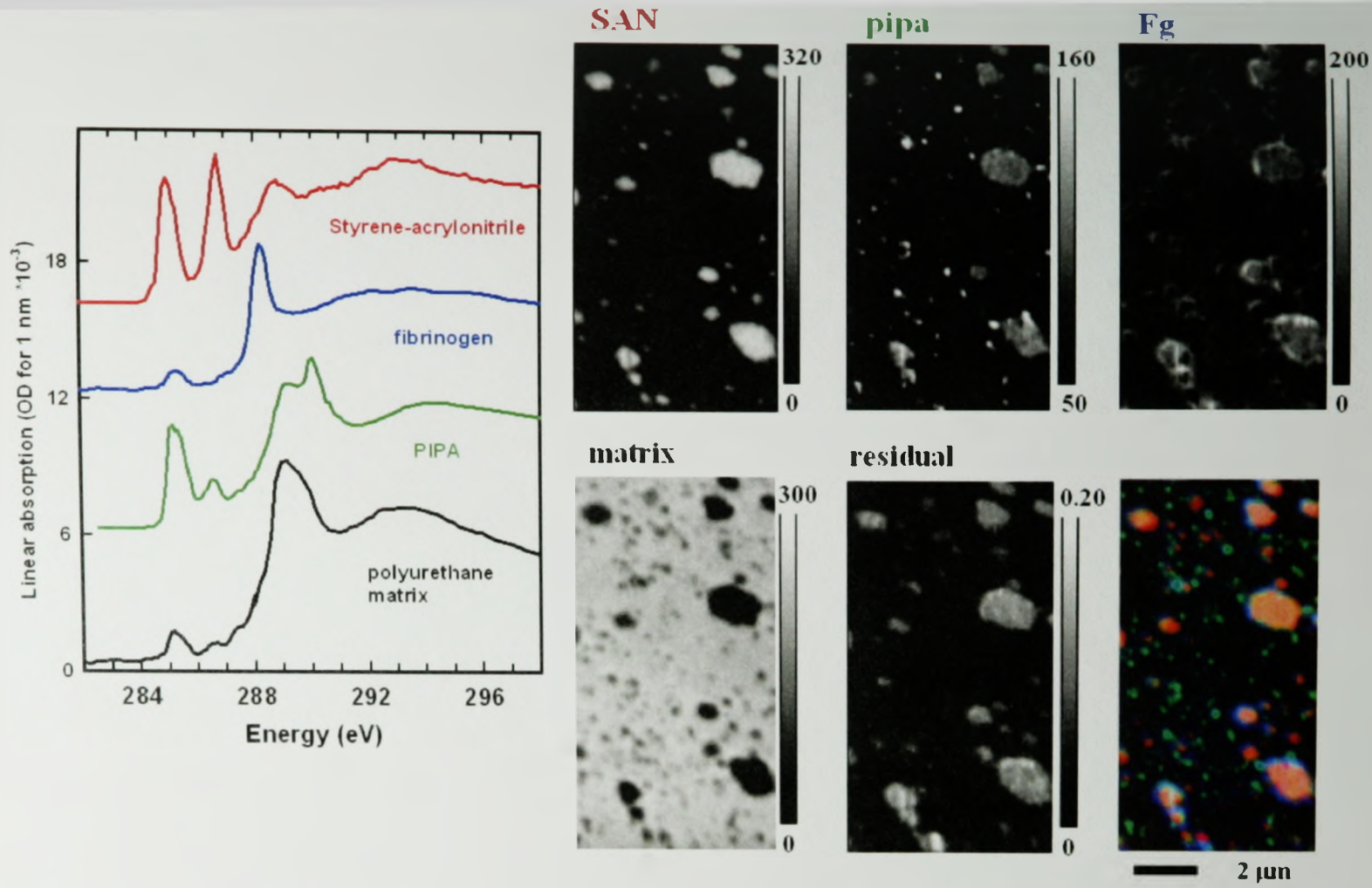


Figure 4 Analysis of STXM of fibrinogen adsorbed on #355 (TDI polyurethane with PIPA and SAN filler particles) measured in the dry state. The sample was prepared by a true adsorption process from buffer at low concentration (0.1 mg/ml) followed by carefully washing off the excess protein then drying (left) reference spectra, placed on absolute linear absorption scales. Four of the six 'image' panels are the quantitative component maps of the SAN, PIPA, fibrinogen and matrix components, the vertical gray scale of each is the approximate thickness of that component in nm. The other two are the map of the residuals averaged over the full energy range measured and a color coded component map (red = SAN, green = PIPA, blue = Fg)

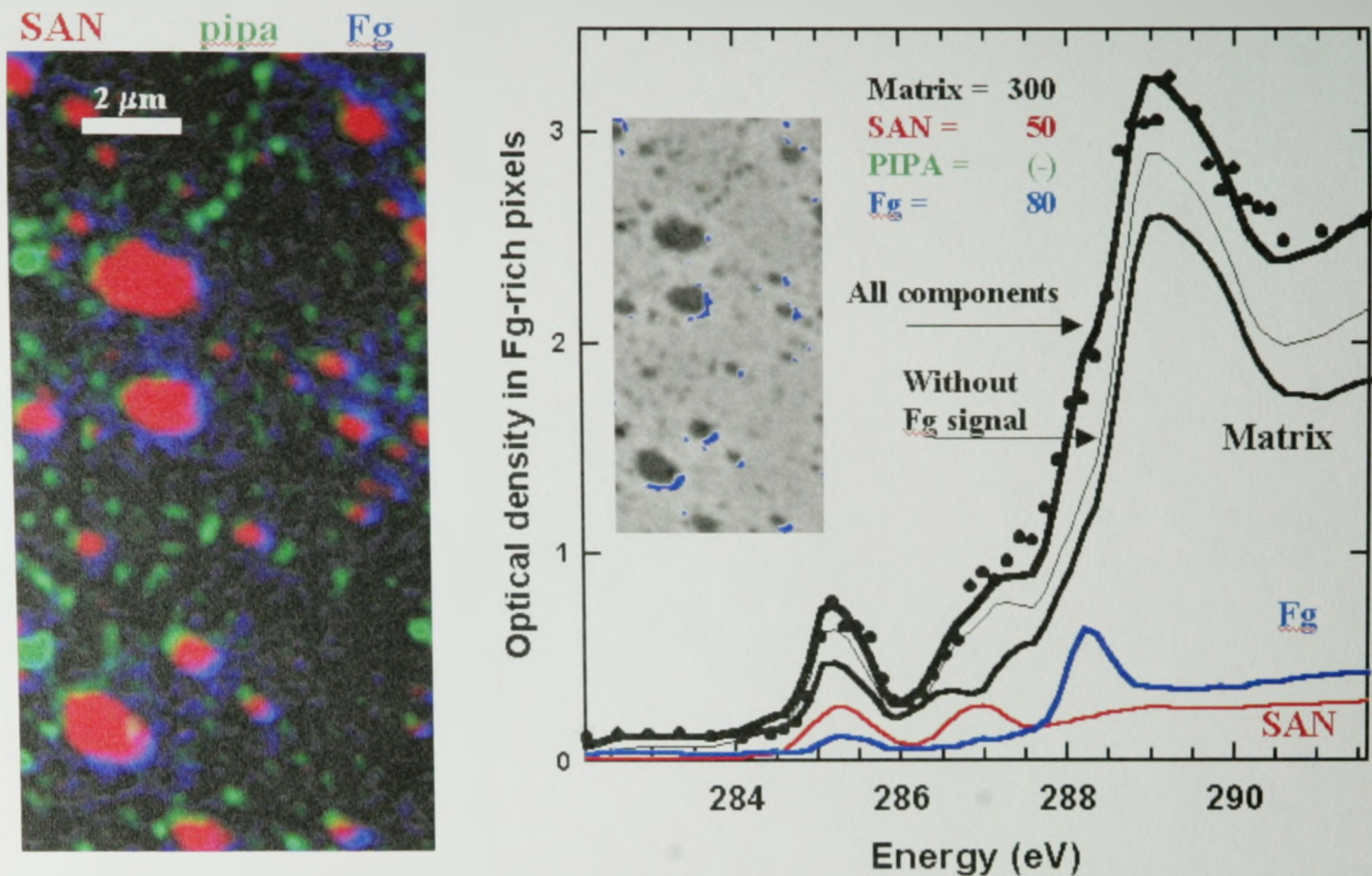


Figure 5 (left) Color-coded composite image derived from a C 1s STXM image sequence of fibrinogen adsorbed from a 0.1 mg/ml buffer solution onto #355 substrate. The measurements were made with the sample rehydrated by a $\sim 1 \mu\text{m}$ thick layer of deionized water in a silicon nitride wet cell, in order to explore the masking effect of overlayer water. The combined byte-scaled SAN (red), PIPA (green) and protein (blue) component maps displays the spatial relationship of the protein relative to the two types of filler particles and the matrix. (right) Spectrum of the blue highlighted regions in the insert image (pixels where the Fg signal indicates more than 60 nm) along with decomposition into the four fitted components. The points are data, the thickest solid line the fit with all components, the thinnest line the fit without fibrinogen, and the other lines the individual components.

These results indicate that fibrinogen has a strong preference to adsorb at the edges of the SAN particles but still to be attached to polyurethane matrix rather than SAN. Similarly, on the #530 substrate the albumin is seen to adsorb preferentially at the edges of the PIPA particles (see Fig. 3). Several factors might explain this preference. First there could be special aspects of this substrate at the interface of the CPP particles and the polyurethane matrix that enhance bonding to proteins. Second, adsorption at edges of harder, aromatic filler particles could reflect 'mechanical trapping'. The SAN particles protrude significantly from the matrix as much as 50 nm based on the total sample thickness derived in the analysis. A simple, perhaps overly naïve, model of such trapping would be entanglement of protein molecules (possibly partially denaturing in the process) on the protruding filler particles. A more sophisticated mechanism could be entropically driven deposition [25] in which the protein in solution would be considered to play a role. At this point it is not possible to define the mechanism of preferential attachment, simply to note there is a clear preference for fibrinogen to adsorb on the matrix side of the boundary of the CPP particles (particularly SAN) and the polyurethane matrix, and that the STXM technique is capable of detecting that fibrinogen in a quantitative manner.

Figure 6 presents the color coded component map derived from a C 1s image sequence measured from a filler-polyurethane sample (#355) with an overlayer of solution containing 0.01 mg/ml fibrinogen in buffer. In this presentation the (R = SAN, G = PIPA, B fibrinogen) map has been superimposed on the gray scale map of the polyurethane matrix component. This is essentially the type of 'in situ' system which is the experiment of ultimate interest, since the solution overlayer contains both buffer salts and protein. These additional solution components might be expected to reduce the contrast of the adsorbed protein relative to the other components. At first we were concerned that the C 1s signal of the protein in the solution could mask the adsorbed protein. Relative to monolayer surface levels, the amount of protein present in a 10 μm high, 1 μm diameter column of a 0.01 mg/ml fibrinogen solution is about the same as that adsorbed at a monolayer coverage on a 1 μm diameter circle of a surface. Thus one might expect a background signal from the free protein over the whole surface, which could mask detection of surface adsorption sites. However, this background signal has not been detected. We speculate that local heating of the solution from the X-ray beam could induce increased thermal motion which might tend to move protein in the solution away from the impinging beam. Experiments to seek the threshold for interference from solution protein will be performed. So far, these results indicate that it is possible to map protein on surfaces from 0.01 mg/ml and even considerably more concentrated solutions since we have measured surface adsorbed protein with protein solution overlayers of up to 0.1 mg/ml concentration.

Figure 7 shows the same Fg/#355 sample investigated at the N 1s edge. This figure plots the N 1s reference spectra of the matrix, PIPA, SAN and fibrinogen, along with the color coded composite map of the SAN, PIPA and fibrinogen

components. The N 1s edge is particularly favorable for studies of protein relative to polymer substrates since proteins have a strong N 1s $\rightarrow \pi^*_{\text{amide}}$ transition at 402 eV, [26] whereas many polymers do not contain unsaturated N environments. The SAN also has a strong N 1s $\rightarrow \pi^*_{\text{CN}}$ transition at 399.8 eV which is readily distinguishable from the higher energy protein signal. However the PIPA and matrix have very similar N 1s signals and thus the PIPA component is less well detected than at the C 1s edge. The quantitative chemical analysis at the N 1s edge gives similar results to that at the C 1s edge (note that the areas measured for Figs 6 and 7 are different). The interesting aspects of the results shown in Figs 6 and 7 are: (1) There was no interference from the protein or buffer salts present in the overlayer solution. (2) The mapping of the fibrinogen derived from the C 1s and N 1s edges is very similar, indicating that detection is not an artifact of a mismatch of model spectra and the unknown. (3) The location of the protein is consistently at the sides of the SAN particles but on the matrix, not on the SAN, in all studies of the protein exposed sample #355.

Together these results constitute clear evidence that STXM can detect proteins at polymer surfaces under aqueous layers containing inorganic buffer salts and protein. We do note that the quantitative accuracy is limited and that the enclosed results may be affected to some degree by residual misalignment. In the as-recorded image sequences there are drifts as large as a few microns in the field of view associated with poor tracking of the zone plate along the X-ray axis (it is necessary to move the ZP with photon energy to maintain focus). Software procedures [10, 14] remove most of this misalignment but there is residual jitter of as much as a hundred nanometers. Recently we have measured the dry Fg/#355 system using a new STXM at the ALS, one which uses a two dimensional interferometer system [12] to maintain a constant field of view. The results were very similar to those presented here.

4. DISCUSSION AND SUMMARY

These results demonstrate that STXM is a viable technique to address questions of chemical differentiation of substrates and protein localization at the surfaces of biomaterials under conditions which are relatively close to their actual use. This is in distinct contrast to vacuum based techniques such as TOF-SIMS, XPS or XPEEM where there is always a question whether the absence of water or buffer changes the character of the interface, e.g. by inducing surface segregation of hydrophobic components. STXM provides information on lateral morphology for both dry and wet samples. This is potentially useful for studying artificially patterned biomaterials, chemical mapping of biomaterial substrates, and quantitative mapping of adsorbed protein relative to the substrate. Perhaps the weakest aspect of the STXM method is the lack of intrinsic depth resolution since the signal at any location is a column average. It is very unlikely that the protein signal arises from anywhere but the polymer surface. However the same cannot be said for the signal from the underlying polymer. In that respect XPEEM should be a

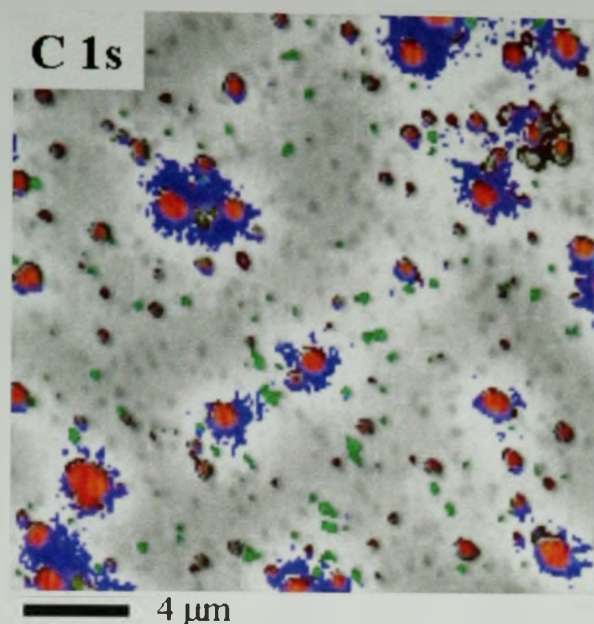


Figure 6. Color-coded composite image derived from a C 1s STXM image sequence of a #355 sample covered with a protein solution (fibrinogen in buffer, 0.01 mg/ml). In this case a byte-scaled combination of the SAN (red), PIPA (green) and protein (blue) component maps has been superimposed on a gray scale image of the polyurethane matrix map. This result was derived from an image sequence measurement of a sample with the fibrinogen buffer solution left over the surface. The overlayer of buffer is estimated from the pre-edge signal to be ~5 microns thick.

useful complement to STXM since it has the potential to provide better surface characterization of polymer substrates at similar spatial resolution. Indeed recently we have made a detailed AFM — STXM — XPEEM comparison of the surfaces of polystyrene— polymethylmethacrylate blends [27] which showed very considerable differences between composition and morphology of the bulk as sampled by STXM, and that of the surface as sampled by XPEEM. The XPEEM and AFM images showed similar morphology, but the conventional interpretation of the AFM based on comparing bulk sample composition with relative areas of the continuous and discontinuous domains, was found to give an inverted assignment of the chemical identity of the domains. On the other hand the much higher spatial resolution of the AFM revealed micro-domain features which were not detected by XPEEM, and were just barely detectable by STXM. As in many other fields, the most effective way to solve complex problems such as biomaterial interfaces is to use multiple techniques with proper recognition of the strengths and weaknesses of each technique. This philosophy has been a hallmark of the scientific career of Dr. Brash, to whom this article is dedicated.

Dramatic improvements are currently underway in scanning transmission X-ray microscopy instrumentation, performance and analysis methodology. Cryo-STXM has been implemented recently at NSLS [28]. Two microscopes with interferometric

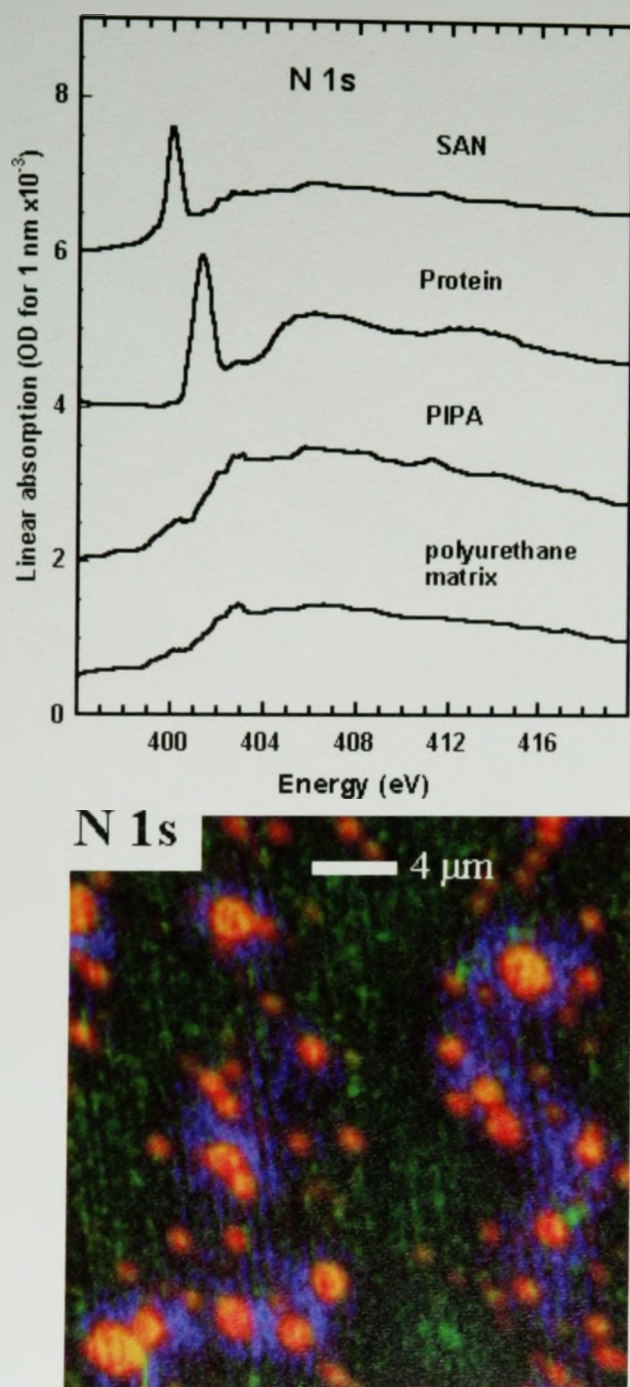


Figure 7. Color-coded composite image derived from a N 1s STXM image sequence of fibrinogen adsorbed from a 0.01 mg/ml buffer solution onto #355 substrate. This is a different area of the same sample for which the C 1s results are plotted in Fig. 6. The N 1s spectra of the pure reference materials are also plotted. The protein spectrum is from albumin recorded at a different synchrotron facility [26], while the N 1s spectra of SAN, PIPA and the matrix were those of the pure #355 material [23].

control of sample-zone plate position have recently been commissioned at the ALS [11]. The interferometric signal provides a precise solution to a major problem in earlier instruments, namely drift in the field of view as the photon energy is scanned. These new instruments will allow detailed studies of many biomaterials problems. In a few years it will be possible to readily carry out orientation contrast studies. Early studies [29] showed that orientation contrast can be an important aspect of polymer X-ray microscopy. However those measurements were extremely tedious since the sample had to be removed, rotated, and the same region found in the new orientation. In a few years time there will be STXM microscopes on beam lines at the ALS, Swiss Light Source, and the Canadian Light Source, which will be illuminated by elliptically polarized undulators (EPU). When proper control of the phase shifting of the separate sections is employed, EPUs can produce linearly polarized light with user selectable, arbitrary orientation [30]. This will allow routine exploitation of polarization contrast which will be important for studying polymeric biomaterials with aligned molecules. Finally, a significant portion of the polymer and biomaterial soft X-ray microscopy research carried out to date has been performed by, or in collaboration with industrial researchers. The rapid recognition by industry of the remarkable value of soft X-ray microscopy techniques attests to the added value NEXAFS microscopy brings to practical problem solving relative to other, more accessible, lab-based analytical microscopy techniques. It may be anticipated that the biomaterials industry will recognize the benefits of STXM for investigating and thus advancing their materials.

Acknowledgements

This work is funded by the Natural Science and Engineering Research Council (Canada) and the Canada Research Chair program. The ALS STXM was developed by T. Warwick (ALS), B. P. Tonner (U Wisconsin Milwaukee) and collaborators, with support from the US DOE under contract DE-ACO3-76SF00098. Zone plates used at the ALS were provided by Eric Anderson of CXRO, LBNL. We thank ALS staff for much assistance and expert operation. We thank especially Ed Rightor, Werner Lidy and Gary Mitchell (Dow Chemical) for providing the polyurethane substrates, and Rick Steele, George Meigs, Eli Rotenberg and Tony Warwick (Advanced Light Source, Berkeley) for their capable work in developing and maintaining the ALS 7.0 beamline and STXM.

REFERENCES

1. R.M. Cornelius and J. L. Brash, *Biomaterials*, **20**, 341 (1999).
2. A.M. Botelho do Rego, O. Pellegrino, J.M.G. Martinho and J. Lopes da Silva, *Langmuir* **16**, 2385 (2000).
3. J. Kirz, C. Jacobsen and M. Howells, *Q. Rev. Biophys.*, **28**, 33, (1995).
4. H. Ade, in *Experimental Methods In The Physical Sciences*, **32**, J.A.R. Samson and D.L. Ederer Ed., Vol. 32, p. 225. Academic Press (1998)
5. H. Ade and S.G. Urquhart, in "Chemical Applications of Synchrotron Radiation" T. K. Sham, ed. World Scientific Publishing (2002)
6. A.P. Hitchcock, *J. Synchrotron Radiation* **8**, 66 (2001)
7. J. Stöhr, *NEXAFS Spectroscopy*, Springer Tracts in Surface Science **25** (1992).
8. H. Ade, X. Zhang, S. Cameron, C. Costello, J. Kirz and S. Williams, *Science* **258**, 971 (1992).

9. H. Chapman, C. Jacobsen and S. Williams, *Ultramicroscopy* **62**, 191 (1996).
10. C. Jacobsen, S. Wirick, G. Flynn and C. Zimba, *J. Microscopy* **197**, 173 (2000).
11. T. Warwick, H. Ade, D. Kilcoyne, M. Kritscher, T. Tyliczszak, S. Fakra, A. P. Hitchcock and H. Padmore, *J. Synchrotron Rad.* **9**, 254 (2002).
12. A.L.D. Kilcoyne, T. Tyliczszak, R. Steele, A.Peter Hitchcock, S. Fakra, K. Frank, C. Zimba, E. Rightor, G. Mitchell, I. Koprinarov, E. Anderson, B. Harteneck, Adam. P. Hitchcock, T. Warwick, H. Ade, *J. Synchrotron Rad.* (2002) in press..
13. E.G. Rightor, A.P. Hitchcock, H. Ade, R.D. Leapman, S.G. Urquhart, A.P. Smith, G. Mitchell, D. Fischer, H.J. Shin and T. Warwick, *J. Phys. Chem. B* **101**, 1950 (1997).
14. aXis2000 is an IDL 'widget' (application), which is available from <http://unicorn.mcmaster.ca/aXis2000.html>. IDL is a Kodak company – www.rsinc.com
15. X. Zhang, R. Balhorn, J. Mazrimas and J Kirz; *J. Struc. Biol.* **116**, 335 (1996).
16. I. Koprinarov, A.P. Hitchcock, C.T. McCrory and R.F. Childs, *J. Phys. Chem. B* **106**, 5358 (2002).
17. Silson Ltd. JBJ Business Park, Northampton Road, Blisworth, Northampton England. NN7 3DW
18. R. Herrington, *Flexible Polyurethane Foams*, 2 ed., The DOW Chemical Company (1997).
19. S.G. Urquhart, A.P. Hitchcock, R.D. Leapman, R.D. Priester and E.G. Rightor, *J. Polymer Science B: Polymer Physics*, **33**, 1593 (1995).
20. S.G. Urquhart, H. Ade, A.P. Smith, A.P. Hitchcock, E.G. Rightor and W. Lidy, *J. Physical Chemistry B* **103**, 4603 (1999).
21. S.G. Urquhart, A.P. Hitchcock, A.P. Smith, H. Ade, W. Lidy, E.G. Rightor and G.E. Mitchell, *J. Electron Spectrosc.* **100**, 119 (1999).
22. E.G. Rightor, G.E. Mitchell, S.G. Urquhart, A.P. Smith, H. Ade, A.P. Hitchcock, A. Aneja and R.J. Wilkes, *Macromolecules* **35**, 5873 (2002).
23. A.P. Hitchcock, I. Koprinarov, T. Tyliczszak, E.G. Rightor, G.E. Mitchell, M.T. Dineen, F. Hayes, W. Lidy, R.D. Priester, S.G. Urquhart, A.P. Smith, H. Ade, *Ultramicroscopy* **88**, 33 (2001).
24. K. Kaznachev, A. Osanna, C. Jacobsen, O. Plashkevych, O. Vahtras, H. Agren, V. Carravetta and A.P. Hitchcock, *J. Phys. Chem. B* **106**, 3153 (2002)
25. K.H. Lin, J.C. Crocker, V. Prasad, A. Schofield, D.A. Weitz, T.C. Lubensky and A.G. Yodh, *Phys Rev Lett* **85**, 1770 (2000).
26. B.W. Loo, Jr., I.M. Sauerwald, A.P. Hitchcock and S.S. Rothman, *J. Microscopy* **204**, 69 (2001).
27. C. Morin, H. Ikeura-Sekiguchi, T. Tyliczszak, R. Cornelius, J.L. Brash, A.P. Hitchcock A. Scholl, F. Nolting, G. Appel, A. D. Winesett, K. Kaznachev and H. Ade, *J. Electron Spectroscopy* **121**, 203 (2001).
28. J. Maser, A. Osanna, Y. Wang, C. Jacobsen, J. Kirz, S. Spector, B. Winn, and D. Tennant, *J. Microscopy*, **197**, 68 (2000).
29. A.P. Smith and H. Ade, *Appl Phys Lett* **69**, 3833 (1996).
30. A.T. Young, E. Arenholz, S. Marks, R. Schlueter, C. Steier, H. A. Padmore, A.P. Hitchcock and D.G. Castner, *J. Synchrotron Rad.* **9**, 270 (2002).

Chapter 7

SUMMARY AND FUTURE WORK

This thesis has presented results dealing with the development of soft x-ray spectromicroscopies, namely scanning transmission x-ray microscopy (STXM) and photoemission electron microscopy (X-PEEM), for the detection of proteins on heterogeneous polymeric surfaces. The impact of this work is that the world now has new quantitative (STXM) and semi-quantitative (X-PEEM) techniques to study sub-monolayer amounts of proteins on polymer surfaces. This capability has many possible applications, including that which motivated my thesis, the development of improved biomaterials for medical applications.

There are a number of experimental avenues that can be explored from this point. These can be divided into 4 areas: improvement of instrumentation, exploration of different substrates and different single proteins, competitive multi protein adsorption, and cell adsorption to bare or protein decorated surfaces.

- **Improvement of instrumentation:**

Several new X-PEEMs are under development (SMART: [FWU&97], [SGF&02], and PEEM3: [FPW&02]). These will use aberration compensation optics and are expected to improve the column transmission by a large amount, enabling higher spatial resolution or higher efficiency than existing instruments. The new technology will dramatically assist with present day challenges of radiation damage when applying X-PEEM to polymers and biological materials. Currently, the signal for ~25 Fg molecules is

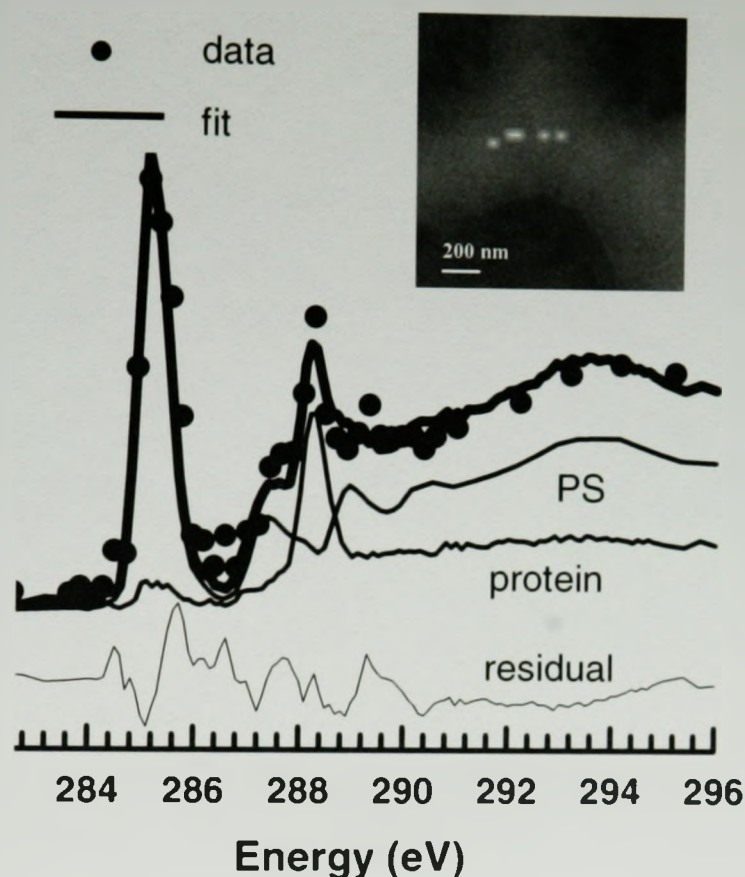


Figure 7.1 Exploring sensitivity for single protein molecule detection with X-PEEM. Fibrinogen (Fg) adsorbed from 0.05 mg/ml prefers the continuous PS domains (lighter) rather than the discrete PMMA domains (darker) of a PS-PMMA blend [MHC&04]. The signal plotted and fit in this figure is from 5 50x50-nm Fg-rich pixels (white) with a total area of ~ 25 Fg molecules.

detectable on PS:PMMA with X-PEEM (see figure 7.1, which is detailed analysis of a subset of figure 5.6). Single proteins may be detected with these improved microscopes, allowing studies of much lower concentrations than have been used in this thesis, and ultimately probing preferential attachment of single proteins on patterned surfaces. A collaborative project is currently in its initial stages to exploit the anticipated enhanced performance of PEEM3 for testing the capability of specially prepared surfaces with templates constructed for binding specific proteins.

- **Substrates:**

The PS:PMMA substrate could continue to be used as a model surface for the future work in competitive multi protein adsorption, cell adsorption to protein decorated surfaces and testing of the improved instrumentation. However, there are some negative aspects associated with this substrate. For example, PMMA is quite radiation sensitive and, at the C1s absorption edge, it has its most intense transition at 288.5 eV, which is only 0.3 eV above that of the strongest feature in proteins (288.2 eV). If one could design a patterned surface with components that are less sensitive to radiation damage, then larger photon fluxes and longer dwell times could be used to measure the sample, and hence better signal statistics, resulting in greater spectral quality and better spatial resolution, could be obtained with the current instruments.

In the hope of improving spectral differentiation, and also dealing with a system with greater differences in bio-affinity, some efforts have lately been deployed in our group by PhD candidate, Li Li, who is using X-PEEM and STXM to study spun cast films of polystyrene grafted with butyl alcohol. Further improvements to the substrates are required to increase the size and density of hydroxyl terminated domains.

A relevant blood compatible biomaterial that could be studied in X-PEEM and STXM is poly [bis(trifluoroethoxy)phosphazene] (PTFEP). This material is inert in biological media because the decomposition products are phosphates and ammonia, and it is known to function well subcutaneously. Also, compared to some materials of medical interests, it was found to adsorb the greatest amount of human serum albumin and the lowest amount of fibrinogen and fibronectin [WGT98]. These trends are considered

favourable for good blood compatibility. Spectroscopically, it would be easy to map this material against proteins because it is rich in phosphorus (P2p at 135 eV), and fluorine (F1s at 697 eV), which are not found in proteins. PTFEP also contains nitrogen (N1s at 390 eV), so NEXAFS differentiation of proteins and this material could be used to generate component maps of the two materials.

- **Competitive multi protein adsorption:**

Another goal of interest is the competitive adsorption of multiple proteins, that is, spatially resolved detection of specific proteins which decorate a polymer surface exposed to a solution containing several proteins. The two proteins I have measured (fibrinogen, albumin) have very similar NEXAFS spectra. However, a study of spider silk (collaboration with M. Pézolet, Université Laval, since September 2004) shows clear spectral differences between the two proteins (sericine and fibroin) of that system. Probably, a more practical method to distinguish different proteins is to use one of a variety of possible tagging methods. For example, Co was found to bind specifically to albumin [BLR03]; immuno-labelling with silver enhanced gold beads has been used in transmission x-ray microscopy (TXM) to locate specific proteins and nucleic acids in cells ([LTJ92], [LYM00], [MDG00]); fluorescent probes have been used in TXM with luminescence detection ([IML94], [M99]). In the latter case, the labelling approach may be supplemented with comparisons to results from confocal microscopy. Recently, our group has made comparisons of STXM (via x-ray absorption spectroscopy) and confocal microscopy (using various fluorescent tags) to map biological components in identical regions of biofilms ([LSL03], [HMZ04]).

- **From proteins to cells:**

Subsequently to the imaging of multi protein surfaces, these surfaces could be exposed to a cell culture, either before or after decorating with a specific protein or peptide (e.g. integrin-type cell adhesion peptides [LFR&97]). Mapping of the interaction of cells on bare or protein patterned surfaces could be explored using X-PEEM or STXM. Cell imaging has already been done extensively in TXM ([FPF&92], [LTJ92], [SNG&95], [KYG&96], [JK98], [LSH&01], [YS02], [LL04]. In STXM, cells and their subcomponents, have also been imaged within biofilm systems ([LSL&03], [HMZ&04]). Imaging of cells in X-PEEM has been a focus of the De Stasio group for a number of years [D94], [DDT&95], [DM97].

In summary, this work has shown the first demonstration of STXM and X-PEEM towards the development of biomaterials. There are several future applications for STXM and X-PEEM to contribute to this field.

Appendix A

This appendix lists some of the projects in which I have been involved since the start of my research career, including the work from this thesis. This is organized into three sections: A.1.) Published work; A.2.) Oral presentations which I presented ; A.3.) Posters which I have presented.

A.1. Published Work

Articles Published, In-Press or Submitted to Peer-Reviewed Journals

10. A. P. Hitchcock, C. Morin, X. Zhang, T. Araki, J. Dynes, H.D.H. Stöver, J. Brash, J. R. Lawrence, G. G. Leppard, *Soft X-ray Spectromicroscopy of Biological and Synthetic Polymer Systems*, J. Electron Spectroscopy (*in press*)
9. C. Morin, A.P. Hitchcock, L. Li, X. Zhang, T. Araki A. Scholl and A. Doran, *Evaluating Radiation Damage in Soft X-ray Microscopy*, J. Electron Spectrosc (*to be submitted*)
8. C. Morin, A. P. Hitchcock, R. M. Cornelius, J. L. Brash, A. Scholl, A. Doran, *Mapping of fibrinogen adsorption PS:PMMA surfaces with photoemission electron microscopy*, J. Electron Spectroscopy 137-140 (2004) 785-794
7. M.L. Gordon, G. Cooper, T. Araki, C. Morin, C. C. Turci, K. Kaznatcheev, and A. P. Hitchcock, *Inner shell spectroscopy of the peptide bond: comparison of the C 1s, N 1s and O 1s spectra glycine, glycyl-glycine and glycyl-glycyl-glycine*, J. Phys. Chem A 107 (2003) 6144-6159

6. L.M. Croll, J. F. Britten, C. Morin A.P. Hitchcock, I. Koprinarov, and H.D.H. Stöver, *Integrating Near Edge X-ray Absorption Fine Structure (NEXAFS) Microscopy and Crystallography: The effects of molecular order on soft x-ray spectromicroscopy*, *J. Synchrotron Rad.* 10 (2003) 265-272
5. A.P. Hitchcock, C. Morin, Y.M. Heng, R.M. Cornelius and J.L. Brash, *Towards practical soft X-ray spectromicroscopy of biomaterials*, *J. Biomaterials Science, Polymer Ed.* 13 (2002) 919-938.
4. A.P. Hitchcock, C. Morin, T. Tyliczszak, I.N. Koprinarov, H. Ikeura-Sekiguchi, J.R. Lawrence and G.G. Leppard, *Soft X-ray microscopy of soft matter - hard information from two softs*, *Surface Reviews and Letters* 9 (2002) 193-202.
3. C. Morin, H. Ikeura-Sekiguchi, T. Tyliczszak, R. Cornelius, J.L. Brash, A.P. Hitchcock A. Scholl, F. Nolting, G. Appel, A. D. Winesett, K. Kaznachejev and H. Ade, *X-ray Spectromicroscopy of immiscible polymer blends: polystyrene-poly(methyl methacrylate)*, *J. Electron Spectroscopy* 121 (2001) 203-224
2. A. S. Wills, N. P. Raju, C. Morin, J. E. Greedan, *Two-Dimensional Short-Range Magnetic Order in the Tetragonal Spinel $\text{Li}_2\text{Mn}_2\text{O}_4$* . *Chem. Mater.* 11 (1999), 1936-1941
1. J. E. Greedan, N. P. Raju, A. S. Wills, C. Morin, S. M. Shaw, J. N. Reimers, *Structure and Magnetism in $\lambda\text{-MnO}_2$. Geometric Frustration in a Defect Spinel*, *Chem. Mater.* 10 (1998), 3058-3067

Not reviewed reports

8. L.M. Croll, C. Morin, I. Koprinarov, A.P.Hitchcock, and H.D.H. Stöver *Optimization of polymer capsules aided by scanning transmission x-ray microscopy* X-ray Microscopy 2002, Grenoble, France, J. de Physique Coll 104 (2003) 507.
7. C. Morin, A.P. Hitchcock, J.L. Brash, A. Scholl, A. Doran, *Developing X-PEEM as a tool for biomaterials analysis: mapping fibrinogen adsorption on PS:PMMA surfaces*, 2002 ALS Compendium, LBNL publication (2003)
6. C. Morin, A.P. Hitchcock, H. Ikeura-Sekiguchi, A. Scholl, A. Doran, K. Kaznachejev, *Optimization of PEEM-2 for studies of organic thin films*, 2001 ALS Compendium, LBNL publication (2002)
5. C. Morin, H. Ikeura-Sekiguchi, T. Tyliczszak, R. Cornelius, J.L. Brash, A.P. Hitchcock, A. Scholl, F. Nolting, G. Appel, A. D. Winesett, K. Kaznachejev and H. Ade, *PS-PMMA blends studied by X ray spectromicroscopy*, 2000 ALS Compendium, LBNL publication (2001)
4. A.P. Hitchcock, C. Morin, H. Ikeura-Sekiguchi, T. Tyliczszak, R. Cornelius, J.L. Brash and H. Ade, *Studies of selectivity in protein interactions with polymer surfaces*, 2000 ALS Compendium, LBNL publication (2001)
3. A.P. Hitchcock, I. Koprinarov, T. Tyliczszak, C. Morin, H. Ikeura Sekiguchi, C. McCrory, R.F. Childs, L.M. Croll and H. Stöver, *Polymer microstructure optimization aided by STXM spectromicroscopy*, 2000 ALS Compendium, LBNL publication (2001)

2. A.P. Hitchcock, C. Morin, H. Ikeura-Sekiguchi, A. Scholl, F. Nolting and D.G. Castner, *X-PEEM studies of protein interactions with patterned polymer surfaces*, 2000 ALS Compendium, LBNL publication (2001)
1. A.P. Hitchcock, I. Koprinarov, T. Tyliczszak, C. Morin, Y.M. Heng, R. Cornelius, J.L. Brash, H. Ade, S. Anders, A. Scholl and F. Notling, *X-ray Spectromicroscopy of Protein - Polymer Interactions* 1999 ALS Compendium, LBNL publication (2000)

A.2. Oral presentations

8. C. Morin, A.P. Hitchcock, R. Cornelius, J.L. Brash, A. Scholl, A. Doran, *Soft X-Ray Spectromicroscopy of Blood Proteins on Patterned Polymer Substrates* IUPAC Congress and Canadian Society for Chemistry, August 10-15, 2003
Ottawa, Ontario, Canada
7. C. Morin, *X-Ray SpectroMicroscopy of Proteins on Polymers*, McMaster University, Chemistry departmental seminar. May 29th, 2003
6. C. Morin, *X-ray microscopy of proteins and polymers*, ALS Science and Technology series, Oct 2002
Berkeley, California, USA
5. C. Morin, H. Ikeura-Sekiguchi, T. Tyliczszak, R. Cornelius, J.L. Brash, A.P. Hitchcock, A. Scholl, F. Nolting, G. Appel, A.D. Winesett, K. Kaznachejev, H. Ade, *Soft X-Ray Spectromicroscopy of Thin Film Polymer Blends* Canadian Society of Chemistry, 84th edition, May 26-30, 2001

Montréal, Québec, Canada

4. C. Morin, H. Ikeura-Sekiguchi, T. Tyliczszak, R. Cornelius, J.L. Brash, A.P. Hitchcock, A. Scholl, F. Nolting, G. Appel, A.D. Winesett, K. Kaznachejev, H. Ade, *Soft X-Ray Spectromicroscopy of Thin Film Polymer Blends*
Materials Research Society, April 16-20, 2001
San Francisco, California, USA
3. C. Morin, A.P. Hitchcock, I. Koprinarov, T. Tyliczszak, Y.M. Heng, R. Cornelius, J.L. Brash and A. Scholl, *X-Ray Spectromicroscopy Studies of Protein-Polymer Interactions*,
ALS User meeting, October 2000 (Student/pdf competition oral presentation)
Berkeley, California, USA
2. C. Morin, A. P. Hitchcock, I. Koprinarov, T. Tyliczszak, R. Cornelius, and J.L. Brash, *X-Ray Spectromicroscopy Studies of Protein-Polymer Interactions*
Canadian Biomaterials Conference 2000, 20th edition, August 22-25, 2000
McMaster University, Hamilton, Ontario, Canada
1. C. Morin, E. Zahidi, P. H. McBreen, *Adsorption du Cyclohexane sur le Carbure de Molybdène, β -Mo₂C*
Association Canadienne Française pour l'Avancement des Sciences, 66th edition,
May 1998
Université Laval, Sainte-Foy, Québec, Canada

A.3. Poster presentation

7. C.Morin, A.P. Hitchcock, T.Araki, R.Cornelius, J.L. Brash *Soft X-Ray Spectromicroscopy of Blood Proteins on Patterned Polymer Substrates*
Chemical Biophysics Conference, 3rd meeting, March 19-21, 2004
University of Toronto, Toronto, Ontario, Canada
6. C. Morin, A.P. Hitchcock, D.G. Castner, A. Scholl, A. Doran, *X-Ray PhotoEmission Electron Microscopy of micro-contact printed protein and polymer coated surfaces*
American Vacuum Society, 49th meeting, November 4-8, 2002
Denver, Colorado, USA
5. C. Morin, H. Ikeura-Sekiguchi, A.P. Hitchcock, A. Scholl, F. Nolting, A. Doran, G. Appel, D.A. Winesett, K. Kaznachejev, H. Ade, *X-ray Spectromicroscopy Studies of PS PMMA blends*
ALS Users' Meeting, Oct 2001
Berkeley, California, USA
4. C. Morin, A. P. Hitchcock, I. Koprinarov, T. Tyliczszak, R. Cornelius, and J.L. Brash, *Soft X-Ray Spectromicroscopy of Protein Adsorption on Polyurethanes*,
Canadian Light Source Users' Meeting, 3rd edition, November 17-18, 2000
University of Saskatchewan, Saskatoon, Canada
3. C. Morin, A.P. Hitchcock, I. Koprinarov, R. Cornelius and J.L. Brash, *Soft X-ray Spectromicroscopy of Protein Adsorption on Polyurethanes*,
American Vacuum Society, 47th edition, October 2-6, 2000

Boston, Massachusetts, USA

2. C. Morin, A. P. Hitchcock, I. Koprinarov, T. Tyliczszak, R. Cornelius, and J.L.

Brash, *X-Ray Spectromicroscopy Studies of Protein-Polymer Interactions*

Surface Canada 2000, 17th edition, May 22-24, 2000

Interface Science Western and *The University of Western Ontario*, London,

Ontario, Canada

1. C. Morin, E. Zahidi, P.H. McBreen, *Adsorption of Cyclohexane and*

Cyclohexanone on Molybdenum Carbide, β -Mo₂C,

Canadian Society of Chemistry, May, 1999

Toronto, Ontario, Canada

Appendix B

This appendix lists all the software packages which I used over the course of my PhD. They appear in alphabetical order below.

1. aXis2000

aXis2000 is a freeware program written in Interactive Data Language (IDL) by Adam Hitchcock, and it is available from <http://unicorn.mcmaster.ca/aXis2000.html>. It was used for the spectromicroscopy data analysis: images, stack and spectral analyses.

2. BAN

BAN is a general purpose data analysis program produced and distributed by Tolek Tyliczszak (former member of the Hitchcock group, now at the Advanced Light Source in Berkeley, tel. 510-486-5188). In some cases, it was used for fitting spectral peaks.

3. ISIS Draw2.4

ISIS Draw 2.4, from MDL Information Systems, Inc., is a program which specializes in two dimensional drawings of small molecules and polymers.

4. Microsoft Office, versions 97, 2000, XP and 2003

Word and Powerpoint were used to write reports and prepare oral and poster presentations. Excel was used for organizing data sets and cataloguing samples, performing regression analyses (on data not shown in this thesis) and making graphical representations.

5. Nanoscope III V5.12r2

This software, by Digital Instruments, was used to acquire and analyse the AFM images that were generated with the Digital Instruments, Nanoscope IIIA. This instrument is located in the Brockhouse Institute for Materials Research at McMaster.

6. NoteTab

Note Tab, by Fookes Software, is a text and HTML editor. It was used to format spectral files in order to use them in various software.

7. PaintShop Pro, version 4

PaintShop Pro, from JASC Incorporated, was used to write images as jpeg files for presentations. These images were either screen saved from the aXis2000 software, pasted from constructed figures in powerpoint, or read from other image formats from aXis2000 and other software.

8. Q-Analysis

Q-Analysis is the software provided by the Quesant Instrument Corporation for the acquisition and processing of AFM images obtained with the Q-Scope 350 AFM. This instrument is located at the Advanced Light Source in Berkeley.

9. Sigma Plot 6.0

Sigma Plot 6.0 (by Jandel Scientific) was used for graphical representations.

10. STXM GUI

This software, written by Tolek Tyliczszak and Peter Hitchcock, was used to acquire data at STXM 5.3.2. It controls the beamline (slit sizes and monochromator) and the microscope.

11. X-PEEM software packages

The software used for operating the X-PEEM at the ALS, PEEM2, are detailed in the following table. Except for Image Pro 4.0, the commercial camera software, these programs were written by various members of the PEEM2 team.

Table B.1 List of PEEM2 software

Program	Function	Computer
Frontend	monochromator, stigmator control, ring current recording	<i>bl7-49.als.lbl.gov (SUN)</i>
PEEM2power	PEEM power supplies, Hotdeck power supply	<i>bl7-49.als.lbl.gov (SUN)</i>
Image Pro 4.0	camera software, image analysis	Peem2 (PC)
Connect Sun	spectromicroscopy, interfaces PC – SUN	Peem2 (PC)

References

- [A85] J.D. Andrade, In *Surface and Interfacial Aspects of Biomedical Polymers*; Andrade, J.D., Ed.; Plenum Press: New York, 1985.
- [A92] H.W. Ade, *Nucl Instr. And Meth.*, A319 (1992) 311-319
- [A99] D. Attwood, *Soft X-Rays and Extreme Ultraviolet Radiation: Principles and Application*, Cambridge University Press, 1999
- [AAS&02] C. Abela-Formanek, M. Amon, G. Schild, J. Schauersberger, G. Heinze, A. Kruger, *J. Cataract Refract Surg.*, 28 (2002) 50-61.
- [AH93] H. Ade, B. Hsiao, *Science*, 262 (1993) 1427
- [AHG93] E. Apen, A.P. Hitchcock and J.L. Gland, *J. Phys. Chem.* 97 (1993) 6859
- [AHS&xx] T. Araki, A.P. Hitchcock, F. Shen, P. Chang, M. Wang, and R.F. Childs, *Biomaterials* (submitted)
- [APD&99] S. Anders, H. A. Padmore, R. M. Duarte, T. Renner, T. Stammer, A. Scholl, M. R. Scheinfein, J. Stöhr, L. Séve, Boris Sinkovic, *Rev. of Sci. Instrum.* 70 (1999) 3973-3981.
- [ASE98] H. Ade, in: J.A.R. Samson, D.L. Ederer (Eds.), *Experimental Methods in the Physical Sciences*, Vol. 32, Academic Press, New York, 1998, p. 225.
- [ASZ&96] H.Ade, A.P. Smith, G.R. Zhuang, B. Woods, I. Plotzker, E. Rightor, D.-J. Liu, S.-C. Lui, C. Sloop, *Synchrotron Radiation News*, 9 (1996) 31-39

- [ASZ&97] H.Ade, A.P. Smith, H. Zhang, G.R. Zhuang, J. Kirz, E. Rightor, A. Hitchcock, *J. Electron. Spectrosc. Relat. Phenom.*, 84 (1997) 53-72
- [AU84] D.T. Attwood, J.H. Underwood, *Physics Today*, 37 (1984) 44
- [AUS00] H. Ade, S.G. Urquhart, in: T.K. Sham (Ed.), *Chemical Applications of Synchrotron Radiation*, World Scientific Publishing, Singapore, 2000
- [AWS&98] H. Ade, D.A. Winesett, A.P. Smith, S. Anders, T. Stammer, C. Heske, D. Slep, M.H. Rafailovich, J. Sokolov, J. Stohr, *Appl. Phys. Lett.*, 73 (1998) 3775.
- [AWS&99] H. Ade, D.A. Winesett, A.P. Smith, S. Qu, S. Ge, J. Sokolov, M. Rafailovich, *Europhys. Lett.*, 45 (1999) 526.
- [AZC&92] H. Ade, X. Zhang, S. Cameron, C. Costello, J. Kirz, and S. Williams, *Science* 258 (1992) 972
- [B01] E. Bauer, *J. Phys. Condens. Matter*, 13 (2001) 11391
- [B80] A. Bianconi, *Appl. Surf. Sci.*, 6 (1980) 392
- [B85] C.E. Brion, *Comments At. Mol. Phys.*, 16 (1985) 249
- [BBF&92] C.J. Buckley, R.E. Burge, G.F. Foster, S.Y. Ali, C.A. Scotchford, J.H. Dunsmuir, S.R. Ferguson, M.L. Rivers, *SPIE Soft X-ray Microscopy*, 1741 (1992) 363-372
- [BEJ86] K.D. Bomben, C.J. Eyermann and W.L. Jolly, *A Table of Absolute Core Electron Binding Energies for Gaseous Atoms and Molecules*, January 1986 Edition

- [BFF&03] T. Beetz, M. Feser, H. Fleckenstein, B. Hornberger, C. Jacobsen, J. Kirz, M. Lerotic, E. Lima, M. Lu, D. Sayre, D. Shapiro, A. Stein, D. Tennant, S. Wirick, *Synchrotron Radiation News*, 16 (2003) 11-15
- [BFM&02] B. Wolf, O. Findl, R. Menapace, G. Rainer, S. Sacu, B. Kiss, V. Petternel, M. Georgopoulos, *J. Cataract Refract Surg.*, 28 (2002) 1105-1111.
- [BGS&87] G. Binnig, C. Gerber, E. Stoll, T. R. Albrecht, C.F. Quate, *Europhys. Lett.*, 3 (1987) 1281
- [BH80] S. D. Bruck and G. Hastings, *Biomaterials*, 1 (1980) 2
- [BIG99] J. Brandrup, E.H. Immergut, E.A. Grulke (Eds.), *Polymer Handbook, 4th Edition*, Wiley, 1999.
- [BLR&03] N.V. Bhagavan, E.M. Lai, P.A. Rios, J. Yang, A.M. Ortega-Lopez, H. Shinoda, S.A. Honda, C.N. Rios, C.E. Sugiyama, C.E. Ha, *Clin. Chem.*, 49 (2003) 581-585
- [BN00] A. Baszkin, W. Norde, *Physical Chemistry of Biological Interfaces*, Marcel Dekker, Inc., 2000
- [BPM&00] A.M. Botelho do Rego, O. Pellegrino, J.M.G. Martinho and J. Lopes da Silva, *Langmuir* 16 (2000) 2385.
- [BQG86] G. Binnig, C. F. Quate, C. Gerber, *Phys. Rev. Lett.*, 56 (1986) 930
- [BT87] A.L. Bloom, P.T. Thomas (Eds.), *Haemostasis and Thrombosis*, Churchill Livingstone, New York, 1987.
- [BVJ&00] J.H. Brown, N. Volkmann, G. Jun, A.H. Henschen-Edman, C. Cohen,

- Proc. Natl. Acad. Sci. U.S.A.* 97 (2000) 85.
- [C94] I.M. Campbell, *Introduction To Synthetic Polymers*, Oxford University Press, New York, 1994
- [CB81] B.M.C. Chan, J.L. Brash, *J. Colloid Interface Sci.*, 82 (1981) 217.
- [CB99] R.M. Cornelius and J. L. Brash, *Biomaterials*, 20 (1999) 341.
- [CBM&03] L. M. Croll, J. F. Britten, C. Morin, A. P. Hitchcock, H. D. H. Stöver, *J. Synchrotron Rad.*, 10 (2003) 265-268
- [CBO80] L.A. Cantarero, J.E. Butler, J.W. Osborne, *Anal. Biochem.*, 105 (1980) 375-382
- [CBP60] R.G. Craig, G.C. Berry, F.A. Peyton, *J. Phys. Chem.*, 64 (1960) 541.
- [CDA&97] A. Cossy-Favre, J. Diaz, S. Anders, H. Padmore, Y. Liu, M. Samant, J. Stöhr, H. Brown, T.P. Russell, *Acta Physica Polonica A*, 91 (1997) 923
- [CDL&98] A. Cossy-Favre, J. Diaz, Y. Liu, H.R. Brown, M.G. Samant, J. Stöhr, A.J. Hanna, S. Anders, T.P. Russell, *Macromolecules*, 31 (1998) 4957-4962
- [CGT&04] G. Cooper, M. Gordon, D. Tulumello, C.C. Turci, K. Kaznatcheyev and A.P. Hitchcock, *J. Electron Spectroscopy* (2004) in press.
- [CJW96] H. Chapman, C. Jacobsen and S. Williams, *Ultramicroscopy*, 62 (1996) 191
- [CN60] V.E. Cosslett, W.C. Nixon, *X-Ray Microscopy*, Cambridge University, Cambridge, 1960
- [CN99] S. C. Clear, P. F. Nealey, *J. Colloid Interface. Sci.*, 213 (1999) 238-250

- [COT&00] R.G. Chapman, E. Ostuni, S. Takayama, E. Homlin, L. Yan, G.M. Whitesides, *J. Am Chem. Soc.*, 122 (2000) 1848-1860
- [CR02] D.G. Castner, B.D. Ratner, *Surf. Sci.*, 500 (2002) 28-60
- [CUA02] T. Coffey, S. G. Urquhart, H. Ade, *J. Electron. Spectrosc. Relat. Phenom.*, 122 (2002) 65-78
- [D94] G. De Stasio, *Journal de Physique IV*, 4 (1994), C9-287
- [DCL&98] G. De Stasio, M. Capozzi, G.F. Lorusso, P. A. Baudat, T. C. Droubay, P. Perfetti, G. Margaritondo, B. P. Tonner, *Rev. Sci. Instrum.*, 69 (1998) 2062
- [DD75] J.L. Dehmer, D. Dill, *Phys. Rev. Lett.*, 35 (1975) 213
- [DD76] J.L. Dehmer, D. Dill, *J. Chem. Phys.*, 65 (1976) 5327
- [DDT&95] G. De Stasio, D. Dunham, B.P. Tonner, D. Mercanti, M.T. Ciotti, P. Perfetti, G. Margaritondo, *J. Synchrotron Rad.*, 2 (1995) 106-112
- [DFS&97] K. Dalnoki-Veress, J.A. Forrest, J.R. Stevens, J.R. Dutcher, *Physica A*, 239 (1997) 87
- [DM97] G. De Stasio, G. Margaritondo, *J. Electron. Spectrosc. Rel. Phenom.*, 84 (1997) 137-147
- [DSB&00] L. Dai, H.A.W. St John, J. Bi, P. Zientek, R.C. Chatelier, H.J. Griesser, *Surf. Interf. Anal.*, 29 (2000) 46-55.
- [DSD&02] T. Daynes, T. S. Spencer, K. Doan, N. Mamalis, R. J. Olson, *J Cataract Refract Surg*, 28 (2002) 1124-1129

- [E66] A. Engström, in *Physical Techniques in Biological Research*, 2nd ed., edited by A. W. Pollister (Academic, New York, 1966), Vol. 3, part A, p. 87
- [EAI&87] H. Elwing, A. Askendal, B. Ivarsson, U. Nilsson, S. Welin, I. Lundstrom, *Am. Chem. Soc. Symp. Ser.*, 343 (1987) 468.
- [EKR&91] W. Engel, M.E. Kordesch, H.H. Rothermund, S. Kubala, and A. von Oertzen, *Ultramicroscopy*, 36 (1991) 148
- [EWA&87] H. Elwing, S. Welin, A. Askendal, U. Nilsson, I. Lundstrom, *J. Colloid Interface Sci.*, 119 (1987) 203.
- [F92] J. Frommer, *Angew. Chem. Int. Ed. Engl.*, 31 (1992) 1298-1328
- [FCJ&98] M. Feser, M. Carlucci-Dayton, C. Jacobsen, J. Kirz, U. Neuhausler, G. Smith, B. Yu, *X-ray Microfocusing: Applications and Techniques, I. McNulty (Ed.), SPIE Proc.*, 3449 (1998) 19.
- [FPF&92] T.W. Ford, A.M. Page, G.F. Foster, A.D. Stead, *SPIE Soft X-ray Microscopy*, 1741 (1992) 325-332
- [FPW&02] J. Feng, H. Padmore, D.H. Wei, S. Anders, Y. Wu, A. Scholl, D. Robin, *Review of Scientific Instruments*, 73 (2002) 1514
- [FWU&97] R. Fink, M.R. Weiss, E. Umbach, D. Preikszas, H. Rose, R. Spehr, P. Hartel, W. Engel, R. Degenhardt, R. Wichtendahl, H. Kuhlenbeck, W. Erlebach, K. Ihmann, R. Schlögl, H.-J. Freund, A.M. Bradshaw, G. Lilienkamp, Th. Schmidt, E. Bauer, G. Benner, *J. Electron. Spectrosc.* 84 (1997) 231

- [G78] W. Gudat, *Nucl. Instrum. Methods*, 152 (1978) 279
- [GCA&03] M. Gordon, G. Cooper, T. Araki, C. Morin, C.C. Turci, K. Kaznatcheev, A.P. Hitchcock, *J. Phys. Chem. A*, 107 (2003) 6144–6159.
- [H48] D.C. Harris, *Quantitative Chemical Analysis, 3rd Edition*, W.H. Freeman and Company, New York, 1948
- [H61] B.L. Henke, in *The Encyclopedia of Microscopy*, edited by G.L. Clark, Reinhold, New York, 1961
- [H78] P. Horowitz, *Ann. N.Y. Acad. Sci.*, 306 (1978) 203
- [H82] A.P. Hitchcock, *J. Electron. Spectrosc.* 25 (1982) 245
- [Hxx] A.P. Hitchcock, et al., private communication.
- [H93] T.A. Horbett, *Cardiovasc. Pathol.*, 2 (1993) 137S-148S
- [H97] R. Herrington, *Flexible Polyurethane Foams*, 2 ed., The DOW Chemical Company (1997).
- [H01] A.P. Hitchcock, *J. Synchrotron Radiation*, 8 (2001) 66
- [HGD93] B.L. Henke, E.M. Gullikson, J.C. Davis, *At. Data Nucl. Data Tables* 54 (1993) 181
- [HH72] P. Horowitz, J.A. Howell, *Science*, 178 (1972) 608
- [HHT90] G. R. Harp, Z-L Han, B. P. Tonner, *Phys. Scrip.*, T31 (1990) 25
- [HK84] F. J. Himpsel, R.W. Klaffky, SPIE Conference Proceedings Vol. 447 (SPIE, Bellingham, WA, 1984)

- [HKT&00] A.P. Hitchcock, I.N. Koprinarov, T. Tyliczszak, C. Morin, Y.M. Heng, R. Cornelius, J.L. Brash, H. Ade, S. Anders, A. Scholl, F. Notling, *ALS Compendium*, **2000**, LBNL publication, 47838.
- [HKT&01] A.P. Hitchcock, I.N. Koprinarov, T. Tyliczszak, E.G. Rightor, G.E. Mitchell, M.T. Dineen, F. Hayes, W. Lidy, R.D. Priester, S.G. Urquhart, A.P. Smith, H. Ade, *Ultramicroscopy* **88** (2001) 33-49
- [HLT&82] B.L. Henke, P. Lee, T.J. Tanaka, R.L. Shimabukuro, B.K. Fujikawa, *At. Nucl. Data Tables* **27** (1982) 1.
- [HMH&02] A.P. Hitchcock, C. Morin, H. M. Heng, R.M. Cornelius, J.L. Brash, *J. Biomaterials Science Polymer Ed.*, **13** (2002) 919-938.
- [HMT&02] A.P. Hitchcock, C. Morin, T. Tyliczszak, I.N. Koprinarov, H. Ikeura-Sekiguchi, J.R. Lawrence and G.G. Leppard, *Surface Reviews and Letters*, **9** (2002) 193-202.
- [HMZ&04] A. P. Hitchcock, C. Morin, X. Zhang, T. Araki, J. Dynes, H. Stöver, J. Brash, J. R. Lawrence, G.G. Leppard, *J. Electron. Spectrosc. Rel. Phenom.*, accepted for publication
- [HRP&93] D.K. Han, G.H. Ryu, K.D. Park, S.Y. Jeong, Y.H. Kim, B.G. Min, *J. Biomater. Sci. Polym. Ed.*, **4** (1993) 401.
- [HRS72] T.A. Hall, H.O.E. Rockert, R.L. deC. Saunders, *X-Ray Microscopy in Clinical and Experimental Medicine* (C.C. Thomas, Springfield, IL, **1972**).
- [HSH&85] J.A. Horsley, J. Stöhr, A.P. Hitchcock, D.C. Newbury, A.L. Johnson and F. Sette, *J. Chem. Phys.*, **83** (1985) 6099

- [IH87] I. Ishii, A.P. Hitchcock, *J.Chem. Phys.*, 87 (1987) 830-839
- [IML&94] A. Irtel von Brenndorff, M.M. Moronne, C. Larabell, P. Selvin, W. Meyer-Ilse, *X-Ray Microscopy IV: Proceedings of the Fourth International Conference, Chernogolovka, Russia, September 20-24, 1993* (ed. by V.V. Aristov and A.I. Erko). Bogorodskii Pechatnik, Chernogolovka
- [ISN&99] Y. Iwasaki, S.-I. Sawada, N. Nakabayashi, G. Khang, H.B. Lee, K. Ishihara, *Biomaterials*, 20 (1999) 2185-2191
- [JCF&96] C. Jacobsen, H.N. Chapman, J. Fu, A. Kalinovsky, J. Kirz, J. Maser, A. Osanna, S. Spector, D. Tennant, S. Wang, S. Wirick, X. Zhang, *J. Electron. Spectrosc. Rel. Phenom.*, 80 (1996) 337
- [JK98] C. Jacobsen, J. Kirz, *Natural Structural Biology, Synchrotron Supplement*, August 1998, 650-653
- [JAK&92] C. Jacobsen, H. Ade, J. Kirz, C.-H. Ko, S. Williams, X. Zhang, E. Anderson, D. Kern, *Scanning soft X-ray microscopy*, in (Eds.) P.B. Kenway, P.J. Duke, G.W. Lorimer, T. Mulvey, I.W. Drummond, G. Love, A.G. Michette, M. Stedman, *X-ray Optics and Microanalysis*, 1992 Bristol, 10P Publishing 571
- [JWA&91] C. Jacobsen, S. Williams, E. Anderson, M.T. Browne, C.J. Buckley, D. Kern, J. Kirz, M. Rivers, X. Zhang, *Optics Communications*, 86 (1991) 351-364
- [JWF&00] C. Jacobsen, S. Wirick, G. Flynn, C. Zimba, *J. Microsc.*, 197 (2000) 173

- [JWR&91] B.E. Jarrell, S.K. Williams, D. Rose, D.Garibaldi, C. Talbot, B. Kapelan, *J. of Biomed. Eng.*, 113(2) (1991), 120-122.
- [K20a] W. Kossel, *Z. Phys.*, 1 (1920) 119
- [K20b] W. Kossel, *Z. Phys.*, 2 (1920) 470
- [K31] R. de L. Kronig, *Z. Phys.*, 70 (1931) 317
- [K32] R. de L. Kronig, *Z. Phys.*, 75 (1932) 468
- [KA86] J. Kirz and D.T. Attwood, Center for X-ray Optics, *X-ray Data Booklet*, Lawrence Berkeley Lab, Rev 1 (1986)
- [KHL&01] I.N. Koprinarov, A.P. Hitchcock, W.H. Li, Y.M. Heng, H.D.H. Stover, *Macromolecules*, 34 (2001) 4424.
- [KHM&02] I.N. Koprinarov, A.P. Hitchcock, C. McCrory, R.F. Childs, *J. Phys. Chem. B* 106 (2002) 5358
- [KJH95] J. Kirz, C. Jacobsen, M. Howells, *Q. Rev. Biophys.*, 28 (1995) 33-130
- [KKA&94] C.-H. Ko, J. Kirz, H. Ade, E. Johnson, S. Hulbert, E. Anderson, *Rev. Sci. Instrum.*, 66 (1995) 1416
- [KLW&97] E. Kumacheva, L. Li, M.A. Winnik, D.M. Shinozaki, P.C. Cheng, *Langmuir*, 13 (1997) 2483.
- [KOJ&02] K. Kaznachev, A. Osanna, C. Jacobsen, O. Plashkevych, O. Vahtras, H. Ågren, V. Carravetta and A.P. Hitchcock, *J. Phys. Chem. B*, 106 (2002) 3153
- [KP57] P. Kirkpatrick, H.H. Pattee, Jr., in *Hanbuch der Physik*, edited by S. Flügge (Springer, Berlin, 1957), Vol. 30

- [KR85] J. Kirz, H. Rarback, *Rev. Sci. Instrum.*, 56 (1985) 1-13
- [KS80] J. Kirz, D. Sayre, in *Synchrotron Radiation Research*, edited by H. Winick and S. Doniach, Plenum, New York, 1980
- [KSK&98] A. Karim, T.M. Slaweck, S.K. Kumar, J.F. Douglas, S. Satija, C.C. Han, T.P. Russell, Y. Liu, R. Overney, J. Sokolov, M.H. Rafailovich, *Macromolecules*, 31 (1998) 857
- [KTS&03] A.L.D. Kilcoyne, T. Tyliszczak, W.F. Steele, S. Fakra, P. Hitchcock, K. Franck, E. Anderson, B. Harteneck, E.G. Rightor, G.E. Mitchell, A.P. Hitchcock, L. Yang, T. Warwick and H. Ade, *J. Synchrotron Rad.*, 10 (2003) 125
- [KVE&00] G.L. Kenausis, J. Voros, D.L. Elbert, N. Huang, R. Hofer, L. Ruiz-Taylor, M. Textor, J.A. Hubbell, N.D. Spencer, *J. Phys. Chem. B*, 104 (2000) 3298-3309
- [KYG&96] H. Kihara, A. Yamamoto, P. Guttmann, G. Schmahl, *J. Electron. Spectrosc. Rel. Phenom.*, 80 (1996) 369
- [L36] P. Lamarque, *C.R. Acad. Sci.*, 202 (1936) 684
- [LC96] J.-T. Li, K.D. Caldwell, *Coll. Surf. B: Biointerfaces*, 7 (1996) 9-22
- [LCP&00] K.H. Lin, J.C. Crocker, V. Prasad, A. Schofield, D.A. Weitz, T.C. Lubensky and A.G. Yodh, *Phys Rev Lett.*, 85 (2000) 1770
- [LFR&97] P. Lanza, B. Felding-Habermann, Z.M. Ruggeri, M. Zanetti, R. Billetta, *Blood Cells, Molecules, and Diseases*, 23 (1997) 230-241
- [LL04] C.A. Larabell, M.A. Le Gros, *Mol. Biol. Cell*, 15 (2004) 957-962

- [LP01] B. Loo, N.D. Padliya, *Multivariate Statistical Analysis Applied to X-Ray Spectromicroscopy*, Chemistry 4G06 thesis, Chemistry Department, McMaster University, April 2001
- [LRR&93] G.P. Lopez, B.D. Ratner, R.J. Raposa, T.A. Horbett, *Macromolecules*, 26 (1993) 3247-3253
- [LSH&01] B.W. Loo, Jr., I.M. Sauerwald, A.P. Hitchcock and S.S. Rothman, *J. Microscopy*, 204 (2001) 69.
- [LSL&03] J.R. Lawrence, G. D.W. Swerhone, G.G. Leppard, T. Araki, X. Zhang, M.M. West and A.P. Hitchcock, *Applied Environmental Microbiology*, 69 (2003) 5543
- [LT36] P. Lamarque, J. Turchini, *C. R. Soc. Biol. Paris*, 122 (1936) 294
- [LTJ92] R.A. London, J.E. Trebes, C.J. Jacobsen, *SPIE Soft X-ray Microscopy*, 1741 (1992) 333-340
- [LYM00] C.A. Larabell, D. Yager, W. Meyer-Ilse, *X-Ray Microscopy: Proceedings of the VI International Conference on X-Ray Microscopy, Berkeley, August 2-6, 1999*, (ed. By W. Meyer-Ilse, T. Warwick and D.T. Attwood), pp. 107-112. AIP Conference Proceedings 507. American Institute of Physics, College Park.
- [M92] E.W. Merrill, J.M. Harris (Ed.), *Poly(ethylene glycol) chemistry: Biotechnical and biomedical applications*, Plenum Press, New York, 1992, pp. 199-220

- [MB93] A.G. Michette, C.J. Buckley, *X-ray Science and Technology*, The Institute of Physics, **1993**
- [M99] M.M. Moronne, *Ultramicroscopy*, 77 (**1999**) 23-26
- [MBL&97] E.L. Montei, V.W. Ballarotto, M.E. Little, M.E. Kordesch, *J. Electron. Spectrosc. Rel. Phenom.*, 84 (**1997**) 129
- [MC99] M. Morra, C. Cassinelli, *Langmuir*, 15 (**1999**) 4658-4663
- [MDG&00] W. Meyer-Isle, G. Denbeaux, G. Johnson, L.E. Bates, W. Lucero, A. Anderson, *X-Ray Microscopy: Proceedings of the VI International Conference on X-Ray Microscopy, Berkeley, August 2-6, 1999*, (ed. By W. Meyer-Isle, T. Warwick and D.T. Attwood), pp. 129-134. AIP Conference Proceedings 507. American Institute of Physics, College Park.
- [MHC&04] C. Morin, A.P. Hitchcock, R.M. Cornelius, J.L. Brash, S.G. Urquhart, A. Scholl, A. Doran, *J. Electron. Spectrosc.*, 137 (**2004**) 785
- [MHI&02] C. Morin, A.P. Hitchcock, H. Ikeura-Sekiguchi, A. Scholl, A. Doran, K. Kaznatcheyev, *2001 ALS Compendium*, LBNL Publication, **2002**.
- [MHL&xx] C. Morin, A.P. Hitchcock, L. Li, X. Zhang, T. Araki, A. Scholl, A. Doran, private communication
- [MHT&95] I. McNulty, W.S. Haddad, J.E. Trebes, E.H. Anderson, *Rev. Sci. Instrum.*, 66 (**1995**) 1431

- [MIT&01] C. Morin, H. Ikeura-Sekiguchi, T. Tyliczszak, R. Cornelius, J.L. Brash, A.P. Hitchcock A. Scholl, F. Nolting, G. Appel, A. D. Winesett, K. Kaznachejev and H. Ade, *J. Electron. Spectrosc.*, 121 (2001) 203.
- [MLH&97] P. Mansky, Y. Liu, E. Huang, T.P. Russell, C. Hawker, *Science*, 275 (1997) 1458.
- [MOW&00] J. Maser, A. Osanna, Y. Wang, C. Jacobsen, J. Kirz, S. Spector, B. Winn, and D. Tennant, *J. Microscopy*, 197 (2000) 68.
- [MR97] S. Magonov, D. H. Reneker, *Annu. Rev. Mater. Sci.*, 27 (1997) 175-222
- [MRY99] M.N. Mar, B.D. Ratner, S.S. Yee, *Sensors and Actuators B*, 54 (1999) 125-131
- [MWD&02] G.E. Mitchell, L.R. Wilson, M.T. Dineen, S.G. Urquhart, F. Hayes, E.G. Rightor, A.P. Hitchcock, H. Ade, *Macromolecules*, 35 (2002) 1336-1341
- [NVL 87] A. Noy, D. V. Vezenov, C. M. Lieber, *Annu. Rev. Mater. Sci.*, 27 (1997) 381- 421
- [P] H. Padmore, private communication
- [P80] D. Parsons, *Ultrasoft X-ray Microscopy; Its Applications to Biological and Physical Sciences*, New York Academy of Science, New York, 1980
- [PBA&98] A.P. Smith, C. Bai, H. Ade, R. J. Spontak, C. M. Balik, C. C. Koch *Macromol. Rapid Commun.* 19 (1998) 557-561
- [PS03] R.J. Phaneuf, A.K. Schmid, *Physics Today*, March 2003, 50-5599

- [PW93] K.L. Prime, G.M. Whitesides, *J. Am. Chem. Soc.*, 115 (1993) 10714-10721
- [Q94] C. F. Quate, *Surf. Sci.*, 299/300 (1994) 980-995
- [QCL&97] S. Qu, C.J. Clarke, Y. Liu, M.H. Rafailovich, J. Sokolov, K.C. Phelan, G. Krausch, *Macromolecules*, 30 (1997) 3640.
- [R83] H.M. Rarback, *The development of a scanning soft X-ray microscope*, Ph.D. thesis, Department of Physics, State University of New York at Stony Brook, 1983
- [R84] E. Regoeczi, *Iodine-Labeled Plasma Proteins*, vol. 1, CRC Press, Boca Raton, FL, 1984.
- [R93a] B.D. Ratner, *J. Biomed. Mater. Res.*, 27 (1993) 283-287
- [R93b] B.D. Ratner, *J. Biomed. Mater. Res.*, 27 (1993) 837-850
- [R97] B.D. Ratner, *J. Moc. Rec.*, 9 (1997) 617-625
- [R98] B.D. Ratner, *Macromol. Symp.*, 130 (1998) 327-335
- [REK&91] H.H. Rotermund, W. Engel, S. Jakubith, A. von Oertzen, G. Ertl, *Ultramicroscopy*, 36 (1991) 164
- [RH90] R.J. Rapoza, T.A. Horbett, *J. Biomed. Mater. Res.*, 24 (1990) 1263.
- [RHA&97] E.G. Rightor, A.P.Hitchcock, H.Ade, R.D. Leapman, S.G. Urquhart, A.P.Smith, G. Mitchell, D. Fischer, H.J. Shin, and T. Warwick, *J. Phys. Chem. B*, 101 (1997) 1950-1960
- [RMU&02] E.G. Rightor, G.E. Mitchell, S.G. Urquhart, A.P. Smith, H. Ade, A.P. Hitchcock, A. Aneja and R.J. Wilkes, *Macromolecules*, 35 (2002) 5873.

- [S81] P. R. Stuart, in *Microfocal Radiography*, edited by R.V. Ely, (Academic, London, **1981**)
- [S83] E. Spiller, in *Handbook on Synchrotron Radiation*, Vol. 1, edited by E.E. Koch, North-Holland, Amsterdam, **1983**
- [S92] J. Stohr, *NEXAFS Spectroscopy*, Series in Surface Science, Vol. 25, Springer, Berlin, **1992**.
- [SA96] A.P. Smith and H. Ade, *Appl. Phys. Lett.*, 69 (**1996**) 3833.
- [SAR&98] D. Slep, J. Asselta, M.H. Rafailovich, J. Sokolov, D.A. Winesett, A.P. Smith, H. Ade, Y. Strzhemechny, S.A. Schwarz, B.B. Sauer, *Langmuir*, 14 (**1998**) 4860.
- [SAR&00] D. Slep, J. Asselta, M.H. Rafailovich, J. Sokolov, D.A. Winesett, A.P. Smith, H. Ade, S. Anders, *Langmuir*, 16 (**2000**) 2369.
- [SC95] D. Sayre, H.N. Chapman, *Acta Crystallogr. A*, 51 (**1995**) 237.
- [SDN82] G. Schmahl, D. Rudolph, and B. Niehmann, in *Uses of Synchrotron Radiation in Biology*, edited by H. Stuhrmann, Academic, London, **1982**
- [SGF&02] T. Schmidt, U. Groh, R. Fink, E. Umbach, O. Schaff, W. Engel, B. Richter, H. Kühlenbeck, R. Schlögl, H.-J. Freund, A.M. Bradshaw, D. Preikszas, P. Hartel, R. Spehr, H. Rose, G. Lilienkamp, E. Bauer, G. Benner, *Surf. Rev. Lett.*, 9 (**2002**) 223
- [SGS&00] T. Schmitt, P. Guttman, O. Schmidt, P. Müller-Buschbaum, M. Stamm, G. Schonhense, G. Schmahl, *X-ray Microscopy, Publishing*, 571. *AIP Conf. Proc.*, 507 (**2000**) 245, editors: W. Meyer Ilse, T. Warwick and D.

Attwood.

- [SH91] S.M. Slack, T.A. Horbett, *J. Biomater. Sci. Polym. Ed.*, 2 (1991) 227.
- [SJ82] J. Stohr, R. Jaeger, *Phys. Rev. B*, 26 (1982) 4111
- [SMG&02] M.Y. Speer, M.D. McKee, R.E. Guldberg, L. Liaw, H.Y. Yang, E. Tung, G. Karsenty, C.M. Giachelli, *J Exp Med*, 196 (2002) 1047-1055
- [SML&02] S. A. Steitz, M.D. McKee, L. Liaw, C.M. Giachelli, *Amer J Path*, 16 (2002) 2035-2046
- [SNG&95] G. Schneider, B. Niehmann, P. Guttmann, D. Rudolph, G. Schmahl, *Synchrotron Radiation News*, 8 (1995) 19-28
- [SR84] G. Schmahl, D. Rudolph, *X-Ray Microscopy*, Springer, Berlin, 1984
- [SSC&01] S.A. Steitz, M.Y. Speer, G. Curinga, H. Ying-Yang, P. Haynes, R. Aebersold, T. Schinke, G. Karsenty, C.M. Giachelli, *Circ Res*, 89(12) (2001) 1147-1154
- [TAG&01] A.C. Thompson, D.T. Attwood, E.M. Gullikson, M.R. Howells, J. B. Kortright, A.L. Robinson, J. H. Underwood, K-J. Kim, J. Kirz, I. Lindau, P. Pianetta, H. Winick, G.P. Williams, J. H. Scofield, D. Vaughan, *X-ray Data Booklet, Lawrence Berkeley Lab, Rev.2* (2001)
- [TB85] W. Telieps, E. Bauer, *Surf. Sci.*, 162 (1985) 163
- [TDD&95] B.P. Tonner, D. Dunham, T. Droubay, J. Kimuna, J. Denliger, E. Rotenberg, A. Warwick, *J. Electron. Spectrosc. Relat. Phenom.*, 75 (1995) 309
- [TH88] B. P. Tonner, G. R. Harp, *Rev. Sci. Instrum.*, 59 (1988) 853

- [THK&92] B.P.Tonner, G.R. Harp, S.F. Koranda, J. Zhang, *Rev. Sci. Instrum.*, 63 (1992) 564
- [TKB02] M. Tirrell, E. Kokkoli, M. Biesalski, *Surf. Sci.* 500 (2002) 61.
- [TPY00] S. Thanigaraj, A. Panneerselvam, J. Yanos, *CHEST*, 117 (2000) 1209–1211
- [TR91] R. M. Tromp, M.C. Reuter, *Ultramicroscopy*, 36 (1991) 99
- [TSD&00] C. Thon-That, A.G. Shard, R. Dalay, R.H. Bradley, *Macromolecules*, 33 (2000) 8453.
- [TSK&00] T. Thurn-Albrecht, J. Schotter, C.A. Kastle, N. Emley, T. Shibauchi, L. Krusin-Elbaum, K. Guarini, C.T. Black, M.T. Tuominen, T.P. Russell, *Science*, 290 (2000) 2126.
- [TST&01] C. Thon-That, A.G. Shard, D.O.H. Teare, R.H. Bradley, *Polymer*, 42 (2001) 1121.
- [TTK99] K. Tanaka, K. Takahara, T. Kajiyama, *Macromolecules*, 29 (1999) 3232.
- [TTT&85] K.Takayanagi, Y. Tanishiro, S. Takahashi, M. Takahashi, *Surf. Sci.*, 164 (1985) 367
- [UAS&99] S.G. Urquhart, H. Ade, A.P. Smith, A.P. Hitchcock, E.G. Rightor and W. Lidy, *J. Physical Chemistry B*, 103 (1999) 4603.
- [UHL&95] S.G. Urquhart, A.P. Hitchcock, R.D. Leapman, R.D. Priester and E.G. Rightor, *J. Polymer Science B: Polymer Physics*, 33 (1995) 1593.
- [UHS&99] S.G. Urquhart, A.P. Hitchcock, A.P. Smith, H. Ade, W. Lidy, E.G. Rightor and G.E. Mitchell, *J. Electron Spectrosc.*, 100 (1999) 119.

- [W70] S. Wu, *J. Phys. Chem.*, 74 (1970) 632
- [W84] A.D. Wilson, *X-Ray Lithography and Applications of Soft X Rays to Technology*, SPIE Conference Proceedings Vol. 448 (SPIE, Bellingham, WA, 1984).
- [W87] D.F. Williams, *Progress in Biomedical Engineering: Definitions in Biomaterials*. Elsevier (1987)
- [W94] H. Winick, *Synchrotron Radiation Sources A Primer*, Series on Synchrotron Radiation Techniques and Applications –Volume 1, World Scientific, Singapore, 1994
- [W95] S.K. Williams, *Cell Transplantation*, 4 (1995) 401-410
- [W01] J. J. Weems, *Postgraduate Medicine*, 110, No. 4 (2001) 24-36
- [WAB&00] B. Winn, H. Ade, C. Buckley, M. Feser, M. Howells, S. Hulbert, C. Jacobsen, K. Kaznatcheyev, J. Kirz, A. Osanna, J. Maser, I. McNulty, J. Miao, T. Oversluisen, S. Spector, B. Sullivan, Y. Wang, S. Wirick, H. Zhang, *J. Sunchrotron Rad.*, 7 (2000) 395-404
- [WAK&02] T. Warwick, H. Ade, D. Kilcoyne, M. Kritscher, T. Tyliczszak, S. Fakra, A. Hitchcock, P. Hitchcock, H. Padmore, *J. Synchrotron Rad.*, 9 (2002) 254-257.
- [WBH81] H. Winick, G. Brown, K. Halbach and J. Harris, *Physics Today*, May 1981, 50-63

- [WBM&97] S. Walheim, M. Boltau, J. Mlynek, G. Krausch, U. Steiner, *Macromolecules*, 30 (1997) 4995.
- [WBV73] G.R. Wright, C.E. Brion, M.J. van der Wiel, *J. Electron Spectrosc.*, 1 (1973), 457
- [WFK&98] T. Warwick, K. Franck, J.B. Kortright, G. Meigs, M. Moronne, S. Myneni, E. Rotenberg, S. Seal, W. F. Steele, H. Ade, A. Garcia, S. Cerasari, J. Denlinger, S. Hayakawa, A.P. Hitchcock, T. Tyliczszak, J. Kikuma, E.G. Rightor, H.-J. Shin, B.P. Tonner, *Rev. of Sci. Instrum.*, 69 (1998) 2964-2973.
- [WGT98] A. Welle, M. Grunze, D. Tur, *J. Colloid Interf. Sci.*, 197 (1998) 263-274
- [WJ96] S.K. Williams, B.E. Jarrell, *Nature Medicine*, 2 (1996) 32-34.
- [WJK94] S.K. Williams, B.E. Jarrell, L.B. Kleinert, *Journal of Investigative Surgery*, 7 (1994) 503-517
- [WJK&95] S. Williams, C. Jacobsen, J. Kirz, J. Maser, S. Wirick, H. Ade, M. Rivers, *Rev. Sci. Instrum.*, 66 (1995) 1271
- [WJM&00] Y. Wang, C. Jacobsen, J. Maser, A. Osanna, *J. Microsc.*, 197 (2000) 80
- [WLL&97] R.N. Watts, S. Liang, Z.H. Levine, T.B. Lucatorto, F. Polack, M.R. Scheinfein, *Rev. Sci. Instrum.*, 68 (1997) 3464
- [WMR&97] L. A. Wenzler, G. L. Moyes, G. N. Raikar, R. L. Hansen, J. M. Harris, T. P. Beebe, Jr., *Langmuir*, 13 (1997) 3761-3768

- [WPA98] T. Warwick, H. Padmore, H. Ade, *Proc. SPIE*, 3449 (1998) 12-18
- [WRJ94] S.K. Williams, D.G. Rose, B.E. Jarrell, *Journal of Biomedical Materials Research*, 28 (1994) 203-212.
- [WSM&99] S. Walheim, E. Schaffer, J. Mlynek, U. Steiner, *Science*, 283 (1999) 520
- [WSQ&98] J.G. Wagner, D.W. Schmidtke, C.P. Quinn, T.F. Fleming, B. Bernacky, A. Heller, *Proc. Natl. Acad. Sci. USA*, 95 (1998) 6379-82
- [WZS&00] D.A. Winesett, S. Zhu, J. Sokolov, M. Rafailovitch, H. Ade, *J. High Perf. Polymers*, 49 (2000) 458.
- [YAM&02] A.T. Young, E. Arenholz, S. Marks, R. Schlueter, C. Steier, H. A. Padmore, A.P. Hitchcock and D.G. Castner, *J. Synchrotron Rad.* 9 (2002) 270
- [YS02] Y. Yamamoto, K. Shinohara, *Anat Rec (New Anat)* 269 (2002) 217-223
- [ZBM&96] X. Zhang, R. Balhorn, J. Mazrimas, J. Kirz, *J. Struc. Biol.*, 116 (1996) 355.

Thode

R

857

. M3 M67

2004

c.2